ISSN 2187-2260

Proceedings of the 13th Meeting of Japan CF Research Society, JCF13

December 8 - 9, 2012
WincAichi, Nagoya, Japan

Japan CF-Research Society

Edited by Akira Kitamura

PREFACE

This is the Proceedings of the 13th Meeting of Japan CF-Research Society (JCF13), which was held at Winc-Aichi, Nagoya, Japan on December 8 - 9, 2012. In this meeting were given 20 oral presentations, out of which 17 papers were submitted for the proceedings to the editorial board, and 3 presentations were left unsubmitted as the JCF13 proceedings papers to avoid duplication with those submitted to Proc. ICCF17. The submitted papers have been peer-reviewed by referees, and accepted for publication either as-is or after some revision.

We publish the Proceedings on our web-site, http://jcfrs.org/proc_jcf.html, as well as the Abstracts of all the presentations, http://jcfrs.org/JCF13/jcf13-abstracts.pdf. For almost all meetings after JCF4, we published electronic versions of the Proceedings in addition to their printed versions. However, in view of efficiency and effectiveness in distributing information, we decided to discontinue the printed version for the last meeting, JCF12. Only the electronic version will be published hereafter. Needless to say, any responses from the world scientists will be welcomed.

We, Japan CF-Research Society members, have started the research of the cold fusion more than two dozens of years ago. The cold fusion has a potential ability to establish a small-scale, radiationless nuclear reactor, and hopefully to shorten half-lives of radioactive wastes by nuclear transmutation. We believe that our approach is one of the most challenging way not only to realize an environmentally-sound nuclear power system with zero emission of the greenhouse gases and other harmful oxides, but also to develop a novel technique for disposal of the nuclear wastes produced mainly by fission reactors.

Recently, we find a few grandstanding activities based apparently on commercial purposes on various internet sites. We believe, however, that priority has to be given to clarification of the underlying physics and development of scientifically firm and sound technology. It is therefore very important for us to continue and further develop scientific approach.

Finally, we would like to thank all the participants, and also the people who have collaborated in organizing this meeting. In particular, we would appreciate the moral and material support by The Thermal & Electric Energy Technology Inc. Foundation.

Editor-in-Chief
Akira Kitamura, Technova Inc.
May 2013

CONTENTS

The Quantum States of the System Including Two Species of Charged Bosons in Ion Traps

Ken-ichi TSUCHIYA†, Shinnosuke KIKUCHI and Soichiro ASAMI

Department of Chemical Science and Engineering, Tokyo National College of Technology, 1220-2 Kunugida, Hachioji, Tokyo 193-0997, Japan

† e-mail: tsuchiya@tokyo-ct.ac.jp

Abstract

Using equivalent linear two-body (ELTB) method developed by Y.E.Kim et al. [1], we have considered the method for the numerical calculation in order to obtain the self-consistent states of the system including two species of positively charged bosons in ion trap. We have calculated the quantum states of two cases. One is the mixture of D^+-$^6Li^+$and the other is D^+-$^{58}Ni^{2+}$. The self-consistent solutions are obtained successfully.

1. Introduction

Y.E.Kim et al. have developed the theory of cold fusion based on Bose-Einstein Condensation (BEC) using equivalent linear two-body (ELTB) method [1]. Furthermore, they have applied the theory to the system including two species of positively charged bosons in ion trap [2] in order to explain the Rossi's experiments [3]. In their experiments of hydrogen permeation into Ni powder, excess heat was generated and Cu was produced.

In the work of Y.E.Kim, it was suggested that nuclear fusions between $D^+$and $^6Li^+$were induced [1]. Moreover, Rossi reported the transmutation from Ni to Cu. In this study, we have performed the numerical calculations based on Kim's theory for the mixture of positively charged two bosons in ion traps by choosing D^+, $^6Li^+$and $^{58}Ni^{2+}$as the positively charged bosons. As a result, we have obtained self-consistent quantum states of the mixture of D^+-$^6Li^+$and D^+-$^{58}Ni^{2+}$in an ion trap.

2. Theoretical Background

At the begining, we show the relations between the charge distributions n_i for boson i and the electro-static potentials W_i, where the two species are labeled by $i = 1, 2$. It is well-known as the Poisson's equation which is written as

$$\nabla^2 W_i(\mathbf{r}) = -\frac{e^2}{\varepsilon_0} Z_i \left\{ Z_i n_i(\mathbf{r}) + Z_j n_j(\mathbf{r}) \right\}, \tag{1}$$

where eZ_i is the charge of an ionized boson i and ε_0 means the dielectric constant

of the vacuum. If we use the Green's function for Helmholtz equation, we obtain Poisson's equation in integral form as

$$W_i(\mathbf{r}) = \int d\mathbf{r}' G_k(\mathbf{r}-\mathbf{r}') \left[\frac{e^2}{\varepsilon_0} Z_i \left\{ Z_i n_i(\mathbf{r}') + Z_j n_j(\mathbf{r}') \right\} + k^2 W_i(\mathbf{r}') \right]. \tag{2}$$

The Green's function for Helmholtz equation is defined as

$$G_k(\mathbf{r}-\mathbf{r}') = \frac{e^{-k|\mathbf{r}-\mathbf{r}'|}}{4\pi|\mathbf{r}-\mathbf{r}'|}, \tag{3}$$

where k is a positive real constant. This function satisfies

$$\left(\nabla^2 - k^2\right) G_k(\mathbf{r}-\mathbf{r}') = -\delta(\mathbf{r}-\mathbf{r}'), \tag{4}$$

where $\delta(\mathbf{r})$ is the 3-dimensional Dirac's delta function.

The Schrödinger equation for the mixture of two different species of positive charged bosons are written as

$$\left\{ -\frac{\hbar^2}{2m_i}\nabla^2 + V_i(\mathbf{r}) + W_i(\mathbf{r}) \right\} \psi_i(\mathbf{r}) = \mu_i \psi_i(\mathbf{r}), \tag{5}$$

where the first term of the left hand side means the kinetic energy of the boson i and the second and third terms mean following potentials. The potential V_i is the harmonic potential induced by the electromagnetic ion trap. In the real lattice, it corresponds to the interaction between a boson and host metal ions. The potential W_i corresponds to the electro-static potential, which means the Coulomb interaction between charged bosons. Therefore, W_i depends on the both states ψ_i and ψ_j. The energy eigenvalue μ_i in the right hand side means chemical potential of the system. If we regard $W_i(\mathbf{r}')$, $n_i(\mathbf{r}')$ and $n_j(\mathbf{r}')$ in the right hand side of eq.(2) as old quantities, they will make new $W_i(\mathbf{r})$ in the left hand side through the volume integration over the all space.

If we consider the ground state of the system, n_i and W_i should have spherical symmetries. Then, we can easily calculate the angular components of the volume integration in eq.(2) and it reduces to the function of $r = |\mathbf{r}|$ as

$$W_i(r) = \frac{e^{-kr}}{kr} \int_0^r dr' r' \sinh(kr') F_i(r') + \frac{\sinh(kr)}{kr} \int_r^\infty dr' r' e^{-kr'} F_i(r'), \tag{6}$$

where the function F_i is defined as

$$F_i(r) = \frac{e^2}{\varepsilon_0} Z_i \left\{ Z_i n_i(r) + Z_j n_j(r) \right\} + k^2 W_i(r). \tag{7}$$

The electro-static potential written in this formula has no divergence difficulties in the numerical calculations at the origin. The harmonic potential is also defined as

$$V_i(r) = \frac{1}{2} m_i \omega_i^2 r^2, \tag{8}$$

where m_i and ω_i mean mass of the boson i and trapping frequency for the boson i, respectively. Using these potentials, the radial Schrödinger equation for s-like ground state is written as

$$\left\{ -\frac{\hbar^2}{2m_i} \frac{1}{r^2} \frac{d}{dr} \left(r^2 \frac{d}{dr} \right) + V_i(r) + W_i(r) \right\} \psi_i(r) = \mu_i \psi_i(r). \tag{9}$$

Seeing these equations described above, the variables for i and j are connected. Therefore, we have used iterative calculations which are characterized by the flow chart sketched in Fig.1.

In order to begin the iterative calculations, we assumed the initial functions for the quantities in the right hand side of eq.(6) as $W_i(r') = 0$ and $n_i(r') = n_{0i}\theta(R_i - r')$, where the step function θ is defined as $\theta(x) = 1$ for $x > 0$ and $\theta(x) = 0$ for $x < 0$. The parameters n_{0i} and R_i should satisfy

$$\frac{4}{3}\pi R_i^3 n_{0i} = N_i. \tag{10}$$

This means that the initial boson distributions are uniform in the sphere of radius R_i neglecting the interaction between charged bosons. Starting from these assumptions, we can solve eq.(5) numerically, and the first solutions give the normalized new densities. These densities are used for obtaining the new W_i by solving eq.(2). After that, new W_i is substituted into eq.(5) again and the second wave functions are obtained. These procedures will be continued until the enough self-consistency is obtained. It is checked by seeing the stability of the energy eigenvalue.

Using same unit system with that of the pure harmonic problem, we have obtained more convenient equations in non-dimension. By using these transformations, the radial Schrödinger equations are rewritten as

$$\left\{ -\frac{d^2}{d\xi_i^2} - \frac{2}{\xi_i} \frac{d}{d\xi_i} + \xi_i^2 + w_i(\xi_i) \right\} \psi_i(\xi_i) = \varepsilon_i \psi_i(\xi_i), \tag{11}$$

where w_i means the normalized electro-static potential. The formula for w_i is expressed as

$$w_i(\xi_i) = \frac{e^{-k_i\xi_i}}{k_i\xi_i} \int_0^{\xi_i} d\xi_i' \xi_i' \sinh(k_i\xi_i') f_i(\xi_i') + \frac{\sinh(k_i\xi_i)}{k_i\xi_i} \int_{\xi_i}^{\infty} d\xi_i' \xi_i' e^{-k_i\xi_i'} f_i(\xi_i'), \tag{12}$$

where function f_i is defined as

$$f_i(\xi_i) = C_i Z_i \left\{ Z_i n_i(\xi_i) + Z_j n_j \left(\frac{\alpha_j}{\alpha_i} \xi_i \right) \right\} + k_i^2 w_i(\xi_i). \tag{13}$$

In these equations, constants k_i and C_i are defined as $k_i = \frac{k}{\alpha_i}$ and $C_i = \frac{2e^2}{\hbar \omega_i \alpha_i^2 \varepsilon_0}$. Furthermore, we can obtain simpler expression by using a new function $u_i(\xi_i)$, which is defined as

$$u_i(\xi_i) = \xi_i \psi_i(\xi_i). \tag{14}$$

Then the Schrödinger equqtions we should solve are written as

$$\left\{ -\frac{d^2}{d\xi_i^2} + \xi_i^2 + w_i(\xi_i) \right\} u_i(\xi_i) = \varepsilon_i u_i(\xi_i). \tag{15}$$

where $\alpha_i = \sqrt{\frac{m_i \omega_i}{\hbar}}$, and $\xi_i = \alpha_i r$. Here, we can consider that the normalization of r by α_i^{-1} corresponds to ξ_i. The relation between the solution of eq.(15) and the number density is written as

$$n_i(\xi_i) = \left\{ \frac{u_i(\xi_i)}{\xi_i} \right\}^2. \tag{16}$$

Therefore, the normalized solution of the new equation should satisfy

$$4\pi \int_0^\infty d\xi_i \left\{ u_i(\xi_i) \right\}^2 = N_i, \tag{17}$$

where N_i means the number of the boson i. The unperturbed eigenvalue of the ground state is $\varepsilon_i = 3$, because it is a radial component of a 3-dimensional problem. The unperturbed solution corresponding to $\varepsilon_i = 3$ is written as

$$u_i(\xi_i) = \xi_i H_0(\xi_i) e^{-\xi_i^2/2}, \tag{18}$$

where the function $H_0(x) = 1$. At first, the eigenvalues for the perturbed system are unknown. However, we can find them by using the fact that eq.(18) can be regarded as an asymptotic solution of the perturbed system for large ξ_i.

In eqs.(2), (3) and (4), constants k's are regarded as the screening constant because they are positive and real. And they are also regarded as arbitrary, because the subtraction of $k^2 W_i(\mathbf{r})$ from both side of eq.(1) leads to eq.(2). When we solve eq.(15) numerically, Runge-Kutta-Gill method is used for the calculation. Usually, we start the calculation from $r = 0$ and proceed it to large r. At the final region of these calculations, the errors are accumulated larger and larger. However, these errors included in the number density n_i and n_j are eliminated by the damping factor of the Green's function in eq.(2).

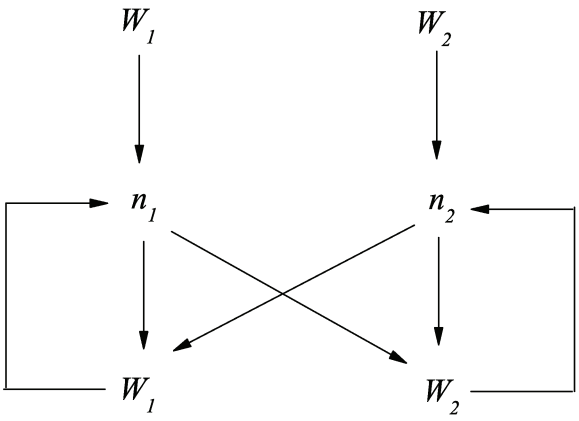

Fig. 1. The flow chart for the self-consistent calculation.

3. Assumptions

We considered two systems. One is D^+-$^6Li^+$and the other is D^+-$^{58}Ni^{2+}$system. Here, we assumed the frequency of the harmonic ion trap as $\omega_i = 4.79 \times 10^{14} s^{-1}$ for both systems. The parameters α_i's for D^+, $^6Li^+$and $^{58}Ni^{2+}$are given by$\sqrt{\frac{m_i\omega_i}{\hbar}}$, and they are $1.23 \times 10^{11} m^{-1}$, $2.14 \times 10^{11} m^{-1}$ and $6.64 \times 10^{11} m^{-1}$, respectively. The parameters k_i's for D^+, $^6Li^+$and $^{58}Ni^{2+}$are assumed to be 29.1, 16.8 and 4.24 , respectively. The value of the screening parameter k is arbitrary, because eq.(2) is derived by substituting k^2W from both sides of the Poisson's equation. Therefore, the results should not depend on parameter k to the extent that the integral domain of eq.(2) is expanded over the all space. However, it is impossible to achieve such a perfect integration in the numerical calculations. The values of the parameter k's are selected for the convenience of the rapid convergence in the iterative calculation.

4. Results and Discussions

We can easily understand that the quantum state of each boson should depend on its species and the number of them, because each boson has different charge and mass. Firstly, we have tried the calculation for the mixture of $D^+$and $^6Li^+$in ion traps. Results are plotted in Figs.2, 3 and 4. In Fig.2, the number of $D^+$is changed from 1 to 3 while the number of $^6Li^+$is fixed at 1. On the contrary in Fig.3, the number of $^6Li^+$is changed while the number of $D^+$is fixed. In Fig.4, both of them are changed. The blue and the red line mean the results for $D^+$and $^6Li^+$, respectively. $D^+$and $^6Li^+$are labeled by small letters and capital letters marked at the main peak, respectively. The numbers written in the bracket in the graph legends mean the number of each boson. For example, if it is written as $D^+(N_1,N_2)$, the line corresponds to a result for $D^+$when the number of $D^+$is N_1 and number of $^6Li^+$is N_2.

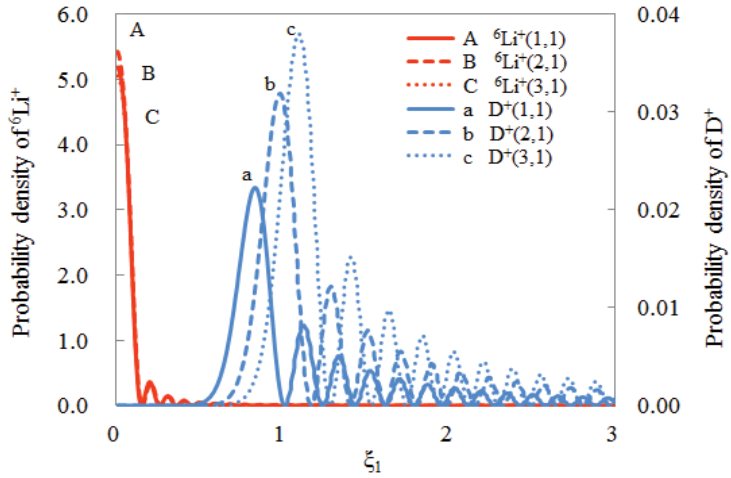

Fig. 2. Distributions of n $D^+$and single $^6Li^+$in the system

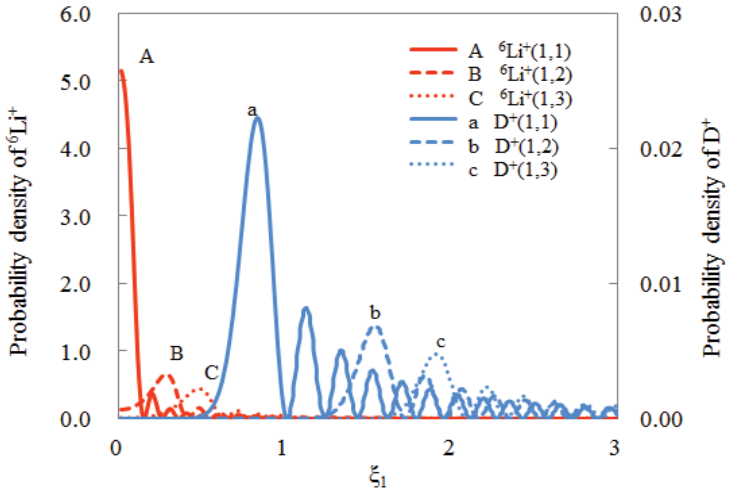

Fig. 3. Distributions of single $D^+$and n $^6Li^+$in the system.

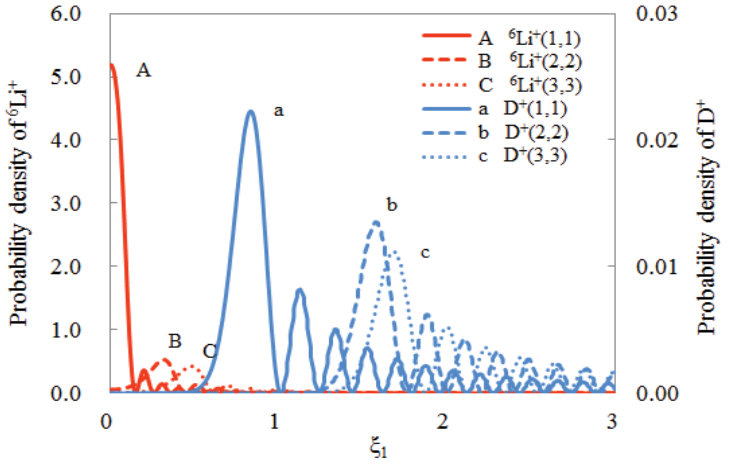

Fig. 4. Distributions of n $D^+$and m $^6Li^+$in the system.

Seeing Fig.2, main peak of $^{6}Li^{+}$exists around the center of the ion trap and that of D^{+}does at off-centered position. This is because the mass of $^{6}Li^{+}$is larger than that of D^{+}. Increasing the number of D^{+}, the main peak of D^{+}shifts to the right. We estimate that the shifts are caused by Coulomb repulsions between D^{+}'s. In this case, the nuclear reaction rates will be decreasing because the overlap of each wave function becomes smaller. Seeing Fig.3, increasing the number of $^{6}Li^{+}$, the main peaks of $D^{+}$and $^{6}Li^{+}$shift to the right. This is because Coulomb repulsions between $^{6}Li^{+}$'s. The nuclear reaction rates will also be decreasing because the overlap becomes smaller. On the other hand, seeing Fig.4, increasing the number of each boson, distances between main peak of $D^{+}$and $^{6}Li^{+}$become smaller. For this reason, we think the nuclear reaction rates could be higher when the same number of $D^{+}$and $^{6}Li^{+}$is mixed.

Secondly, we have tried the calculation for the mixture of $D^{+}$and $^{58}Ni^{2+}$in ion traps. Results are plotted in Figs.5, 6 and 7, which are drawn in the same notation with Figs.2, 3 and 4. Seeing Figs.5, 6 and 7, main peak of $^{58}Ni^{2+}$exists around the center of the ion traps. The reason for this is the same with $^{6}Li^{+}$cases. However, a small empty space exists at the center of the ion trap since electro-static potential of divalent $^{58}Ni^{2+}$is stronger than that of monovalent $^{6}Li^{+}$. Verifying this, we have assumed imaginary ions like $^{58}Ni^{+}$ and $^{58}Ni^{3+}$, where monovalent and trivalent Ni ions do not exists in natural. We have tried the same calculations by using those ions. Results are plotted in Fig.8. Seeing Fig.8, the larger the valence of Ni ion is, the larger the empty space at the center is. Then, we have found the same cause of the empty space again.

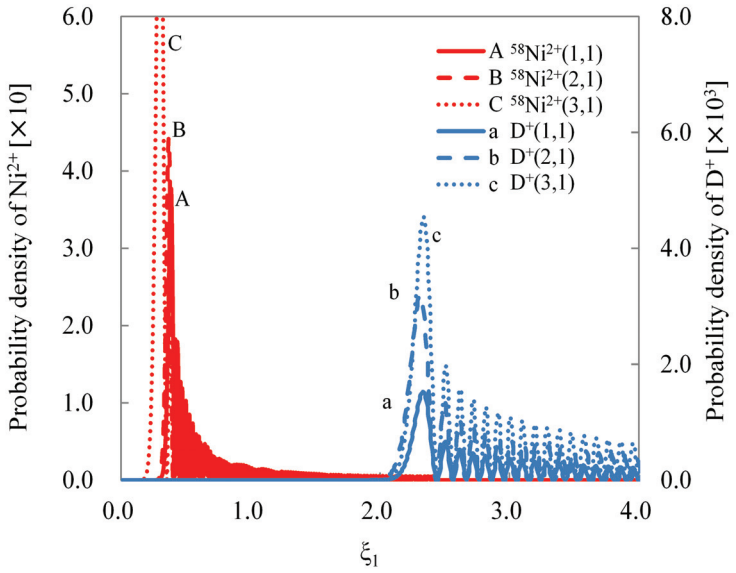

Fig. 5. Distributions of n $D^{+}$and single $^{58}Ni^{2+}$in the system.

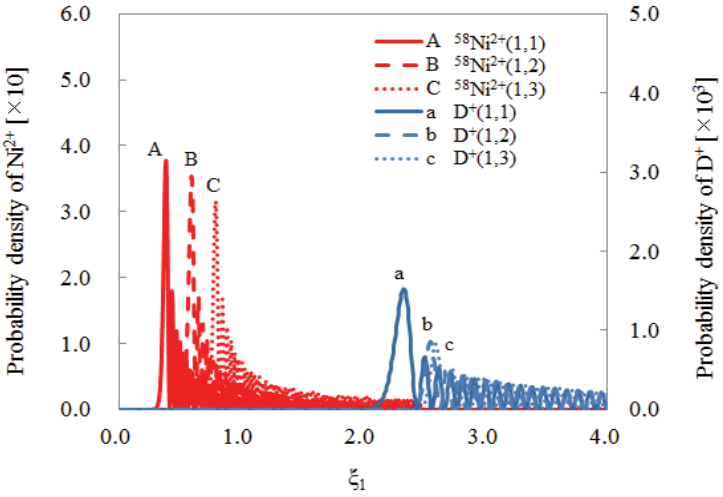

Fig. 6. Distributions of single $D^+$and n $^{58}Ni^{2+}$in the system.

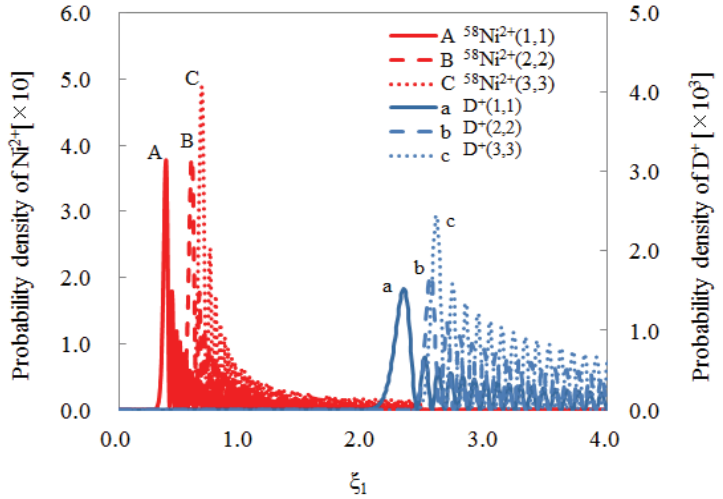

Fig. 7. Distributions of n $D^+$and m $^{58}Ni^{2+}$in the system.

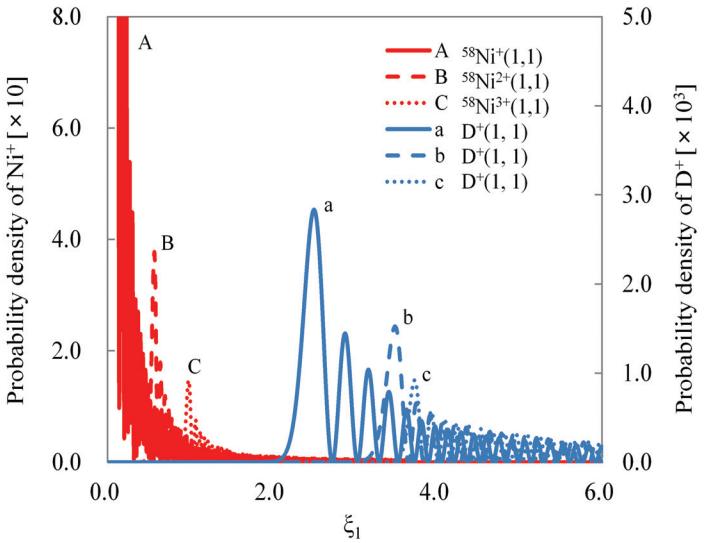

Fig. 8. Distributions of single $D^+$and single $^{58}Ni^+$, $^{58}Ni^{2+}$and $^{58}Ni^{3+}$ in the system.

5. Conclusions

In this study, we have done iterative calculations for two species of positively charged bosons in ion traps. We have tried the calculations for the mixture of D^+-$^6Li^+$and D^+-$^{58}Ni^{2+}$in ion traps and obtained the self-consistent probability density. We have found that $^6Li^+$exists around the center of the ion trap and D^+does at off-centered position in the D^+-$^6Li^+$system. In the same way, $^{58}Ni^{2+}$exists around the center of the ion traps in the D^+-$^{58}Ni^{2+}$system. We have considered that D^+shifts to the outer side in the ion trap because the mass of $D^+$is much smaller than that of $^6Li^+$or $^{58}Ni^{2+}$. On the other hand, we have also found that heavy and large valence ion exists around the empty space at the center of the ion traps. For example, a small empty core is created at the center and Ni ion exists around it (see Fig.8). Moreover, it is known that the nuclear reaction rates are estimated from the overlap of each wave function. Due to this, we predict that the nuclear reaction rates are higher when the same number of $D^+$and $^6Li^+$is mixed. In the near future, we will calculate them actually by using Kim's theory [1].

Acknowledgements

The authors wish to thank Prof. Y.E.Kim of Purdue Univ. for his advices about BEC.

References

[1] Y.E.Kim and A.L.Zubarev, "Mixtures of Charged Bosons Confined in Harmonic Traps and Bose-Einstein Condensation Mechanism for Low Energy Nuclear Reactions and Transmutation Process in Condensed Matter", Condensed matter Nuclear Science, Proc. of ICCF11, France, p.711-717

[2] Y.E.Kim, "Generalized Theory of Bose-Einstein Condensation Nuclear Fusion for Hydrogen-Metal System", Purdue Nuclear and Many Body Theory Group (PNMBTG) Preprint PNMBTG-6-2011 (June 2011).

[3] A. Rossi, "Method and apparatus for carrying out nickel and hydrogen exothermal reaction" , United States Patent Application Publication, p.1-2, 2011.

Nucleon Halo Model of ^{8}Be*

Akito Takahashi[1*] and Daniel Rocha[2]

[1]Technova Inc., Tokyo Japan, [2]Rio de Janeiro, Brazil
*akito@sutv.zaq.ne.jp

[Abstract]

A model of final state interaction for ^{8}Be* of 4D/TSC fusion is proposed. The ^{8}Be*(Ex=47.6MeV) may damp its excited energy by major BOLEP (burst of low energy photons) process from <n-h-h-n> nucleon-helion halo state to ^{8}Be-ground state. Intermediate decay states from the nucleon-halo states are scaled by number of effective binding PEF values for mean strong field interaction. A complex decay scheme is proposed. Minor two-alpha break-up channels emit characteristic discrete kinetic energy alpha-particles, which meets wonderful coincidence with observed data by Roussetski et al. X-ray burst data observed by Karabut et al may be photons by BOLEP.

Keywords: 4D/TSC, final state interaction, ^{8}Be* decay, nucleon-halo, BOLEP, alpha-particle

1. Introduction

Explanation for heat/^{4}He correlation, without neutron emission, by experimental CF claims (The first claim was done by M. Miles et al.: The Science of Cold Fusion, Italian Physical Society, 1991, pp. 363-372, and confirming claims by several other groups) is of great interest on possible novel nuclear reaction that is peculiar to condensed matter environments of deuterium-loaded metals. Our 4D/TSC theory predicts the consequence of 23.8 MeV/^{4}He with very low-level n/t secondary/minor production [1-3]. However, the final state interaction of ^{8}Be* at highly excited energy is very complex and yet to be studied in detail. This paper discusses on our new proposal of nucleon-halo model of ^{8}Be* and possible EM transitions (BOLEP) with 1 - 10 keV burst-photons-emission and with competing minor hadronic break-up channels, namely mostly going out to two alpha-particles with specific peaks of kinetic energy.

To make theoretical modeling on possible nuclear effects, we need to theorize the three steps of nuclear and electro-magnetic field interaction processes, as shown in Fig.1, rationally and quantitatively. In our past works of TSC theory [1-3], we have intensively studied on the initial state interactions and intermediate states. The final state interaction was very briefly speculated. The situation, including the consequence of this work, is

shown by the simplified scheme of 4 steps in Fig.2.

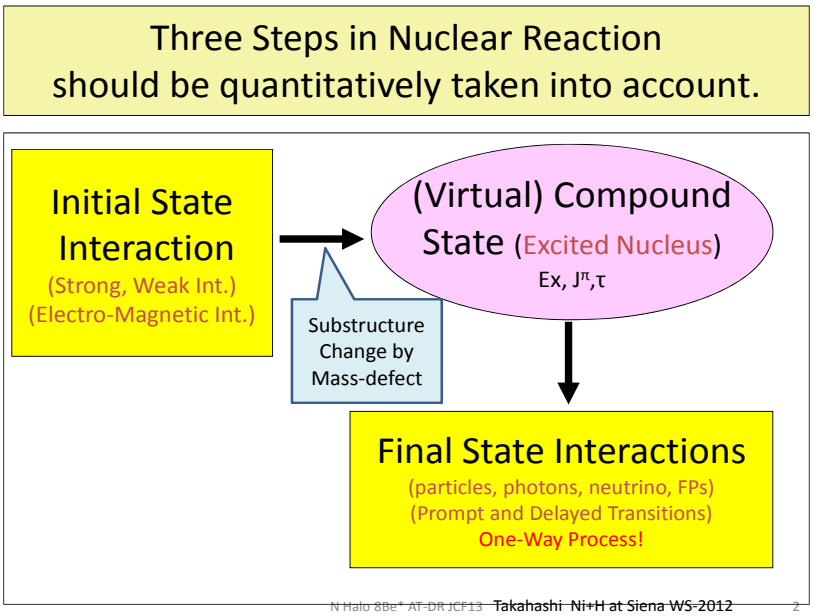

Fig.1: Three steps to be theoretically treated for condensed matter nuclear reactions

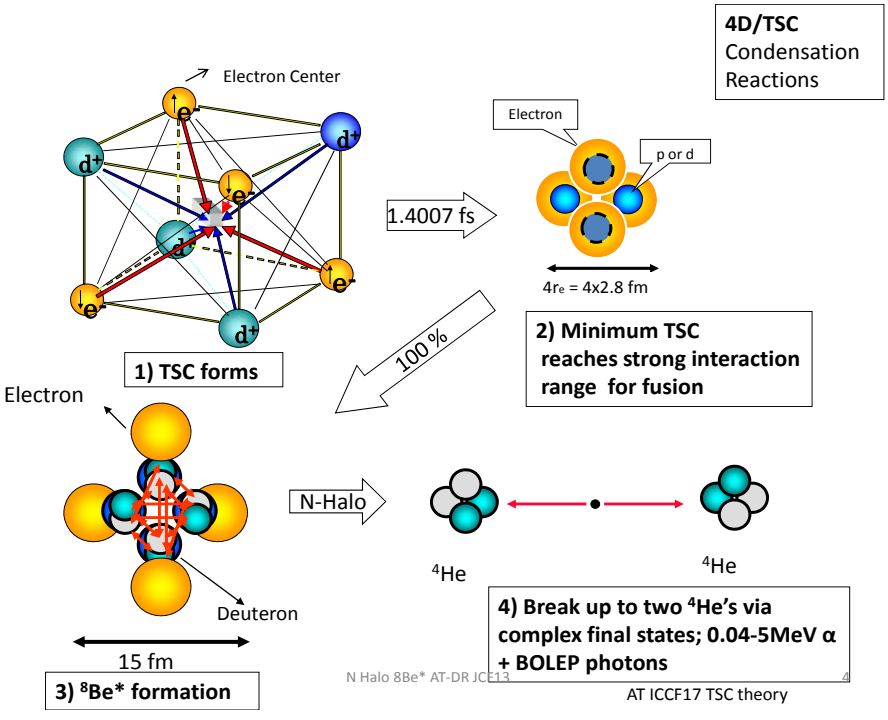

Fig.2: Process in four steps for 4D/TSC fusion model by the TSC theory [1-3]

2. Brief View on Recent Nucleon Halo Theories for Light Nuclei

L. Subshukin and H. Toki wrote a good text book [4] on recent progress of nuclear physics. They treated mean field-theory components as pionic exchanges and spin-orbital coupling tensor force based on a relativistic Dirac equation. An example of their book for nuclear binding energy calculation on light elements is picked up in Fig.3.

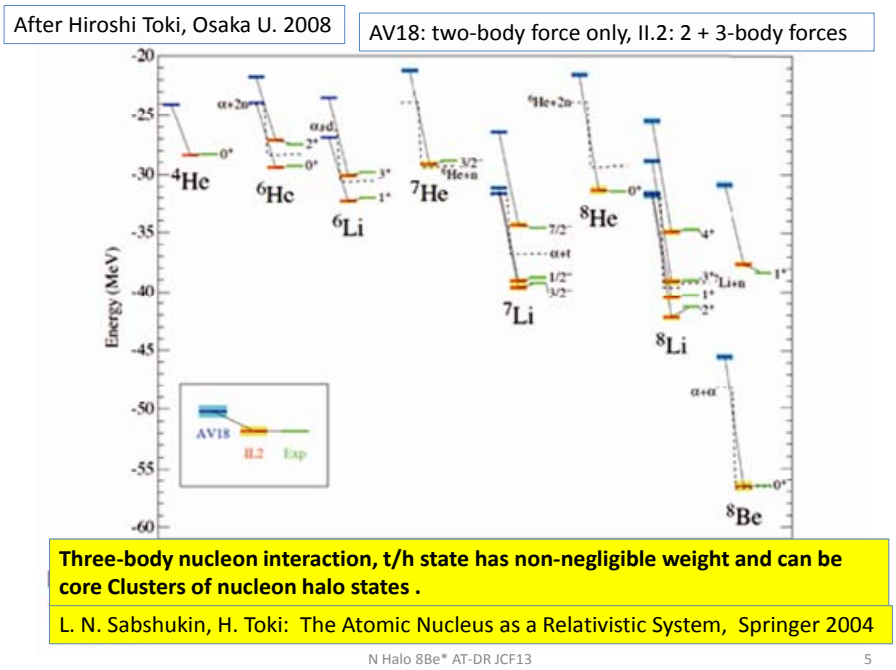

Fig.3: Nuclear binding energy calculated for light nuclei [4]

The component of two-body pionic interactions between nucleons (n-p, n-n and p-p) is the main force as expected by the mean field theory. However, three-body nucleon interaction, t/h state has non-negligible weight and can be core-clusters of nucleon halo state. Such helion (h) or triton (t) cluster state is considered to appear at highly excited states of light nuclei or even at ground states of halo-nuclei as ^{8}He, ^{8}Li, ^{8}B, ^{10}Li, ^{12}Li, and so forth [5]. At highly excited states of ^{12}C, three-alpha cluster state appears first in the intermediate excited state range and the chaotic gaseous nucleon states bound each-others as shown in Fig.4 [5] appears finally at very highly excited state. In a simple image of understanding, very highly excited states of light nucleus must be sustained by vibration energies between 'isolated' α- or h/t-clusters and also by coupled rotation energies of 'halo' nucleons (neutron-halo state in many cases). When the excitation energy goes up to extremely high, the QM chaotic energy states must appear to sustain the very high excited energy. The ground state of ^{8}Be is exceptional among

A=8 nuclides: the recent precise 8-body calculation [6] showed a clear image of two-alpha-cluster state as shown in Fig.5. The n-halo states of Be isotopes are imaged in Fig.6 [5].

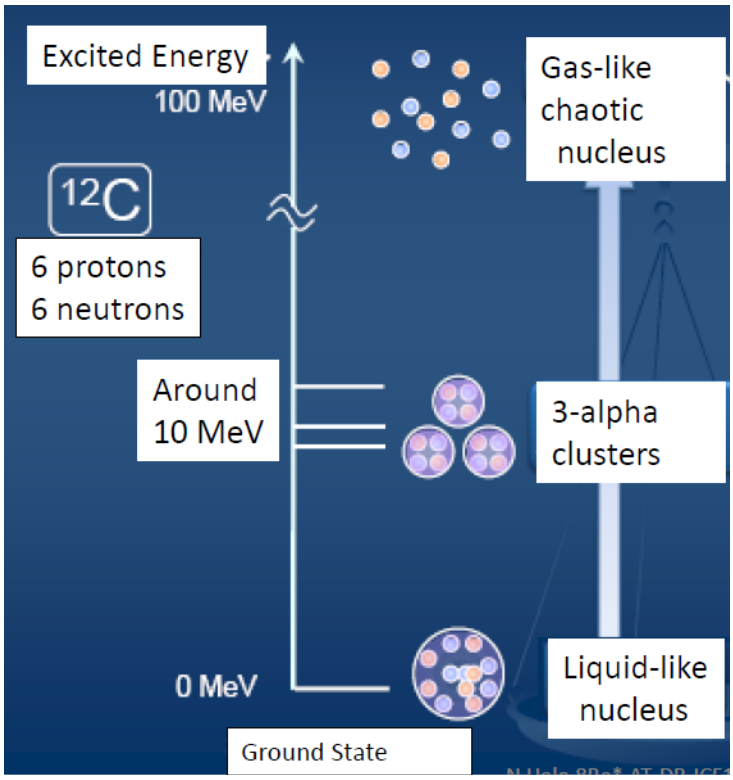

Fig.4: Cluster and chaotic gaseous states of nucleons at highly excited light nucleus ^{12}C [5]

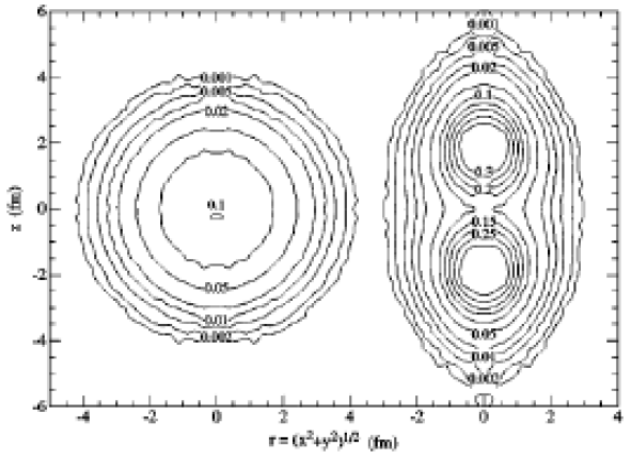

Fig.5: Precise 8 body calculation for ^{8}Be ground state [6] showing the tandem two-alpha clusters; view from top (left) and from side (right)

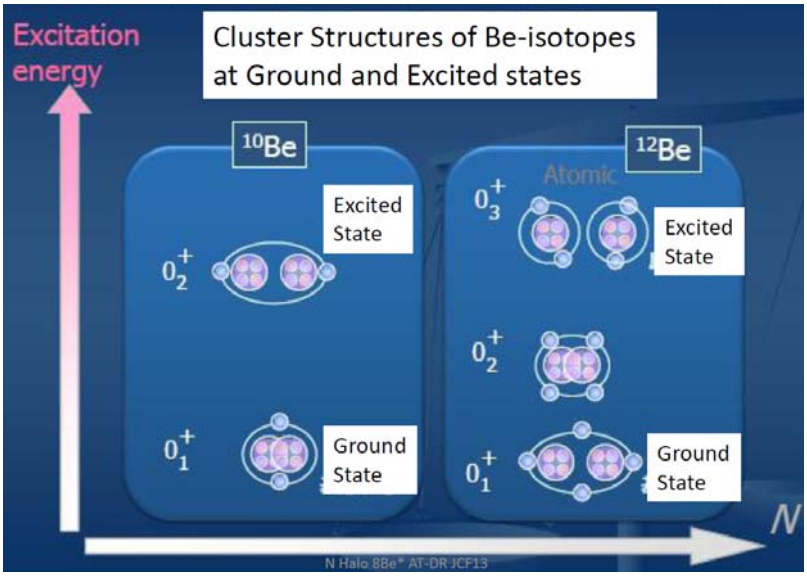

Fig.6: Nucleon halo modeling for highly excited states of Be isotopes [5]

3. Modeling for Nucleon-Halo States of ^{8}Be*

The tetrahedral/octahedral configuration of ^{8}Be* nucleons as intermediate compound state of 4d fusion needs further study. Pion (isospin) exchange between n and p states of nucleons may suggest 3-dimensional symmetric arrangement as n-p-n-p-n-p-n-p to form nuclear TSC state, which will have rotation energy level scheme as deformed from an ideal sphere. However, such non-cluster state should correspond to the QM chaotic 'gaseous' state of very high excited energy as shown in Fig.4. ^{8}Be (as well as most of light nuclei) can be described better as 2 clusters of alpha particles, each cluster being 2 protons and 2 neutrons in the 1s nuclear-shell. Excited states ^{8}Be* are described by excitations between these 2 clusters. However, at very highly excited state as ^{8}Be*(Ex=47.6 MeV) after 4D/TSC fusion, the deformed state configuration seems quite different, as we will discuss and model below.

Now, if we concentrate in a condition of a lot of energy together, maybe the force can fuse these 2 clusters in one core. The difference would be that this fusion would be endothermic and would create exotic excited states. For example:

1) Cluster A would lose 2 neutrons to cluster B, so, cluster B would have 2 extra neutrons, like ^{6}He. ^{6}He has a halo-sate of two satellite neutrons. Maybe this excited state will have a halo of h-cluster.
2) Cluster A would lose 1 neutron and 1 proton. So, cluster B would have a

configuration of ^{6}Li, cluster A would be like a deuteron. But, because of the symmetry, cluster A could be also a ^{6}Li and B is a deuteron. So, there could be 2 alpha-weird mode of excitation: 1 proton and 1 neutron would come and go from cluster A to B.

3) Cluster A and B could lose 1 neutron and 1 proton at the same time. So, cluster A and cluster B would both share a deuteron.

Now we are considering a PEF-number-to-effective-spring-potential model, for formulating a simplified effective Hamiltonian of ^{8}Be* for the final state interactions. Here PEF (pion exchange force) is a measure of mean charged pion exchange field based on Yukawa-Wigner force and isopin [1].

The h- and t-cluster are the same nuclear-equivalent state as nucleon is (<n> + <p>)/2 because of very rapid pion-exchange between neutron <n> and proton <p> state of nucleon inside nucleus.

In Fig.7, ^{4}He*(Ex=23.8MeV) state is imagined as a n-halo state with Ex > $(1/2)K_2R_{halo}^2$ (PEF spring potential). This may correspond to a rapid break-up to n + h + 3.25MeV channel. Binding PEF number is 2 there, which is not strong enough to sustain the 23.8 MeV excitation energy and causes a prompt break-up to n + h or p + t.

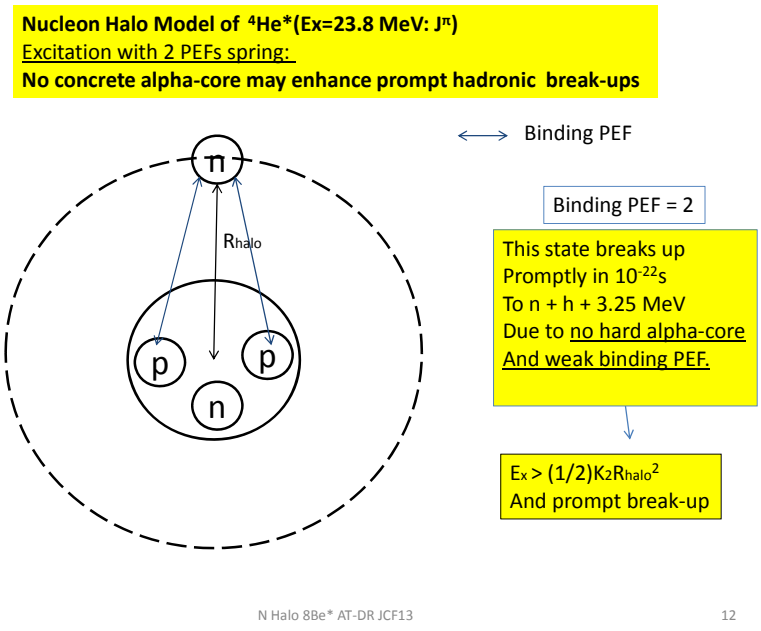

Fig.7: n-halo model for ^{4}He (Ex=23.8MeV) after d-d two-body fusion

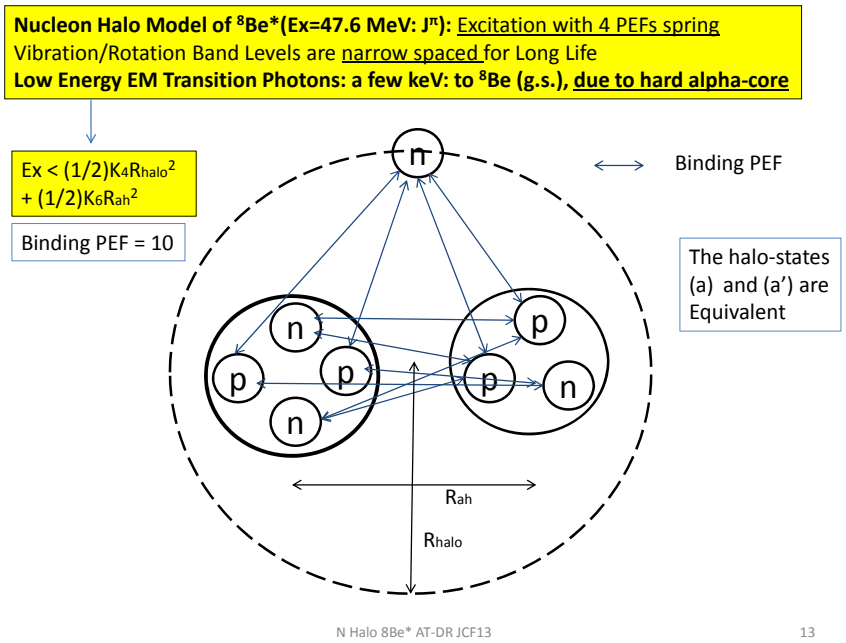

Fig.8: Nucleon-halo model for ^{8}Be* at highly excited state (Ex= 42 MeV)

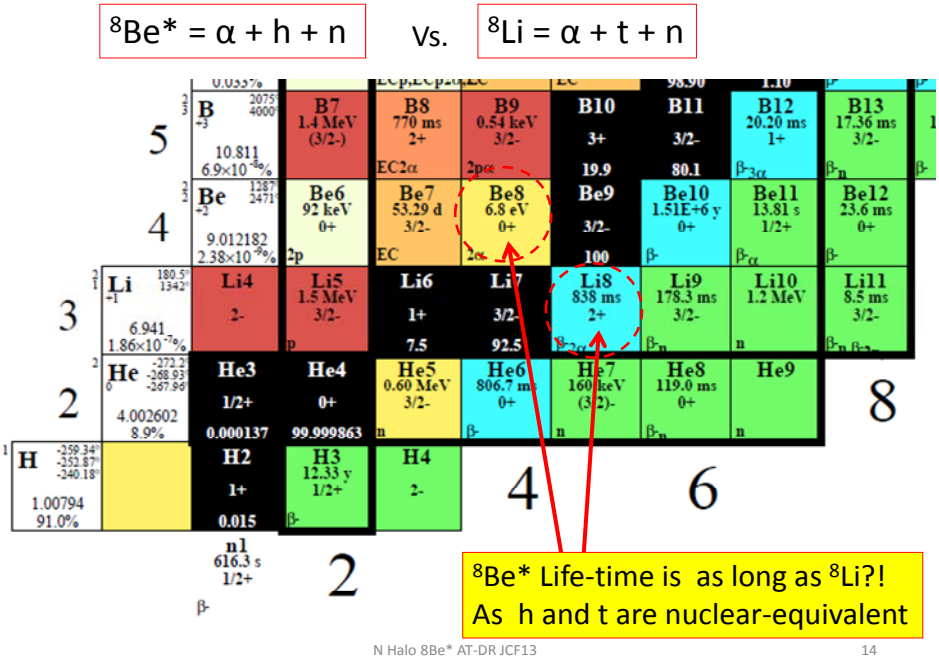

Fig.9: Nuclide chart for light elements and A=8 nuclides for comparison

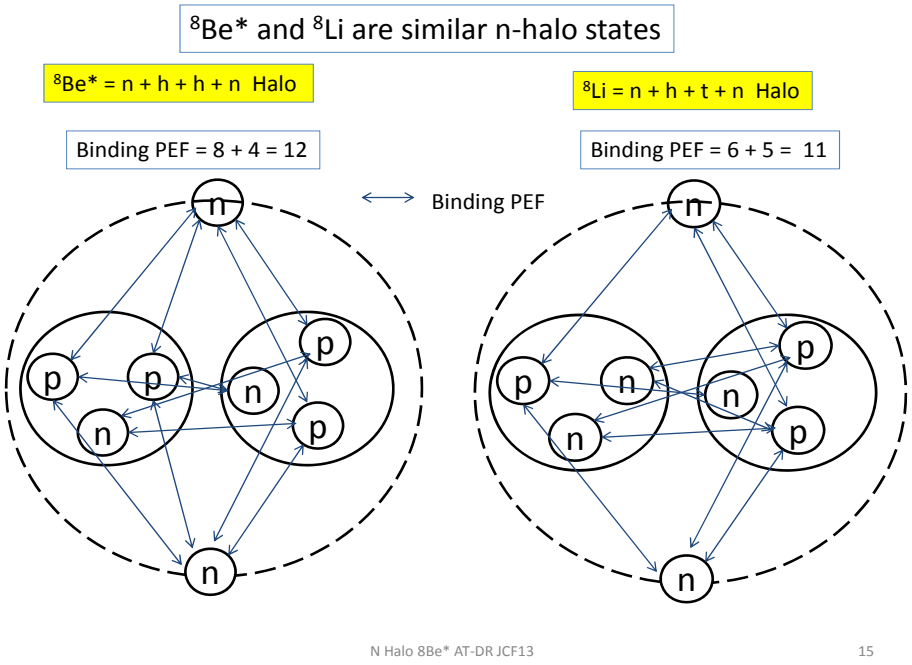

Fig.10: The proposed <n-h-h-n> halo-state of ^{8}Be*(Ex=47.6MeV) compared with ^{8}Li halo-state

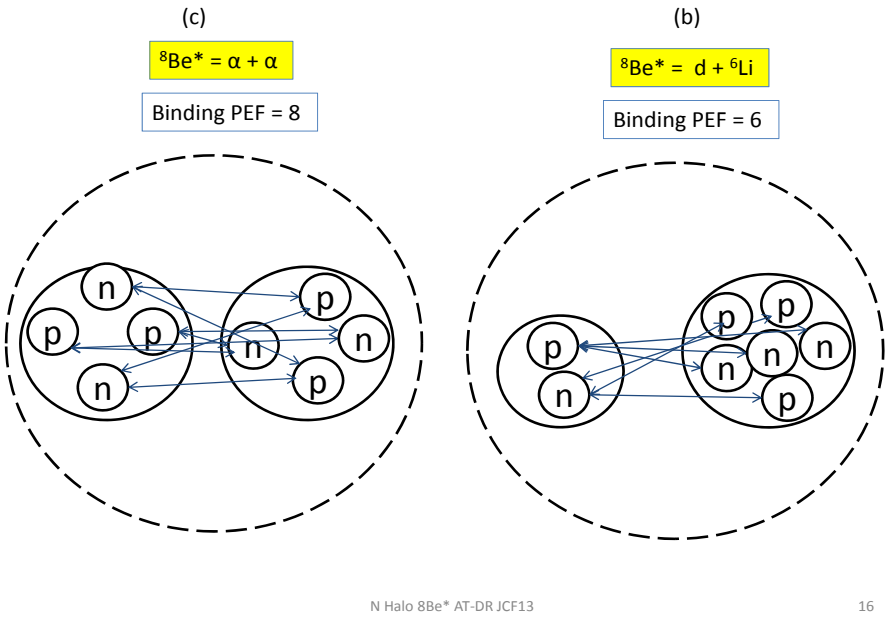

Fig.11: PEF model for cluster states of ^{8}Be* at lower excited states Ex $\leqq$ 34 MeV

Similarly, when we consider the inter-nuclear configuration of 'virtual' ^{4}H nucleus, we may model it as a n-halo with a t-cluster, which has only 1 binding PEF and therefore

weak enough to break up to n + t channels very promptly in 10^{-23} s.

In Fig. 8, ^{8}Be*(Ex=47.6MeV) state is speculated as a n-halo state with Ex < (spring potential of n-halo) + (alpha-h vibration potential). Excess inertia by the rotation of n-halo will make the ^{8}Be* state more meta-stable to generate narrow-spaced rotation-vibration energy-eigen-values. It also seems that ^{8}B is also a halo nucleus, but with protons. Similarly ^{8}Li has a halo state with halo neutrons. So, it seems that A=8 is a magical number for halos. We will also try to test the idea with ^{4}He, considering it that t and ^{3}He (h: helion) are nuclear-symmetrical, as discussed above already. To this respect it is interesting to see Fig.9, which compares life-times and decay-schemes of A=8 nuclei. Most A=8 nuclei have long life times as several hundred ms at their ground states, except for ^{8}Be that decays to two-alphas with 0.067 fs life time. As seen by Figs.8, 10 and 11, ^{8}Be* (excited state) may have very similar nucleon-halo states to that of ^{8}Li, with similar binding PEF numbers. Such analogous states suggest us that the life time of ^{8}Be*(Ex=47.6 MeV) may be 'rather' long as a few ms or more.

The ^{4}He-cluster has a very powerful binding (PEF=4 in inside binding) for keeping its rest mass because of the symmetry between h- and t-cluster inside it. We can think of a pair of t and h sharing a deuteron there. Also, we may consider the coincident completion of the shell model.

The ^{6}Li-cluster can be split to a pair of h and t clusters. These clusters are weakly bound (binding PEF = 5, as seen in Fig.10, compared with binding PEF = 6 for h-h coupling) which explains the experimentally verified very low average nuclear binding. This configuration should be more stable than the shell model, which may let a deuteron alone around the alpha core. Next, we consider that ^{8}Be* can be 2-alpha clusters. It should be h and t clusters with 2 halo neutrons, also, at higher excitation energy than the threshold of two-alpha cluster state (see Table-1). Note that the evidence of a cluster of h and t can be seen considering the reactions: ^{6}Li + n → ^{4}He + ^{3}T and ^{7}Li + p → ^{8}Be → 2^{4}He, as evaluated in TUNL Library [7].

Possible maximum excitation energy (Ex) states of ^{8}Be* can be scaled by the measure of binding pion-exchange-force number (Binding PEF) as shown in Table-1. This evaluation was deduced by comparing the TUNL level scheme [7] of ^{8}Be and nucleon-halo status shown in Figs.8, 10 and 11, as we know the threshold-energies of two-body reactions as p + ^{7}Li (Binding PEF = 4 and maximum excitation energy 17 MeV) and d + ^{6}Li and their binding PEF numbers (see Table-1). From this speculative extrapolation assuming the proportionality of maximum excitation energy versus binding PEF number, we can define the maximum excited energy of two-alpha cluster state (binding PEF =8) of ^{8}Be* is ca. 34 MeV, over which ^{8}Be* should be 'dissociated'

to the <α-t-n> halo state (binding PEF =10) or the <n-h-h-n> halo state (binding PEF =12) for sustaining definite life-time of such highly excited states.

Table-1: Speculated maximum excitation energies for various cluster/halo states of ^{8}Be*

Possible Maximum Excitation Energy (Ex) States of ^{8}Be* can be scaled by Binding Pion-Exchange-Force Number.

Cluster/Halo State	Binding PEF	Maximum Ex	Dominance
(e) p + ^{7}Li (n + ^{7}Be)	4	17 MeV	Minor
(c) ^{6}Li + d	6	25 MeV	Minor
(b) α + α	8	34 MeV	Minor
(a) h + α + n (a') t + α + p	10	42 MeV	**2nd**
(d) n +h + h + n (p+t+t+p)	12	50 MeV	Main for 4D/TSC
(f) 4p + 4n chaotic admixture	16	ca. 66 MeV	None

N Halo 8Be* AT-DR JCF13 17

Consequently, the ^{8}Be*(Ex=47.6MeV) state is defined as the <n-h-h-n> halo state to sustain the very high excitation energy of 47.6 MeV and might have a few ms life time. From such an evaluation, we can draw the decay scheme of ^{8}Be* as shown in Fig.12.

See also Fig.13, for understanding relations between A=8 nuclei. The ground state of ^{8}Be is peculiar in comparison with ^{8}He, ^{8}Li and ^{8}B ground states which have very long life-times to allow beta- and positron decay. The ground state ^{8}Be has a definite life-time but as short as 0.067fs and decays to two alpha-particles. However, the highly excited states ^{8}Be* may behave somewhat similarly to ^{8}Li due to possible nucleon-halo states and may have prolonged life time (maybe on the order of a few ms or more).

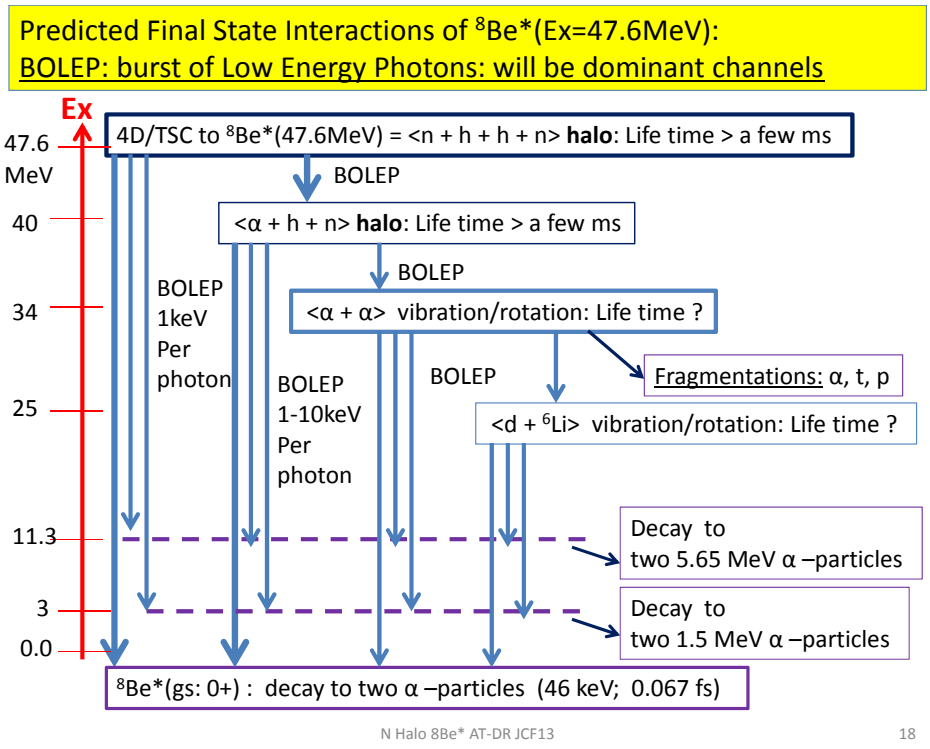

Fig.12: Proposed final state decay scheme of ^{8}Be*(Ex=47.6MeV) by 4D/TSC fusion; There are several even spin-parity states (see Table-2) between 34 and 11.3 MeV, which are not drawn here to avoid complexity of scheme-figure.

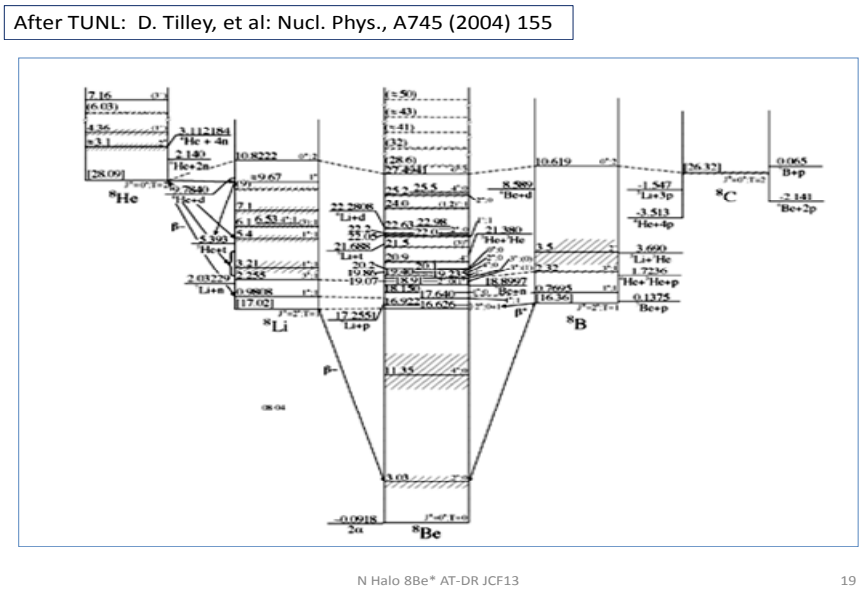

Fig.13: Level scheme of A=8 nuclides from TUNL library [7]

After: RIKEN Nishina Center talk0707 2007

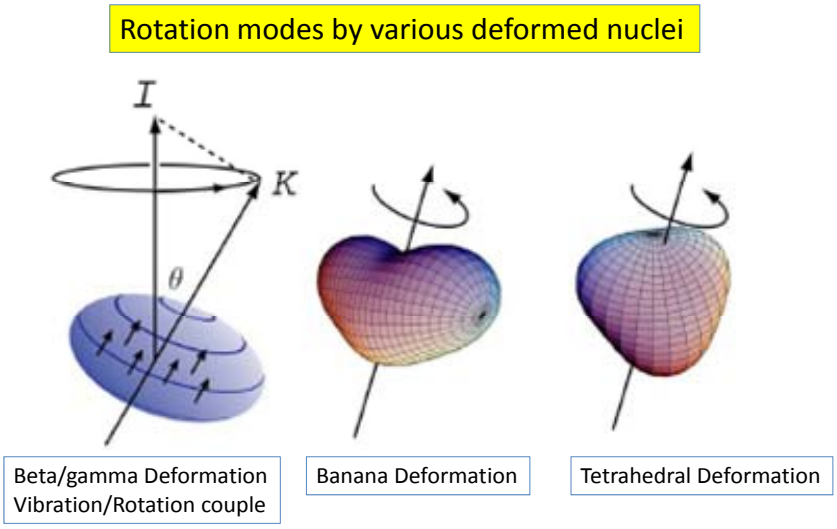

Fig.14: Rotation mode of typical deformed nuclei [8]

After: RIKEN Nishina Center talk 0707 2007

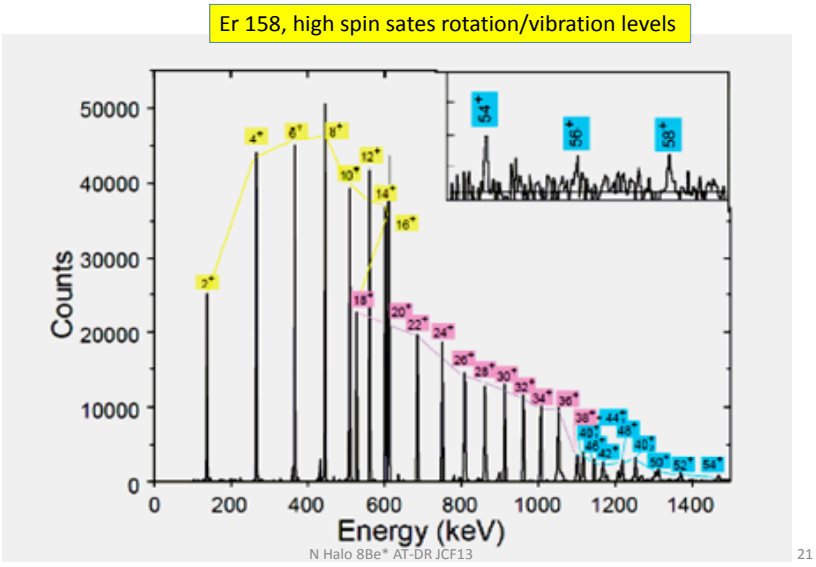

Fig.15: Very high spin state rotation-vibration coupled modes for Er-158 excitation [8]

4. Discussions on the Burst of Low Energy Photons (BOLEP) and Minor Alpha-Emitting Channels

It is possible for ^{8}Be* to exist a large multi-pole momentum for the <n-h-h-n> halo state. We consider, as a rough example: 2^((2(incoming tetrahedral)+2(recoil tetrahedral))*2(at least 1 extra transverse node between each incoming and outgoing components)=2^{16} (=65,536) pole momentum. Considering that it is possible to describe ~15,000 or more independent waves, and each of those carry a quantum of high deformation. The high deformation state could share 47.6 MeV of ^{8}Be* nuclear excitation energy between many 1.5 KeV wave-packets (Low Energy photons), and burst of low energy photons (BOLEP) will happen like as thermal black-body radiation. See Fig.16 for imagined deformed state for ^{8}Be*(Ex=47.6MeV) as very high spherical harmonics mode [9].

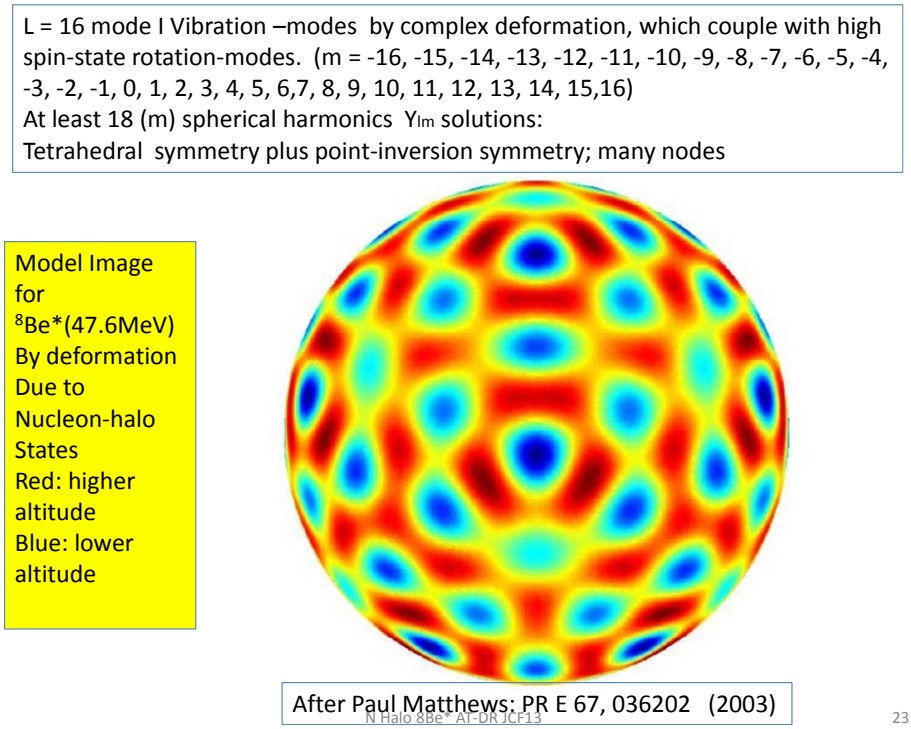

Fig.16: Highly deformed spherical harmonics state (l=16) imagined for ^{8}Be*(Ex=47.6MeV) [9]

A rotation-vibration coupled high spin state of nucleon-halo ^{8}Be* will make such a highly deformed state in 3-dim image. Concerning the deformed nuclei, we did mention about very high deformation modes, which we think is an important point as an

example. If 4 nuclei coalesce like liquid drops, the deformation will be higher than a tetrahedral deformation (see Figs. 14 and 16), since the collision shock waves can have radial inward and outward (recoil) components and also transverse modes since each incoming proton collides with 3 other protons. We thought that it is possible to enhance existence of a large multi-pole momentum. Also, note that the number of node deformation in the picture is small, but we think there is need to see the superposition with longer wavelength nodes that are not present in the picture. We probably have to think more:

1. The surface of the excited nucleus is deformed in a sea wavelike fashion, extending the liquid drop idea to a more literal vision, which is partially classical.
2. Individually, the undulation carries small energy relative to the ground state. All of them together carry highly excited energy.
3. The n-pole momentum is not necessarily a solution to a quantum problem, but of a classical equation wave equation of a surface.
4. Every node of the excitation of the n-pole momentum corresponds to a wave which caries a quantum of energy of the BOLEP.
5. Radial excitations are suppressed exponentially, also in analogy with classical waves.
6. Every wave has about the same order of magnitude in energy, due to the equipartition theorem. So, all the $\sim 2^{14}$ nodes share about the same energy at a given excitation.
7. The sum of the amplitudes waves should give a similar picture to the colorful picture of a ball which is presented in Fig.16, since it has about the symmetries of a collapsing tetrahedron impact.

In the basis of alpha-cluster model we shall do modeling. The n-, p-, d-halo state of highly (Ex=47.6 MeV) excited state of ^{8}Be*, as very deformed nuclei has been considered above. A nucleon-halo admixture will have rotation-vibration combined level states with small level-gap band structure (See a case of collision experiment for high mass nucleus Er*, in Fig.15). As ^{8}Li n-halo state has ‘very’ long life (ca. 0.8 s), ^{8}Be* halo-state may have long life time, due to h/t cluster’s nuclear equivalence, which allow cascade-EM-transitions dominant (see Fig.12, accordingly).

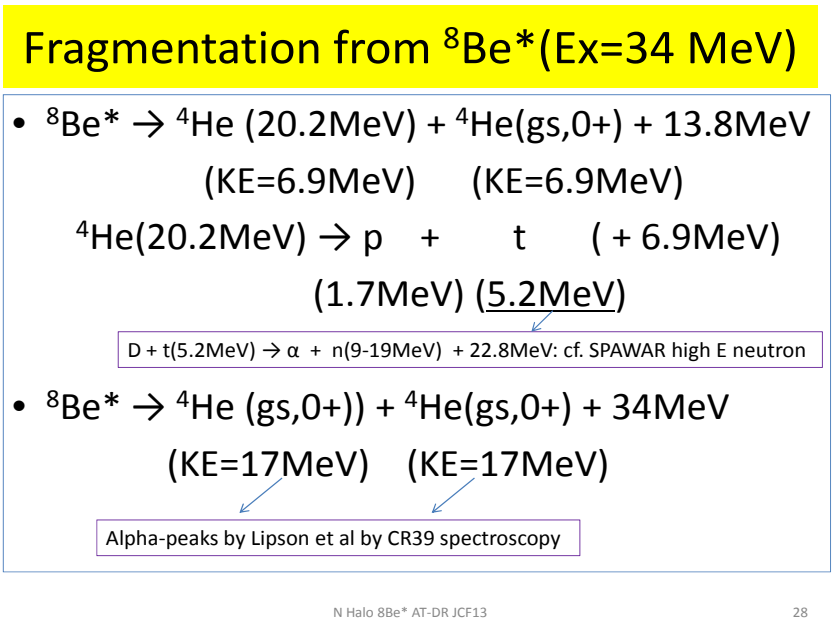

Fig.17: fragmentations from the highest excited state of two-alpha cluster of ^{8}Be*

To extend quantitative analysis, we need to define effective Hamiltonians for various types in Figs. 8,10, 11 and 16. Core oscillator (α-h or α-t) plus n-(or p-) halo rotator makes band structure of energy-eigen-values: so called rotation/vibration coupled band (see standard nuclear physics text book). Coupled Schroedinger equations for rotation and vibration, for so many modes should be solved. Competition with CP (charged particle) fragmentation channels should be studied. These are difficult task for future.

Possible hadronic break-ups of ^{8}Be* via symmetric fragmentation or asymmetric fragmentation should be considered (See Fig.17). Cascade break-ups via lower excited states of ^{8}Be* to two α-particles after the BOLEP transition should be considered. These states are in competition with main EM transitions (BOLEP: black-body radiation-like mechanism) of nucleon-halo rotation/vibration states, damping nuclear excited energy by burst photons to transit to the ground state ^{8}Be(gs:0+) which decays to two 46 keV alpha-particles.

Emitted alpha-particle energies are predicted as follows (see Table-2 also):

Major channel: **46 keV** from ^{8}Be(gs:0+) break-up after BOLEP transitions

(Secondary neutron yield by 46 keV alpha may be negligible, cf. Hagelstein limit[17], by heterogeneous matter for 4D/TSC generation without other local Ds.)

Minor channels: 1.55MeV, 5.65 MeV, 6.9 MeV, 8.3 MeV, 10 MeV, 11 MeV, 11.5 MeV, 13.8 MeV, **17** MeV (cf. Lipson and Roussetski exp.)

Minor triton emission: 5.2 MeV (cf. SPAWAR exp. and Fig.17.)

A lot of works are needed for knowing branching ratios, by experiments and theories.

Fig.18 is added for Roussetski's alpha-spectrum data (beautiful) [10], which is compared with the prediction of this work (Table-2). We find wonderful coincidence for discrete energies (KE) of alpha-particles between Roussetski experiment and the present prediction. This coincidence of alpha-spectrum between our theoretical prediction and other group experiment is a convincing result for the present nucleon halo ^{8}Be* model.

Table-2: Predicted alpha emission channels and their kinetic energies

4D → ^{8}Be*(47.6MeV) → BOLEP + ^{8}Be*(34MeV)
and possible intermediate states which decay to 2α
(Note: only 11.4 and 3.04 MeV states are drawn in Fig.12)

Ex (MeV)	Spin-Parity	Isospin (T)	KE of α-particle (MeV)
34	(0+)	(0)	17
27.5	0+	2	13.8
22.98	(0+)	(0)	11.5
22.0	2+	0	11
20.1	2+	0	10
16.6	2+	0	8.3
11.4	(2+)	(0)	5.7
3.04	2+	0	1.55
-0.092(gs)	0+	0	0.046

N Halo 8Be* AT-DR JCF13 30

Alpha particle energy spectra (fine structure) demonstrates few bands in the range 10 – 17 MeV

After A. Roussetski et al, Siena WS 2012: for TiDx system under e-X beam stimulation
JETP Vol.112 (2011) 952

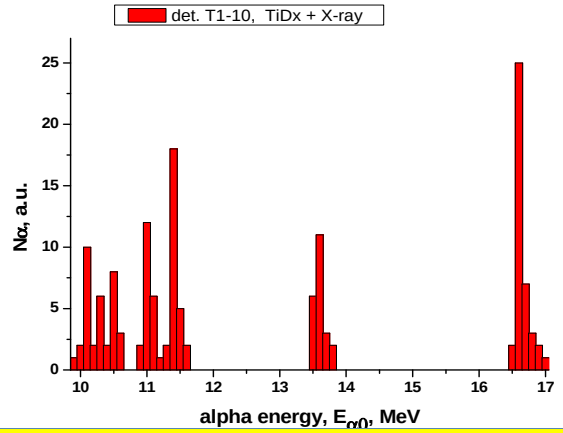

Prediction by N-Halo Model: 17, 13.8, 11.5, 11, 10, 8.3, 5.7, 1.55 and 0.046 (in MeV): Good Agreement with Roussetski Exp.

N Halo 8Be* AT-DR JCF13 33

Fig.18: Discrete alpha-particle energies observed by Roussetski et al are all agreed with the prediction of minor channels by the 4D/TSC to n-halo ^{8}Be* model

X-ray (0.6-6keV: peak around 1.5 keV)bursts observed by Karabut et al for D-Glow Discharge Experiment with various metals, JCMNS Vol.6, 2012

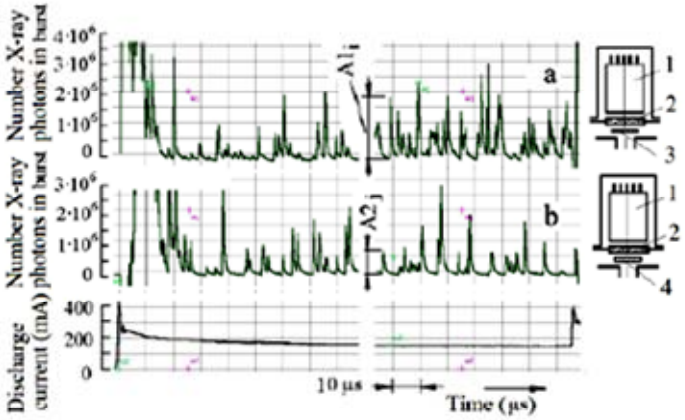

Figure 6. Typical oscillograms of X-ray emission from the PMMA/PM scintillator detector covered with Be foils with different thicknesses: (a) covered with a 15 μm Be foil; (b) covered with a 30 μm Be foil. In this case the cathode was Pd, the gas was D_2, and the discharge current was 150 mA.

N Halo 8Be* AT-DR JCF13 34

Fig.19: Low energy X-ray burst observed by Karabut et al.[14]; BOLEP may explain it.

Now the story of TSC theory [1-3] looks more rational and more fitting to main experimental observations: Miles et al [10] for the original heat-^{4}He correlation which have been followed by McKubre et al and others[15,16], Lipson [11] for ca.15MeV alpha-particle peak (probably a bunched peak of 17 and 13.8 MeV) from PdDx system, Boss[12] for ^{12}C(n,n')3α reaction by En>14MeV neutrons – see also Fig.4.

We know what Hagelstein spoke and wrote at ICCF17. One of authors questioned him at the Meeting that he did not treat yet nuclear (strong interaction/intermediate/final state) process properly. His 'going-forth and -back oscillation model' is wrong in the nuclear physics view, as pointed out by Fig.1, of one-way stochastic process flow from the initial state to the final state interactions. However, it seems that the Karabut-Karabut- Hagelstein work [14] might see the very BOLEP in their observed hot spots, although they interpreted as those were being from the radiation from electrons of each kind of metal in Hagelstein's theory of collective atoms, as referred in [14], or downloadable at:

http://www.iscmns.org/CMNS/JCMNS-Vol6.pdf :

"Experimental results on Excess Heat Power, Impurity Nuclides and X-ray Production in Experiments with a High-Voltage Electric Discharge System", A.B. Karabut, E.A. Karabut. See page 223(214 in journal), figure 15. Where we see black-body radiation type spectrum that peaks at 1.5KeV. The high nucleon momentum should have an emission that would look like a black body since its distribution is similar to the gas of photons in a box. Compare: downloadable at:

http://en.wikipedia.org/wiki/Bose-Einstein_statistics#A_derivation_of_the_Bose.E2.80.93Einstein_distribution

with http://en.wikipedia.org/wiki/Spherical_harmonics#Spherical_harmonics_expansion

:"Spectral and Temporal Characteristics of X-ray Emission from Metal Electrodes in a High-current Glow Discharge" A.B. Karabut, E.A. Karabut, P.L. Hagelstein. See page See page 231(264 in journal), figure 6, the time between bursts, BOLEP, is around 0.1 to 1ms. Compatible to what we would expect from halo orbits.

We saw the beautiful alpha-particle data by Roussetski et al at the last Siena Workshop, with great impression. We are now studying a nucleon-halo model of ^{8}Be* by 4D/TSC fusion. We have compared our consequence of alpha-particle energies (discrete) and his Siena data:

http://www.iscmns.org/work10/program.htm

Although the predicted alpha discrete energies are from minor channels of the final state interaction of ^{8}Be*(47.6MeV), no other models than that could find such beautiful

coincidence with several alpha-peak-energies (see Fig.18).

Why do we not include the blackbody radiation from the Karabut-Karabut-Hagelstein work in conclusion? They tried to explain it with the Hagelstein's collective theory, but the theory is too high for that. They say they still cannot explain it properly. The 1.5KeV peak is however within the range of the BOLEP. We think it would be good to include it due to BOLEP in our conclusion.

Mean photon energy by BOLEP was speculated on the order of 1-2 keV, albeit not precise QM calculations done. We shall reserve 'coincident agreement issue' for future quantitative QM analysis. We think it is possible to do a reasonable approximation to relate BOLEP and the thermal black body radiation, using similarities between the photon gas in a box and the photons from the rotation/vibration of spherical harmonics modes/nodes. We will think about it more. The mere division by the number of states to get 1.5KeV assumes the equivalent-partition theorem as valid. While this might be reasonable because of the relatively large number of states, it is about the peak energy of the black body radiation, as seen in the Karabut-Karabut-Hagelstein spectrum. So, that treating this problem as a classical problem is not enough.

The n-halo state of ^{8}Be*(47.6MeV) may be close to quantum-chaos (4n + 4p chaotic admixture to sustain that very high excitation energy) but still keeping order of helion (h) clusters. So we need QM study for the complexity. Comparing it with Fig.13 for A=8 nuclides and Table-1, we may imagine 'rather long life time' of ^{8}Be*(Ex=47.6MeV) as imagined as more than a few ms. The equilibrium time should be much shorter than the wavelength of the emission time, that is, the wavelength of the outgoing radiation. Since we are thinking about radiation with energies below 10KeV, which is 2 orders of magnitude less than typical nuclear reactions, this is a likely explanation. "Broadening due to local conditions is due to effects which hold in a small region around the emitting element, usually small enough to assure local thermodynamic equilibrium".

We may imagine a burst of low energy photons from a highly excited nucleus with high spin rotation/vibration mixture of isolated/clustered nucleons, since that has no paths to direct fragmentations like ^{8}Be*(47.6MeV) to two 23.8MeV alphas but the multi-photon EM transition (BOLEP) down to lower excited states where alpha-alpha cluster states of excitation (with Ex less than 34 MeV, see Table-1) are of possible sub-structure of excited nucleus.

The ground state of ^{8}Li decays by beta emission, weak interaction, to ^{8}Be*(3MeV:2+),

more than 90 % branch, (then breaks up to two alphas), since ^{8}Li is at ground state and cannot have any EM paths to change nuclear substructure. Decays by weak interactions for ^{8}Be*(47.6MeV) are however defeated by the BOLEP EM transition, in contrast, because of its excited state having freedom going to lower states.

However, the BOLEP transition is not a photon emission process with such continuous wave length distribution as the thermal black-body radiation, since it has discrete wave length structure of distribution reflecting QM states of near 'chaotic' rotation/vibration sates of the <n-h-h-n> halo nucleus.

We may have intuition that the BOLEP state can be 'approximately' treated as classical black-body radiation. To prove it we need however some precise QM studies on discrete energy levels structure, maybe strongly coupled mutually as bosonic states (nuclear phonons) of discrete energies, of the <n-h-h-n> halo nucleus under 47.6MeV excited energy. The strong bosonic coupling between 'excitons' will lead to a catastrophic/spontaneous-avalanche of burst-photons (BOLEP) dominantly damping directly to the ground state ^{8}Be(gs:0+).

We may however consider that we are talking about trillions of photons detected by the Karabut-Karabut-Hagelstein work [14]. Also, the interval they detected was small, from ~0.5KeV to 10KeV. That means less than 1eV for every level. We may consider variations due to large recoil, since H/D is light, and the non linear variation of the levels. So, trillions of detections would form a continuous spectrum. Yes it may be so, but we have to take it into account that first BOLEP photons with 1.5keV mean discrete energies may be emitted from the ^{8}Be*(Ex=47.6MeV) state and they ionized surrounding metals outer electron-orbits. The recombination of ionized metal atoms emits a few eV photons as is usual process. We observe EM radiations by all possible primary and secondary reactions. So far distinction or direct observation of BOLEP from deformed (excited) nuclei is not easy. It is not easy. So, we may be proposing that the Karabut-Karabut-Hagelstein spectra was due to BOLEPs, as a conjecture of direct observation. Secondary radiation could be related to hot spots.

5. Summary and Conclusion

A model of final state interaction for ^{8}Be* of 4D/TSC fusion is proposed. The ^{8}Be*(Ex=47.6MeV) may damp its excited energy by major BOLEP (burst of low energy photons) process from <n-h-h-n> nucleon-helion halo state to the ^{8}Be-ground state.

Intermediate decay states from the nucleon-halo states are scaled by number of effective binding PEF values for mean strong field interaction. Analogous states to A=8 ground state nuclei as ^{8}He, ^{8}Li and ^{8}B which are typical neutron-halo states with rather long life times as 838 ms for ^{8}Li are discussed, to speculate that the life time of <n-h-h-n> halo sate of ^{8}Be*(Ex=47.6 MeV) may be as long as a few ms or more and the dominant BOLEP electro-magnetic transition will be sustained. More quantitative QM analysis is to be done to know the detail of discrete energy states for the very deformed halo state.

A complex decay scheme is proposed. Major decay channel is modeled as an electro-magnetic transition of BOLEP to the ^{8}Be-ground state which breaks up to two 46 keV alpha-particles with 0.067fs life time. BOLEP is modeled as emission of rather slow (in a few ms) and stochastic burst events of ca. 1.5 keV averaged energy photons due to strongly coupled bosonic (nuclear phonon) states of many high spin quanta by the rotation-vibration coupled motion of very deformed <n-h-h-n> halo state of ^{8}Be*(Ex=47.6 MeV). Minor channels are modeled as BOLEP transitions to lower even spin-parity excited states (Ex = 34, 27.5, 22.98, 22.0, 20.1, 16.6, 11.4 and 3.04 MeV), from where two-alpha break-up channels open. Minor two-alpha break-up channels emit characteristic discrete kinetic energy alpha-particles at 17, 13.8, 11.5, 11, 10, 8.3, 6.9, 5.7 and 1.55 MeV, which meets wonderful coincidence with observed data by Roussetski et al. The asymmetric break-up from the Ex = 34 MeV state has a branch to emit 5.2 MeV triton, which will induce secondary D-t reaction in deuterium contained metal to emit 9-19 MeV (En) neutrons that would have 3-alpha tracks of CR39 detector by ^{12}C(n,n')3α reaction as observed by Boss et al. X-ray burst data observed by Karabut et al may be photons by BOLEP. Further confirmation data by experiments for checking such consequences of the present work is expected.

Acknowledgment: Kind support to this work by Technova colleagues (A. Kitamura, R. Seto and Y. Fujita) is appreciated. Critical comments given by Dr. Abd ul-Laman Lomax, Dr. L. Kowalski and Dr. A. Roussetski are also grateful.

References:

[1] A. Takahashi: Physics of cold fusion by TSC theory, Proc. ICCF17, August 12-17, 2012, Daejeon, Korea

[2] A. Takahashi: JCMNS, Vol.4 (2011) 269-281

[3] A. Takahashi: The basics of deuteron cluster dynamics as shown by Langevin equation, ACS LENRSB Vol.2 (2009) 193-217

[4] L. Subshukin, H. Toki: The atomic nucleus as a relativistic system, Springer 2004

[5] Y. Kanada-Enyo, H. Horiuchi, A. Dote: Nucl. Phys. 687 (2001) 146

[6] R. B. Wiringa, et al: Phys. Rev. C, 62 (2006) 14001

[7] D. Tilley, et al: Nucl. Phys., A745 (2004) 155

[8] RIKEN Nishina Center: seminar slide talk0707 2007

[9] Paul Matthews: Phys. Review E 67, 036202 (2003)

[10] M. Miles et al.: The Science of Cold Fusion, Italian Physical Society, 1991, pp. 363-372

[11] A. Lipson et al,: Phenomenon of an energetic charged particle from hydrogen/deuterium loaded metals, Proc. ICCF10, Condensed Matter Nuclear Science, World Scientific Pub., p.539 (2006)

[12] P. Boss, et al: JCNMS, Vol.6 (2012)13

[13] A. Roussetski et al, Siena WS 2012: for TiDx system under e-X beam stimulation
See also: Russian J. Exp. Theor. Phys., Vol.112 (2011) 952

[14] A. Karabut, et al: JCMNS, Vol.6 (2012) 214

[15] M. McKubre, et al.: The emergence of a coherent explanation for anomalies observed in D/Pd and H/Pd systems: Evidence for ^{4}He and ^{3}H production, Conf. Proc. Vol.70, ICCF8, Italian Physical Society, pp.3-10 (2000)

[16] Y. Arata, Y. Zhang: Definitive difference among [DS-D_2O], [DS-H_2O] and [Bulk-D2O] cells in the deuterization and deuterium reaction, Conf. Proc. Vol.70, ICCF8, Italian Physical Society, pp.11-16 (2000)

[17] P. Hagelstein: JCMNS, Vol.3 (2010) 41-49

Quantum Nucleodynamics (QND): Moving beyond nuclear "models"

Norman D. Cook
Department of Informatics, Kansai University,
Takatsuki, Osaka, 569-1095 Japan
cook@res.kutc.kansai-u.ac.jp
Tel: +81-726-90-2447

Abstract

The basic ideas underlying a quantitative theory of nuclear structure, i.e., quantum nucleodynamics (QND), are introduced. The replacement of the fictitious "mean-field" approximation of the nuclear force with the empirically-known nuclear potential-well is the essential first step. From there, calculation of short-range nucleon-nucleon effects can be achieved on the basis of the lattice representation of nuclear space, as introduced by Wigner in 1937.

I. Introduction

"Quantum nucleodynamics" (QND) is a phrase that was used in the 1950s to describe the formalization of nuclear structure theory along the lines of quantum electrodynamics (QED). Unfortunately, despite the early development of a quantum mechanical foundation for nuclear theory (the independent-particle model, IPM), the nuclear version of QED turned out to be "so difficult that no one has ever been able to figure out what the consequences of the theory are" (Feynman, 1963, p. 39) and the promise of a unified, quantitative explanation of the atomic nucleus has not been realized.

The principal problem still lies in our understanding of the "strong" nuclear force. Unlike classical electromagnetic theory, from which charge interactions can be calculated, a fundamental theory of nucleon-nucleon interactions has not been established. In the hope of such a discovery, most theorists in the 1960s turned their attention to *particle* physics and, jumping over the chronic problems of nuclear structure, engaged in the development of the high-energy theory known as quantum chromodynamics (QCD). Meanwhile, the enticing QND phrase has been effectively abandoned and is rarely even mentioned in the physics literature (Feynman, 1963; Karastoyanov, 2000). Here, I argue that: (i) the foundational concepts of a quantitative QND are already known, and (ii) its development awaits a focused research effort.

II. Quantum Electrodynamics

At the very beginnings of quantum theory, several profound and still-unresolved philosophical debates concerning its interpretation were initiated. Bizarre and untested arguments (concerning parallel universes, time travel, parapsychology, and so on) continue to be made on the basis of those non-classical interpretations, but, as a matter of fact,

practicing physicists can rely on the mathematical formalism of quantum mechanics to predict a broad range of atomic, molecular and solid-state phenomena. In that respect – and regardless of philosophical arguments – there is no doubt that (i) quantum theory is fundamentally correct and, moreover, that (ii) its most precise applications are currently found in QED. Notably, unlike the debates concerning the interpretation of quantum mechanics (the collapse of the wave function, the implications of the uncertainty principle, the wave-particle duality, the stochastic nature of reality, etc.), there are today virtually no dissenting opinions concerning the unprecedented precision of QED – "the jewel of physics" (Feynman, 1985, p. 6). As a quantitative theory that allows for an understanding of the absorption and emission of photons in terms of the transitions of electrons from one quantal state to another, QED remains unchallenged.

Despite the technical complexity of quantum mechanics, in general, and QED, in particular, the conceptual *simplicity* of atomic theory can be illustrated as in Figure 1. As first understood by Niels Bohr in the 1920s, for a hydrogen-like atom in which there is one electron orbiting around a central nucleus containing Z-charges, the entire set of excited states, their transitions and light spectra can be calculated on the basis of quantum theory (Figure 1A). Adding a second electron introduces electron-electron effects that can be computed, and further electrons introduce screening effects that must be handled on an *ad hoc* basis, but the fully developed theory of atomic structure remains qualitatively accurate and, with suitable parameter adjustments, quantitatively precise (Figure 1B).

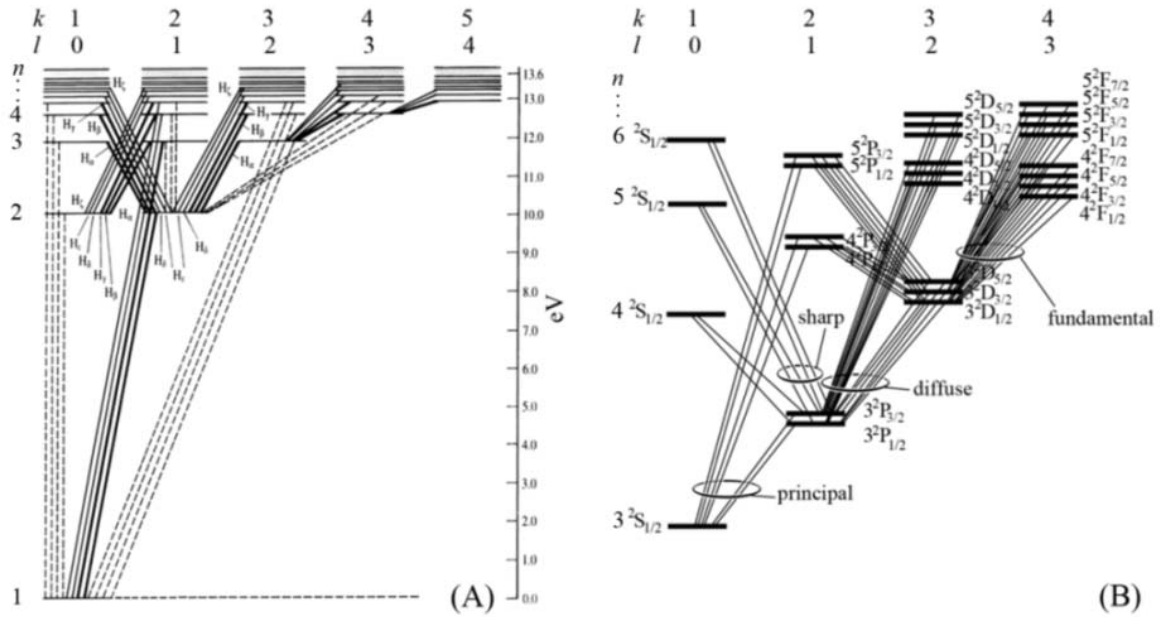

Figure 1: (A) The energy states of hydrogen – all of which can be calculated in quantum mechanics. (B) Related energy levels and allowed one-electron transitions of the sodium atom.

Quantum mechanical results concerning the light spectra are the most spectacular, because theoretical predictions can be compared *directly* with experimental data. The central idea that makes prediction possible is that there is an underlying quantal "texture" of all possible electron states. As illustrated in Figure 1, any atomic state is a specific configuration of electrons with known ***n***, ***l*** and ***m*** quantum numbers that are used in the calculation of photon energies and of the allowed and forbidden transitions. The wave-function for electrons specifies the relationships among the quantum numbers as:

$$\Psi_{n,l,m} = R_{n,l}(r)\, Y_{m,l}(\theta, \phi) \qquad \text{Eq. 1}$$

The permutations of ***n***, ***l*** and ***m*** – and their dual occupancy with spin-up and spin-down electrons (***s***) provides the entire theoretical framework for determining the energy states of electrons (Eqs. 2-5, Table 1), and consequently light spectra. As stated in all textbooks on atomic theory, ***n***, ***l***, m_l and m_s can take certain integer or half-integer values:

n =1, 2, 3, 4, … Eq. 2
l = 0, 1, 2, …, n-1 Eq. 3
m_l = -l, …, -2, -1, 0, 1, 2, …, l Eq. 4
m_s =s = 1/2, -1/2 Eq. 5

Based on the occupancy of the shells and subshells of Eqs. 1-5, it was possible to explain the length of the periods in the Periodic Table of the elements. That theoretical achievement was a decisive factor in establishing quantum theory as the core explanation of atomic structure. Today, it can be said that the pattern of electron states, as shown in Table 1, is: (i) the bedrock of atomic theory, (ii) the foundation upon which an understanding of the Periodic Table is built, and (iii) the conceptual framework for essentially all of modern chemistry.

		K	L		M			N			O		N	O	P	
Quantum Numbers	n	1	2		3			4			5		4	5	6	
	l	0	0	1	0	1	2	0	1	2	0	1	3	2	0	1
		s	s	p	s	p	d	s	p	d	s	p	f	d	s	p
	m_l	0	0	-1 0 1	0	-1 0 1	-2 -1 0 1 2	0	-1 0 1	-2 -1 0 1 2	0	-1 0 1	-3 -2 -1 0 1 2 3	-2 -1 0 1 2	0	-1 0 1
	m_s	⇑⇓	⇑⇓	⇑⇓⇑⇓⇑⇓	⇑⇓	⇑⇓⇑⇓⇑⇓	⇑⇓⇑⇓⇑⇓⇑⇓⇑⇓	⇑⇓	⇑⇓⇑⇓⇑⇓	⇑⇓⇑⇓⇑⇓⇑⇓⇑⇓	⇑⇓	⇑⇓⇑⇓⇑⇓	⇑⇓⇑⇓⇑⇓⇑⇓⇑⇓⇑⇓⇑⇓⇑⇓	⇑⇓⇑⇓⇑⇓⇑⇓⇑⇓	⇑⇓	⇑⇓⇑⇓⇑⇓
Closed (sub)Shells		K	(L1)	L2	(M1)	M2	(M3)	(N1)	N2	(N3)	(O1)	O2	(N4)	(O3)	(P1)	P2
Number of States		2	2	6	2	6	10	2	6	10	2	6	14	10	2	6
Total Electrons		2	10		18		36			54			86			

Table 1: The full set of ***n***-, ***l***-, m_l- and m_s-quantal states of the first 86 electrons (after Herzberg, 1937). The "spherical harmonics" of electron orbitals (expressed by r, θ and ϕ) make atomic structure geometrically complex, but the underlying simplicity is due to the integer relationships among the quantum numbers.

III. The Road Toward Quantum Nucleodynamics

Although QED techniques were adapted to the problems of nuclear theory in the 1940s and 1950s, they did *not* lead to a rigorous QND, primarily because the fundamental force

holding nuclei together remained uncertain. As a consequence, theorists did *not* produce a quantitative explanation of the properties of nuclear ground- and excited-states. Instead, nuclear structure theory has remained a field where many mutually-contradictory "models" were employed – interesting, but imperfect analogies with macroscopic objects, all of which have known problems and only limited applications.

The atomic and nuclear systems are remarkably *different* in that the atom is a low-density "gas," whereas the nucleus is an extremely high-density liquid whose macroscopic properties are accurately described in the liquid-drop model (LDM). Remarkably, although different forces hold these systems together, the atom and the nucleus are strikingly *similar* in terms of the quantal states of their constituent fermions. Their similarity can be described most clearly in terms of the wave-functions used in both realms.

The nuclear version of the wave-function is shown in Eq. 6. In comparison to atomic theory, there are two factors that increase the complexity of the nuclear equation. The first is that the nucleus contains two types of nucleon, protons and neutrons, that are distinguished in terms of the so-called isospin quantum number, ***i***. The second is the notion of the coupling of orbital angular momentum (***l***) with intrinsic angular momentum (***s***) – giving each nucleon a total angular momentum quantum value (***j***=***l***$\pm$***s***). As a consequence, the nuclear wave-equation has two additional subscripts and a slightly more complex pattern of shell/subshell occupancy (Table 2).

$$\Psi_{n,j\,(l+s),m,i} = R_{n,j\,(l+s),i}\,(r)\; Y_{m,j\,(l+s),i}\,(\theta, \phi) \qquad \text{Eq. 6}$$

Quantum Numbers																											
	n	0	1			2						3									4						
	l	0	1		0	2		1		0		3			2		1		0		4						…
	j	1/2	3/2		1/2	5/2		3/2		1/2		7/2			5/2		3/2		1/2		9/2						…
	$\|m\|$	1/2	3/2	1/2	1/2	5/2	3/2	1/2	3/2	1/2	1/2	7/2	5/2	3/2	1/2	5/2	3/2	1/2	3/2	1/2	1/2	9/2	7/2	5/2	3/2	1/2	7/2
	s	⇑⇓	⇑⇓	⇑⇓	⇑⇓	⇑⇓	⇑⇓	⇑⇓	⇑⇓	⇑⇓	⇑⇓	⇑⇓	⇑⇓	⇑⇓	⇑⇓	⇑⇓	⇑⇓	⇑⇓	⇑⇓	⇑⇓	⇑⇓	⇑⇓	⇑⇓	⇑⇓	⇑⇓	⇑⇓	⇑⇓	⇑⇓
Number of States		2	4		2	6		4		2		8			6		4		2		10						…
(Semi)magic Numbers		**2**	(6)		**8**	(14)		(18)		**20**		**28**			(34)		(38)		(40)		**50**						…
Total Nucleons	i	4	12		16	28		36		40		56			68		76		80		100						…

Table 2: The quantum states of the first 100 nucleons in the nuclear independent-particle model. As in atomic physics the sequential filling of the theoretical shells and subshells can be adjusted to explain the existence of closed shells at the "magic" numbers.

The theoretical foundation of the nuclear IPM (Eq. 6) is remarkably similar to that of atomic structure (Eq. 1). Moreover, the range of values that the quantum numbers in the nucleus can take (Eqs. 7-12) was found to be similar to those of electron states (Eqs. 2-5):

n =0, 1, 2, 3, …	Eq. 7
l = 0, 1, 2, …, (2***n***)/2	Eq. 8
j =1/2, 3/2, 5/2, …, (2***n***+1)/2	Eq. 9
m = -***j***, …, -5/2, -3/2, -1/2, 1/2, 3/2, 5/2, …, ***j***	Eq. 10
s =1/2, -1/2	Eq. 11
i =1, -1	Eq. 12

While many questions with regard to the nuclear force remain unanswered, these equations are a concise statement of the established quantum mechanical behavior of the nucleus. Moreover, similar to the prediction of electron-shell closure, the "magic" numbers of the nuclear shell model can be obtained by manipulations of the occupancy of the ***n***-shells and ***j***-subshells (Table 2). The achievement of a theoretical framework within which the regularities of both atomic and nuclear structure could be explained was understood as demonstration that quantum mechanics lies at the heart of both systems. That argument – acknowledged by virtually every theorist involved in atomic or nuclear physics – remains a remarkable triumph of quantum theory.

The main merit of the nuclear IPM lies in the fact that each nucleon in the model has a unique set of quantum numbers (***n, j, m, l, s, i***), as summarized in Table 2. Using that foundation for describing individual nucleons, the IPM made it possible to explain all *nuclear* states as the simple summation of the properties of its "independent" *nucleons* (e.g., Figure 2). In fact, the predictions of total angular momentum and parity states (J^{π}) were great successes in the early 1950s, but a rigorous, quantitative QND theory of nuclear structure did not emerge.

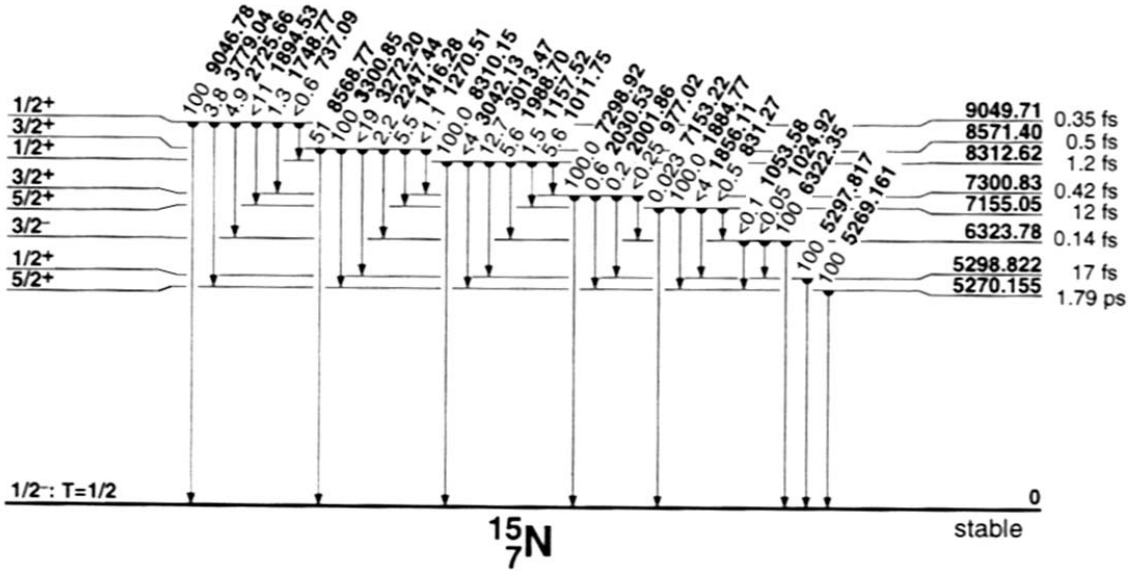

Figure 2: An example of the level of experimental detail known from nuclear spectroscopy (Firestone, 1996). The ***J***-values, parities, lifetimes, relative transition probabilities and energies of low-lying excited states have been measured for 2800+ isotopes. Although the ***J***-values and parities (far left) for ^{15}N are consistent with the IPM, the complex pattern of excitation energies, transition probabilities and lifetimes (center and far right) remains to be explained.

The development of the nuclear IPM began soon after the discovery of the neutron in 1932 and, in the late 1930s, Wigner noted that the quantal symmetries of the nucleus correspond to the symmetries of a face-centered lattice (1937). That theoretical work was

immediately recognized as important – and eventually led to his sharing the Nobel Prize in physics, together with the inventors of the shell model. Wigner's lattice representation of nuclear states was unfortunately ignored. In its modern form (including both spin-orbit coupling and isospin), the lattice representation means that nucleon quantum numbers can be used to deduce the fcc coordinates (x, y, z) of the nucleons (Eqs. 13-15):

$$x = |2\boldsymbol{m}|(-1)^{(\boldsymbol{m}-1/2)} \quad \text{Eq. 13}$$
$$y = (2\boldsymbol{j}+1-|x|)(-1)^{(\boldsymbol{i}/2+\boldsymbol{j}+\boldsymbol{m}+1/2)} \quad \text{Eq. 14}$$
$$z = (2\boldsymbol{n}+3-|x|-|y|)(-1)^{(\boldsymbol{i}/2+\boldsymbol{n}-\boldsymbol{j}+1)} \quad \text{Eq. 15}$$

And, vice versa, the unique Cartesian coordinates for each nucleon can be used to define their quantal characteristics (Eqs. 16-22):

$$\boldsymbol{n} = (|x| + |y| + |z| - 3) / 2 \quad \text{Eq. 16}$$
$$\boldsymbol{l} = (|x| + |y| - 2) / 2 \quad \text{Eq. 17}$$
$$\boldsymbol{j} = (|x| + |y| - 1) / 2 \quad \text{Eq. 18}$$
$$\boldsymbol{m} = |x| * (-1)^{((x-1)/2)} / 2 \quad \text{Eq. 19}$$
$$\boldsymbol{s} = (-1)^{((x-1)/2)} / 2 \quad \text{Eq. 20}$$
$$\boldsymbol{i} = (-1)^{((z-1)/2)} \quad \text{Eq. 21}$$
$$\boldsymbol{parity} = \boldsymbol{\pi} = \text{sign}(x*y*z) \quad \text{Eq. 22}$$

The significance of Eqs.13~22 lies in the fact that: *if we know the IPM structure of a nucleus, then we also know its lattice structure*, and vice versa. The ***known*** pattern of quantum numbers and the ***known*** occupancy of protons and neutrons in the ***n***-shells and in the ***j***- and ***m***-subshells are *identical* in both descriptions, but, in coordinate space, the abstract symmetries of the wave-function exhibit macroscopic geometrical symmetries, as well. The ***n***-shells and, ***j***- and ***m***-subshells have spherical, cylindrical and conical symmetries, respectively, while ***s***- and ***i***-values produce orthogonal layering. Numerical examination of the symmetries in relation to the Cartesian coordinates shows the validity of Eqs. 13-22 (see the Appendix) and the quantal texture of even the large nuclei can be easily visualized and verified using software designed for that purpose (Cook et al., 1999). The mathematically unambiguous isomorphism between quantum space and lattice space has been elaborated on in many publications over the past three decades, but the potential implications for the establishment of QND are new, and are outlined below.

The foundations of the solid-phase model were laid in Eugene Wigner's Nobel Prize winning publications from the 1930s, and later developed by Everling (1958, 1988, 2008), Lezuo (1974, 1975a, b), Cook (1976-2011), Dallacasa (1981, 1987, 2010), DasGupta (1996, 1997, 1998), Musulmanbekov (2003, 2008), Pan (1995, 1998) and various others. The key insight, *explicitly stated by Wigner in 1937*, is that the quantal symmetries of nucleon eigenvalues correspond to the symmetries of a face-centered cubic (fcc) lattice: "the quantum numbers are all half-integers [whose] combinations form a face centered lattice…" (p. 106). Wigner himself discussed nuclear states in terms of an abstract, multidimensional

"momentum space," but all subsequent developments of the lattice model of nuclear structure have been in relation to coordinate space, i.e., 3D geometry.

From the perspective of the traditional, gaseous-phase nuclear IPM that has dominated nuclear structure theory since 1949, the lattice representation of nuclear symmetries might be dismissed as a "lucky coincidence" between the known quantal symmetries of the nucleus and the inevitable arithmetic regularities of crystal symmetries, but the opposite view is worth considering: Could the low-density nuclear IPM fortuitously mimic the symmetries of a lattice of nucleons, rather than vice versa? In terms of the known spatial dimensions of nucleons and nuclei, the high-density lattice is a far more realistic approximation of the nuclear texture than a Fermi gas and essentially reproduces all of the macroscopic nuclear properties for which the LDM is justifiably famous. Moreover, the development of a theory of nuclear structure on the basis of the *known* short-range nuclear force is far more straight-forward than creating *de novo* a theoretical "mean-field" that is required to justify a gaseous model.

The identity between the IPM and the lattice (outlined above) implies that *every* known nuclear state in the IPM has an analog in 3D coordinate space. *Every* transition of nucleons from one quantal state to another – explicable in terms of integral changes in the quantum numbers in the wave-equation – necessarily corresponds to a specific vector in the nuclear lattice space. From a computational perspective, the most significant aspect of the lattice is that its geometry can be used in the development of a realistic, local-interaction version of the IPM, i.e., what might be considered as the structural foundations of QND.

At an abstract level, the conventional IPM and the lattice IPM are similar insofar as quantitative results that could be compared directly with experimental data require a full explication of the interactions of all nucleon pairs. Noteworthy is the fact that the lattice geometry provides important constraints on permutations due to the fixed spatial dimensions of the lattice. That implies a "parameter adjustment" procedure not unlike the gaseous IPM, but the lattice IPM makes it theoretically possible to insert a model of the nuclear force directly into the lattice to obtain quantitative nuclear binding energies (etc.) without *post hoc* adjustments. In principle, all possible permutations of $\boldsymbol{n}$, $\boldsymbol{l}$, $\boldsymbol{j}$, $\boldsymbol{m}$, $\boldsymbol{s}$ and $\boldsymbol{i}$ for each of the relevant distances between lattice sites can be tabulated and the strength of each solved using a simultaneous equations technique. Currently, lattice QND is still semi-quantitative. Specifically, although a first-order description of nuclear ground-states in the lattice was achieved in the 1980s, attempts at a more detailed specification of nuclear force effects have begun only recently. It is noteworthy that, as of today, calculation of all permutations of $\boldsymbol{n}$, $\boldsymbol{l}$, $\boldsymbol{j}$, $\boldsymbol{m}$, $\boldsymbol{s}$ and $\boldsymbol{i}$ at various (1^{st}~3^{rd} nearest-neighbor) internucleon distances within the lattice IPM can be calculated and parameter sets for nucleon-nucleon interactions can be explored. However, in order for the lattice model to evolve into a rigorously quantitative QND (on a par with quantitative QED), it will be necessary to implement a realistic nuclear force within the lattice. In principle, that is already possible, but fine-tuning will require the efforts of many researchers.

Preliminary results on nuclear binding energies have been obtained using multiple regression techniques and the results of four such analyses are shown in Tables 3-6. In all four analyses, a y-intercept of zero was chosen. In effect, forcing the regression line through the origin implicitly assumes that, in each analysis, there are no other relevant factors (that

normally lead to a non-zero intercept). Such an assumption is of course physically unrealistic, but it allows for an evaluation of the overall ability of the assumed parameters in each analysis to account for nuclear binding energies.

The first analysis was done to determine the mean binding energy among nearest-neighbor nucleons in a close-packed lattice. For that purpose, 273 representative (stable and meta-stable) nuclei (A=16~209) were built following the lattice definitions in Eqs. 13-22. Lattice structures were optimized only in the sense that the lattice structure for each isotope had total spin and parity values (J^{π}) that were consistent with experimental values and, under that constraint, had (i) maximal nearest-neighbor nucleon-nucleon bonds and (ii) minimal Coulomb repulsion among protons. Note that the total Coulomb repulsion in the fcc lattice was also calculated, and added to the experimental total binding energy before solving for the mean binding energy per bond. Table 3 shows that a surprisingly-small mean value of 2.733 MeV per nearest-neighbor nucleon-nucleon bond accounts for the total binding energy of nuclei.

Needless to say, this analysis is not a realistic view of nuclear binding because a one-factor design ignores all possible higher-order effects on binding due to spin, isospin, etc. Nonetheless, it is of interest that 2.6~2.8 MeV is found to be the mean value per nearest-neighbor bond for nuclei ranging from ^{40}Ca (2.779 MeV) to ^{104}Pd (2.790 MeV) to ^{170}Yt (2.693 MeV) to ^{209}Bi (2.676 MeV). This theoretical result indicates that the lattice model has properties similar to the LDM, and exhibits saturation of the nuclear binding force solely as a consequence of the binding energy among nearest-neighbors.

Table 3: Multiple Regression with 1 Factor

Multiple Regression				
R	0.999947			
R2	0.999894			
Corr. R2	0.996217			
Std Dev	15.10207			
No. Obs.	273			
	Coeff.	*Std Dev*	*t*	*P-value*
1st Neighbors	2.733	0.002	1599.216	0.000

A slightly more realistic analysis was then done on the same set of nuclei, with consideration of the factor of distance among nucleons up to third nearest-neighbors. Table 4 shows that, on average, first-nearest neighbor interactions are attractive (2.697 MeV), second-nearest neighbors are repulsive (-1.172 MeV) and third-nearest neighbors are, on average, weakly attractive (0.592 MeV). Note that this analysis does not include the factor of isospin; all nucleons are treated as identical, with only the distance among lattice sites taken into consideration. It is noteworthy that the antiferromagnetic array of nucleons with alternating isospin layering implies attractive nearest-neighbors and repulsive second nearest-neighbors, due to magnetic effects, while third-nearest neighbors are weakly attractive. In other words, the raw data obtained from the lattice build-up is consistent with the antiferromagnetic ordering of nucleons.

Table 4: Multiple Regression with 3 Factors

Multiple Regression				
R	0.99997			
R2	0.99995			
Corr. R2	0.99624			
Std. Dev.	10.6808			
No. Obs.	273			
	Coeff.	*Std. Dev.*	*t*	*P-value*
1st Neighbors	2.697	0.034	78.226	0.000
2nd Neighbors	-1.172	0.072	-16.236	0.000
3rd Neighbors	0.592	0.047	12.505	0.000

The third analysis (Table 5) takes isospin and distance among the nucleons into consideration. Note that, in the antiferromagnetic fcc lattice with alternating isospin layers, first-neighbor and third-neighbor like-isospin combinations (PP1, NN1, PP3, NN3) are necessarily singlet pairs and second-neighbor like-isospin pairs (PP2 and NN2) are necessarily triplet pairs. There are no PN-pairs (PN2) at a distance of the second nearest-neighbor PP2 and NN2 pairs in the fcc lattice, while proton-neutron pairs (PN1 and PN3) include both singlet and triplet pairs. The relatively large coefficients for the first-neighbor bonds (and the correspondingly high-t and low-P values) are indication that nearest-neighbors have the strongest influence on nuclear binding, while second and third nearest-neighbors have weaker effects. All eight factors in this analysis were, however, statistically significant ($p<0.009$) – again indicating that the raw data on bonding within the lattice are consistent with the known binding energies.

Note that, typical of multiple regression analysis in general, R-values soon approach unity (1.0) in all the analyses. The large R-values *cannot* be interpreted as indicating a high statistical likelihood that the values obtained for the nuclear force coefficients accurately reflect the character of the nuclear force, but R~1.0 and relatively low standard deviations do indicate that there are few anomalies in the raw data (i.e., the data on the numbers of different types of nucleon-nucleon bonds within the lattice structures are self-consistent).

Table 5: Multiple Regression with 8 Factors

Multiple Regression				
R	0.99999			
R2	0.99998			
Corr. R2	0.99620			
Std Dev	7.48748			
No. Obs.	273			
	Coeff.	*Std. Dev.*	*t*	*P-value*
PP1	2.596	0.298	8.723	0.000
PP2	-0.867	0.226	-3.828	0.000
PP3	1.363	0.168	8.113	0.000
NN1	1.762	0.217	8.133	0.000
NN2	-0.380	0.142	-2.677	0.008
NN3	-0.605	0.117	-5.191	0.000
PN1	2.681	0.125	21.437	0.000
PN3	0.796	0.072	11.046	0.000

Finally, a regression analysis that includes spin effects among the proton-neutron pairs is shown in Table 6. Note that first and third nearest-neighbor, like-isospin combinations are necessarily singlet-pairs ("s") in the lattice (PP1s, PP3s, NN1s, NN3s) and second nearest-neighbor pairs are triplets ("t"). In contrast, first and third nearest-neighbor PN pairs include both singlet and triplet combinations (PN1s, PN1t, PN3s, PN3t). There are no second nearest-neighbor singlet or triplet PN2 pairs in the antiferromagnetic fcc lattice with alternating isospin layers.

Table 6: Multiple Regression with 10 Factors

Multiple Regression				
R	0.99999			
R2	0.99998			
Corr. R2	0.99620			
Std Dev	7.44021			
No. Obs.	273			
	Coeff.	*Std. Dev.*	*t*	*P-value*
PP1s	2.715	0.301	9.035	0.000
PP2t	-0.918	0.226	-4.054	0.000
PP3s	1.436	0.170	8.449	0.000
NN1s	1.804	0.217	8.306	0.000
NN2t	-0.332	0.145	-2.284	0.020
NN3s	-0.615	0.116	-5.298	0.000
PN1t	3.025	0.447	6.772	0.000
PN1s	2.258	0.470	4.807	0.000
PN3t	1.208	0.195	6.209	0.000
PN3s	0.338	0.210	1.607	0.109

As is typical of regression analysis, in general, an increase in the number of regression coefficients leads to greater R-values and lower standard deviations. Although those statistics indicate increasingly better "fits" between the data and the model, the statistical strength of the individual coefficients gradually weakens, and confidence in the physical validity of the model can be strengthened only by increasing the data set. Note that the standard deviation of ~7.44 MeV for the predictions of 273 nuclei with binding energies ranging from 127 to 1640 MeV is comparable to the conventional LDM. Moreover, it is noteworthy that all of the nuclear coefficients lend themselves to physically realistic interpretations in terms of a short-range nuclear force, and there is no need to append shell-correction terms or to include adjustable parameters associated with the nuclear volume, deformation or surface area.

A similar analysis using the full set of permutations of nucleon states is the next obvious step to take. Unfortunately, the large number of permutations of nucleon combinations – each with distinct spin, isospin, ***j***- and ***m***-quantum values (Table 7) – makes statistical analysis impossible until the data from many thousands of lattice structures are included. Such analysis is, in principle, possible, but will require a large-scale team research effort, as was indeed undertaken for the development of the shell model in the 1950s.

Table 7: Nuclear force coefficients for the 80 permutations (***j, m, s, i***) among 1st (PP1, NN1, PN1), 2nd (PP2, NN2) and 3rd (PP3, NN3, PN3) nearest-neighbor nucleon-nucleon combinations, up to j=5/2 and m=5/2. All nearest-neighbor PP and NN combinations are singlet pairs (s), all 2nd nearest-neighbor PP and NN combinations are triplet pairs (t), whereas PN1 and PN3 pairs include both singlet and triplet combinations. These coefficients correspond to a subset of the Clebsch-Gordon coefficients used in the conventional IPM.

Lattice Definitions	Force Coeffs.	Lattice Definitions	Force Coeffs.
$PP1_{(j1/2\text{-}1/2)(m1/2\text{-}1/2)s}$	-	$NN1_{(j1/2\text{-}1/2)(m1/2\text{-}1/2)s}$	-
$PP1_{(j1/2\text{-}3/2)(m1/2\text{-}1/2)s}$	-	$NN1_{(j1/2\text{-}1/2)(m1/2\text{-}1/2)s}$	-
$PP1_{(j1/2\text{-}3/2)(m1/2\text{-}3/2)s}$	-	$NN1_{(j1/2\text{-}1/2)(m1/2\text{-}1/2)s}$	-
$PP1_{(j1/2\text{-}5/2)(m1/2\text{-}1/2)s}$	-	$NN1_{(j1/2\text{-}5/2)(m1/2\text{-}1/2)s}$	-
$PP1_{(j1/2\text{-}5/2)(m1/2\text{-}3/2)s}$	-	$NN1_{(j1/2\text{-}5/2)(m1/2\text{-}3/2)s}$	-
$PP1_{(j3/2\text{-}3/2)(m1/2\text{-}1/2)s}$	-	$NN1_{(j3/2\text{-}3/2)(m1/2\text{-}1/2)s}$	-
$PP1_{(j3/2\text{-}3/2)(m1/2\text{-}3/2)s}$	-	$NN1_{(j3/2\text{-}3/2)(m1/2\text{-}3/2)s}$	-
$PP1_{(j3/2\text{-}3/2)(m3/2\text{-}5/2)s}$	-	$NN1_{(j3/2\text{-}3/2)(m3/2\text{-}5/2)s}$	-
$PP2_{(j1/2\text{-}1/2)(m1/2\text{-}1/2)t}$	-	$NN2_{(j1/2\text{-}1/2)(m1/2\text{-}1/2)t}$	-
$PP2_{(j1/2\text{-}3/2)(m1/2\text{-}1/2)t}$	-	$NN2_{(j1/2\text{-}1/2)(m1/2\text{-}1/2)t}$	-
$PP2_{(j1/2\text{-}3/2)(m1/2\text{-}3/2)t}$	-	$NN2_{(j1/2\text{-}1/2)(m1/2\text{-}1/2)t}$	-
$PP2_{(j1/2\text{-}5/2)(m1/2\text{-}1/2)t}$	-	$NN2_{(j1/2\text{-}5/2)(m1/2\text{-}1/2)t}$	-
$PP2_{(j1/2\text{-}5/2)(m1/2\text{-}3/2)t}$	-	$NN2_{(j1/2\text{-}5/2)(m1/2\text{-}3/2)t}$	-
$PP2_{(j3/2\text{-}3/2)(m1/2\text{-}1/2)t}$	-	$NN2_{(j3/2\text{-}3/2)(m1/2\text{-}1/2)t}$	-
$PP2_{(j3/2\text{-}3/2)(m1/2\text{-}3/2)t}$	-	$NN2_{(j3/2\text{-}3/2)(m1/2\text{-}3/2)t}$	-
$PP2_{(j3/2\text{-}3/2)(m3/2\text{-}5/2)t}$	-	$NN2_{(j3/2\text{-}3/2)(m3/2\text{-}5/2)t}$	-
$PP3_{(j1/2\text{-}1/2)(m1/2\text{-}1/2)s}$	-	$NN3_{(j1/2\text{-}1/2)(m1/2\text{-}1/2)s}$	-
$PP3_{(j1/2\text{-}3/2)(m1/2\text{-}1/2)s}$	-	$NN3_{(j1/2\text{-}1/2)(m1/2\text{-}1/2)s}$	-
$PP3_{(j1/2\text{-}3/2)(m1/2\text{-}3/2)s}$	-	$NN3_{(j1/2\text{-}1/2)(m1/2\text{-}1/2)s}$	-
$PP3_{(j1/2\text{-}5/2)(m1/2\text{-}1/2)s}$	-	$NN3_{(j1/2\text{-}5/2)(m1/2\text{-}1/2)s}$	-
$PP3_{(j1/2\text{-}5/2)(m1/2\text{-}3/2)s}$	-	$NN3_{(j1/2\text{-}5/2)(m1/2\text{-}3/2)s}$	-
$PP3_{(j3/2\text{-}3/2)(m1/2\text{-}1/2)s}$	-	$NN3_{(j3/2\text{-}3/2)(m1/2\text{-}1/2)s}$	-
$PP3_{(j3/2\text{-}3/2)(m1/2\text{-}3/2)s}$	-	$NN3_{(j3/2\text{-}3/2)(m1/2\text{-}3/2)s}$	-
$PP3_{(j3/2\text{-}3/2)(m3/2\text{-}5/2)s}$	-	$NN3_{(j3/2\text{-}3/2)(m3/2\text{-}5/2)s}$	-
$PN1_{(j1/2\text{-}1/2)(m1/2\text{-}1/2)s,t}$	-	$PN3_{(j1/2\text{-}1/2)(m1/2\text{-}1/2)s,t}$	-
$PN1_{(j1/2\text{-}3/2)(m1/2\text{-}1/2)s,t}$	-	$PN3_{(j1/2\text{-}3/2)(m1/2\text{-}1/2)s,t}$	-
$PN1_{(j1/2\text{-}3/2)(m1/2\text{-}3/2)s,t}$	-	$PN3_{(j1/2\text{-}3/2)(m1/2\text{-}3/2)s,t}$	-
$PN1_{(j1/2\text{-}5/2)(m1/2\text{-}1/2)s,t}$	-	$PN3_{(j1/2\text{-}5/2)(m1/2\text{-}1/2)s,t}$	-
$PN1_{(j1/2\text{-}5/2)(m1/2\text{-}3/2)s,t}$	-	$PN3_{(j1/2\text{-}5/2)(m1/2\text{-}3/2)s,t}$	-
$PN1_{(j3/2\text{-}3/2)(m1/2\text{-}1/2)s,t}$	-	$PN3_{(j3/2\text{-}3/2)(m1/2\text{-}1/2)s,t}$	-
$PN1_{(j3/2\text{-}3/2)(m1/2\text{-}3/2)s,t}$	-	$PN3_{(j3/2\text{-}3/2)(m1/2\text{-}3/2)s,t}$	-
$PN1_{(j3/2\text{-}3/2)(m3/2\text{-}5/2)s,t}$	-	$PN3_{(j3/2\text{-}3/2)(m3/2\text{-}5/2)s,t}$	-

Whatever the final outcome of such statistical analysis, the essential merit of the lattice version of the IPM is that *all* two-body nucleon-nucleon interactions in a given nucleus can be specified in terms of nucleon quantum numbers (known from the conventional IPM) and distances/orientations within the lattice. By discarding the assumption of "intranuclear orbiting" of nucleons, each nucleon has a relatively small number of neighbors that can be expected to influence nuclear binding. Specifically, each nucleon in the close-packed lattice has a maximum of 12 nearest-neighbors, 6 second nearest-neighbors and 24 third nearest-neighbors. The effects among even further neighbors can of course be calculated, but would likely be a small correction on total binding energies. In either case, the fixed dimensions of a lattice of nucleons with a core density of 0.17 nucleons/fm^3 mean that any realistic model of the nuclear force (Paris, Bonn, Argonne, Idaho, etc.) that makes use of those same parameters (internucleon distance, spin, isospin, $\boldsymbol{j}$ and $\boldsymbol{m}$) should plug directly into the lattice, and allow for quantitative predictions concerning both ground-state binding energies and excited states.

IV. Conclusion

The hypothesis of lattice-based QND clearly remains an unfinished task and will require the efforts of many researchers to complete. The strongest argument in favor of lattice QND is the remarkable (but largely overlooked) identity of IPM symmetries and the fcc lattice (together with the widely acknowledged *failure* of conventional nuclear structure modeling since the 1930s). Arguments against lattice QND, on the other hand, rest on inherently controversial ideas concerning the various interpretations of quantum theory – ideas that have been debated without resolution by the "giants" of quantum theory: Bohr, Einstein, Schrödinger, Heisenberg, Pauli, Bohm, Born, deBroglie and others. In this regard, it is of interest that the successful completion of lattice QND would arguably resolve the century-old debate about the correct interpretation of QM in favor of Bohm's interpretation, insofar as Bohmian mechanics does not insist on the indeterminist, Copenhagen interpretation of the uncertainty relations (Cushing, 1994; Dürr et al., 2013).

References

Cook, N.D., *Atomkernenergie* 28, 195, 1976.
Cook, N.D., *Journal of Physics* G 13, L103, 1987.
Cook, N.D., *Modern Physics Letters* A5, 1321, 1990.
Cook, N.D., *Journal of Physics* G25, 1, 1999.
Cook, N.D., *St. Andrews Conference on Nuclear Fission*, World Scientific, 1999, pp. 217-225.
Cook, N.D., *Models of the Atomic Nucleus*, 2nd Edition, Springer, 2010.
Cook, N.D., The inherent geometry of the nuclear Hamiltonian, *arXiv*:1101.4251, 2011.
Cook, N.D., and Dallacasa, V., *Physical Review* C36, 1883, 1987.
Cook, N.D., and Dallacasa, V., *Proceedings of ICCF15*, Rome, October, 2009.
Cook, N.D., Hayashi, T., and Yoshida, N., *IEEE Computer Graphics and Applications* 19, 54, 1999.
Cushing, J.T., *Quantum Mechanics: Historical contingency and the Copenhagen hegemony*, University of Chicago Press, Chicago, 1994.
Dallacasa, V., *Atomkernenergie* 37, 143, 1981.

Dallacasa, V., and Cook, N.D., *Il Nuovo Cimento* A97, 157, 1987.
Dallacasa, V., DeSia, P., and Cook, N.D., The magnetic force between nucleons. In, *Models of the Atomic Nucleus*, 2nd Edition, Springer, 2010, pp. 217-221.
DasGupta, S., and Pan, J., *Physical Review* C53, 1319, 1996.
DasGupta, S., et al., *NuclearPhysics* A621, 897, 1997.
DasGupta, S., et al., *Physical Review Letters* 80, 1182, 1998.
Dűrr, D., Goldstein, S., & Zanghi, N., *Quantum Physics Without Quantum Philosophy*, Springer, Berlin, 2013.
Everling, F., personal communication concerning a notarized document from 1958.
Everling, F., *Physikalische Verhandlungen* 6, 210, 1988.
Everling, F., *Proceedings of an International Workshop PINGST 2000*, 204, 2008.
Feynman, R., *Six Easy Pieces*, Basic Books, 1963.
Feynman, R., *QED: The Strange Theory of Light and Matter*, Princeton University Press, Princeton, 1985.
Firestone, R.B., *Table of Isotopes*, 8th Edition, Wiley, 1996.
Herzberg, G., *Atomic Spectra and Atomic Structure*, Prentice-Hall, New York, 1937, p. 39.
Karastoyanov, A.S., *Bulgarian Journal of Physics* 27, 16, 2000.
Lezuo, K., *Atomkernenergie* 23, 285, 1974.
Lezuo, K., *Zeitschrift fűr Naturforschung* 30a, 158, 1975a.
Lezuo, K., *Zeitschrift fűr Naturforschung* 30a, 1018, 1975b.
Musulmanbekov, G., *arXiv:hep-ph/0304262*, 2003.
Musulmanbekov, G., *Yadernaya Fizika* 71, 1254, 2008.
Pan, J., and DasGupta, S., *Physical Review* C51, 1384, 1995.
Pan, J., and DasGupta, S., *Physical Review* C57, 1839, 1998.
Wigner, E., *Physical Review* 51, 106, 1937.

Appendix

A	B	C	D	E	F	G	H	I	J	K	L	M	N	O	P
		(Keyboard Input)			Quantum Numbers and Parities Calculated							Lattice Sites Calculated from the			X,Y,Z
Nucleon Sequence		FCC Lattice Sites			from the Lattice Sites (Eqs. 16-22)							Quantum Numbers (Eqs. 13-15)			coords.
Proton No.	Neutron No.	X	Y	Z	***n***	***L***	***j***	***m***	***s***	***i***	***parity***	X	Y	Z	Check
	1	1	-1	-1	0	0	1/2	1/2	1/2	-1	1	1	-1	-1	ok
1		1	1	1	0	0	1/2	1/2	1/2	1	1	1	1	1	ok
	2	-1	1	-1	0	0	1/2	-1/2	-1/2	-1	1	-1	1	-1	ok
2		-1	-1	1	0	0	1/2	-1/2	-1/2	1	1	-1	-1	1	ok
	3	1	3	-1	1	1	3/2	1/2	1/2	-1	-1	1	3	-1	ok
3		3	-1	1	1	1	3/2	-3/2	-1/2	1	-1	3	-1	1	ok
	4	-1	-3	-1	1	1	3/2	-1/2	-1/2	-1	-1	-1	-3	-1	ok
4		-1	3	1	1	1	3/2	-1/2	-1/2	1	-1	-1	3	1	ok
	5	3	1	-1	1	1	3/2	-3/2	-1/2	-1	-1	3	1	-1	ok
5		-3	1	1	1	1	3/2	3/2	1/2	1	-1	-3	1	1	ok
	6	-3	-1	-1	1	1	3/2	3/2	1/2	-1	-1	-3	-1	-1	ok
6		1	-3	1	1	1	3/2	1/2	1/2	1	-1	1	-3	1	ok
	7	-1	1	3	1	0	1/2	-1/2	-1/2	-1	-1	-1	1	3	ok
7		1	1	-3	1	0	1/2	1/2	1/2	1	-1	1	1	-3	ok
	8	1	-1	3	1	0	1/2	1/2	1/2	-1	-1	1	-1	3	ok
8		-1	-1	-3	1	0	1/2	-1/2	-1/2	1	-1	-1	-1	-3	ok
	9	3	-3	-1	2	2	5/2	-3/2	-1/2	-1	1	3	-3	-1	ok
9		3	3	1	2	2	5/2	-3/2	-1/2	1	1	3	3	1	ok
	10	-3	3	-1	2	2	5/2	3/2	1/2	-1	1	-3	3	-1	ok
10		-3	-3	1	2	2	5/2	3/2	1/2	1	1	-3	-3	1	ok
	11	5	-1	-1	2	2	5/2	5/2	1/2	-1	1	5	-1	-1	ok
11		5	1	1	2	2	5/2	5/2	1/2	1	1	5	1	1	ok
	12	-5	1	-1	2	2	5/2	-5/2	-1/2	-1	1	-5	1	-1	ok
12		1	5	1	2	2	5/2	1/2	1/2	1	1	1	5	1	ok
	13	1	-5	-1	2	2	5/2	1/2	1/2	-1	1	1	-5	-1	ok
13		-1	-5	1	2	2	5/2	-1/2	-1/2	1	1	-1	-5	1	ok
	14	-1	5	-1	2	2	5/2	-1/2	-1/2	-1	1	-1	5	-1	ok
14		-5	-1	1	2	2	5/2	-5/2	-1/2	1	1	-5	-1	1	ok
	15	3	1	3	2	1	3/2	-3/2	-1/2	-1	1	3	1	3	ok
15		-1	3	-3	2	1	3/2	-1/2	-1/2	1	1	-1	3	-3	ok
	16	1	3	3	2	1	3/2	1/2	1/2	-1	1	1	3	3	ok
16		1	-3	-3	2	1	3/2	1/2	1/2	1	1	1	-3	-3	ok
	17	-1	-3	3	2	1	3/2	-1/2	-1/2	-1	1	-1	-3	3	ok
17		3	-1	-3	2	1	3/2	-3/2	-1/2	1	1	3	-1	-3	ok
	18	-3	-1	3	2	1	3/2	3/2	1/2	-1	1	-3	-1	3	ok
18		-3	1	-3	2	1	3/2	3/2	1/2	1	1	-3	1	-3	ok
	19	-1	1	-5	2	0	1/2	-1/2	-1/2	-1	1	-1	1	-5	ok
19		1	1	5	2	0	1/2	1/2	1/2	1	1	1	1	5	ok
	20	1	-1	-5	2	0	1/2	1/2	1/2	-1	1	1	-1	-5	ok
20		-1	-1	5	2	0	1/2	-1/2	-1/2	1	1	-1	-1	5	ok
Proton No.	Neutron No.	X	Y	Z	***n***	***L***	***j***	***m***	***s***	***i***	***parity***	X	Y	Z	Check

Figure 3: Snapshot of an Excel spreadsheet in which nucleon quantum values (Columns F~L) are calculated from the lattice coordinates (Columns C~E). Conversely, Columns M~O are the lattice coordinates calculated from the nucleon quantum numbers, and Column P is a check on the equivalence between Columns C~E and M~O. Their identity ("ok") means that there is a one-to-one mapping of lattice coordinates of each nucleon to its quantum numbers.

Columns A and B are lists of the *approximate* empirical sequence of protons and neutrons. In detail, the build-up sequence is known to vary substantially, isotope-by-isotope. Not only does the proton or neutron sequence differ by isotope, but the addition of further neutrons can affect the proton sequence, and vice versa. This known variability ("configuration-mixing," "intruder states," etc.) implies that nuclear properties cannot be calculated (in either the conventional IPM or lattice QND) using an inflexible nucleon build-up sequence. Instead, the locations of the nucleons in each isotope must be shuffled to positions that reproduce the known ***J***-value and parity, π, while minimizing Coulomb repulsion among the protons and maximizing the total number of nucleon-nucleon bonds. The good news is that appropriate $\boldsymbol{J(\pi)}$ lattice structures can *always* be constructed (if the conventional IPM can describe the quantal state of a nucleus, so can lattice QND). The bad news is that the full set of lattice coordinates that reproduce the experimental $\boldsymbol{J(\pi)}$ is only rarely unique, and "optimal" structures must be determined on the basis of the summation of nuclear binding effects. The encircled region lists all of the quantum characteristics of the first 40 nucleons. Just as there are no two nucleons with identical Cartesian coordinates, there are no two nucleons with the same set of quantum numbers. All further nucleon shells can be similarly defined in the lattice.

Clearly, the *interpretation* of the mathematical identity between nuclear "quantum space" and the 3D geometry of the fcc lattice leads into controversy, but it can be said that much of science is concerned with the search for patterns and mathematical regularities. The match between the fcc lattice and the QM regularities of nuclear structure theory is self-evident, but the interpretation of the identity inevitably raises questions about the meaning of nucleons as particle/waves, and about the character of the nuclear force. On the one hand, the existence of the (sub)shells of the shell model and alpha cluster configurations within a "frozen" liquid-drop suggests an easy "unification" of the diverse models of traditional nuclear structure theory. On the other hand, although the extremely short-range of the nuclear force within the nucleon lattice is similar to the Paris, Bonn, Argonne and Idaho potentials, the implementation of those kinds of realistic nuclear forces in lattice QND implies the rejection of several decades of theoretical work on the "mean-field" approximation of the nuclear force as a fundamentally *unrealistic* approach to nuclear binding energies.

The spreadsheet and related computer algorithms (using Excel functions and the C-language, respectively) for calculating nuclear lattice properties can be downloaded at: www.res.kutc.kansai-u.ac.jp/~cook/. They provide unambiguous, numerical demonstration of the identity between the lattice and the well-established nuclear IPM. In order to formally give this approach to nuclear structure the "QND" label, however, it will be necessary to confront the numerical and, inevitably, the political problems of the long-standing enigma of nuclear physics, i.e., the nuclear force.

Narrowing down the candidate of the nuclear active environment (NAE)

Tetsuo Sawada
Institute of Quantum Science, Nihon University, Tokyo, 1018308, Japan

[Abstract]

We search for the underlying mechanism of the nuclear cold fusion reaction in this article. In the search, we use the fact that open channels of the d+d reaction change from $d+d \rightarrow t+p$ and $d+d \rightarrow {}^3He+n$ in vacuum to $d+d \rightarrow {}^4He$ in the cold nuclear fusion. This change of the open channel is sufficient to narrow down the candidates of the underlying mechanism of the nuclear cold fusion uniquely.

1. Introduction

In the separate paper "Proposal to extend the nuclear physics to include the magnetic monopole as an additional ingredient (T. Sawada) ", we showed the existence of the bound states of the nucleon and the magnetic monopole, by solving the Schrödinger equation. The magnetic moment of the nucleon in the magnetic Coulomb field produced by the magnetic monopole is responsible for the appearance of large attractive force, whenever the orientation of the magnetic dipole moment of the nucleon is outward (hedgehog solution). The orbital radius of the ground state is around several fm. The situation of the system of the small nuclei with non-zero spin and magnetic monopole (*e) is nearly the same and so it has the bound states. On the other hand, since alpha-particle does not have spin, the bound state with *e does not exist.

When two deuterons are trapped by the same magnetic monopole, the system becomes unstable because the two deuterons can transit to the much more stable state alpha-particle, namely the alpha particle must be emitted from the monopole (*e). There remains the fresh magnetic monopole, and it starts to attract the surrounding deuterons again. In this way the magnetic monopole plays the role as the catalyst of the nuclear cold fusion: namely (magnetic monopole $\rightarrow$ cold nuclear fusion).

In the present article, we shall consider whether the reversed statement that (cold nuclear fusion $\rightarrow$ magnetic monopole) is correct. In general, when the nuclear cold fusion exists, there are many candidates of the underlying mechanism. Our problem is to narrow down the candidates of the underlying mechanism by using the phenomena which are characteristic to the nuclear cold fusion and which are completely different from the ordinary nuclear reactions in vacuum. In Section 2, such phenomena of the nuclear fusion are listed. In Section 3, the energy-momentum conservation law is applied to such phenomena, and which serves to narrow down the candidate of the underlying mechanism uniquely.

In Section 4, the change of the open channels of the final states of the d+d reaction is considered. In Section 5, we consider how the smallness of the penetration factor P of the zero-incident energy d+d reaction is modified when we add the term of the magnetic dipole in the magnetic Coulomb field to the ordinary (electric) Coulomb

repulsion term. In Section 6, experiments are proposed to check the underlying mechanism. Comments and conclusion are given in Section 7.

2. Three important properties of the nuclear cold fusion

In addition to the large extra heat production, there are phenomena which are characteristic to the nuclear cold fusion although they do not occur in the ordinary nuclear reaction in vacuum. They are:

(1) Opening of the channel $d+d\rightarrow{}^4He$ at zero incident energy.

(2) Closing of the channels $d+d\rightarrow t+p$ and $d+d\rightarrow{}^3He+n$, which are the main channels of the low energy d+d reaction in vacuum.

(3) Drastic lowering of the repulsive (electric) Coulomb potential between deuterons, which prevent for the two deuterons to come close and to fuse.

We shall see that the first property is sufficient to narrow down the candidate of the NAE (nuclear active environment) of the nuclear cold fusion uniquely, and so the second and the third properties will be derived from the first one.

3. Implications of the energy-momentum conservation

(A) Energy-momentum conservation in vacuum

As an example, let us start by considering $d+d\rightarrow t+p$ reaction in vacuum with very low incident energy (fig.1). The energy Q of the final state is shared by the two particles of mass m_1 and m_2 as

$$Q=\vec{p}'^2/2m_1+(-\vec{p}')^2/2m_2$$

in the center of mass system. Namely the triton gets 25% whereas the proton gets 75% of Q.

However when the mass is zero, we must use the relativistic form of the energy

$$E=\sqrt{p^2c^2+m^2c^4}$$

instead. So the equation of the energy balance of $d+d\rightarrow\alpha+\gamma$ is:

$$Q=p'c+p'^2/2M_4$$

where Q is the Q-value and is 23.9 MeV, and M_4 is the mass of the alpha particle, whose value is 3732 MeV.

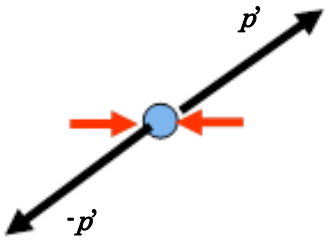

Fig.1. The momentum is conserved in vacuum.

So the sharing of Q is

$$p'c/Q=1-(1-\sqrt{1+2Q/M_4})/(1+\sqrt{1+2Q/M_4})$$

for the gamma-ray, whose value is 0.99682. Therefore only 0.318% of Q becomes the kinetic energy of the alpha-particle.

(B) Energy-momentum conservation of the nuclear cold fusion

Let us examine the conservation law of $d+d\rightarrow{}^4He$ of the nuclear cold fusion, or generally (two body) → (one body) type reaction. It will be shown that the conservations of the energy and the momentum are not compatible (fig.2)

(Proof): In the center of mass system, the momentum $\vec{p}'$ of the final state particle is zero from the momentum conservation, whereas from the energy conservation the magnitude of $\vec{p}'$ must satisfy

$$|\vec{p}'|^2=(2MQ)\,. \qquad \text{(QED.)}$$

Therefore the reaction of the nuclear cold fusion indicates the existence of the external potential outside of the nuclear system, which receives the momentum transfer (fig.3).

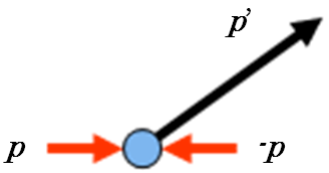

Fig. 2. Violation of the Conservation law.

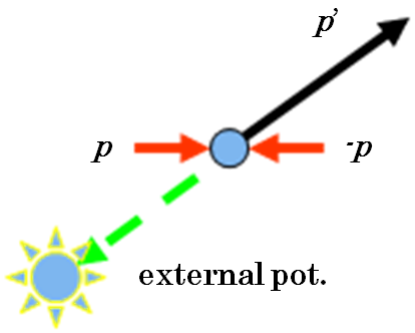

Fig.3. External potential helps to recover the law of the momentum conservation.

(C) Narrowing down the candidate of the external potential

For our $d+d\rightarrow{}^4He$ reaction, the momentum transfer is as large as q = 422 MeV./c, whose De Broglie wave length is $\lambda/2\pi=\hbar/q=0.56\,fm.$ So we expect that the external potential cannot be soft and spread but it must be sharply localized in order to do the job to receive such large **q** .

More precisely, the probability of the momentum transfer **q** by the external potential $V_{ext}(r)$ is the square of the scattering amplitude f(q) given by:

$$f(q)=-(2m/4\pi\hbar)\int d^3r\exp[i\vec{q}\cdot\vec{r}]V_{ext}(r)\ ,$$

which is essentially the Fourier transformation of the external potential. When the variations of the exponential factor and the potential V_{ext} coincides, f(q) becomes reasonably large. The following example will help to understand the situations.

When the electric charge distribution $\rho(r)$ is exponential form of $\rho(r)=C\exp[-br]$, the external potential has the form:

$$\varphi(R)=\frac{C}{R}\left\{1-e^{-bR}(1+\frac{bR}{2})\right\}$$

which reduces to the Coulomb potential at large R. The Fourier transformation $\tilde{\varphi}(q)$ of the potential is:

$$\tilde{\varphi}(q)=\frac{C}{q^2}\frac{1}{(1+q^2/b^2)^2}$$

in which b and $\sqrt{<r^2>}$ relate by $<r^2>=12/b^2$. Since the size of the wave packet of the electron cloud is the order of 1Å, and $\hbar/q$ of the nuclear reaction is 0.56 fm. In our case, the ratio q/b becomes ~ 60000. Therefore the probability of the occurrence of the

momentum transfer $|f(q)|^2$ becomes extremely small. So the electron cloud cannot do the job to absorb such a large momentum transfer q of the nuclear reaction $d+d\rightarrow{}^4He$.

(D) Unique candidate of the external field

There are two candidates of the external fields, to which the nucleus can responds. They are the electric field **E** and the magnetic field **B**, because the nucleus has two attributes, namely the (positive) electric charge Ze and the magnetic dipole moment $\vec{\mu}$. The interaction energy V of these attributes and the external fields are $Ze\varphi$ and $-\vec{\mu}\cdot\vec{B}$ respectively, where φ is the scalar potential of the electric field: $\vec{E}=-\vec{\nabla}\varphi$. Among them, we already observed that **E** produced by the electron cloud cannot do the job.

On the other hand, since the magnetic Coulomb field produced by the magnetically charged particle (magnetic monopole) is $\vec{B}=*e\hat{r}/r^2$, the external potential of the nucleon V_m is:

$$V_m(r)=-\kappa_{tot}(e/2m_p)(*e/r^2)\vec{\sigma}\cdot\hat{r}\,F(r),$$

where

$$F(r)=1-e^{-ar}(1+ar+a^2r^2/2),\ \text{with}\ a=6.04\mu_\pi,$$

in which F(r) is the form factor of the nucleon.

The Fourier transformation of the external potential $V_m(r)$ is

$$\tilde{V}_m(q)=-i\kappa_{tot}(*ee/2m_p)(2\pi/a)\frac{(a/q)^5}{(1+a^2/q^2)^2}\vec{\sigma}\cdot\hat{q}$$

However since, in our $d+d\rightarrow{}^4He$ reaction q=422 MeV./c =3.02 μ_π and , $a=6.04\mu_\pi$, the ratio becomes (a/q)=2.0. Therefore the Fourier transformation of $V_m(r)$ stays reasonably large. Contrarily to the case of the electric field produced by the electron cloud, the momentum transfer **q** from the nuclear system goes smoothly when the external field is the magnetic field produced by the magnetic monopole. In this way, the first mystery of the nuclear cold fusion is solved if the fusion reaction proceeds under the influence of the magnetic monopole. Therefore the NAE (nuclear active environment) is the magnetic Coulomb field produced by the magnetic monopole.

(E) Charge quantization condition of Dirac

Before we consider the mechanism to close the channels $d+d\rightarrow t+p$ and $d+d\rightarrow{}^3He+n$, which are the main channels of the nuclear reaction in vacuum, it is important to know the strength of the magnetic Coulomb field. Since the momentum density of the electro-magnetic field is $(\vec{E}\times\vec{H})/c$, the angular momentum density is $\vec{r}'\times(\vec{E}\times\vec{H})/c$. Let us consider a system where the electric charge Q and the magnetically charged particle *Q coexist. When the magnetic charged particle is fixed at the origin (**r'**= **0**) and the electric charge is fixed at (**r'**= **r**), we can compute total angular momentum **M** of such a system by making the integration of **r'** in whole the space. The result of such integration is $\vec{M}=-(*QQ/c)\hat{r}$, in which $\hat{r}$ is the unit vector connecting both charges: $\hat{r}=\vec{r}/r$. [1]

If we remember that in the quantum theory a component of the angular momentum can assume only the integer multiple of $\hbar/2$, we obtain the charge quantization condition of Dirac $(*QQ/c)=(D\hbar/2)n$ with $n=0,\pm1,\pm2\cdots$. D is 1 and 2 for Dirac monopole and Schwinger monopole respectively, and D is the magnetic counterpart of the electric charge number Z.

If we substitute the charges *Q and Q by the smallest non-zero *e and e, then we get the relation between the fine structure constant and its magnetic counterpart: $(*e^2/\hbar c)(e^2/\hbar c)=D^2/4$. Since $(e^2/\hbar c)=1/137.04$, we obtain $(*e^2/\hbar c)=137.04\,D^2/4$ which is super-strong. Finally we must point out that the strength of the interaction of the magnetic dipole moment of the nucleon and the magnetic monopole is the order of the strong interaction because of $(*ee/\hbar c)=D/2$.

Another important role of the super-strong monopole is that the deuterons are trapped by the monopole deeply enough to be prevented to transit to the continuous t+p or ^3He+n channels. We shall see this in the next section.

4. How the channels $d+d\rightarrow t+p$ and $d+d\rightarrow{}^3He+n$ are closed.

Since the binding energies of the deuteron, triton and ^3He are $B_d=2.2MeV$, $B_t=8.5MeV$ and $B_{He(3)}=7.7MeV$, respectively, for zero incident energy d+d reaction, the kinetic energies of the final states are 4.1MeV and 3.3MeV, respectively for t+p and He(3)+n channels. However if the d+d reaction proceeds after the two deuterons are trapped by the magnetic monopole *e with the binding energy B_{*e-d}, then the kinetic energies of the final states change to $(B_t-2(B_d+B_{*e-d}))$ and $(B_{He(3)}-2(B_d+B_{*e-d}))$ respectively for t+p and He(3)+n channels. Or numerically they are $(4.1MeV.-2B_{*e-d})$ and $(3.3MeV.-2B_{*e-d})$ respectively for t+p and He(3)+n channels. As the binding energy B_{*e-d} increases the kinetic energies become negative, which mean the channels are closed. The critical values of the d-*e binding energies are 2.05 MeV. and 1.65 MeV. respectively for t+p and He(3)+n channel.

We shall see that the binding energy of the ground state of the *e-d system is around 2.3 MeV., so the channels of t+p and He(3)+n must be closed. We know the hamiltonian of the (magnetic monopole)-nuclear system which is for the deuteron-monopole: [3]

$$H=H_0^{(p)}+H_0^{(n)}+V_N \quad \text{with}$$

$$H_0=\frac{1}{2m}(-i\vec{\nabla}-Ze\vec{A})^2+\kappa_{tot}(*eDe/2m_p)(\vec{\sigma}\cdot\hat{r})F(r)/r^2,$$

where **A** is the vector potential of the magnetic Coulomb field and Z=1 for the proton and Z=0 for the neutron. κ_{tot} is 2.79 and - 1.91 for p and n respectively. V_N is the nuclear potential whose parameters are chosen to reproduce the binding energy of the deuteron B_d =2.2 MeV. well. By making the variational calculation we can determine the binding energy of the ground state B_{*e-d}. In the calculation the trial functions are the chosen as the sum of the Gaussian functions whose range parameters are the geometric

series. The result is $B_{*e-d} = 2.3 MeV$. If we remember that in general the variational calculation gives the upper bound of the energy levels, the true binding energy can be a little larger compared to our value 2.3MeV. However we need not alter our conclusion that the t + p and $^3He + n$ channels are closed, because the fact that B_{*e-d} exceeds the critical values, which are 2.05 and 1.65 MeV for t + p and for $^3He + n$ respectively as mentioned above, is not changed.

Figure 4 is the energy levels of various channels of Z=2 and A=4 states, in which the energy level where all the nucleons are separated infinitely is chosen as the origin of E (E=0).

5. Penetration of the repulsive Coulomb barrier

The nuclear cold fusion proceeds when the two deuterons are trapped by the same magnetic monopole *e, the orbital size of the bound state is several fm.. The trapping of the first deuteron goes rather smoothly. However the potential $V_1(x)$ felt by the second deuteron is the sum of the repulsive Coulomb and the attractive potential between the magnetic monopole and the magnetic dipole moment of the nucleus when the spin orientates properly. The explicit form of $V_1(x)$ is:

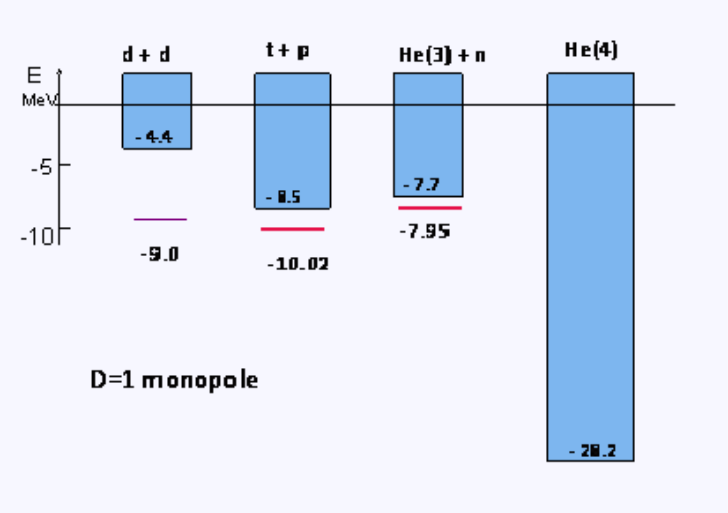

Fig. 4. Energy levels of four channels of Z=2 and A=4, in the magnetic Coulomb field produced by the magnetic monopole of D=1. The blue belts are the continuous states of the scattering. If we start from the ground state of (d-*e-d) of E= - 9.0 MeV, it cannot reach to the continuous states of t+p and ^{3}He+n by the energy conservation. On the other hand, it can transit to He(4) state as long as the momentum conservation is recovered by the external field.

$$V_1(x) = +e^2 / x - (\kappa_{tot} / 4m_p) / x^2$$

in which the charge quantization condition of Dirac, *ee=1/2, is used. Here and hereafter we shall adopt the natural units ($\hbar = c = 1$).

Because of the attractive second term, the peak value of $V_1(x)$ deceases to 17keV., which should be compared with the peak value 1MeV. of the pure Coulomb potential $V_C(x)$.

Further help to increase the penetration factor P comes, when we consider the electron wave function in the magnetic Coulomb potential produced by the magnetic

monopole. Since the binding energy is the order of magnitude of the electron mass m_e, the relativistic treatment is necessary, so we must solve the Dirac equation in the external magnetic Coulomb field produced by the magnetic monopole. This is explained in the separate paper. Here we shall only use the result [4]. In the electron rich circumstance, the magnetic monopole is shielded by the electron cloud and the penetration potential becomes:

$$V_2(x) = +(e^2/r)\exp[-2m_e x] - (\kappa_{tot}/4m_p)/x^2 \ .$$

If we substitute $V_2(x)$ to the formula of the penetration factor P for E=0:

$$P = \exp[-2\tau] \quad with \quad \tau = \sqrt{2\mu_{red}}\int_a^b \sqrt{V(x)}\,dx/\hbar \ ,$$

we obtain $P = 6.2\times10^{-9}$ which should be compared with $P = 5\times10^{-106}$ of the case of $V_C(x)$. Thus the third mystery (3) of the cold fusion is solved.

We saw that the $d + d \rightarrow {}^4He$ reaction occurs when two deuterons form a bound state with the same magnetic monopole *e. Since such a state is unstable and transits to more stable alpha-particle. Because the spin of the alpha particle is zero, it is not attracted by *e. The magnetic monopole simply emit the alpha particle, and there remains fresh monopole *e, and which starts to attract surrounding fuel deuterons again. In this way the magnetic monopole plays the roll of the "one-particle catalyst " of the nuclear cold fusion.

At present, since we rely on the floating magnetic monopole in nature and it is a very rare particle, we must wait for long time before the magnetic monopole *e comes into and stops in the region where the deuteron density is sufficiently high. Therefore the starting of the nuclear cold fusion is governed by the probability. We may facilitate the nuclear cold fusion, if we succeed to gather the floating magnetic monopole to the region where the deuteron density is high. In the next section we shall consider this possibility.

6. Proposal of experiments and the devices for the monopole *e

In this section we shall consider three devices necessary to handle the magnetic monopole *e. They are:

(A) Trapper : necessary to store the magnetic monopole *e.
(B) Detector: super-conducting ring can do the job.
(C) Collector: magnetic dipole can collect the floating magnetic monopole.

(A) Magnetic monopole *e is trapped in the lattice

In order to learn the process of trapping of the magnetic monopole *e by a lattice, by a rare earth for example, let us compute the trapping energy ΔE by using a simple model. We consider a lattice of atoms with large magnetic moment $\kappa\cdot(e/2m_e)$ whose directions are random (Fig. 5)

When a magnetic monopole *eD comes in, the magnetic moment align spherically (Fig. 6).

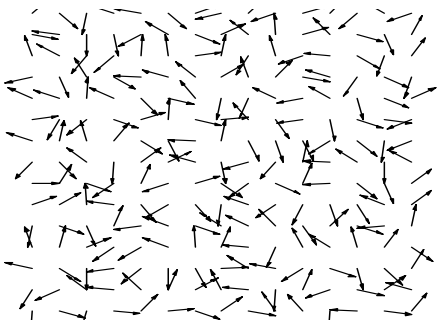

Fig. 5. Random orientation

Because of the thermal agitation, the directions of the spins are random outside of the blue sphere of radius R, and R is determined by:

$$\kappa \frac{e}{2m_e}\frac{{}^*eD}{R^2} = \frac{1}{2}k_B T ,$$

where k_B is the Boltzmann constant.

The trapping energy ΔE is the sum of the contributions of the magnetic moment κ measured by the unit of the Bohr magneton $e/2m_e$ in the magnetic Coulomb field ${}^*eD/r^2$.

$$\Delta E = \frac{4\pi}{a^3}\int_0^R r^2 dr \frac{\kappa e}{2m_e}\frac{{}^*eD}{r^2} = \frac{\pi}{a^3}\frac{D}{m_e}R ,$$

where a is the lattice constant.

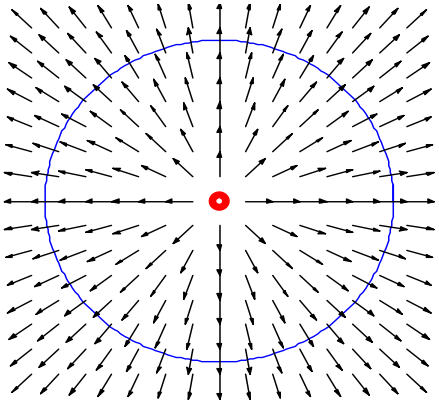

Fig. 6. After *e moves in, spins are aligned spherically.

When the lattice constant a is 1Å, the numerical value of ΔE and R are:

$$\Delta E = \left(\frac{\kappa D}{2}\right)^{3/2}\frac{14.24\, keV.}{\sqrt{T}} \quad and \quad R = \sqrt{\frac{\kappa D}{2}}\frac{2.97\times 10^{-6} cm}{\sqrt{T}} .$$

It is remarkable that ΔE and R are proportional to $1/\sqrt{T}$. Since at room temperature T=300˚ ΔE is order of 1keV. And R is few nm.

It is interesting that the trapping potential ΔE decreases when the temperature goes up. If we remember that the track length of the alpha-particle of our energy region (20MeV.) is around 0.1mm, the kinetic energy of the alpha-particles emitted from the monopole is stored in the small neighborhood of the magnetic monopole. Therefore the temperature goes up, and the ability of the trapping the magnetic monopole is lost. It must hop to neighboring cooler place. In fact such a phenomenon is known when we observe the surface of the cathode by using the infrared camera.

(B) Detector of the magnetic monopole *e

Total magnetic flux $\Delta\phi$ produced by the magnetic charge *eD is

$$\Delta\phi = 4\pi\, {}^*eD .$$

Therefore when the magnetic charge *eD passes through the super-conducting ring of the torus shape as indicated by the figure, the magnetic flux trapped by the ring must increase by $\Delta\phi$.

Since the super-conducting current I circulating the inner surface of the super-conducting ring is proportional to the total magnetic flux trap by the ring, we can determine the

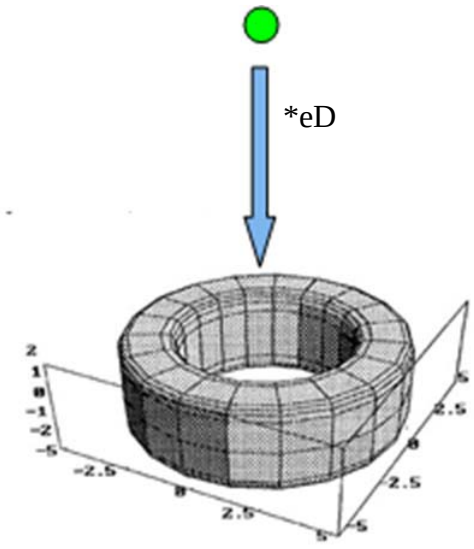

Fig. 7. When a magnetic charge *eD passes through the torus hole, the permanent current of the inner surface changes.

change of the flux by observing the change of the surface current ΔI.

In order to obtain the relation between the change of the current and the magnetic charge *eD, which passes the ring, let us change the equation

$$rot\,\vec{H} = 4\pi\,\vec{i}\,/\,c$$

to the integral form, in which the red line of the figure is the contour C of the Stokes theorem. Because of the Meisner effect that magnetic field inside of the super-conductor is zero, we get the relation between the surface current I and the magnetic field strength ϕ / S, where S is the area of the inner hole of the torus. Therefore the change of the current ΔI on the inner surface becomes:

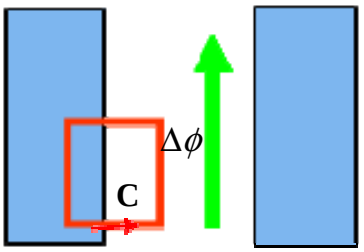

Fig.8. The cross section of the torus of the super-conductor.

$$\Delta I = \frac{c}{4\pi}\frac{2\phi_0 D}{S} = 0.328\frac{D}{S(cm^2)}\,\mu A/cm,$$

where ϕ_0 is the quantum unit of the magnetic flux: $\phi_0 = \pi\hbar c / e$ and numerically it is

$$\phi_0 = 2.07\times10^{-11}\ Wb\ (in\ MKS) \quad or$$

$$\phi_0 = 2.07\times10^{-7}\ G\,cm^2\ (in\ CGS)$$

By using the SQUID we can observe the change of the surface current I.

(C) Collector of the magnetic monopole *e

The magnetic dipole or the solenoid of the electric current can serve as the collector of the magnetic monopole, because the magnetically charged particle *e with very slow velocity moves on the line of force of the magnetic field.

After Gilbert, we may regard the earth as a huge magnetic dipole, then we can expect to find the magnetic monopole with better probability in the neighborhood of the magnetic north (or south) pole of the earth. In the next part, we shall consider how to slow down the speed of the monopole more to make it be trapped by the potential of the order of 1keV in depth.

In general, the charged particle losses its energy in the form of the radiation, when it enters into the region of the potential. $-dE/dt = -(2/3)e^2a^2$ is Larmor's formula of the radiation loss, in which a is the acceleration. For the case of the magnetic monopole, formula of the radiation loss must become

$$\frac{dE}{dt} = -\frac{2}{3}(*eD)^2\,|\,\vec{a}\,|^2\,.$$

Therefore the energy loss occurs at the surface of the metals of the high magnetic permeability, and so in order to slow down *e particle effectively, use of the powder of nm size is desirable. In the figure, the green points are the place where the radiation is emitted.

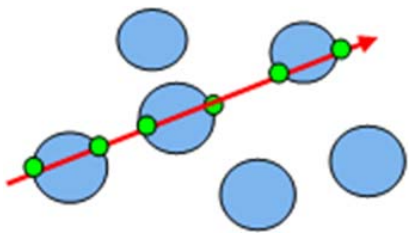

Fig.9. Location of the Larmor radiation when *e goes through the powder.

7. Comments and Conclusion

In the separate paper, we saw that if we consider the system of nucleons and magnetic monopole *e, the nuclear fusion reaction at zero incident energy can proceed, namely (magnetic monopole *e $\rightarrow$ nuclear cold fusion). In the present article we tried to reverse the statement, namely to (nuclear cold fusion $\rightarrow$ existence of the magnetic monopole). We found that if the conservation law of the energy-momentum is to be satisfied, and $d + d \rightarrow {}^4He$ is the main channel of the cold nuclear fusion reaction, then there must exist an external field, which absorbs the momentum of q=422 MeV./c released from the nuclear system. Since the De Broglie wave length of such a large momentum transfer q is $\lambda / 2\pi = \hbar / q = 0.56\ fm.$, the size of the source of the external field must be sharply localized (size is order of 1 fm.). The nucleons have two attributes other than the strong nuclear interactions, they are electric charge and the magnetic dipole moment. Therefore the required external fields are the electric or the magnetic fields. However the electric field cannot do the job, since the source of the electric field is the electron cloud whose size is the order of 1Å. On the other hand the magnetic field can do the job, because the size of the source is order of 1fm..

References

1. P.A.M.Dirac, Proc.R.Soc. London **A133**, 60 (1931);
   J.Schwinger, Science **165**, 757 (1969);
   A,O.Barut, Phys.Rev. **D3**, 1747 (1971);
   T.Sawada, Phys.Lett. **43B**, 517 (1973)
2. T.T.Wu and C.N.Yang, Nucl.Phys. **B107**, 365 (1976)
3. T.Sawada, Foundations of Physics, **23**, 291 (1993)
4. Y.Kazama and C.N.Yang, Phys.Rev. **D15**, 2300 5 (1977)
5 PDG, " Particle Physics Booklet" or http://pdg.lbl.gov/

Characteristics of Solid-State Nuclear Track Detectors for Heavy Charged Particles – A Review

H. Kozima

Cold Fusion Research Laboratory, 421-1202 Yatsu, Aoi, Shizuoka, 421-1202 Japan

Abstract

Since Silk and Barnes observed the tracks of uranium fission fragments on the mica films, the formation of latent tracks by heavy charged particles in solids has been recognized as one of fundamental phenomena of the radiation damage. And then, the investigation of the latent tracks became an important device for detection of charged particles by the success of etch-pit technique developed by Price and Walker.

The technique to identify incident charged particles using their latent tracks in target solid-state detectors, especially CR-39, has been developed enthusiastically and used widely in many fields of science. While the application of this technique is in progress prosperously, the mechanisms of the latent track formation in the target solids have been under investigation and several proposals have been given for them. The "ion explosion mechanism" and the "electron thermal spike mechanism" are two main mechanisms considered as fundamental even if there remain many unknown factors in the relation between the characteristics of incident particles and their latent tracks in solids.

The technique to use the particle track detector in identification of charged particles is not an accomplished and completed one but is developing rapidly at present as introduced in our paper presented at this Conference for the identification of particles generated in the cold fusion phenomenon (CFP). We have to consider that the immediate and visible scientific problems of the particle track field are solid state physics questions not completely solved yet: How does a track form? What atomic processes take place? What is the ultimate atomic configuration along and around a track? Investigation of these problems is in progress and new knowledge about the mechanism of latent track formation and its investigation has been obtained, especially for organic detectors.

The proposed mechanisms of nuclear track formation are summarized and problems in visualization of the tracks by chemical etchings and possible application to identify charged particles and to determine their energies are reviewed in intimate relation to the CFP.

1. Introduction

Since Silk and Barnes [Silk 1959] observed the tracks of uranium fission fragments on the mica films, the formation of latent tracks by heavy charged particles in solids has been recognized as one of fundamental phenomena of the radiation damage. The formation of the latent tracks became an important device for detection of charged particles by the success of the etch-pit technique developed by Price and Walker [Price 1962].

The technique to identify incident charged particles using their latent tracks in target solid-state detectors, especially CR-39, has been developed enthusiastically and used widely in nuclear physics, nuclear chemistry, nuclear energy, space science and archeology. While the application of this technique is prosperous, the mechanism of the latent track formation in the target solids has been investigated actively and several proposals have been given. The "ion explosion mechanism" by Fleischer, Price and

Walker [Fleischer 1959] and the “electron thermal spike mechanism” developed by Merkle [Merkle 1963], Chadderton [Chadderton 1966] and others are two mechanisms considered as fundamental even if there remain many unknown factors in the relation between the characteristics of incident particles and their latent tracks in solids.

The technique to use the particle track detector in identification of charged particles should not be considered as a completed one due to the complexity of materials used as the detector but as a developing one rapidly at present. We have to remember that the words expressed by pioneering researchers in this field are true even now; “The first, most immediate and visible scientific problems of the particle track field were solid state physics questions: How does a track form? What atomic processes take place? What is the ultimate atomic configuration along and around a track? Curiously enough these problems remain as some of the least studied, presumably because of the intense interest in the many applications of track etching that has directed attention to the assortment of fields considered in Chapter 4 through 10.” [Fleischer 1975].

The situation around this field has been improved largely while there remain many problems to be solved to use the solid-state particle detectors for determination of characteristics of incident charged particles. One of recent works related to these problems is the investigation of nuclear tracks in CF-39 by Yamauchi et al. [Yamauchi 2005].

In this paper, we would like to summarize the mechanism of nuclear track formation and discuss its possible application to identify charged particles emitted in the cold fusion (CF) reactions. An interesting use of CR-39 to determine high energy neutrons [Mosier-Boss 2008] is introduced. The latent track formations by false causes (environmental radiation, surface defects in handling process etc.) will give uncertainty in the measurements but is not considered in this paper.

2. Stopping Powers of and Radiation Damages in Target Materials

Interaction of a charged particle and a target material has several facets depending on the point of view to observe the effect caused by the interaction. From a point looking into the behavior of the incident particle, we are interested in the behavior of the particle in the target in temporal sequence. How the particle decelerated and how far the particle reaches in the material. Stopping power of the target material is the title of the investigation in this case.

On the other hand, from a point looking into the effect in the target made by the

particle, we are interested in the radiation damages induced by the particle in the material. While the two phenomena are closely related each other, there are characteristic factors in each and their investigation has been developed to form two big research fields neighboring each other. It is useful to survey essential points of these fields for investigation of solid-state particle detectors belonging to the field of radiation damage.

2.1 Stopping Powers of Target Material for Incident Heavy Charged Particles

Particle interaction of an incident charged particle with a target material is treated as a stopping power of the material for the particle on one side and as a radiation damage in the material given by the particle on the other. The two effects are of course closely related each other and the knowledge in each problem is useful to understand another problem.

The interaction of an incident charged particle and a target solid is not so simple with variety of interactions between component particles of the both incident and target agents explained below. Furthermore, the latent tracks remaining after the interaction contain many information in a part of which can be read out using the etching technique having been developed day by day.

As shown below, stopping power of and therefore radiation damage of a target material for an incident particle depends on the charge Z_1 of the incident particle and atomic number Z_2 of atoms in the target, on the velocity v_1 (or the ratio of the energy E_1 and the mass M_1 , E_1/M_1) of the incident particle. On the other hand, the structure of radiation damages or latent nuclear tracks in the target is a statistical result of individual atomic processes and depends on detailed dynamics of particles excited by the interaction between the incident particle and atoms in the target and it is necessary to take into consideration new factors not considered in the calculation of the stopping power.

We summarize the physics of stopping power in this section [Doke 1970] and that of radiation damage, especially nuclear tracks [Doke 1969] in next section.

2.1.1 Three Energy Regions of Incident Particles Characteristic for the Stopping Power

As Doke explains in his review article [Doke 1969], trajectory formation by heavy ions in solids has been investigated as a fundamental phenomenon in the radiation damage and also investigated widely as a characteristic detector of radiation in recent years after the development of the etch pit method by Price and Walker [Price 1962].

Due to the different effects of the interaction between the incident charged particles and the nuclei on the lattice of the target material, there are three regions of the incident particle energy, high, intermediate and low energy regions, in formulation of the stopping power for an incident charged particle in a target material. It should be noticed that the radiation damage from the initial to the final parts of the latent track relates to the energy regions as a whole while the stopping power has to be investigated in these energy regions separately,.

2.1.1a Theory for High Energy Region ($v \gg v_0 Z_1$)

The Bethe's formula of the energy dissipation rate for a high energy incident particle is written down as follows;

$$-\mathrm{d}E/\mathrm{d}x = (4\pi Z_1^2 e^4/m_e v_1^2)\, N_2 B, \quad (1)$$

$$B = Z_2 \ln (2m_e v_1^2/I), \quad (2)$$

where Z_1 and v_1 are the nuclear charge and the velocity of the incident heavy charged particle, respectively, N_2 and Z_2 are the number density and the atomic number of the atom in the target material, respectively, and e and m_e are the charge and the mass of an electron, respectively. The symbol I is the average excitation energy (potential) of the material and B given in Eq. (2) is the so-called "stopping number." The average excitation energy I is only calculated for simple nuclei such as proton and alpha. In general, the value of I is most questionable and gives ambiguity in the calculation of stopping powers.

In the non-relativistic approximation, the velocity v_1 is related to the energy of the particle by

$$E_1 = (1/2)M_1 v_1^2, \text{ or } v_1 = (2E_1/M_1)^{1/2}$$

The equation (1) shows a dependence of the stopping power on the charge Z_1, the velocity v_1 (or the ratio of energy E_1 and mass M_1, E_1/M_1) of the incident particle and on the charge Z_2 of the target atom.

1) Stopping number *B* and its inner-shell correction

The Bethe's formula is deduced using the Born approximation and applicable to high energy particles with velocity v_1 satisfying the following two conditions;

$$v_1 \gg Z_1 e^2/\hbar \equiv v_0 Z_1 \ (v_0 \equiv e^2/\hbar) \quad (3)$$

related to the ionization of the incident particle and

$$v_1 \gg v_0 Z_2 \quad (4)$$

related to the ionization of the inner shell electrons of the target atom.

For light incident particles proton p ($Z_1 = 1$) and deuteron d ($Z_1 = 2$), usually appear in the cold fusion phenomenon (CFP), the equation (4) is the more severe condition to satisfy.

The condition (3) with the value of $v_0 \equiv e^2/\hbar = 2.2 \times 10^8$ cm/s demands the energies of proton, deuteron and alpha to be $E_p \gg 25$ keV, $E_d \gg 50$ keV and $E_\alpha \gg 100$ keV:

$E_p \gg 25$ keV, $E_d \gg 50$ keV and $E_\alpha \gg 100$ keV

The condition (4) should be remedied by the so-called the "inner-shell correction" B' instead of the stopping number B for an incident particle with energies not so large but satisfying the condition (3),

$$B' = Z_2 \ln (2mv^2/I) - \sum_i C_i \qquad (5)$$

where C_i is the correction for the i-th shell of the target nucleus and I is the average excitation potential already appeared in Eq. (2).

2) Average excitation energy of a compound material and Bragg's additivity law

The average excitation energy (AEE) I_c of a compound material is given by

$$\ln I_c = \sum_i N_i Z_i \ln Ii / \sum_i N_i Z_i \qquad (6)$$

where N_i, Z_i and I_i are the number density, the atomic number and the AEE of the i-th component of the compound material, respectively. This additivity is applicable to the compound material where the change of valence electrons by chemical bonds is ignored.

3) Organic material

There is an important question for organic materials how much the Bragg's additivity law is applicable especially at low energy region. The work by Sauter and Zimmermann [Sauter 1965] has shown that the Bragg's additivity law is not applicable below 150 keV for the stopping power of organic material for protons by experiments using $(CH_2)_n$, $(C_8H_8)_n$, (C_9H_{10}), $(C_3H_6)_n$, $(C_8H_8 + C_4H_6)_n$, (C_2H_4), and (C_3H_8).

Recently, Yamauchi et al. [Yamauchi 2005] investigated yields of CO_2 formation and scissions at ether bonds along nuclear tracks in CR-39. More details of their work will be given in Sec. 2.2.3.

2.1.1b Theory for Low Energy Region ($v \ll v_0 Z_1$)

The stopping power for heavy charged particles increases with the incident energy E until the velocity v becomes near $v_0 Z_1^{2/3}$ and then decreases gradually. For the region where $v \gg v_0 Z_1$, the theory given above is applicable. On the other hand, for the low energy region where $v \ll v_0 Z_1$, there are several theories applicable to this region.

When the velocity of heavy incident charged particles becomes less than $v_0 Z_1$, we can use a classical theory for the calculation of the stopping power. In this low energy region, the incident particles lose energy by i) excitation and ionization of atoms in the target and also by ii) elastic collisions with nuclei in the target. Therefore, the total stopping power $(dE/dx)_T$ is expressed as a sum of two terms, $(dE/dx)_e$ by the process i) and $(dE/dx)_n$ by the process ii);

$$(dE/dx)_T = (dE/dx)_e + (dE/dx)_n. \quad (7)$$

1) LSS theory for low energy particles

Lindhard et al. [Lindhard 1963] have given a formula (7) written in dimensionless parameters which is sometimes called "unified range-theory" for heavy ions.

The two terms on the right-hand side of the equation (7) applicable for $0 < v < v_0 Z_1^{2/3}$ are given as follows:

$$-(dE/dx)_e = \xi_e \, 8\pi e^2 a_0 N (Z_1 Z_2/Z)(v/v_0), \quad (8)$$

$$-(dE/dx)_n = (2\pi/e)(Z_1 Z_2 e^2 a_0/S) M_1/(M_1 + M_2), \ (2Z_1 S e^4/\hbar v^2 \geq 1) \quad (8')$$

where $S = (Z_1^{2/3} + Z_2^{2/3})^{1/2}$, $v_0 = e^2/\hbar$, $a_0 = \hbar^2/m_e e^2$.

Or

$$(d\varepsilon/d\rho)_e = k\varepsilon^{1/2}, \quad (9)$$

$$(d\varepsilon/d\rho)_n = (1/2\varepsilon) \ln (1.294\varepsilon), \quad (10)$$

where

$$\xi_e = Z_1^{1/6},$$

$$Z^{2/3} = Z_1^{2/3} + Z_2^{2/3},$$

$$\varepsilon = EaM_2/ Z_1 Z_2 e^2 (M_1 + M_2), \quad (11)$$

$$\rho = RNM_2 \, 4\pi a^2 M_1/(M_1 + M_2)^2, \quad (12)$$

$$a = 0.8853 \, a_0 /(Z_1^{2/3} + Z_2^{2/3})^{-1/2} \quad (13)$$

$$k = \xi_e \times 0.0793 Z_1^{1/2} Z_2^{1/2} (M_1 + M_2)^{3/2} /[(Z_1^{2/3} + Z_2^{2/3})^{3/4} M_1^{3/2} M_2^{1/2}], \quad (14)$$

2) Firsov's theory for low energy particles.

Because the formula (8) in the LSS's theory given without deduction process is inconvenient to use in analyses of experimental results, Firsov [Firsov 1959] has given a formula based on a model using a potential of the Thomas-Fermi type. The stopping power for $Z_2/Z_1 < 4$ is given as follows;

$$-(1/N)(dE/dx)_e = 5.15 \times 10^{-15} (Z_1 + Z_2)(v/v_0). \quad [\text{eV} \cdot \text{cm}^2/\text{atom}] \quad (15)$$

2.1.1c Theory for the Intermediate Energy Region ($v \sim v_0 Z_1^{2/3}$)

At the intermediate energy region where $v \sim v_0 Z_1^{2/3}$ and the charge exchange is not

negligible, theoretical treatment of stopping power of heavy ions ($Z_1 \geq 15$) is difficult and we have to use semi-empirical formulae. Sometimes, formulae deduced in high or low energy regions have been extended into this region.

2.2 Radiation Damages and Latent Tracks – Formation of Nuclear Tracks in Solids

The radiation damage depends sensitively on the energy of the incident particle. The latent track in a target material induced by an incident charged particle is determined by the whole process from the initial to the final (at rest) stage of the interaction between the particle and the target. Therefore, formation of a latent track is characterized by properties of the target material in relation to its interaction with the particle during deceleration to the stop.

Detection of an energetic charged particle is realized by using any recording medium which register the interaction of the particle and the medium. The first and simplest medium we used to register the charged particle is the cloud chamber invented by C.T.R. Wilson in 1911 which has been used in physics over the century.

Any detector of the charged particle is composed of three factors. (1) The first factor is the stopping power of the medium for the incident particle which we want to identify its characteristics; mass, charge and energy. (2) The second factor is the radiation damage or latent track of the passing particle in the medium induced by the incident particle. (3) The third factor is the visualization of the latent track.

The first factor was discussed in the previous section and showed its complexity already.

As is explained below, the second factor includes also complex atomic and sometimes nuclear processes and identification of the charged particle by the solid-state detector is not a simple and easy method if we use it alone. It is recommended to use it with other methods supplementing each other. The third factor depends strongly on the property of the target material and is considered in papers on practical application of the detector.

2.2.1 Formation of Nuclear Tracks in Solids

Silk and Barnes [Silk 1959] observed nuclear tracks of fission fragments of uranium in mica as a fundamental event of the radiation damage. Then, the etch pit method developed by Price and Walker [Price 1962a – c] has made the nuclear tracks a powerful method to detect charged particles and the mechanism of nuclear track formation had been investigated intensively.

Several mechanisms were proposed to explain experimentally observed nuclear

tracks by heavy charged particles in solids. It is not easy to determine the mechanism that made the observed tracks. This situation means inevitably existence of ambiguity in determination of the characteristics of the incident particle generating the nuclear track. We have to remember the fundamental properties of the interaction between incident particle and the target resulting in the nuclear track.

There have been proposed four main mechanisms of the track formation by incident heavy ions, a) displacement cascade (spike) theory, b) "electron thermal spike" theory, c) "ion explosion" theory and d) "direct ionization damage" theory.

a) Displacement cascade (spike) theory

The energy loss of a heavy ion passing through a material is expressed by a term $(dE/dx)_e$ due to electronic processes (ionization and excitation) and another $(dE/dx)_n$ due to elastic nuclear collision (Coulomb scattering) as mentioned in Section 2. In the case of the fission fragment in mica, a large part (~ 95%) of the energy loss is by the electronic process and the remaining part by the nuclear process. Furthermore, the latter is eminent at the final part of the track where the knocked out atoms collide with other atoms causing the displacement cascade and finally the displacement spike [Silk 1959].

b) Electron thermal spike theory

The energy loss of heavy ions in a material is caused mainly by the electronic processes and the energy transferred to electrons may be consumed to heat up the crystal lattice along the particle tracks. The formation of nuclear tracks by this mechanism is called the electron thermal spike theory.

c) Ion explosion theory

Fleischer at al. [Fleischer 1965] proposed a mechanism of track formation by heavy ions as follows: A heavy charged particle passing through a material knocks out electrons along its path forming cylindrical region occupied by ions. The ions in this cylinder repel each other out from this region forming a cylinder made of vacancies surrounded by interstitial atoms (nuclear track) [Fleischer 1965].

d) "Direct ionization damage" theory.

To explain the nuclear track formation in organic materials, characteristics of the organic molecules have been taken into consideration. The broken bonds of organic molecules due to the ion propagation may be activity centers for etchant and molecular fragments produced by breaking bond may be more soluble by etching [Fleischer 1965].

Afterward, there have been proposed two new mechanisms by Katz and Kobetich [Katz 1968] and by Benton and Nix [Benton 1969] supplementing the theories explained above.

A recent work on the CR-39 detector by Yamauchi et al. [Yamauchi 2005] has given concrete data on the broken bond and molecular fragments in the detector (cf. Sec. 2.2.3).

In conclusion, there are proposed several theories or criterions for nuclear track formation in materials, especially in organic materials, to understand this complicated phenomena related to the interaction of incident charged particles and target materials which is sensitively dependent on the energies of the incident particles.

We have to careful to apply these theories to the CFP not falling into mistakes committed by blind people as told in a Buddhist parable [cf. Appendix].

2.2.2 Track Formation and Detection of Charged Particles

It should be noticed that we can not say at present which one of these mechanisms proposed is an appropriate one to explain the phenomena occurring in trajectory formation by heavy ions in solids. Especially, the trajectory formation by heavy ions in organic materials has been discussed thoroughly in relation to their application to detectors.

There have been proposed also several mechanisms including the “primary ionization” mechanism by Fleischer, Price and Walker [Fleischer 1965], the “electron thermal spike” theory by Chadderton, Morgan, Torrens and Van Vliet [Chadderton 1966], the “specific energy loss along the track” mechanism by Katz and Kobetich [Katz 1968], and the “restricted energy loss” mechanism by Benton and Nix [Benton 1969].

The latter two have been proposed to remedy the defect of the mechanism proposed by Fleischer et al. Doke [Doke 1969] commented his feeling to favor the mechanisms proposed by Katz et al. and Benton et al. rather than that proposed by Fleischer et al.
Anyway, the method of heavy ion identification and energy determination by the etch pit methods is not so simple in principle and in application and should not be considered as a completed method without reservation.

A charged particle suffers inevitably deceleration in their passage from its origin to a detector by strong electromagnetic interaction with charged particles on the route in the target. Therefore, it is very difficult to identify the nuclear reaction causing the emission of the charged particle even if the existence of the nuclear reaction is confirmed.

2.2.3 Track Formation related to CR-39

We review the data of charged particles obtained extensively by CR-39 track detector in the cold fusion phenomenon (CFP) from about the year of 2000 in another paper presented at JCF13 [Kozima 2013]. In this section, we cite a recent remarkable paper on the CR-39 detector which shed a light on the discussion of the track formation.

Yamauchi et al. [Yamauchi 2005] investigated the chemical phase of track formation process by observation of CO_2 formation and scissions at ether bonds along nuclear tracks in CR-39. Their overview on the nuclear track formation process in CF-39 at present is summarized as follow:

(a) The parts between the two carbonate ester bonds should be segmented into small molecules, including CO_2 gases, along the particle trajectory;

(b) After the segmentation, the CO_2 gases were diffused away and a lower density region with chemically active end-points was formed simultaneously (the role of the other small molecules is unknown);

(c) Subsequent chemical modifications, including a reaction with dissolved oxygen, derived an OH group as new end-points in the polymer network.

This is surely one of steady steps to the determination of characteristics of the detector for identification of charged particles and determination of their energies.

Anyway, the method of heavy ion identification and energy determination by the etch pit methods depends sensitively on the target material and is not so simple in principle and in application and should not be considered as a completed method without reservation.

2.3 Etching of nuclear tracks does not give definite values of parameters of the incident particle

Etching of nuclear tracks in a target material is another process than the formation of latent nuclear tracks. In addition to the etching technique of latent tracks in a material, there is a fundamental problem about the mechanism of track formation as explained in Sec. 2.2. There are proposed several mechanisms for the formation of nuclear tracks in the target solids by incident heavy charged particles. Therefore, the analysis of the nuclear tracks in relation to the characteristics of the unknown incident particle is inevitably performed by analogy to a standard (or reference) track generated by known incident particles.

The etching process will give new data related to its formation process but give another problem than the formation of nuclear tracks. By using various etching

techniques, we can obtain necessary information related to the mechanism that produced the nuclear tracks. If we know some factors of the incident particle out of the etched track, we can guess some unknown parameters related to the particle which produced the latent tracks. However, the latent nuclear tracks are results by complex interactions between the incident particle and the target and, therefore, the information we can get from the etched tracks is complex function of the parameters of the incident particle even if we know everything about the target. The information obtained from the latent tracks is inevitably qualitative and we have to rely on analogy between a calibration data (or reference) obtained by a known incident particle and experimental data registered by unknown particles which we want to identify.

2.3.1 Revealing nuclear tracks by etching

The observation of the nuclear tracks of fission fragment from uranium was made by Silk and Barnes on the mica films in 1959 [Silk 1959]. This experiment accelerated the use of nuclear tracks as a detector of charged particles in physics and astronomy.

Furthermore, the etch pit method developed by Price and Walker [Price 1962] made the observation of the nuclear tracks tractable with optical microscopes and the use of nuclear track detector prevailed to wider fields of researches including nuclear physics, nuclear chemistry, atomic power, cosmology, archeology etc.

2.3.2 Track-Diameter Kinetics in Dielectric Track Detectors [Somogyi 1973]

The diameters of the etched tracks are specifically sensitive to the parameters characteristic of the nuclear particles (the energy and the type of particle). The experimental methods based on the determination of the lengths (track-length method) and diameters (track-diameter method) of etch-pits can be regarded as natural complements of each other only when the etched tracks are completely determined throughout its length. Then, the track-diameter method is useful, in particular when track-length measurements give less reliable results, in the case of particles causing ionization energy losses near the so-called critical primary ionization $(dJ/dx)_c$, determining the detection limit [Somogyi 1973].

Concerning the track-length method several detailed theoretical and experimental works are available even if there are several assumptions about the mechanism of track formation. As is explained in Section 2.1, the mechanism of stopping power depends on the charge and the velocity (or the energy and the mass) of the incident particle and on the charge of target nucleus, and therefore the mechanism of track formation is too complex to be approximated by a specific assumption. We have to be cautious to apply

the formulae obtained on rather simplified assumptions to a real situation too arbitrarily.

As Somogyi et al. have discussed [Somogyi 1973], the introduction of the parameters R_c, $V(x)$, the range R_0 and the angle θ is completely sufficient for the theoretical description of the most general details of track-diameter kinetics where R_c is the critical residual range along which the track etch rate ratio $V = V_T/V_B > 1$ is fulfilled (V_T and V_B are track and bulk etch rates, respectively), $V(x) = V_T(x)/V_B$ where $V_T(x)$ is the track etch rate varying along the particle trajectory, R_0 is the etchable range of the solid detector from the original surface to the end of track, and θ is the incident angle measured from the original surface plane.

The function $V(x)$ is not definitely determined by experimental data and assumed rather arbitrary as the constant average value V of $V(x)$ for a shorter etched track portion of a length L defined as

$V^{-1} = (1/L) \int_0^L V(x)^{-1} \, dx$.

In addition to introducing these parameters R_c, $V(x)$, R_0 and θ, some basic assumptions must be set up for isotropic and anisotropic solids separately to deduce relations describing etch-pit geometries and charged particle parameters.

Using these assumptions on the model of the latent tracks and etched tracks, Somogyi et al. deduced the relation between the etch-pit diameter and particle parameters for isotropic and anisotropic solids. Then, we can evaluate V, θ and R_0 from the experimentally measureable curves $d(h, \theta)$ and $D(h, \theta)$ using the theoretically obtained relations where $d(h, \theta)$ ($D(h, \theta)$) is the minor (major) axis d (D) of an etch-pit as a function of the surface removal h at an entrance angle θ.

Furthermore, it is necessary to make a standard (or reference) sample for comparison by irradiating know species of charged particles on the detector solid to evaluate V and θ distributions from tracks generated in the detector.

Thus, they have shown that the changes of the etch-pits revealed in dielectric track detectors through chemical etching can be described on the grounds of geometrical considerations and on some physically realistic basic assumptions. On the strength of this model, explicit relations and/or general methods can be given for the determination of the minor and major axes of the track pits in solids displaying isotropic and anisotropic etching properties.

If it is possible to determine the minor and major axes of the pit and the thickness of the layer removed from the detector surface accurately, we may be able to determine the values of the particle parameters inherent in the etch-pits as far as the conditions of the model satisfied. We have to be nervous to use the track-diameter method for identification of unknown charged particles in relation to the applicability of the model

especially when there are several unknown particles to be identified.

2.3.3 Difficulty in Simultaneous Determination of Species and Energies of Incident Particles

Fleischer et al. say as follows [Fleischer 1965]:

"In short, widespread technical use is being made of defects whose real nature is relatively incompletely known. There are several levels on which we would like to develop our understanding of particle tracks.

Most of the existing work has taken its incentives from the desire to use tracks with more quantitative rigor, for example to identify individual particles and to measure their energies. Success here would lie in finding for each detector a precise function that relates etching rates to the velocity and nuclear species of the track-forming particle."

However, the track formation of the incident particle in the target solids is governed principally by the charge and the velocity (or the energy and the mass) of the incident particle and the charge of the target nucleus as shown in Sections 2.1.1 and 2.1.2. Therefore, the following condition expressed by Fleischer et al. is not easily satisfied experimentally even now: "- - - in finding for each detector a precise function that relates etching rates to the velocity and nuclear species (charge and mass) of the track-forming particle."

The recent work by Yamauchi et al. (cf. Sec. 2.2.3) [Yamauchi 2005] has shown clearly the difficulty in determination of the precise function that relates etching rates to the velocity and nuclear species of the track-forming particle. Therefore, we have to compare the tracks observed in the experiments with the standard (or reference) tracks obtained using a known particle and deduce our conclusion by analogy while we do not know the precise function. The conclusion thus deduced is not necessarily quantitative but qualitative. One of the most quantitative experiments we know at present is introduced in Section 3 where iron isotopes of known energy are discriminated their mass as precisely as 0.22 ± 0.03 amu in rms [Kodaira 2007]. So, we have to be similarly cautious to use the solid-state particle detector in the CFP quantitatively as the case of the mass resolution by Kodaira et al.

3. Application of Solid-State Track Detector to Several Problems

There are many applications of the solid-state track detector to problems where we want to know the energies and species of charged particles influencing target materials. We choose only two cases of these applications of CR-39 to show one for precision measurement with it and another used in the cold fusion phenomenon (CFP) where

there are many difficulties due to the existence of several unknown particles with various possible energies.

3.1 **Identification of Heavy Ion Isotopes using CR-39:** An Example of Precision Measurement using CR-39 by Kodaira et al. [Kodaira 2007, 2008]

To determine chemical compositions of trans-iron nuclei ($Z \geq 30$) in galactic cosmic rays precisely, Kodaira et al. [Kodaira 2007, 2008] improved the accuracies of microscopic image analysis and detector thickness measurement of the CF-39 track detector to obtain the mass resolution for iron isotopes of 0.22 ± 0.03 amu in rms. To confirm this accuracy, they used ^{56}Fe and ^{55}Fe beams from the heavy ion accelerator HIMAC (Heavy Ion Medical Accelerator in Chiba) of the NIRS (National Institute of Radiological Sciences).

It is expected that the CR-39 detector will have better resolution of particle identification because the CR-39 detector essentially responds to only low-energy δ-rays (electrons emitted by the incident charged particle with energies enough for secondary ionization of atoms in the target) ejected by the “distant-collisions” in ionization energy loss [Benton 1969].

The range of a particle with a definite charge and velocity (energy) is proportional to tits mass. This is the principle we can determine the mass of charged particles

To improve the mass resolution of 0.28 ± 0.12 amu in rms for iron nuclei in the CR-39 detector, they improved their measuring system for 1) the “surface position” of the latent tracks (radiation damage trails) and 2) the “CR-39 sheet thickness.”

Improving their measuring apparatus for these two error causes, they obtained the mass resolution for iron isotopes in the CR-39 detector of 0.22 ± 0.03 amu in rms. It should be helpful to understand what the precision determination of parameters of an incident charged particle means by citation of essential parts of their experiment [Kodaira 2007]

A swift charged particle passing through the SSTD (solid-state track detector) leaves a radiation damage trail called a "latent track," that can appear by chemical etching in a suitable etchant. The etchant removes material in a very narrow region around the latent track at rate V_t, while it also removes material from undamaged regions at bulk etch rate V_b. As a consequence of chemical etching, a conical etch pit appears in the SSTD, as shown in Fig. 1 [Kodaira 2007].

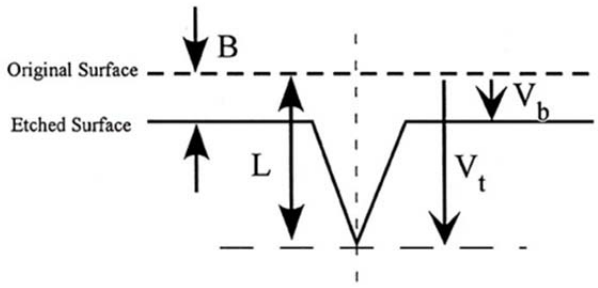

Fig. 3.1 Schematic cross-sectional view of etch pit geometry. An etch pit grows along the track with length L at etch rate V_t for the amount of bulk etch B at rate V_b [Kodaira 2007].

The track registration sensitivity (S) is defined as the ratio of etch rates ($V_t/V_b - 1$), and is thought to be a function of the restricted energy loss (REL) of the incident charged particle. REL is defined as the energy loss rate along the track core region near the particle trajectory. Namely, this criterion for track registration assumes that δ-rays with energies greater than the cut off-energy (ω_0) carry away their energy from the track core region and hence do not contribute to latent track formation. For the CR-39 detector, the cut-off energy (ω_0) has been considered to be 200 eV. By using the measurable parameters, that is the cone length (L) of the etch pit and amount of bulk etch (B), the track registration sensitivity (S) is obtained by

$S = (L/B) - 1$.

Here, L is a function of REL of the incident charged particle. The range of a particle with a definite charge and velocity is proportional to its mass. In this work, the mass of an incident charged particle is determined from the variation in the cone length (L) of the etch pit produced in the detector as a function of its residual range (R), as shown in Fig. 2 [Kodaira 2007], which shows the schematic drawing of the trajectory of stopping particles from the stopping layer ($i = 0$) to the upstream layers ($i > 1$) in a stack. In general, the so-called "L-R" technique in the SSTD is analogous to the $\Delta E - E$ technique in the Si detector telescope.

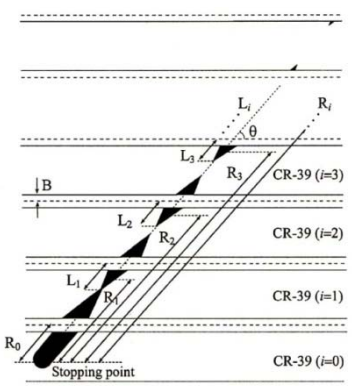

Fig. 3.2 Schematic drawing of etch pits produced in each CR-39 detector layer. Cone length (L_i) in the i-th layer is defined as the distance between the etched surface and the tip of the etch pit as shown in the figure. Residual range (R_i) is the distance from the stopping point in part of the spherical end to the center point of the cone length. In this work, only L_i produced in the upstream surface is measured [Kodaira 2007].

The incident angle θ is given by

$$\theta = \sin^{-1}\{(4B^2 + d^2)/[16D^2B^2 + (4B^2 - d^2)^2]\}$$

D and d denote the major and minor axes of the elliptical opening mouth of the etch pit on the detector surface, respectively, as shown in Fig. 4 and B is the amount of bulk etch as shown in Figs. 3.1, 3.2 and 3.3 [Kodaira 2007].

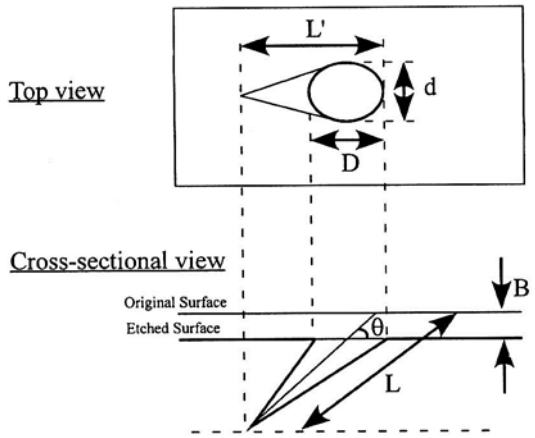

Fig. 3.3 Schematic drawing of geometrical structure of etch pit with incident angle θ [Kodaira 2007].

3.2 Identification of Charged Particles in the Cold Fusion Phenomenon (CFP)

We give here a short introduction of researches in the CFP using CR-39 to identify emitted charged particles from cold fusion (CF) materials composed of mainly transition metals and hydrogen isotopes. Details of the use of CR-39 detector in the CFP will be discussed in another paper presented at JCF13 and published in *Proc. JCF13* [Kozima 2013].

The first use of a plastic track detector CR-39 in the cold fusion research was performed by Chinese scientists [Li 1991] in the early days of cold fusion research after the discovery of the "cold fusion" by Fleischmann et al. [Fleischmann 1989]. In these researches, they have confirmed the nuclear nature of curious events related to extravagant excess energy and unbelievable generation of new nuclides occurring in cold fusion materials composed of transition metals and hydrogen isotopes.

After an interval of about ten years, there is a revival of the use of CR-39 in the cold

fusion research to identify charged particles emitted from CF materials. Several of excellent works with CR-39 detector were reported by Mosier-Boss et al. [Mosier-Boss 2009] to confirm energetic neutrons emitted from a Pd/D co-deposition sample and Aizawa et al. [Aizawa 2012] to show two kinds of charged particles from NiD_x and NiH_x ($x < 1.0$) samples in electrolytic systems $Ni/Li_2SO_4 + D_2O$ (H_2O)/Pt and Ni/LiOH + D_2O (H_2O)/Pt. Other experiments with CR-39 performed to detect charged particles in the CFP be given in the paper given in JCF13 and published in *Proc. JCF13* [Kozima 2013].

4. Conclusion

In the long investigation of the cold fusion phenomenon (CFP) since 1989, we have tried to make clear the nuclear feature of the various events observed in CF materials mainly composed of transition metals (and carbon compounds) and hydrogen isotopes. The enormous amount of excess energy inexplicable with chemical reactions and generation of neutron, proton, tritium, alpha and transmuted nuclei with atomic numbers up to 92 are evidences showing the nuclear character of reactions occurring in the CF materials. It has been eager desire to detect charged particles with large energies of the order of several MeV emitted from CF materials which give also a decisive evidence of the nuclear nature of reactions in the CFP.

The solid-state nuclear track detectors, especially CR-39 used frequently recent years in this field, will be powerful tools to give us the above mentioned evidence to support our premise that the various events in the CFP are induced by some kind of nuclear reactions occurring in the CF materials at near room temperature without any artificial acceleration mechanism.

The detection of charged particles in the CFP is characterized by following points: (1) proximity of the source of charged particles to the detector and necessarily therefore a large variety of incident angles in the case of experiments at ordinary ambient conditions, (2) a variety of particles from proton, deuteron, triton, ^3_2He and ^4_2He expected by presumed nuclear reactions to unexpected ones, (3) necessity to discriminate species of charged particles incident to the detector and to determine their energies simultaneously, and accordingly (4) necessity to discriminate two kinds of particles, one generated by nuclear reactions and another accelerated by the former.

It is necessary to use the solid-state track detectors carefully to give persuasive data for people who are not necessarily favorable for the existence of the CFP. To do so, the careful use of the CR-39 detector given by Kodaira et al. in the determination of iron isotopes introduced in Section 3 is suggestive [Kodaira 2007]. We have to remember the

fundamental nature of the radiation damage in solids by incident charged particles and characteristics of complex processes from latent track formation to the visualization of latent tracks by chemical etching.

Acknowledgement

The author would like to express his thanks to Prof. X.Z. Li of Tsinghua University, China for his valuable discussions on the use of CF-39 in the research of the CFP. He is also indebted to Prof. Hiroshi Yamada of Iwate University and Prof. T. Tsuruta of Kinki University for information about their use of CF-39 in their researches.

References

[Aizawa 2012] H. Aizawa, K. Mita, D. Mizukami, H. Uno and H. Yamada, "Detecting Energetic Charged Particle in D_2O and H_2O Electrolysis Using a Simple Arrangement of Cathode and CR-39," *Preprint of the ICCF-17 Proceedings*, P-1050.

[Benton 1969] E.V. Benton and W.D. Nix, "The Restricted Energy Loss Criterion for Registration of Charged Particles in Plastics," *Nucl. Instr. Meth.* **67**, 343 – 347 (1969).

[Bohr 1948] N. Bohr, Kgl. Danske Viennskab. Selskab. Matt.-Fys. Medd. 18, No.8 (1948).

[Chadderton 1966] L.T. Chadderton, D.V. Morgan, I.McC. Torrens and D. Van Vliet, "On the Electron Microscopy of Fission Fragment Damage," *Phil. Mag*. **13**, 185 – 195 (1966).

[Doke 1969] T. Doke, "Mechanisms of Trajectory Formation in Solid Track Detectors," (in Japanese), *Oyo Butsuri* (Applied Physics) **38**, pp. 1065 – 1076 (1969). UDC 539.1.073

[Doke 1970] T. Doke, "Stopping Powers of Gases and Solids for Heavy Charged Particles," *Oyo Butsuri*, **49**, 1086 – 1100 (1970). (in Japanese)

[Firsov 1959] O.B. Firsov, J.E.T.P., 36, 1076 (1959)

[Fleischer 1965] R.L. Fleischer, P.B. Price and R.M. Walker, "Ion Explosion Spike Mechanism for Formation of Charged-Particle Tracks in Solids," *J. Appl. Phys.* 36, pp. 3645 – 3652 (1965)

[Fleischer 1975] R.L. Fleischer, P.B. Price and R.M. Walker, *Nuclear Tracks in Solids*, University of California Press, 1975. ISBN 0-520-02665-9

[Fleischmann 1989] M. Fleischmann, S. Pons and M. Hawkins, "Electrochemically induced Nuclear Fusion of Deuterium," *J. Electroanal. Chem*., **261**, 301 – 308 (1989).

[Katz 1968] R. Katz and E.J. Kobetich, "Formation of Etchable Tracks in Dielectrics," *Phys. Rev*. **170,** 401 – 405 (1968).

[Kodaira 2007] S. Kodaira, N. Yasuda, N. Hasebe et al., "Improvement of Mass Resolution for Iron Isotopes in CR-39 Track Detector," *Jpn. J. Appl. Physics*, 46, pp. 5281 – 5287 (2007).

[Kodaira 2008] S. Kodaira, "Identification of Heavy-Ion Isotopes using CR-39 Solid-State Track Detector," *Oyo Butsuri* (*Applied Physics*), 77, pp. 36 – 40 (2008). (In Japanese)

[Kozima 2013] H. Kozima and M. Tada, "Emission of Charged Particles in the Cold Fusion Phenomenon," *Proc. JCF13* (Dec. 8 – 9, 2012, Nagoya, Japan) (to be published in 2013). http://jcfrs.org/file/jcf13-proceedings.pdf
And also *Reports of CFRL* **13-1**, pp. 1 – 18 (2013).
http://www.geocities.jp/hjrfq930/Papers/paperr/paperr.html

[Li 1991] X.Z. Li, "Chinese Effort in Understanding the 'Cold Fusion' Phenomena," *Proc. ICCF2*, pp. 309 – 317 (1991). And also his private communication in the year of 2012.

[Lindhard 1963] J. Lindhard, M. Scharff and H.E. Schioff, *Danske Viennskab. Selskab. Matt.-Fys. Medd.* 33, No.14 (1963)

[Merkle 1962] K.L. Merkle, "Fission-fragment Tracks in Metal and Oxide Films," *Phys. Rev. Lett*. **9,** 150 – 152 (1962).

[Mosier-Boss 2009] P.A. Mosier-Boss, S. Szpak, F.E. Gordon, and L.P.G. Forsley, **"**Triple Tracks in CR-39 as the Result of Pd/D Co-deposition: Evidence of Energetic Neutrons," *Naturwissenschaften*, **96** (2009) 135-142.

[Price 1962a] P.B. Price and R.M. Walker, "Electron Microscope Observation of Etched Tracks from Spallation Recoils in Mica," *Phys. Rev. Lett.* 3, 217 – 219 (1962).

[Price 1962b] P.B. Price and R.M. Walker, "Chemical Etching of Charged Particle Tracks in Solids," *J. Appl. Phys*. 33, 3407 – 3412 (1962)

[Price 1962c] P.B. Price and R.M. Walker, "A New Track Detector for Heavy Particle Studies," *Phys. Lett.* 3, 113 – 115 (1962).

[Sauter 1965] C.A. Sauter and E.J. Zimmerman, *Phys. Rev*. 140, A490 – A498 (1965).

[Silk 1959] E.C.H. Silk and R.S. Barnes, "Examination of Fission Fragment Tracks with an Electron Microscope," *Phil. Mag*. **4**, 970 – 972 (1959).

[Somogyi 1973] G. Somogyi and S.A. Szalay, "Track-Diameter Kinetics in Dielectric Track Detectors," *Nucl. Instr. Meth.*, 109, 211 – 232 (1973).

[Yamauchi 2005] T. Yamauchi, R. Barillon, E. Balanzat, T. Asuka, K. Izumi, T. Masutani, and K. Oda, "Yields of CO_2 Formation and Scissions at Ether Bonds along Nuclear Tracks in CR-39," *Radiat. Meas.* 40, 224 – 228 (2005).

Emission of Charged Particles in the Cold Fusion Phenomenon

H. Kozima* and M. Tada**

* Cold Fusion Research Laboratory, 421-1202 Yatsu, Aoi, Shizuoka, 421-1202 Japan

**Institute of Natural Medicine, Toyama University, 2630 Toyama, 930-0194 Japan

Abstract

We summarize experimental data sets of charged particle emission obtained after 1990 and investigate them from our point of view that the whole experimental data obtained in the CFP from excess energy to nuclear transmutation through emissions of neutron and light charged particles should be interpreted consistently if these phenomena have a common cause in the physics of the cold fusion phenomenon.

Based on the TNCF model proposed by us in 1993 at ICCF4 held in Hawaii, USA, we have given a consistent explanation of the data of charged particles emitted from CF materials in accordance with other data obtained in the CFP from excess energy generation to nuclear transmutation through neutron emission.

We confine our investigation in this paper to the experiments where are used no artificial excitations by such particles as proton, deuteron or photon with energies higher than 1 keV. In our opinion, the physics of events caused by energetic particles in CF materials belongs to the low energy nuclear physics under the influence of CF materials even if it is a part of the solid-state nuclear physics or condensed material nuclear science.

1. Introduction

The cold fusion phenomenon (CFP) is a name used to express nuclear events as a whole including excess energy production and nuclear transmutations occurring in condensed materials composed of host elements (transition metals; Ti, Ni, Pd, and carbon) and hydrogen isotopes (H and D). The cold fusion is the name used to express the events observed by pioneers in this field at the earlier stage from 1989 and the name CFP stands for the field born from the original concept of the pioneers.

The most solid evidence of nuclear reactions is the change of a nucleus to another and this is detected by observing the change itself (nuclear transmutation) and emission of neutron and charged particles accompanied to the transmutation. The experimental data sets including the nuclear transmutation and excess energy production obtained mainly in 20th century had been analyzed successfully by our TNCF model [Kozima 1998, 2006] assuming a new state of neutrons in solids composed of host elements and hydrogen isotopes.

On the other hand, detection of the charged particles has been one of main targets for confirmation of nuclear reactions involved in the CFP. The detection of charged particles as they are emitted from nuclei has difficulty in elimination of severe influence of charged particles surrounding the cold fusion (CF) materials with little success. So, the observation of tritons and alpha particles has been mainly done as detection of tritium ($^3_1$H) and helium-4 ($^4_2$He) in CF and surrounding materials in electrolytic

systems. Another problem related to the charged particle observation is difficulty to measure other observables simultaneously to identify nuclear reactions causing the emission of the charged particle and the other observables.

However, the use of CR-39 solid-state particle detector in the CFP proposed by Chinese group in 1989 [Li 1990] made the measurement of charged particles practical and applied frequently in recent years. Frequency and accuracy of detection of charged particles in electrolytic systems have been extensively increased in these several years by the use of the CR-39 detector even if there remains ambiguity in identification of charged particles and determination of their energies.

The CFP has been investigated for more than 20 years in various materials mainly in transition-metal hydrides and deuterides and sometimes in proton conductors and such organic compounds as polyethylene. And we know much about its complicated effects from excess heat generation to heavy nuclides production by nuclear transmutations through emissions of proton, deuteron, neutron, alpha-particle and gamma and X-ray from CF samples in non-equilibrium condition without artificial excitation.

On the other hand, there are trials to check effects of external excitations on the CFP. To enhance the nuclear reactions in and accompanying emission of charged particles from CF materials, artificial excitation by energetic particles (electron, proton and deuteron) and laser beams has often been applied. The results obtained by these experiments have shown enormous enhancement of the *d-d* fusion reaction by sometimes 9 orders of magnitude by 1 keV deuteron irradiation on PdD samples.

The artificial excitation not only surely enhances the cause-effects relation in the CFP but also add complex factors to the analysis. Each effect obtained in these experiments with artificial excitations is a part of the CFP but with complication including an extra factor to the original cold fusion phenomenon. So, we will confine our discussion in this paper only to the genuine CFP without artificial excitation by particles and photons with energies larger than 1 keV.

In this paper, we give a review on the experimental data of charged particles emission from CF materials leaving the explanation of CR-39 track detector to another paper presented at this conference [Kozima 2013a]. We explain our TNCF model in relation to the charged particle emission in the CFP. We will then give finally a consistent explanation of the data of charged particles emitted from CF materials based on our model in accordance with other data of neutron emission and nuclear transmutation in addition to the excess energy generation in the CFP.

2. Emission of Charged Particles in the CFP and Use of CR-39

The detection of the charged particles has been one of main techniques for confirmation of nuclear reactions involved in the CFP as explained in the Introduction of this paper. The detection of charged particles as they are emitted from nuclei has difficulty to avoid the severe influence of charged particles surrounding the cold fusion (CF) materials. Therefore, the observation of tritons and alpha particles has been mainly replaced by detection of tritium ($^3_1$H) and helium-4 ($^4_2$He) in CF and surrounding materials in electrolytic systems. The first trial to detect tritium in the electrolytic system where observed tremendous excess heat was performed by the pioneers of this field and the result was reported in the first paper announcing the cold fusion phenomenon in a PdD_x system [Fleischmann 1989]. The experimental data sets reporting observation of tritium were compiled in our books [Kozima 1998 (Sec. 6.4). 2006 (Sec. 2.6)]. On the other hand, the first detection of helium atoms in Pd samples which generated excess heat was reported by Morrey et al. in 1990 [Morrey 1990]. The experimental data sets reporting observation of helium were compiled in our books [Kozima 1998 (Section 6.5), 2006 (Sec. 2.8)].

Direct detection of charged particles from CF samples has been performed in systems without liquids, i.e. in systems in vacuum (See Sections 2.2 and 2.3). However, the use of the solid-state particle detector made possible detection of charged particles in gaseous and liquid systems. The first proposal to apply the solid-state particle detector CR-39 in the field of the CFP was made by Chinese scientists as early as 1991 [Li 1991]. It is emphasized that CR-39 has high sensitivity and low background and need not any high voltage power supply; therefore, it has low electronic noise and is particularly suitable for experiments in the high pressure vessel such as that used by Frascati group in Italy (e.g. [De Ninno 1989]).

Recently, the CR-39 has been used frequently due to its advantages of high sensitivity and low background rather easily and some easy conclusions seem to be deduced. We have to be careful to deduce a conclusion from limited data as always noticed in our daily experience as typically expressed in the famous Buddhist parable for our self-reproach [Appendix Tittha Sutta].

One of the most important demerits of the use of CR-39 detector is the limitation to simultaneous use of this detector with apparatuses to observe other observables such as excess energy, neutron, tritium and nuclear transmutations. With several quantities observed simultaneously, we can access the entity of the physics occurring in the material more effectively. Another demerit is the lack of time resolution for the occurrence of nuclear reactions (cf. next section).

2.1 Experimental data of charged particle emission in the CFP research

From the first stage of the investigation of the cold fusion phenomenon (CFP), the charged particles, proton, triton and helium-3 and helium-4, expected from the presumed nuclear reactions between deuterons are main targets of search. While Chinese scientists noticed efficacy of the use of CR-39 for the CF research as early as 1991 [Li 1991], they have recognized the qualitative nature of this detector. Therefore, quantitative investigation of the emitted charged particles in the CFP did not make great progress as summarized in this Section.

2.1.1 Merits and demerits of CR-39 detector in the CFP

As is discussed in our previous paper [Kozima 2013a], there are several difficulties to be overcome in identification of charged particles and their energies by using the CR-39 detector at present.

Besides these difficulties, there are other problems inherit in the CFP where we do not know physics of the nuclear reactions in CF materials at present. Therefore, it will be useful to recognize the characteristics of the plastic solid-state particle detector CR-39 in relation to the CF researches. Because we do not know the true mechanism of the cold fusion phenomenon (CFP), it is necessary to obtain as many observables as possible, hopefully them simultaneously. Merits and demerits of the CR-39 detector necessarily relate to these points.

Merits.

As is expressed in the paper by X.Z. Li, CR-39 detector has high sensitivity and high efficiency without dead time and needs no any high voltage power supply resulting in low background noise [Li 1991]. In addition to these characteristics preferable for the CF research, it is very convenient to measure several charged particles simultaneously such as protons, deuterons and tritons expected from the *d*-*d* reactions (3.6) and (3.7) below. The CR-39 detector is also easy to use close to CF materials where occur nuclear reactions, minimizing the energy loss by interaction with other particles.

Demerits.

First of all, the complex mechanisms of latent track formation in the detector make the identification of charged particles and determination of their energies qualitative.

In principle, the CR-39 detector has cumulative nature and needs a definite length of time to accumulate signals of charged particles emitted by reactions in CF materials. It is, therefore, not possible to determine the temporal characteristics of events in the CFP. Also, this characteristic is not compatible with simultaneous measurements of such dynamical variables as rates of excess energy production and of neutron emission.

2.2 First experimental data obtained by Chinese researchers with CR-39 detector

The CR-39 plastic track detector was used first by several research groups in China for qualitative determination of the nuclear character of the CFP [Li 1991, Mo 1991, Shangxian 1991, Wang K.L. 1991, Wang S.C. 1991].

In the experiment by Mo et al. [Mo 1991], Pd and Ti foils in a stainless steel vessel were deuterized by D_2 gas with a pressure of 1 atm. The plastic track detector CR-39 and thermoluminescence detector (TLD) were used for the energetic charged particles and for the low energy EM radiation (the precursor of the former), respectively. They observed peaks corresponding to energies of about 5 MeV which does not fit with any conventional binary D-D reaction.

In the experiment by Shangxian et al. [Shangxian 1991], they observed intense bursts of charged particles which were reproducibly detected by using CR-39 detector during either a high voltage discharge between deuterated Pd electrodes or a non-equilibrium out-diffusion of deuterons in Pd.

In the experiment by S.C. Wang et al. [Wang S.C. 1991], CR-39 detector has been used in search for charged particles from PdD_x and TiD_x foils. From a Pd and Ti foils, they found etch pits on the detector whose track parameter suggested the charged particles with charges $Z = 2$ and $Z = 3$ are responsible for the etch pits. In order to identify the charge Z more accurately, they needed further calibration of the response of CR-39 using alpha particle irradiation under the condition of high-pressure D_2 gas and temperature cycle.

X.Z. Li reported a review article on the use of CR-39 in China together with his data [Li 1991]. He is not using the CR-39 detector recently for years due to its demerits (especially its qualitative nature and lack of time resolution) listed up above [Li 2012].

Their experimental data are tabulated in Table 2.1 and depicted in Fig. 2.1.

Table 2.1 Experimental data obtained by Chinese researchers

Authors and References	**Species**	**Energies of observed particle**
[Mo 1991]	?	5 MeV
[Shangxian 1991]	Bursts	?
[Wang K.L. 1991]	?	?
[Wang S.C. 1991]	?	2 and 3 MeV
[Li 1991]	?	$Z > 1$, $E > 5$ MeV

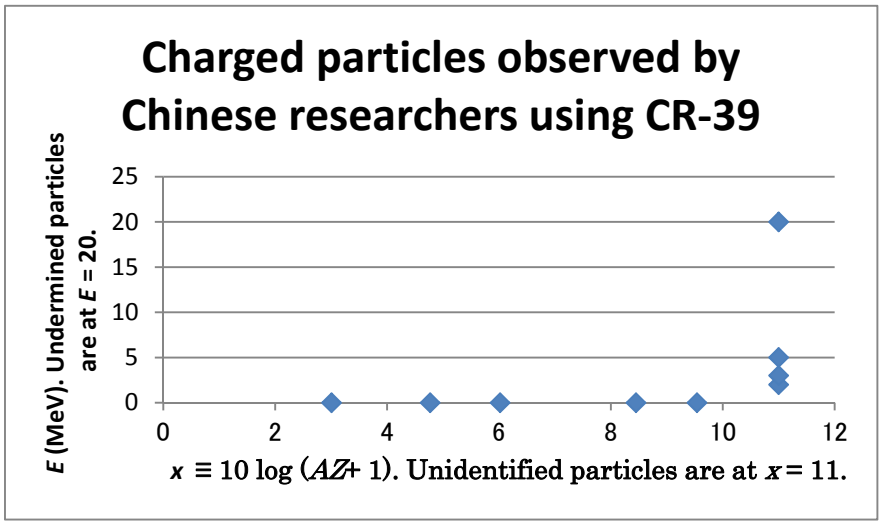

Fig. 2.1 Charged particles observed by Chinese researchers in 1990 – 1991 using CR-39 for the first time in the research of the CFP. The abscissa is x = 10 log (AZ + 1) and the ordinate is the energy E in MeV. Proton, deuteron, triton, ^{3}He and ^{4}He correspond to x = 3.01, 4.77, 6.02, 8.45 and 9.54, respectively. Data of unspecified particles are placed at x = 11 and unidentified energies are at E = 20 MeV. Marks on the abscissa are for identification of particles.

2.3 Experimental data sets showing emission of charged particles in the CFP

Emission of heavy charged particles is a decisive proof of nuclear reactions in the cold fusion phenomenon (CFP) and therefore has been investigated from the first stage of the research in this field. Several methods have been used for the detection of charged particles appropriate for the experimental setup. It is natural that the emitted charged particles were measured mainly in vacuum systems where the energy losses of the particle seem negligible.

2.3.1 Beddingfield et al.

Beddingfield et al. [Beddingfield 1991] have observed intense bursts of charged particles from thin Ti foils (Ti662 sample containing 6% V, 6% Al and 2% Sn) loaded by deuterium. The dimension of the foil was 1 cm × 2 cm × 100 μm.

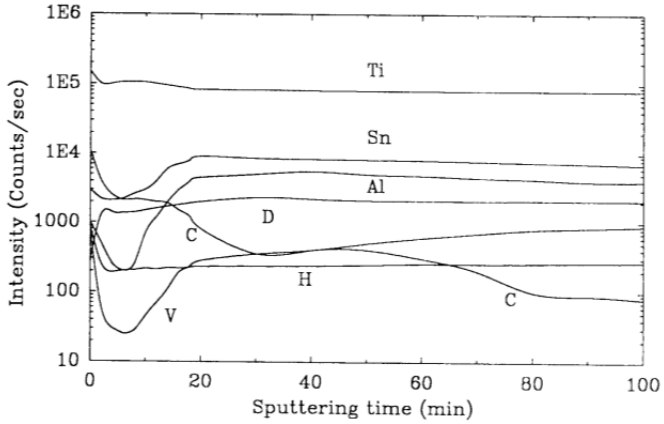

Fig. 2.2 SIMS profile of elements in one of the Ti-D samples [Beddingfield 1991]. The maximum sputtering time of 100 min. corresponds to a depth of about 2 μm.

It is very interesting to notice that they observed changes of density of the minor elements as shown in Fig. 2.2 [Beddingfield 1991 (Fig. 3)]. The decreases of Al, V and Sn in the surface region of a width of about 0.4 μm observed by Beddingfield et al. remind us the similar data obtained by Okamoto et al. [Okamoto 1993]. Okamoto et al. observed a decrease of Al and an increase of Si in the surface region of width about 0.5 μm which were explained by the nuclear transmutation catalyzed by trapped neutrons according to our TNCF model [Kozima 2003]:

$$n + {}^{27}_{13}\mathrm{Al} \rightarrow {}^{28}_{13}\mathrm{Al}^* \rightarrow {}^{28}_{14}\mathrm{Si} + \mathrm{e}^- + \underline{\nu}_\mathrm{e} \qquad (2.1)$$

where $\underline{\nu}_\mathrm{e}$ is the antiparticle of the electron neutrino.

Similarly, the observation by Beddingfield et al. will be explained by the reactions (2.2) – (2.4):

$$n + {}^{27}_{13}\mathrm{Al} \rightarrow {}^{28}_{13}\mathrm{Al}^* \rightarrow {}^{28}_{14}\mathrm{Si} + \mathrm{e}^- + \underline{\nu}_\mathrm{e}, \qquad (2.2)$$

$$n + {}^{51}_{23}\mathrm{V} \rightarrow {}^{52}_{23}\mathrm{V}^* \rightarrow {}^{52}_{24}\mathrm{Cr} + \mathrm{e}^- + \underline{\nu}_\mathrm{e}, \qquad (2.3)$$

$$n + {}^{120}_{50}\mathrm{Sn} \rightarrow {}^{121}_{50}\mathrm{Sn}^* \rightarrow {}^{121}_{51}\mathrm{Sb} + \mathrm{e}^- + \underline{\nu}_\mathrm{e}, \qquad (2.4)$$

while they did not check increases of the elements Si, Cr and Sb corresponding to the observed decreases of Al, V and Sn, respectively.

If the nuclear transmutations expressed by Equations (2.1), (2.3) and (2.4) occurred according to the assumed formulae in free space, there might be a lot of radiation giving hazardous effects on people in the laboratory. However, the reactions in CF materials seem not to emit radiations outside due to absorption by atoms in them (beta decay) or due to a specific mechanism assumed in Equations (3.1) and (3.2) below (gamma decay).

It is desirable to check the sample used in the experiment by Beddingfield et al. repeatedly if it gives a temporal change or not. Such an investigation in any experiment in this field will give supplementary data to explore the physics of the CFP.

2.3.2 Yamaguchi et al.

The first reliable measurement of charged particles was performed by Yamaguchi et al. [Yamaguchi 1993] in a vacuum system with a heterostructure of deuterated Pd (MnO_x/Pd:D/Au). They detected α-particles and protons in addition to excess heat and helium-4. The α-particles with energies of 4.5 – 6 MeV and protons with an energy of 3 MeV were emitted from the oxide surface of their heterostructure sample.

2.3.3 Taniguchi et al.

Taniguchi et al. observed bursts of charged particles emitted from Pd foil cathodes of a D_2O (LiOD) electrolysis with electrolyte LiOD and Pt anode [Taniguchi 1993]. The energy of the burst particles corresponds to 0 – 0.3 MeV if they are protons and to 0 – 1.5 MeV range recorded if they are electrons. A NE102a plastic scintillation counter was used to detect the charged particles.

Taniguchi also measured the strange structures in the charged particle spectrum in 4 – 10 MeV during D_2O electrolysis [Taniguchi 1994]. The peak patterns of the strange structure corresponded neither to that of any back-ground sources nor to that of the D-D reactions.

2.3.4 Karabut et al.

Karabut et al. [Karabut 1995] observed charged particles from a glow discharge system with cathodes of Pd, Zr, Nb, Mo and others at discharge voltages of 200 – 600 V. They used CR-39 and SSB (silicon surface barrier) detectors. Types and energies of charged particles were determined by the energy shift between the two spectra obtained by with 2 mm sapphire plate and 0.1 mm aluminum foil. They concluded that candidates for the charged particles observed were He, Li, B and/or C nuclei with energies of 5 – 6 MeV.

2.3.5 Keeney et al.

Keeney et al. observed charged particles from 25-micron thick TiD_x foil samples under non-equilibrium conditions using a photo-multiplier tube, plastic and glass scintillators [Keeney 2006]. The charged particles are identified as protons with 2.6 MeV in one experiment and are coincident charged particles consistent with protons and tritons in another. Their modest expression “It is possible that other nuclear reactions besides *d-d* fusion are involved” is scientific and appropriate in view of their limited results.

It is interesting to notice that one of the necessary conditions they demand for the observation of the charged particle emission is the loading of deuterium in the presence of LiD. This effect of Li on the CFP is also noticed in the experiment by Aizawa et al. introduced in Sec. 2.4.2 below. Discussion of the effect of lithium on the CFP will be given there.

2.3.6 Storms and Scanlan

Storms and Scanlan observed emission of charged particles having energy with peaks between 0.5 and 3 MeV in low-voltage gas discharge in deuterium with cathodes Al, Cu, Pd, Pd + Pt, Ti, etc. [Storms 2011]. They used a silicon surface barrier (SSB)

detector and considered the particles to be deuterons.

2.3.7 Jiang et al.

Jiang et al. performed experiments on deuterium loaded Ti foil and powder at low temperature [Jiang 2011]. The silicon dioxide-passivated ion-implanted detectors with active area of 600 mm^2 were used. The depleted layer of the detectors is 100 μm thick. The observed charged particle from TiD_x foil sample is identified as proton having energy of about 2.8 MeV.

It is also too hasty in this case to conclude the *d-d* fusion reactions for the observed proton only from its energy of 2.8 MeV without detection of triton of 1.01 MeV and $^3_2$He of 0.82 MeV or neutron of 2.45 MeV.

The data of the charged particles obtained by using detectors other than CR-39 introduced above is tabulated in Table 2.2 and depicted in Fig. 2.3.

Table 2.2 Experimental data of charged particles emitted from CF materials. Charged particles emitted from CF materials

Authors and References	Species	Energies of observed particle
[Beddingfield 1991]	? Burst	?
[Yamaguchi 1993]	α, *p*	4.5 – 6 MeV, 3 MeV
[Iida 1993]	α, ?	8 MeV, 5 MeV
[Taniguchi 1993]	? (*p*)	0 – 0.3 MeV
[Karabut 1995]	He	5 – 6 MeV
[Storms 2011]	?	0.5 – 3 MeV
[Jiang 2011]	*p*	2.8 MeV
[Keeney 2006]	*p*	2.6 MeV

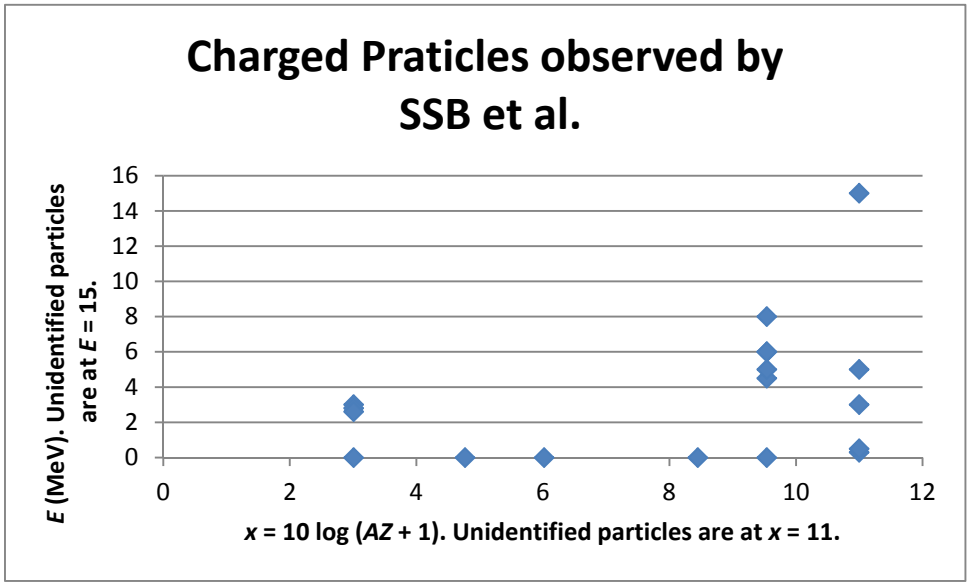

Fig. 2.3 Experimental data of charged particle observation. The abscissa is x = 10 log (AZ + 1) and the ordinate is the energy E in MeV. Proton, deuteron, triton, ^{3}He and ^{4}He correspond to 10 log (AZ + 1) = 3.01, 4.77, 6.02, 8.45 and 9.54, respectively. Data of unspecified particles are placed at x = 11 and unidentified energies are at E = 15 MeV. Marks on the abscissa are for identification of particles.

2.3.8 Data sets obtained by using artificial excitations

There are several experiments with artificial excitation with energetic particles having energies of higher than 100 keV including the experiments by Iida et al. [Iida 1993] and Kasagi et al. [Kasagi 1993].

Iida et al. [Iida 1993] used 240 keV deuterons to irradiate Ti and Pd foils with thicknesses of 5 – 25 μm and 5 – 25 μm, respectively, and observed α-particles with energies of 5 and 8 MeV from Ti foils with Al_2O_3 layer on the surface after the deuterium implantation. They used Si surface barrier detector placed behind the foil sample. Similarly, Kasagi et al. [Kasagi 1993] observed energetic protons with energies up to ~ 17.5 MeV when 150 keV deuterons were bombarded at highly deuterated Ti rods.

As noticed above in Introduction, however, we will confine our investigation in this paper to the cold fusion phenomenon (CFP) without such artificial excitation, while these experiments with energetic particles have close relation to the CFP and surely contribute in elucidation of physics of the CFP.

2.4 Experimental Data obtained by using CR-39

Recently, the solid state detector CR-39 used by Chinese researchers in the early stage of CF research as introduced in Sec. 2.2 has been used fairly frequently in the

experiments in the CFP to determine emission of charged particles.

One of the wonderful uses of CR-39 is the determination of high energy neutrons by the observation of charged particles caused by the neutron [Mosier-Boss 2008, 2009, Kozima 2010]. The triple tracks observed by Mosier-Boss et al. are interpreted as the detection of the three alphas generated by the breakup reaction of carbon-12 $^{12}C(n, n')3\alpha$ with the threshold energy of 9.6 MeV for the neutron to cause this reaction.

Other data to determine the species and their energies of charged particles emitted from CF materials have been given with an ambiguity as shown below and have to be contemplated further.

2.4.1 Experimental data obtained by Roussetski and his collaborators

Roussetski and his collaborators have used CR-39 detectors in their works to investigate nuclear reactions in CF materials. We cite here only a few papers presented by them. The first paper by Roussetski in 1998 reported detection of charged particles by CR-39. He measured also neutrons by a plastic scintillation counter with Cd and by $^3_2$He counter [Roussetski 1998]. He has given a paper at ICCF11 reviewing works done by his group [Roussetski 2006a]. To confirm validity of their measurements, they checked their method carefully using calibration tracks (or standards) of protons (up to 2 MeV) and of alphas (up to 20 MeV) [Roussetski 2006b].

Though the elaborate works by Roussetski and his collaborators have shown new features of the charged particle emission from CF materials of several types sometimes with artificial excitation, their data need more careful check in relation to other data in the CFP and in nuclear physics.

First of all, it is necessary to detect triton (1.01 MeV), proton (3.02 MeV) and $^3_2$He (0.82 MeV) simultaneously to conclude the occurrence of the *d-d* reactions:

$$d\,(\varepsilon) + d = t\,(1.01\ \text{MeV}) + p\,(3.02\ \text{MeV}), \quad (2.\ 5)$$

$$= {}^3_2\text{He}\,(0.82\ \text{MeV}) + n\,(2.45\ \text{MeV}), \quad (2.\ 6)$$

$$= {}^4_2\text{He}\,(76.0\ \text{keV}) + \gamma\,(23.8\ \text{MeV}). \quad (2.\ 7)$$

The probability ratios of these reactions in free space are known to be $1 : 1 : 10^{-7}$.

Second, we want to have a consistent explanation of their data claiming observation of protons and alphas; (1) protons (1.4 – 1.7 and 5.6 – 7.8 MeV) and alphas (9.2 – 14.0 MeV) [Roussetski 2006a] and (2) protons (1.7 – 1.9 MeV) and alphas (10 – 13 and 15 – 17.5 MeV) [Roussetski 2006b].

As we will show in the next section, there are possibilities to expect various particles emitted and accelerated in CF materials according to our model which has been successful to give a consistent explanation for various events in the CFP. So, we

should open our eyes in front of a vast field of unknown events to see a consistent view in accordance with principles and knowledge in physics not falling into the black hole where blinds were (cf. [Appendix]).

2.4.2 Heavy and light water electrolysis with Ni film cathode by Aizawa et al.

The CR-39 detector in the CF research is also used by Aizawa et al. in Iwate University [Aizawa 2012]. They have concluded the detection of charged particles in the experiment where electrolysis of D_2O and H_2O solutions is carried out under several DC current patterns using a Ni film cathode. A CR-39 track detector is set in close contact with the cathode to detect energetic charged particles. An impressive increasing in number of etch pits on the detector is occasionally observed without specification of species and energies of the charged particles responsible to the observed etch pits. Anomalous increase in the number of etch pits has been observed in 1 out of 7 and 2 out of 5 runs for D_2O and H_2O solutions, respectively. The result suggests that the nuclear reactions have been occurring on the Ni film cathodes during the light water electrolysis as well as the heavy water one. The common factors to increase the number of the anomalous etch pits in the CR-39 chip might be the Ni film cathode, the long electrolysis time and Li in the electrolyte solution. All the results indicate that the reaction does not always takes place in every electrolysis experiment but occasionally does under the same experimental condition.

The important role of lithium isotopes for the emission of charged particles observed in this work reminds us several experimental facts related to the role of lithium observed hitherto. The nucleus ${}^6_3\mathrm{Li}$ absorbs a thermal neutron with a fairly large cross section of 940.4 b to be ${}^7_3\mathrm{Li}^*$ which decays into ${}^4_2\mathrm{He}$ and ${}^3_1\mathrm{H}$ (or t) as shown in Eq. (3.3) given in Sec. 3.1 below. This reaction has been used to explain several experimental data sets. Two of them are the detection of ${}^4_2\mathrm{He}$ by Morrey et al. [Morrey 1998, Kozima 2006 (Sec. 2.8)] and depletion of ${}^6_3\mathrm{Li}$ by Passell [Passell 2003]. Recently, Keeney et al. have shown important role of Li to give a positive result of charged particle emission from a TiD_x foil as introduced in Sec. 2.3.5 [Keeney 2006].

2.5 Difficulty in simultaneous determination of particle species and their energies using CR-39

As we have shown in the review paper presented at JCF13 [Kozima 2013a], the interaction of an incident charged particle with atoms in a target material depends fundamentally on the velocity v_1 (or the ratio of the energy E_1 and the mass M_1) and the charge Z_1 of the incident particle and the atomic numbers Z_2's of the atoms in the target

material even if we do not take into our consideration of the atomic structure of the target which is very important as shown by the recent work by Yamauchi et al. [Yamauchi 2005].

Therefore, determination of characteristics of the incident charged particle by the radiation damage or the nuclear track in the target material generated by the incident particle requires at least three independent physical quantities depending on the parameters v_1 (or the ratio of E_1 and M_1), Z_1 and Z_2's. If we use a calibration (or standard) nuclear tracks obtained by reference experiments using known particles with a definite energy, the deduced conclusion should be taken as a qualitative one especially when we do not know what kinds of particles are emitted.

To determine quantitative parameters of the incident charged particles observed by experiments [Kozima 2013a], we need elaborate procedure as illustrated experimentally by Kodaira et al. [Kodaira 2007] and theoretically in the next section in terms of the TNCF model.

3. **TNCF Model and Its Conclusion on the Charged Particle Emission**

The cold fusion phenomenon (CFP), a part of which was discovered in 1989 by Fleischmann et al. at first [Fleischmann 1989] and then by Jones et al. [Jones 1989], includes various events from excess energy production, neutron emission, and production of new elements by nuclear transmutation [Kozima 1998, 2004, 2006]. The events also include production of ^{4}He, emissions of charged particles, gamma and X-rays with a little probability compared to the events noted above.

The main events of the CFP except the emission of charged particles have been explained by us using the phenomenological TNCF model including a single adjustable parameter n_n (the density of trapped thermal neutrons); the experimental data sets until about 2005 have been explained in our books [Kozima 1998, Kozima 2006] and further explanations of neutron emission [Kozima 2010], nuclear transmutation [Kozima 2009], localization of nuclear reactions in the CFP [Kozima 2011a] have been given using the TNCF model. Furthermore, the complexity in the CFP has been pointed out [Kozima 2012] and qualitatively explained in conjunction with the basic assumptions presumed in the TNCF model [Kozima 2013b].

One of the most interesting results explained by the TNCF model is the ratios of numbers N_x's of events X's observed simultaneously. Determining the parameter n_n by the data of the number N_x of an event X, we can calculate the number N_y of another event Y using the model and compare the theoretical ratio $(N_x/N_y)_{th}$ thus calculated with the experimental value $(N_x/N_y)_{ex}$. As shown before [Kozima 1998 (Section 11.1),

Kozima 2006 (Section 2.3)], we have obtained fairly good coincidence of these values within a factor about 3 as expressed by the following relation:

$$(N_x/N_y)_{th} = \alpha(N_x/N_y)_{ex}$$

with $\alpha \sim 3$.

Another quantitative explanation of the experimental data sets where were observed nuclear transmutations from one nuclide to another has been given by the TNCF model [Kozima 1998 (Section 9.1), Kozima 2006 (Section 3.3.5), Kozima 2011b]. One of such quantitative explanations is the variation of Ti isotopes observed in Portland State University [Kozima 2006 (Appendix C7)]. The changes of the amount of ${}^{A}_{22}\mathrm{Ti}$'s (A = 46 – 50) during the experiment are consistently explained by adjusting the single parameter n_n.

It is therefore natural to expect an explanation of the emission of charged particles introduced in Section 2 consistently to other data in the CFP given by our TNCF model. We give a brief introduction of the model in this section and then an explanation of the data on the charged particle emission by our model.

3.1 The TNCF model

The TNCF (trapped neutron catalysed fusion) model proposed as early as 1994 at ICCF4 (Lahaina, Maui, Hawaii, USA, Dec. 6 – 9 (1993)) has been successfully applied to give a unified understanding of the cold fusion phenomenon (CFP) [Kozima 1994]. The model uses an adjustable parameter n_n with several premises based on the experimental facts and has given semi-quantitative relations between several observables measured simultaneously. The theoretical relations among observed values are in agreement with relations deduced from experimental data sets. We will give a brief review on the expected emission of charged particles from our model to compare with experimental data. Another important premise of our model is the emission of phonons in CF materials instead of photons in nuclear reactions in free space. This premise is based on the fact that there are no photons even if there are many nuclear products observed in the CFP and is going to be investigated from the quantum mechanical approach developed recently [Kozima 2008].

3.1.1 Trigger reactions.

A trapped thermal neutron assumed in our TNCF model can fuse effectively in the free space by the following reactions (3.1) and (3.2) with a proton and a deuteron with fusion cross sections 3.32×10^{-1} b and 5.5×10^{-4} b, respectively:

$$n + p = d\ (1.33\ \mathrm{keV}) + \gamma\ (2.22\ \mathrm{MeV}), \qquad (3.1)$$

$n + d = t$ (6.98 keV) + γ (6.25 MeV). (3.2)

The gammas in these reactions in free space should be read as phonons ϕs in CF materials with a reason for this assumption mentioned later. The same translation should be done in reactions formulae which appear in this section hereafter. The first reaction (3.1) will be effective in protium systems and the second (4.2) in deuterium systems.

In the electrolytic systems with electrolytes including lithium, the trapped thermal neutron can fuse with the $^{6}_{3}$Li and $^{7}_{3}$Li nuclei in the surface/boundary regions electroplated on the cathode by the reactions (3.3) and (3.4) below with large cross sections $\approx 1\times10^{3}$ b and 4.54×10^{-2} b, respectively:

$n + {}^{6}_{3}\mathrm{Li} = {}^{4}_{2}\mathrm{He}$ (2.1 MeV) + t (2.7 MeV). (3.3)

$n + {}^{7}_{3}\mathrm{Li} = {}^{8}_{3}\mathrm{Li}^{*} = {}^{8}_{4}\mathrm{Be}^{*} + e^{-} + \underline{\nu}_{e}$ + *13 MeV,* (3.4)

${}^{8}_{4}\mathrm{Be}^{*} = {}^{4}_{2}\mathrm{He}$ (1.6 MeV) + ${}^{4}_{2}$He (1.6 MeV) (3.5)

When there are other nuclides like $^{10}_{5}$B and $^{3}_{2}$He, there will be following reactions (in free space);

$n + {}^{10}_{5}\mathrm{B} = {}^{7}_{3}\mathrm{Li}$ (1.01 MeV) + ${}^{4}_{2}$He (1.78 MeV). (3.6)

$= {}^{7}_{3}\mathrm{Li}^{*}$ (0.85 MeV) + ${}^{4}_{2}$He (1.47 MeV). (3.7)

${}^{7}_{3}\mathrm{Li}^{*} = {}^{7}_{3}\mathrm{Li} + \gamma$ (0.48 MeV). (3.8)

$n + {}^{3}_{2}\mathrm{He} = t$ (0.17 MeV) + n (0.50 MeV). (3.9)

In other electrolytic systems, nuclear reactions $n - {}^{23}_{11}$Na [Bush, R.T. 1992], $n - {}^{39}_{19}$K [Bush, R.T. 1992, Notoya 1996], $n - {}^{88}_{37}$Rb [Bush, R.T. 1993] participate in the CFP as trigger reactions.

The thickness of the surface/boundary regions will be assumed as 1 μm throughout analyses [Kozima 2006 (Premise 8)] although it has been determined as 1 – 10 μm in experiments (allowing one order of magnitude uncertainty in the determined value of the parameter n_{n}). Also, the abundance of the isotope $^{6}_{3}$Li will be assumed as the natural one, i.e. 7.4 % except otherwise described in our analyses.

As was already explained, the photons generated in reactions (3.1), (3.2) and (3.8) in free space are supposed to become phonons in CF materials due to strong interactions of neutrons in them and the liberated energy is thermalized in solids throughout our phenomenological treatment. This is one of the most serious premises in the TNCF model and waits quantum mechanical explanation in the physics of the CFP.

3.1.2 Breeding reactions.

The energetic particles generated in the trigger reactions induced by trapped neutrons in surface/boundary regions in CF materials can induce other nuclear reactions with nuclides, especially with abundant deuterons/protons in a deuterium/protium

system.

When there is an energetic neutron emitted by the above trigger reactions, we expect various reactions including the following elastic collisions, knock out collisions, and splitting reactions;

$$n\,(\varepsilon) + p = n'\,(\varepsilon') + p\,(\varepsilon''), \tag{3.10}$$

$$n\,(\varepsilon) + d = n'\,(\varepsilon') + d'\,(\varepsilon''), \tag{3.11}$$

$$n\,(\varepsilon) + {}^{A}_{Z}\mathrm{X} = {}^{A}_{Z}\mathrm{X}\,(\varepsilon') + n\,(\varepsilon''), \tag{3.12}$$

$$n\,(\varepsilon) + d = n' + p + n'', \tag{3.13}$$

$$n\,(\varepsilon) + {}^{A}_{Z}\mathrm{X} = {}^{A-1}_{Z}\mathrm{X} + n + n', \tag{3.14}$$

$$n\,(\varepsilon) + {}^{A}_{Z}\mathrm{X} = {}^{A-A'+1}_{Z-Z'}\mathrm{X}' + {}^{A'}_{Z'}\mathrm{X}''. \tag{3.15}$$

In these equations, we have used a symbol $n(\varepsilon)$ for an energetic neutron with an energy ε to discriminate it from the thermal neutron expressed as n (or $n(\varepsilon)$ with $\varepsilon = 0$ later) in Equations (3.1) – (3.9).

The triton with an energy ε = 2.7 MeV (or 6.98 keV) generated in the reaction (3.3) (or (3.2)) described as $t(\varepsilon)$ can pass through the crystal along the channelling axes on which is an array of occluded deuterons or can proceed a finite distance determined by the interaction with charged particles in the crystal. In the process of penetration through a crystal, the triton can react with a proton or a deuteron by the following reactions on the path with a length 1 μm [Kozima 2006 (Premise 9)]:

$$t\,(\varepsilon) + p = {}^{4}_{2}\mathrm{He}\ (0.09\ \mathrm{MeV}) + \gamma\ (19.9\ \mathrm{MeV}). \tag{3.16}$$

$$t\,(\varepsilon) + d = {}^{4}_{2}\mathrm{He}\ (3.5\ \mathrm{MeV}) + n\ (14.1\ \mathrm{MeV}). \tag{3.17}$$

The cross section of the reaction (3.17) is $\sigma_{\text{t-d}} \cong 1.4 \times 10^{-1}$ b for ε = 2.7 MeV and 3.04×10^{-6} b for 6.98 keV.

The elastic collisions (3.10) – (3.12) of an energetic neutron having an energy ε with a nuclide in the sample give energy ε's to the target nuclei. When ε is 14.1 MeV, the target nuclei p ($^{1}_{1}$H), d ($^{2}_{1}$H) and $^{4}_{2}$He will have maximum energy of 14.1, 12.5 and 8.0 MeV, respectively, by a head-on collision. Thus, there is a possibility to detect a recoil proton with energies lower than 14 MeV or decelerated from the maximum by electromagnetic interactions with charged particles in the CF material.

One of the flaws in CF researches has been not trying to detect higher energy neutrons up to 15 MeV expected to be generated in this reaction (3.17) except a few cases [Kozima 2010]. Recently, Mosier-Boss et al. observed a $^{12}\mathrm{C}(n, n')3\alpha$ reaction caused by a high energy neutron with an energy higher than 9.6 MeV as introduced in the beginning of Sec. 2.4 [Mosier-Boss 2008, 2009].

In these reactions (3.11) – (3.15), the original high-energy neutron loses its energy to be thermalized or generates another low energy neutron to be trapped in the sample

(breeding processes Eqs. (3.13) and (3.14)) or generate transmuted nuclei (Equations (3.14) and (3.15)).

The recoil deuteron having an energy up to 12.5 MeV produced by an elastic collision with the neutron with 14.1 MeV (Eq. (3.11)) can fuse with another deuteron by two main modes by the reactions with a fairly large cross section of the order of 0.1 b each and by a minor mode with a negligible branching ratio about 10^{-7}:

$$d\,(\varepsilon) + d = t\,(1.01\ \text{MeV}) + p\,(3.02\ \text{MeV}), \tag{3.18}$$

$$= {}^{3}{}_{2}\text{He}\,(0.82\ \text{MeV}) + n\,(2.45\ \text{MeV}), \tag{3.19}$$

$$= {}^{4}{}_{2}\text{He}\,(76.0\ \text{keV}) + \gamma\,(23.8\ \text{MeV}). \tag{3.20}$$

The branching ratios of these three reactions in the free space with ε up to a few MeV are, as is well known, $1 : 1 : 10^{-7}$.

In the case of solids with protium but deuterium, the following breeding reaction between the energetic deuteron and a proton is possible (in the free space):

$$d\,(\varepsilon) + p = {}^{3}{}_{2}\text{He}\,(5.35\ \text{keV}) + \gamma\,(5.49\ \text{MeV}). \tag{3.21}$$

The following reaction is also probable with the energetic deuteron:

$$d\,(\varepsilon) + {}^{3}{}_{2}\text{He} = {}^{4}{}_{2}\text{He}\,(3.67\ \text{MeV}) + p\,(14.68\ \text{MeV}). \tag{3.22}$$

Depending on the situation in CF materials, the trapped thermal neutron can induce such trigger reactions as the reactions (3.1) – (3.9) and the energetic particles generated in them can sustain the breeding chain reactions (3.10) – (3.22) producing a lot of excess heat and/or the nuclear products.

The energetic gamma emitted by the reaction (3.15) (and (3.18)) in free space can induce the dissociation of a deuteron as follows;

$$\gamma\,(\varepsilon) + d = n\,(\varepsilon') + p\,(\varepsilon'') \qquad (\varepsilon > 2.2\ \text{MeV}) \tag{3.23}$$

We have to read the gammas in Equations (3.20) – (3.23) in free space as phonons in CF materials as explained already above on the end of Sec. 3.1.1.

The particles generated by nuclear reactions catalysed by the trapped neutrons assumed in the TNCF model are summarized in Tables 3.1 and 3.2 for the trigger and breeding reactions, respectively. In the tables, the reactions are divided into protium and deuterium systems and designated by equation numbers in this paper.

Table 3.1 Reactions Generating Charged Particles in the TNCF Model (Trigger Reactions). The reaction (4.1) in the 3rd line and a-column in this table will be referred as 3-a (T4.1) in the following.

	a ***Protium system***	b ***Deuterium system***	c ***Additional Agent***
1 ***n***	(4.9)*	(4.9)*	$^{3}_{2}$He*
2 ***p***			
3 ***d***	**(4.1)**		
4 ***t***	(4.3)* (4.9)**	**(4.2)** (4.3)* (4.9)**	$^{6}_{3}$Li* $^{3}_{2}$He**
5 **$^{3}_{2}$He**			
6 **$^{4}_{2}$He**	(4.3)* (4.5)** (4.6)***	(4.3)* (4.5)** (4.6)***	$^{6}_{3}$Li* $^{7}_{3}$Li** $^{10}_{5}$Be***

Table 3.2 Reactions Generating Charged Particles in the TNCF Model (Breeding Reactions). The reaction (4.18) in the 2nd line and b-column in this table will be referred as 2-b (T4.2) in the following.

	a ***Protium system***	b ***Deuterium system***	c ***Additional Agent***
1 ***n***		**(4.12)** (4.13)* **(4.17) (4.19)** (4.22)** **(4.23)**	$^{A}_{Z}$X* $^{3}_{2}$He**
2 ***p***	**(4.10)** (4.22)*	**(4.18)**	$^{3}_{2}$He*
3 ***d***		**(4.11)**	
4 ***t***		**(4.18)**	
5 **$^{3}_{2}$He**	**(4.21)**	**(4.19)**	
6 **$^{4}_{2}$He**	**(4.16)**	**(4.17) (4.20)** (4.22)*	$^{3}_{2}$He*

To generate some particles in the CF materials composed of a host material and a hydrogen isotope, it is necessary to have an additional nucleus (or agent) used often in the experiments as tabulated in the fourth columns of Tables 3.1 and 3.2. The most famous agent is $^{A}_{3}$Li (A = 6 and 7) included in electrolyte for electrolytic systems. The equations including these agents are asterisked in these tables for readers' convenience.

As seen from the Tables, we can expect emission of various particles from CF materials where occur cold fusion reactions and we can observe these neutrons and energetic charged particles if it is possible to catch them before they dissipate their energy.

The particles expected by the TNCF model to be emitted in the CFP tabulated in Tables 3.1 and 3.2 are depicted in Fig. 3.1 using an abscissa 10 log (AZ + 1) to discriminate particles with different proton and mass numbers, Z and A, respectively. Neutron, proton, deuteron, triton, $^{3}_{2}$He and $^{4}_{2}$He correspond to 10 log (AZ + 1) = 0, 3.01, 4.77, 6.02, 8.45 and 9.54, respectively.

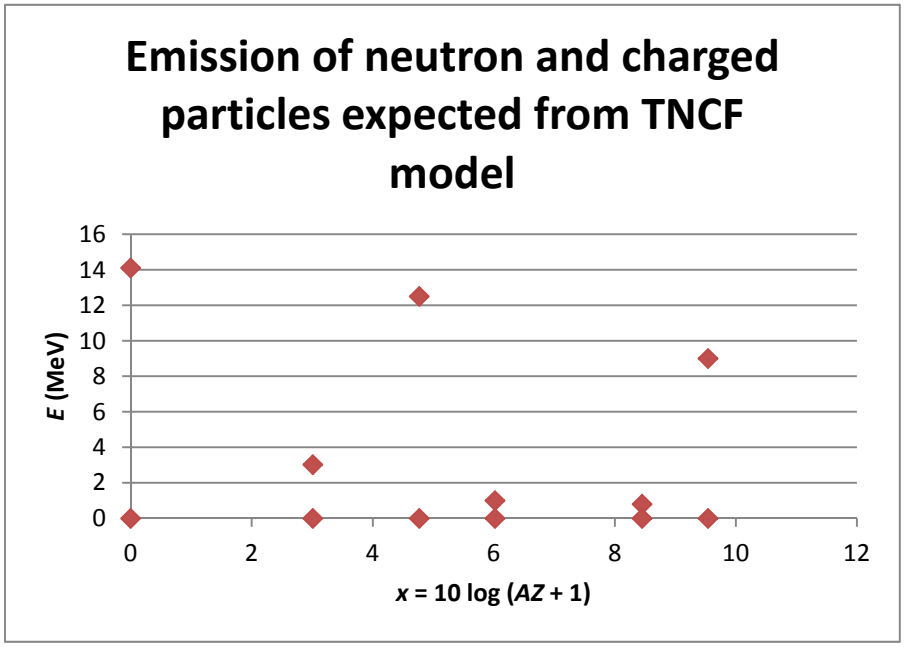

Fig. 3.1 Emission of neutron and charged particles expected from TNCF model. The abscissa is 10 log (AZ + 1) and the ordinate the maximum energy E in MeV expected for particles. Neutron, proton, deuteron, triton, ^{3}He and ^{4}He correspond to 10 log (AZ + 1) = 0, 3.01, 4.77, 6.02, 8.45 and 9.54, respectively. Marks on the abscissa are for identification of particles.

3.2 Explanation of experimental data of charged particle emission in the CFP

Considering the success of unified explanation of various experimental data sets from excess heat generation to nuclear transmutations through neutron emission by the TNCF model [Kozima 1998, 2006], we can expect an explanation of charged particle emissions from CF materials consistent with experimental data of other observables. We summarize first the probable emission of charged particles given in Sec. 3.1 based on the TNCF model and then give comparison of the theoretical expectation with the experimental data.

3.2.1 Probable emission of charged particles from CF materials

From above explanation of the TNCF model, we can deduce possible emission of charged particles in the CF materials as summarized in Table 3.1 for trigger reactions and Table 3.2 for breeding reactions. In principle, the charged particles can be emitted or accelerated by the reactions (3.1) – (3.21) if we do not care their probability. In reality, we have to consider the probability of particle emission in relation to the situation of the CF material where occur nuclear reactions. We survey here the possible emission of charged particles in deuterium and protium systems separately.

(1) Deuterium system

The most probable trigger reaction in the deuterium system will be the reaction between the trapped neutron and the occluded deuteron (Eq. (3.2)) with a cross section 5.5×10^{-4} b (assuming the trapped neutron has a thermal energy) presumably resulting in a triton (6.98 keV) and phonons (in the CF material) instead of a photon in free space. The triton thus generated loses its energy by the electromagnetic interaction with other charged particles in the CF material or makes such breeding nuclear reactions as (3.17) (and possibly (3.16)) generating secondary nuclides $^{4}_{2}$He and neutron.

(2) Protium system

The most probable trigger reaction in the protium system will be the reaction between the trapped neutron and the occluded proton (Eq. (3.1)) with a fairly large cross section 3.32×10^{-1} b (assuming the trapped neutron has a thermal energy) resulting in a deuteron (1.33 keV) and phonons (in the CF material). The deuteron thus generated loses its energy by the electromagnetic interaction with other charged particles in the CF material or makes such breeding nuclear reactions as (3.18) and (3.19) (and possibly (3.20)) generating secondary nuclides *p* ($^{1}_{1}$H), *t* ($^{3}_{1}$H), $^{3}_{2}$He and *n* (and $^{4}_{2}$He).

3.2.2 Explanation of experimental data by the TNCF model

The theoretical expectation of charged particle emissions in the CFP depicted in Fig. 3.1 is compared with experimental data explained in Section 2 and depicted in Figs. 2.2 and 2.3. The data plotted in Figs. 2.2, 2.3 and 3.1 are accumulated in Fig. 3.2.

Figure 3.2 shows that the energies of the observed charged particles (blue points) are below the expected maximum values (red points) from the TNCF model proposed by us. It is natural to have experimental points (blue) below the theoretically expected points (red) because the charged particles lose their energies in the medium before arriving at the detectors used in experiments.

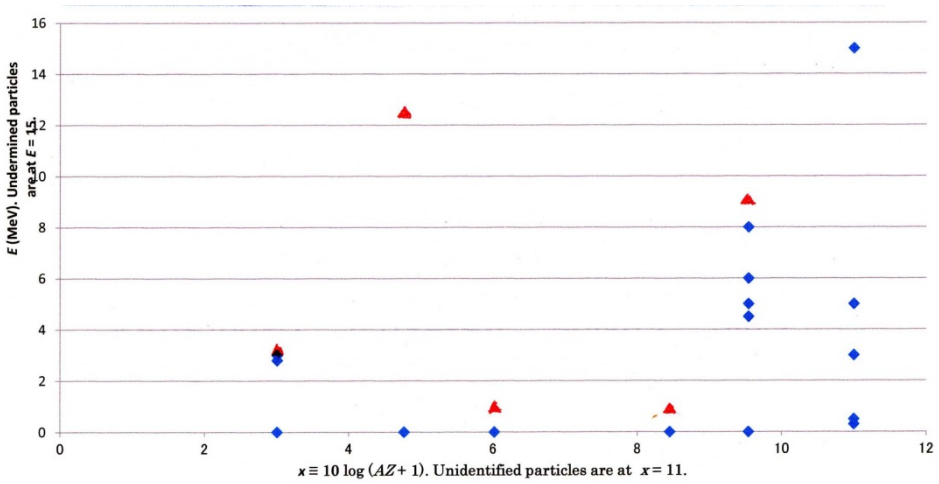

Fig. 3.2 Comparison of experimental data (blue) explained in Section 2 and theoretical expectation (red) explained in this section of charged particles emitted in the cold fusion phenomenon (CFP). The abscissa is $x = 10 \log (AZ + 1)$ and the ordinate is the energy E in MeV. Data of unspecified particles are placed at x = 11 and unidentified energies are at $E = 15$ MeV. Marks on the abscissa are for identification of particles.

4. Discussion

Number of experimental data sets observing charged particles in the CFP is few compared to other events due to the difficulty to catch them as they have born. As we have shown in this paper, we could give a phenomenological explanation for the reliable data on the emission of charged particles by our TNCF model consistently with other events in the CFP such as excess energy generation, neutron emission and nuclear transmutation.

The claims made by some researchers that the *d-d* fusion reactions in the CF-materials have been confirmed using only data of protons with about 3 MeV are not persuasive due to existence of alternative explanations for the data and also to the lack of simultaneous observation of triton and $^{3}_{2}$He expected from Equations (3.18) and (3.19) as we had discussed already.

Confining our consideration for experiments without artificial excitations with energies higher than 1 keV, we can exclude *d-d* fusion reactions from fundamental mechanisms in the CFP by two reasons. The first reason is that the two-body reaction of independent particles occurs with a probability proportional to square of the density x of the particle and behaves as x^2 as shown in Fig. 4.1 [Kozima 2013b (Fig. 1.3)]. This dependence of the reaction probability y on the density x has no critical density for the reaction and is in contradiction with our common knowledge on the dependence of effects on their causes in the CFP. We can pick up an excellent data set out of many such examples, i.e. the extensive work of McKubre et al. showing the excess energy

generation with a critical density of about D/Pd ~ 0.8 [McKubre 1993].

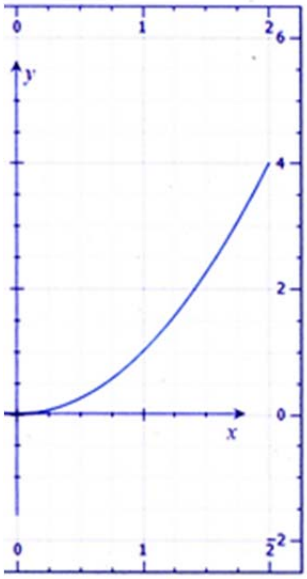

Fig. 4.1 Two-body reaction occurs without a critical density where the reaction rate y of independent particles is proportional to the square of the density x: $y = cx^2$ [Kozima 2013b]. Some of examples applicable to this relation are the combination of Na and Cl in an aqueous solution of NaCl and *d-d* fusion reactions in plasmas and in PdD_x lattice)

The second reason is that the detection of the protons with energies of about 3 MeV is not sufficient to conclude the occurrence of the *d-d* reactions (3.18) – (3.20) due to the existence of alternative candidates for them as discussed in Section 3. If we can observe a triton with 1.01 MeV, a proton with 3.02 MeV and a helium-3 with 0.82 MeV (and hopefully a neutron with 2.45 MeV) simultaneously in an experiment without artificial excitation, then it is possible to conclude that the *d-d* reactions (3.18) and (3.19) have occurred as fundamental reactions in the CFP. Even in this case, it is possible that these reactions occurred as a result of the breeding reactions with $\varepsilon \neq 0$ (cf. Sec. 3.1.2).

In the CF experiments, there are too many sources to produce charged particles with energies around 1 – 3 MeV as we have shown in Sections 3.2.1 and 3.2.2. Therefore, it is very difficult to determine unambiguously the reaction producing charged particles observed by an experiment.

In the case of neutron with an energy of 2.45 MeV, there are no alternative sources of neutron emission of this energy and we may be able conclude that the reaction (3.19) has occurred with little ambiguity.

It is somewhat strange to seek fanatically the *d-d* fusion reactions for explanation of the CFP in deuterium systems discarding the fact that there are a lot of examples of the

CFP in protium systems as we have often claimed (e.g. [Kozima 1998 (Chap. 7), 2006 (Sec. 2.2.1)]. In particular, Hioki et al. [Hioki 2013] have shown recently excess energy generation in PdH_x and PdD_x systems in the same apparatus interchanging hydrogen and deuterium successively. This is decisive evidence showing existence of another cause (or other causes) resulting in the excess energy generation than *d-d* fusion reactions if we are looking for a common cause of the CFP in both protium (H) and deuterium (D) systems.

Such episodes as the conclusion of *d-d* fusion reactions by Roussetski et al. deduced from insufficient data and as the long–lasted negligence of PdH_x systems by some researchers in the CFP remind us the Buddhist parable of ten blinds who touched an elephant cited in Appendix to this paper. At any time, it is necessary to avoid mistakes due to our narrow-mindedness and shortsightedness. Especially in scientific research, we would like to realize our standpoint clearly in the investigation of such complex phenomenon as the cold fusion one occurring in multi-component, non-equilibrium, open dynamical systems [Kozima 2013b].

The cold fusion phenomenon (CFP) including various events from excess energy generation to nuclear transmutation through particle emissions of neutron, proton, deuteron, triton and alpha is challenging us to give its scientific explanation that is too difficult for many scientists who gave up their trial to enjoy the effort to give consistent understanding of the complex events in the CFP.

We have tried to give a phenomenological explanation of the CFP using a model (TNCF model) with an adjustable parameter n_n which is determined by an experimental data of an observable and gives a consistent explanation of another observable when there are several observables measured simultaneously [Kozima 1998, 2006, 2008]. It seems that the TNCF model is fairly successful by now to give a unified understanding of various events in the CFP.

If a model is effective to give a unified understanding of a new phenomenon including various events, the CFP in our case for example, we might be able to consider that the model will be reflecting some truth hidden behind the phenomenon observed by experiments. It is therefore valuable to check the model a little further. The most serious assumptions of the TNCF model are 1) existence of the “trapped neutrons” and 2) nuclear reactions with emission of phonons in solids but not photons in free space.

The existence of the trapped neutrons in CF materials has been explained by possible formation of neutron bands mediated by occluded protons or deuterons in our works [Kozima 2004, 2006 (Sec. 3.5.2), Kozima 2009a].

The nuclear reactions with emission of phonons but not photons, on the other hand,

have been left untouched by now.

We can see the problem in the physics of the CFP from a different point of view, physics of neutrons in solids. There have been several fields of works related to this problem classified into four themes;

1. Neutron trap by stratified structures [Kozima 2004 (Sec. 1), Ebisawa 1998]
2. Neutron guide similar to the wave guide for electromagnetic waves [Kozima 1998 (Sec. 12.3), Abele 2006]
3. Neutron bands mediated by hydrogen isotopes and trapped neutrons in them
4. Nuclear reactions catalyzed by the trapped neutrons with emission of phonons but not photons

The third one has been discussed in our papers [Kozima 2006 (Sec. 3.5.2), Kozima 2009a].

The fourth one is related to the assumption made in Eqs. (3.1) and (3.2), for example, that the gammas emitted in free space by these reactions are replaced by phonons in CF materials. This assumption may have a close relation to the assumption of the drastic shortening of lifetimes made to explain such nuclear transmutations as from $^{40}_{19}$K to $^{40}_{20}$Ca, from $^{107}_{46}$Pd to $^{107}_{47}$Ag, etc. [Kozima 2006 (Sec. 2.5.1.1)]. It should be explained by the interaction of trapped neutrons in the neutron valence bands with exotic unstable nuclei and phonons but is not accomplished yet. From our point of view, this is the most important remaining problem in the solid-state nuclear physics related to the CFP.

5. Conclusion

There are many trials to elucidate fundamental mechanisms of nuclear reactions in the CFP in this research field since its discovery in 1989 by Fleischmann, Pons and Hawkins [Fleischmann 1989]. In these trials we have had a few cases in which the conclusions have been deduced from biased selection of experimental data ignoring characteristics of the CFP as a whole, especially its lack of quantitative reproducibility and variety of products not only in deuterium but also in hydrogen systems. This situation reminds us a famous parable told in Buddhist scriptures of the blind people who observed an elephant by hands [Tittha Sutta, Appendix]; Some said “The elephant is just like a water jar,” some said “The elephant is just like a winnowing basket,” some said “The elephant is just like an iron rod,” some said “The elephant is just like the pole of a plow,” and so forth depending on where they touched the elephant on.

The essential points of investigation of unknown phenomenon in common life and in science are the same. We have to collect as many facts as possible to give a consistent explanation for the whole facts and then look for a fundamental principle (or principles)

for the explanation that is applicable also to other phenomena. Even if the heap of bricks are not a building itself, we may be able to construct a building out of the bricks heaped up by laborious efforts of our pioneers.

Thus, the next work we have to do in this field should be excavation of physics of the cold fusion phenomenon (CFP) hidden behind the premises of the TNCF model that have been successful to give a unified and consistent qualitative and sometimes semi-quantitative explanation of the CFP.

The premises of the existence of trapped neutrons and the phonon emission in CF materials instead of photons in free space are based on the experimental facts. The former is based on the absence of the CFP without thermal neutrons [Kozima 1998 (Chapter 8), 2006 (Sec. 2.2.1.1 and Appendix D (Topic 8), 2010] and the latter is on the data of no photon emission corresponding to other nuclear products. The latter premise should be investigated consistently with the former of trapped neutrons with a density n_n and the first steps for it have been given using an idea of the super-nuclear interaction between lattice nuclei mediated by interstitial hydrogen isotopes [Kozima 2006, 2009a].

Acknowledgement

The author would like to express his sincere thanks to Prof. X.Z. Li of Tsinghua University, China and Prof. Hiroshi Yamada of Iwate University, Japan for the communications on the use of CR-39 detector. He is also grateful to Prof. Hidetomo Yamashita of Shizuoka University for the information about the English version of Tittha Sutta cited in Appendix on the end of this paper.

References

[Abele 2006] H. Abele, D. Dubbers, H. Haese, et al., “Characterization of a Ballistic Supermirror Neutron Guide,” *Nucl. Instr. Methods in Phys. Res.,* A 562-1, 407 – 417 (2006).

[Aizawa 2012] H. Aizawa, K. Mita, D. Mizukami, H. Uno and H. Yamada, “Detecting Energetic Charged Particle in D_2O and H_2O Electrolysis Using a Simple Arrangement of Cathode and CR-39,” *Preprint of the ICCF-17 Proceedings*, P-1050.

[Beddingfield 1991] D.H. Beddingfield, F.E. Cecil, C.S. Galovich, H. Liu and S. Asher, “Characterization of Charged Particle Bursts from Deuterium Loaded Thin Titanium Foils,” *Proc. ICCF2*, pp. 99 – 103 (1991). F.E. Cecil, H. Liu, D. Beddingfield and C.S. Galovich, *Proc. Conf. on Anomalous Nuclear Effects in Deuterium/Solid Systems, AIP Conf. Proc.* #228, pp. 375 – 381 (1991).

[Bush, R.T. 1992] R. T. Bush, "A Light Water Excess Heat Reaction suggests that 'Cold

Fusion' may be 'Alkali-Hydrogen Fusion'," *Fusion Technol.* **22**, 301 (1992).
[Bush, R.T. 1993] R. T. Bush and D. R. Eagleton, "Calorimetric Studies for Several Light Water Electrolyte Cells with Nickel Fibrex Cathodes and Electrolytes with Alkali Salts of Potassium, Rubidium and Cesium," *Proc. ICCF4* (Dec. 6 - 9, 1993, Hawaii, USA) **Vol. 2**, p. 13 (1993), EPRI TR-104188.
[De Ninno 1989] A. De Ninno, A. Frattolillo, G. Lollobattista, G. Martinio, M. Martone, M. Mori, S. Podda and F. Scaramuzzi, "Evidence of Emission of Neutrons from a Titanium-Deuterium System," *Europhys. Lett.* **9**, 221 – 224 (1989).
[Ebisawa 1998] T. Ebisawa, D. Yamazaki, S. Tasaki et al. "Quantum Beat Experiments using a Cold Neutron Spin Interferometer," *J. Phys. Soc. Japan* 67, 1569 – 1573 (1998).
[Fleischmann 1989] M. Fleischmann, S. Pons and M. Hawkins, "Electrochemically induced Nuclear Fusion of Deuterium," *J. Electroanal. Chem*., 261, 301 – 308 (1989).
[Hioki 2013] T. Hioki, N. Sugimoto, T. Nishi, A. Itoh and T. Motohiro, "Influence of Pd Particle Size on Isotope Effect for Heat Generation upon Pressurization with Hydrogen Isotope Gases," *Proc. JCF13* (to be published in 2013) and *Abstract of JCF13*, **13-17** (2012). http://jcfrs.org/file/jcf13-proceedings.pdf
[Iida 1993] T. Iida, M. Fukuhara, H. Miyazaki et al., "Deuteron Fusion Experiment with Ti and Pd Foils Implanted with Deuteron Beams," *Proc. ICCF3*, pp. 201 – 207 (1993). ISBN 4-946443-12-6
[Jiang 2011] S. Jiang, J. Li, M. He, S. Wu, J. Jang, H. Zhang, S. Yao, Y. Zhao and C. Wang, "New Results of Charged Particles Released from Deuterium-Loaded Metals at Low Temperature," *Proc. ICCF14* (Washington D.C., USA, August 10 – 15, 2008), pp. 299 – 309 (2011). ISBN 978-0-578-06694-3.
[Karabut 1995] A.B. Karabut, S.A. Kolomeychenko and I.B. Savvatimova, "High Energy Phenomena in Glow Discharge Experiments," *Proc. ICCF5*, pp. 241 – 250 (1995).
[Kasagi 1993] J. Kasagi, K. Ishii, M. Hiraga and K. Yoshihara, "Observation of High Energy Protons Emitted in the TiD_x + D Reaction at E_d = 150 keV and Anomalous Concentration of ^{3}He," *Proc. ICCF3*, pp. 209 – 215 (1993). ISBN 4-946443-12-6
[Keeney 2006] F.W. Keeney, S.E. Jones, A.C. Johnson et al., "Charge-Particle Emissions from Deuterided Metals," *Proc. ICCF 10*, pp. 509 – 523 (2006). ISBN 981-256-564-7.
[Kodaira 2007] [Kodaira 2007] S. Kodaira, N. Yasuda, N. Hasebe et al., "Improvement of Mass Resolution for Iron Isotopes in CR-39 Track Detector," *Jpn. J. Appl. Physics*, 46, pp. 5281 – 5287 (2007).
[Kozima 1994] H. Kozima, "Trapped Neutron Catalyzed Fusion of Deuterons and

Protons in Inhomogeneous Solids," *Trans. Fusion Technol.* **26-4T**, pp. 508 – 515 (1994). ISSN: 0748-1896.

[Kozima 1998] H. Kozima, *Discovery of the Cold Fusion Phenomenon*, Ohtake Shuppan, Tokyo, Japan, 1998. ISBN 4-87186-044-2.

[Kozima 2004] H. Kozima, "Quantum Physics of Cold Fusion Phenomenon," in *Developments in Quantum Physics* (pp. 167 – 196), Eds. F. Columbus and V. Krasnoholovets, Nova Science Pub. Inc., New York (2004). ISBN 1-59454-003-9.

[Kozima 2006] H. Kozima, *The Science of the Cold Fusion Phenomenon*, Elsevier, Amsterdam, 2006. ISBN-10: 0-080-45110-1.

[Kozima 2008] H. Kozima, "Physics of the Cold Fusion Phenomenon," *Proc. ICCF13,* pp. 690 – 703 (2008). ISBN 978-5-93271-428-7. And also *Reports of CFRL* (*Cold Fusion Research Laboratory*) **11-4**, pp. 1 – 21 (2008).
http://www.geocities.jp/hjrfq930/Papers/paperr/paperr.html

[Kozima 2009a] H. Kozima, "Non-localized Proton/Deuteron Wavefunctions and Neutron Bands in Transition-metal Hydrides/Deuterides," *Proc. JCF9* (March 28 – 29, 2009, Shizuoka, Japan), pp. 84 – 93 (2009). http://jcfrs.org/file/jcf9-proceedings.pdf
And also *Reports of CFRL* (*Cold Fusion Research Laboratory*), **9-3**, pp. 1 – 10 (October, 2009). http://www.geocities.jp/hjrfq930/Papers/paperr/paperr.html

[Kozima 2009b] H. Kozima, "Characterization of Distinctive Materials with which to Generate Nuclear Transmutation" *Report of CFRL* (*Cold Fusion Research Laboratory*) **9–1**, 1 – 12 (January, 2009). http://www.geocities.jp/hjrfq930/Papers/paperr/paperr.html

[Kozima 2010] H. Kozima, "Neutron Emission in the Cold Fusion Phenomenon," *Proc. JCF11*, pp. 76 – 82 (2010). http://jcfrs.org/file/jcf11-proceedings.pdf
And also *Reports of CFRL* (*Cold Fusion Research Laboratory*), **11-3**, pp. 1 – 12 (2011).
http://www.geocities.jp/hjrfq930/Papers/paperr/paperr.html

[Kozima 2011a] H. Kozima, "Localization of Nuclear Reactions in the Cold Fusion Phenomenon," *Proc. JCF11*, pp. 59 – 68 (2010).
http://jcfrs.org/file/jcf11-proceedings.pdf
And also *Reports of CFRL* (*Cold Fusion Research Laboratory*) **11–2**, 1 – 19 (January, 2011). http://www.geocities.jp/hjrfq930/Papers/paperr/paperr.html

[Kozima 2011b] H. Kozima and F. Celani, "Brief Explanation of Experimental Data Set on Excess Heat and Nuclear Transmutation in Multiplly Nanocoated Ni Wire," *Proc. JCF11* pp. 53 - 58 (2011). http://jcfrs.org/file/jcf11-proceedings.pdf
And also *Reports of CFRL* (*Cold Fusion Research Laboratory*) **11–1**, 1 – 8 (January, 2011). http://www.geocities.jp/hjrfq930/Papers/paperr/paperr.html

[Kozima 2012] H. Kozima, "Three Laws in the Cold Fusion Phenomenon and Their

Physical Meaning," *Proc. JCF12* (Kobe, Japan, December 17 –18, 2011), pp. 101 - 114 (2012). http://jcfrs.org/file/jcf12-proceedings.pdf
And also *Reports of CFRL* (*Cold Fusion Research Laboratory*) **11–6**, 1 – 14 (April, 2011). http://www.geocities.jp/hjrfq930/Papers/paperr/paperr.html
[Kozima 2013a] H. Kozima, "Characteristics of Solid-State Nuclear Track Detectors for Heavy Charged Particles – A Review," *Proc. JCF13* (to be published)
http://jcfrs.org/file/jcf13-proceedings.pdf
And also *Reports of CFRL* (*Cold Fusion Research Laboratory*), **13-1**, 1 – 18 (March 2013). http://www.geocities.jp/hjrfq930/Papers/paperr/paperr.html
[Kozima 2013b] H. Kozima, "Cold Fusion Phenomenon in Open, Nonequilibrium, Multi-component Systems – Self-organization of Optimum Structure," *Proc. JCF13* (to be published). http://jcfrs.org/file/jcf13-proceedings.pdf
And also *Reports of CFRL* (*Cold Fusion Research Laboratory*), **13-3**, 1 – 24 (March 2013). http://www.geocities.jp/hjrfq930/Papers/paperr/paperr.html
[Li 1991] X.Z. Li, "Chinese Effort in Understanding the 'Cold Fusion' Phenomena," *Proc. ICCF2*, pp. 309 – 317 (1991).
[Li 2012] X.Z. Li (private communication to the author on June 9, 2012).
[Lipson 2006] A.G. Lipson, G.H. Miley, B.F. Lyakhov and A.S. Roussetski, "Energetic Charged Particle Emission from Hydrogen-loaded Pd and Ti Cathodes and its Enhancement by He-4 Implantation," *Proc. ICCF11*, pp. 324 – 338 (2006). ISBN 981-256-640-6.
[Mo 1991] D.W. Mo, Y.S. Liu, L.Y. Zhou et al., "Search for Precursor and Charged Particles in 'Cold Fusion' " *Proc. ICCF2*, pp. 123 – 127 (1991).
[Morrey 1990] J.R. Morrey, M.R. Caffee, H. Farrar, IV, N.J. Hoffman, G.B. Hudson, R.H. Jones, M.D. Kurz, J. Lupton, B.M. Oliver, B.V. Ruiz, J.F. Wacker and A. Van, "Measurements of Helium in Electrolyzed Palladium," *Fusion Technol*. **18**, 659 (1990).
[Mosier-Boss 2008] P.A. Mosier-Boss, S. Szpak, F.E. Gordon, and L.P.G. Forsley, **"**Triple Tracks in CR-39 as the Result of Pd/D Co-deposition: Evidence of Energetic Neutrons," *Naturwissenschaften*, pp. 135 –142 (2008).
[Mosier-Boss 2009] P.A. Mosier-Boss, S. Szpak, F.E. Gordon, and L.P.G. Forsley, "Characterization of Tracks in CR-39 Detectors obtained as a Result of Pd/D Co-deposition," *Eur. Phys. J. Appl. Phys*. **46**, 30901-1 – 12 (2009).
[Notoya 1996] R. Notoya, T. Ohnishi and Y. Noya, "Nuclear Reaction Caused by Electrolysis in Light and Heavy Water Solution" *Proc. ICCF6*, 675 – 679 (1996).
[Okamoto 1993] M. Okamoto, H. Ogawa, Y. Yoshinaga, T. Kusunoki and O. Odawara, "Behavior of Key Elements in Pd for the Solid State Nuclear Phenomena Occurred in

Heavy Water Electrolysis," *Proc. ICCF4*, 3-14 (1993).
[Oriani 2006a] R.A. Oriani and J.C. Fisher, "Energetic Charged Particles produced in the Gas Phase by Electrolysis," *Proc. ICCF10*, pp. 567 – 575 (2006). ISBN 981-256-564-7
[Oriani 2006b] R.A. Oriani and J.C. Fisher, "Detection of Energetic Charged Particles during Electrolysis," *Proc. ICCF10*, pp. 577 – 584 (2006).
[Passell 2003] T.O. Passell, "Evidence for Lithium-6 depletion in Pd Exposed to Gaseous Deuterium and Hydrogen," *Proc. ICCF9*, pp. 299 – 304 (2003). ISBN 7-302-06489-X.
[Roussetski 1998] A.S. Roussetski, "Observation of (DD) Fusion Reaction Products in Electrolytically Deuterized PdO/Pd Structures," *Proc. ICCF7*, pp. 466 – 477 (1998).
[Roussetski 2006a] A.S. Roussetski, "CR-39 Track Detectors in Cold Fusion Experiments: Review and Perspectives," *Proc. ICCF11*, pp. 274 – 294 (2006). ISBN 981-256-640-6.
[Roussetski 2006b] A.S. Roussetski, A.G. Lipson, B.F. Lyakhov and E.I. Saunin, "Correct Identification of Energetic Alpha and Proton Tracks in Experiments on CR-39 Charged Particle Detection during Hydrogen Desorption from Pd/PdO:H_x Heterostructure," *Proc. ICCF12*, (Yokohama, Japan, November 27 – December 2, 2005) pp. 304 – 313 (2006). ISBN 981-256-901-4
[Shangxian 1991] J. Shangxian, Z. Fuxiang, Y. Decheng and W. Bailu, "Anomalous Nuclear Effects in Deuterium Palladium Systems," *Proc. ICCF2*, pp. 145 – 149 (1991).
[Shani 1989] G. Shani, G., C. Cohen, A. Grayevsky and S. Brokman, "Evidence for a Background Neutron Enhanced Fusion in Deuterium Absorbed Palladium," *Solid State Comm*. **72**, 53 (1989).
[Somogyi 1973] G. Somogyi and S.A. Szalay, "Track-Diameter Kinetics in Dielectric Track Detectors," *Nucl. Instr. Meth.*, 109, 211 – 232 (1973).
[Storms 2008] E. Storms and B. Scanlon, "Detection of Radiation emitted from LENR," *Proc. ICCF14* (Washington D.C., USA, August 10 – 15, 2008), pp. 263 – 287 (2011). ISBN 978-0-578-06694-3.
[Storms 2011] E. Storms and B. Scanlon, "Detection of Radiation emitted from LENR," *Proc. ICCF14* (Washington D.C., USA, August 10 – 15, 2008), pp. 263 – 287 (2011). ISBN 978-0-578-06694-3.
[Taniguchi 1993] R. Taniguchi and T. Yamamoto, "Fine Structure of the Charged particle Bursts induced by D_2O Electrolysis," *Proc. ICCF3*, pp. 519 – 523 (1993). ISBN 4-946443-12-6
[Taniguchi 1994] R. Taniguchi, "Characteristic Peak Structures on Charged particle

Spectra during Electrolysis Experiment," *Trans. Fusion Technol.* **26**, No. 4T (*Proc. ICCF4*) pp. 186 – 191 (1994)
[Wang K.L. 1991] K.L. Wang, X.Z. Li, S.Y. Dong et al., "Search for Better Materials for Cold Fusion Experiment using CR-39 Detector," *Proc. ICCF2*, pp. 163 – 168 (1991).
[Wang S.C. 1991] S.C. Wang, T.S. Kang, K.L. Wang et al., "Identification of the Energetic Charged Particles in Gas-Loading Experiment of 'Cold Fusion' Phenomena," *Proc. ICCF2*, pp. 169 – 173 (1991).
[Yamaguchi 1993] E. Yamaguchi and T. Nishioka, "Direct Evidence for Nuclear Fusion Reactions in Deuterated Palladium," *Proc. ICCF3*, pp. 179 – 188 (1993). ISBN 4-946443-12-6
[Yamauchi 2005] T. Yamauchi, R. Barillon, E. Balanzat, T. Asuka, K. Izumi, T. Masutani, and K. Oda, "Yields of CO_2 Formation and Scissions at Ether Bonds along Nuclear Tracks in CR-39," *Radiat. Meas.* 40, 224 – 228 (2005).

Appendix, "Tittha Sutta: Various Sectarians (1)" (Ud6.4)

I have heard that on one occasion the Blessed One was staying near Savatthi, in Jeta's Grove, Anathapindika's monastery. Now at that time there were many brahmans, contemplatives, and wanderers of various sects living around Savatthi with differing views, differing opinions, differing beliefs, dependent for support on their differing views. Some of the brahmans and contemplatives held this view, this doctrine: "The cosmos is eternal. Only this is true; anything otherwise is worthless."

Some of the brahmans and contemplatives held this view, this doctrine: "The cosmos is not eternal"... "The cosmos is finite"... "The cosmos is infinite"... "The soul and the body are the same"... "The soul is one thing and the body another"... "After death a Tathagata exists"... "After death a Tathagata does not exist"... "After death a Tathagata both does and does not exist"... "After death a Tathagata neither does nor does not exist. Only this is true; anything otherwise is worthless."

And they lived arguing, quarreling, and disputing, wounding one another with weapons of the mouth, saying, "The Dhamma is like this, it's not like that. The Dhamma's not like that, it's like this."

Then in the early morning, a large number of monks, having put on their robes and carrying their bowls and outer robes, went into Savatthi for alms. Having gone for alms in Savatthi, after the meal, returning from their alms round, they went to the Blessed One and, on arrival, having bowed down to him, sat to one side. As they were sitting there, they said to the Blessed One: "Lord, there are many brahmans, contemplatives, and wanderers of various sects living around Savatthi with differing views, differing

opinions, differing beliefs, dependent for support on their differing views... and they live arguing, quarreling, and disputing, wounding one another with weapons of the mouth, saying, 'The Dhamma is like this, it's not like that. The Dhamma's not like that, it's like this.'"

"Monks, the wanderers of other sects are blind and eyeless. They don't know what is beneficial and what is harmful. They don't know what is the Dhamma and what is non-Dhamma. Not knowing what is beneficial and what is harmful, not knowing what is Dhamma and what is non-Dhamma, they live arguing, quarreling, and disputing, wounding one another with weapons of the mouth, saying, 'The Dhamma is like this, it's not like that. The Dhamma's not like that, it's like this.'

"Once, in this same Savatthi, there was a certain king who said to a certain man, 'Gather together all the people in Savatthi who have been blind from birth.'"

"'As you say, your majesty,' the man replied and, rounding up all the people in Savatthi who had been blind from birth, he went to the king and on arrival said, 'Your majesty, the people in Savatthi who have been blind from birth have been gathered together.'

"'Very well then, show the blind people an elephant.'

"'As you say, your majesty,' the man replied and he showed the blind people an elephant. To some of the blind people he showed the head of the elephant, saying, 'This, blind people, is what an elephant is like.' To some of them he showed an ear of the elephant, saying, 'This, blind people, is what an elephant is like.' To some of them he showed a tusk... the trunk... the body... a foot... the hindquarters... the tail... the tuft at the end of the tail, saying, 'This, blind people, is what an elephant is like.'

"Then, having shown the blind people the elephant, the man went to the king and on arrival said, 'Your majesty, the blind people have seen the elephant. May your majesty do what you think it is now time to do.'

"Then the king went to the blind people and on arrival asked them, 'Blind people, have you seen the elephant?'

"'Yes, your majesty. We have seen the elephant.'

"'Now tell me, blind people, what the elephant is like.'

"The blind people who had been shown the head of the elephant replied, 'The elephant, your majesty, is just like a water jar.'

"Those who had been shown the ear of the elephant replied, 'The elephant, your majesty, is just like a winnowing basket.'

"Those who had been shown the tusk of the elephant replied, 'The elephant, your majesty, is just like an iron rod.'

"Those who had been shown the trunk of the elephant replied, 'The elephant, your

majesty, is just like the pole of a plow.'
"Those who had been shown the body of the elephant replied, 'The elephant, your majesty, is just like a granary.'
"Those who had been shown the foot of the elephant replied, 'The elephant, your majesty, is just like a post.'
"Those who had been shown the hindquarters of the elephant replied, 'The elephant, your majesty, is just like a mortar.'
"Those who had been shown the tail of the elephant replied, 'The elephant, your majesty, is just like a pestle.'
"Those who had been shown the tuft at the end of the tail of the elephant replied, 'The elephant, your majesty, is just like a broom.'
"Saying, 'The elephant is like this, it's not like that. The elephant's not like that, it's like this,' they struck one another with their fists. That gratified the king.
"In the same way, monks, the wanderers of other sects are blind and eyeless. They don't know what is beneficial and what is harmful. They don't know what is the Dhamma and what is non-Dhamma. Not knowing what is beneficial and what is harmful, not knowing what is Dhamma and what is non-Dhamma, they live arguing, quarreling, and disputing, wounding one another with weapons of the mouth, saying, 'The Dhamma is like this, it's not like that. The Dhamma's not like that, it's like this.'"
Then, on realizing the significance of that, the Blessed One on that occasion exclaimed:
Some of these so-called brahmans & contemplatives are attached. They quarrel & fight
— people seeing one side.

"Tittha Sutta: Various Sectarians (1)" (Ud 6.4), translated from the Pali by Thanissaro Bhikkhu. *Access to Insight*, 12 February 2012,
http://www.accesstoinsight.org/tipitaka/kn/ud/ud.6.04.than.html .
Retrieved on 5 July 2012.

Computer Simulation of Hydrogen States near T site in Pd Metal

Hidemi Miura
Izumi-ku, Sendai. Japan

Abstract: We simulated the hydrogen (H) states in palladium (Pd) metal using a quantum molecular dynamics on a personal computer. We calculated the total energy, charge density and electronic structure of Pd bulk metal by a computer simulation program within Density Functional Theory based on the local density approximation using pseudo-potentials and a plane-wave basis. Calculations were done about four H atoms near a T site of Pd metal filled with H atoms in all O sites deforming the tetrahedron surrounding the T site. The periodic boundary conditions were imposed on the calculating 2x2x2 super cell of 28 Pd atoms and four vacancies next to some O sites. When an impurity atom of lithium (Li) or calcium (Ca) enters into the T site of Pd metal lattice, it seemed to be improved in the deformation range of atomic vibration at room temperature that four H/D atoms (applying the results to deuterium (D) atoms) are drawn toward the T site to cause condensations and nuclear fusion and/or nuclear transmutation.

Keywords: computer simulation, quantum molecular dynamics, tetrahedron, Pd, H states

1. Introduction

Nuclear fusion and nuclear transmutation phenomena have been reported in many experiments of deuterium (D) and hydrogen (H) with condensed matter. In order to examine what kind of conditions cause two and more H/D atoms to gather in condensed matter such as metals and to squeeze into condensations and these nuclear reactions, we have simulated the hydrogen states in palladium (Pd) metal of face centered cubic lattice using a quantum molecular dynamics on a personal computer.

We carried out simulations of four H atoms surrounding a tetrahedron in the 2x2x2 super cell of Pd atoms filled with occluded H atoms in all O sites, following the last simulation of those surrounding an octahedron without occluded H atoms [1)]. Four of 32 occluded H atoms near the T site were located outside, on or inside the triangular lattices of the tetrahedron composed of four Pd atoms deforming the tetrahedron. Imposing the periodic boundary conditions on the super cell, we calculated the total energy, charge density and electronic structure of Pd bulk metal at temperature 0 K by a computer simulation program within Density Functional Theory based on the local density approximation.

We investigated the energy differences between the total energy with an impurity atom of H or alkali/alkaline-earth metal such as Li, Na, K, Mg, Ca which entered into the T site of Pd metal lattice and the total energy without it. We observed the impurity Li or Ca atom could move from O sites to T sites under the small lattice deformation such as atomic vibration at room temperature, and the Li atom could hop out from the T

site pushed by weak force and the Ca atom could hop out by strong force. It seemed that the Li atom could draw four H/D atoms (applying the results to D atoms) surrounding the tetrahedron and leave them to cause mostly nuclear transmutation/fusion, and the Ca atom could draw four D atoms and leave them to cause mostly nuclear transmutation.

2. Calculations

We made the quantum electronic state calculations under the lattice deformation changing the interatomic distances of the tetrahedron composed of four Pd atoms around a T site near the center of 2x2x2 super cell. And we obtained the total energy, charge density and electronic structure of the simulation system of 28 Pd atoms with four vacancies and occluded 32 H atoms in all O sites at temperature 0 K, that is, we took no motion of the atoms in the simulation system into account.

(1) Hardware and Software Used for Calculation

We used a personal computer which had 4 core / 8 way CPU and 16 GB main memory. And we used the first principles electronic state simulation program ABINIT which was using plane waves for the basis function and norm preservation type pseudo-potentials[2, 3], and we used VESTA for visualization of the charge density of calculation results[4].

(2) Restrictions of the Arrangement of Pd Atoms and Four H Atoms

We applied the following restrictions for the arrangement of Pd atoms and four H atoms because of computational complexity and calculation time.

① Four vacancies are located at four of 32 Pd atoms, which are on the four edges of the large tetrahedron circumscribed around the concerned small regular tetrahedron in the 2x2x2 super cell.

② The locations of Pd atoms outside the concerned small tetrahedron are not altered even when the interatomic distances of the tetrahedron are changed.

(3) Locations of Four of 32 H Atoms

Under the restriction mentioned above, the quantum electronic state calculations of total energy, charge density and electronic structure were made for the bulk Pd metal system in the following four cases of locations of the four of 32 H atoms outside, on or inside the deforming tetrahedron. And each calculation was done when the impurity atom of H or alkali/alkaline-earth metal entered or not entered into the T site in the tetrahedron.

① Keeping tetrahedral symmetry, the four H atoms are located at the four centers of octahedrons (original O sites) adjacent to the tetrahedron respectively.

② The four H atoms are located at four halfway points (O(1/2) points) between the O

sites mentioned above ① and four P points mentioned below ③ respectively.

③ The four H atoms are located at the four centers of triangular lattices (P points) which compose the boundary planes between the four octahedrons mentioned above ① and the tetrahedron respectively.

④ The four H atoms are located at four quarter distance points (T(1/4) points) between the P points mentioned above ③ and the T site respectively.

(4) Relation between T sites, P points, O(1/2) points, O sites and Pd Atoms

The P points, O(1/2) points and O sites where the four H atoms located were geometrically related to the T site in the tetrahedron, the Pd atoms which composed it and the octahedrons which adjacent to it as Fig. 1 shows. When the lattice constant was supposed to be 1 and the coordinates of two Pd atoms on the diagonal of the unit lattice were supposed to be described as (0, 0, 0) and (1, 1, 1) respectively, the coordinates of the representative T site, P point, O(1/2) point and O site were described as (1/4, 1/4, 1/4), (1/3, 1/3, 1/3), (5/12, 5/12, 5/12) and (1/2, 1/2, 1/2) respectively, and the ratio of distances to each position from coordinates (0, 0, 0) was 3 : 4 : 5 : 6.

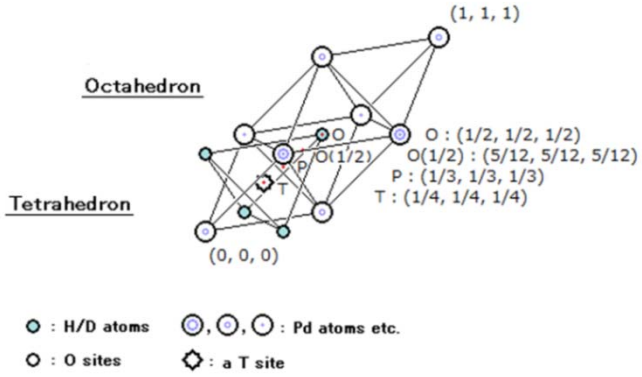

Figure 1 Relation between the T site, T(1/4) point, P point, O(1/2) point, O site and Pd atoms. (The lattice constant is supposed to be 1.)

The four T(1/4) points mentioned above (3) - ④ are significant for this H(D) condensation because the distance of two H atoms next to each other in our simulation system is close to the nuclear distance of H molecule (74pm), and because the edge length of the cube which is circumscribed around the tetrahedron of four H atoms in our simulation system is close to the critical length of Takahashi's TSC (Tetrahedral Symmetric Condensation) Theory which supports H/D-cluster condensation to cause nuclear reactions in condensed matter[5,6].

(5) Deformation of the Tetrahedron

The deformation of the tetrahedron ⊿d/a was defined as the ratio of the edge

length change of the unit cell (⊿d) to the lattice constant (a), and varied from -0.1 to 0.1 in 11 steps changing the interatomic distances of the tetrahedron. Fig. 2 shows the charge density distribution when an impurity Ca atom at the T site (yellowish green surface at lower left front corner) of 2x2x2 super cell of 28 Pd atoms with the four vacancies and H atoms occlude in all O sites at the deformation ⊿d/a = 0.00.

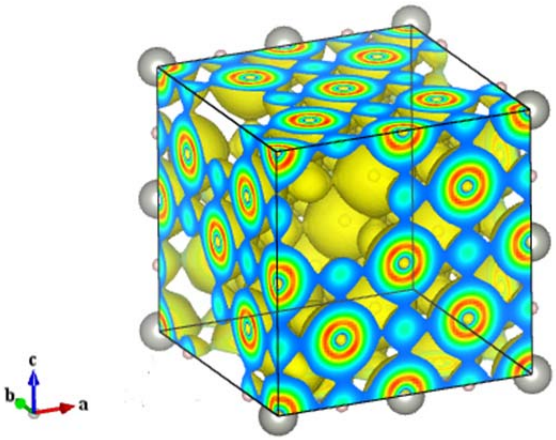

Figure 2 Charge density distribution in Pd lattice of 2x2x2 super cell.
(Red indicates high electron density and blue indicates low.)

3. Results and Discussion

(1) Binding Energy of Four H Atoms around the T site

We calculated the total energy of 28 Pd bulk metal with the four Vacancies, 32 occluded H atoms in the O sites, deforming the tetrahedron when the four of 32 occluded H atoms were located at the original O sites, O(1/2) points, P pointes, T(2/8(=1/4)) points and T(4/8(=1/2)) points around the T site. Where T(4/8) or T(1/2) denotes the halfway between the T site and P point. Fig. 3 shows the energy differences between the total energy with the four H atoms around the T site and the total energy without them respectively by solid lines. Also it shows those with/without the four H atoms around the O site by broken lines which are the last simulation results [1)]. These energy differences due to the four H atoms around the T/O site would mean the binding energy of them, because we carried out the simulations at temperature 0 K, that is, we took no motion or kinetic energy of atoms into account.

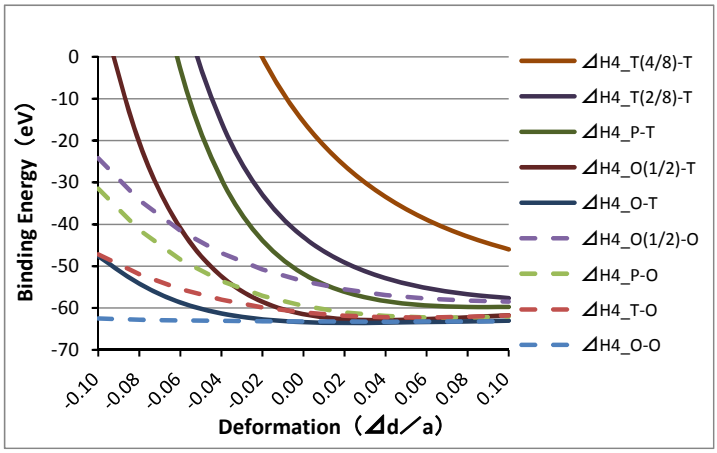

Figure 3 Binding energy of the four H atoms on the original O sites, O(1/2) points, P points, T(1/4) points and T(1/2) points around the T site and the O site.

The state in which all occluded H atoms are at O sites under no contraction or expansion of the tetrahedron/octahedron can be regarded as the basis. The binding energy of the four H atoms located at the four original O sites, O(1/2) points, P pointes, T(1/4) points and T(1/2) points are larger in the order of their increasing Coulomb repulsive forces. The graphs show that the four H atoms around the T site would need about 10 eV to transfer from the original O sites (dark blue solid line) to the P points (dark green solid line) at the deformation ⊿d/a = 0.00. And the four H atoms around the O site would need about 3 eV to transfer from the original O sites (light blue broken line) to the P points (light green broken line). Since it must be difficult for mere atomic vibration at room temperature to add thus large energy to the four H atoms simultaneously, some kind of proper mechanism would be necessary to make it.

(2) Total Energy of Pd Metal Lattice with Impurity Atom at the T/O Site

Next, we calculated the total energy of the Pd bulk metal lattice with the same simulation system as mentioned above, placing an impurity atom of H, Li, Na, K, Mg or Ca on the T site. Fig. 4 shows the total energy with the impurity atom of Ca of the T site by marked solid lines as an example, comparing the total energy without the impurity atom by solid lines, when the four of 32 occluded H atoms are located at the original O sites, O(1/2) points, P pointes and T(1/4) points outside, on or inside the tetrahedron respectively.

Although the total energy of the four H atoms located at the four original O sites, O(1/2) points, P pointes, T(1/4) points and T(1/2) points with the impurity Ca atom of the T site are larger in the order of their increasing Coulomb repulsive forces as mentioned above (1), the total energy with the impurity Ca atom change more rapidly

than those without it and cross them.

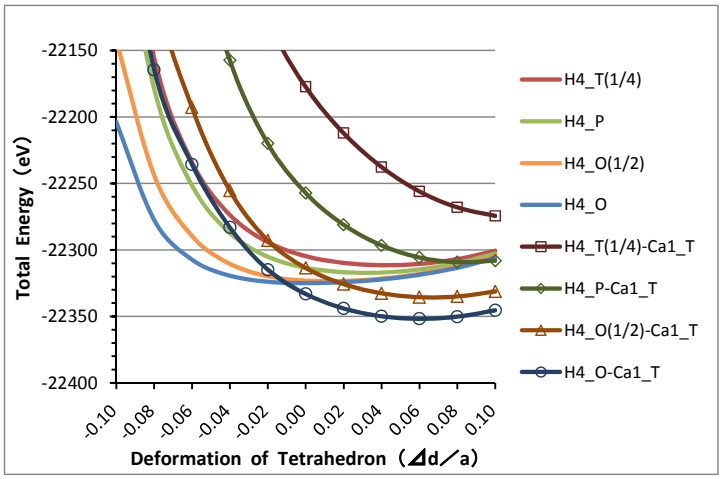

Figure 4 Total energy of 28 Pd bulk metal lattice with the impurity Ca atom in the T site, with the four vacancies, 32 occluded H atoms in the O sites and the four H atoms located at the original O sites, O(1/2) points, P pointes and T(1/4) points.

Since the lattice deformation of atomic vibration at room temperature is about 0.1 Å (|⊿d/a| ～ 0.02), the total energy when the four H atoms are located at the four original O sites with the impurity Ca atom of the T site crosses the total energy without it at the deformation ⊿d/a ～ -0.01 within the deformation range of the atomic vibration. It would mean that when the tetrahedron expands in the atomic vibration the impurity Ca atom could enter into the T site at the deformation ⊿d/a > -0.01, and when the tetrahedron contracts the impurity Ca atom could hop out from it at the deformation ⊿d/a < -0.01.

(3) Effects of Impurity Atom on Total Energy

It would be thought that impurity atoms in the bulk metal lattice move from vacancies to other ones shaken by atomic vibrations or other impulses passing through O sites and T sites in a while.

Then, we considered how the impurity atom entered into the T site and hopped out from it. Fig. 5 shows the energy differences between the total energy with an impurity atom of H, Li, Na, K, Mg or Ca of the T site or the O site and the total energy without it, which are the effects of impurity atom on the total energy, when the four H atoms are located at the original O sites in the in-phase contraction or expansion of the tetrahedron by solid lines and the energy differences of the octahedron by broken lines. Fig. 6 shows the same energy differences in the opposite-phase contraction or expansion of the tetrahedron and the octahedron similarly.

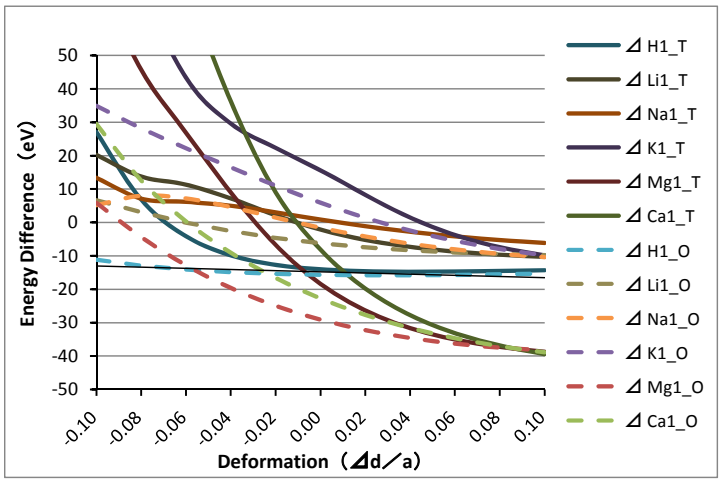

Figure 5 Energy differences between the total energy with the impurity atom and those without it in the in-phase contraction or expansion of the tetrahedron and the octahedron.

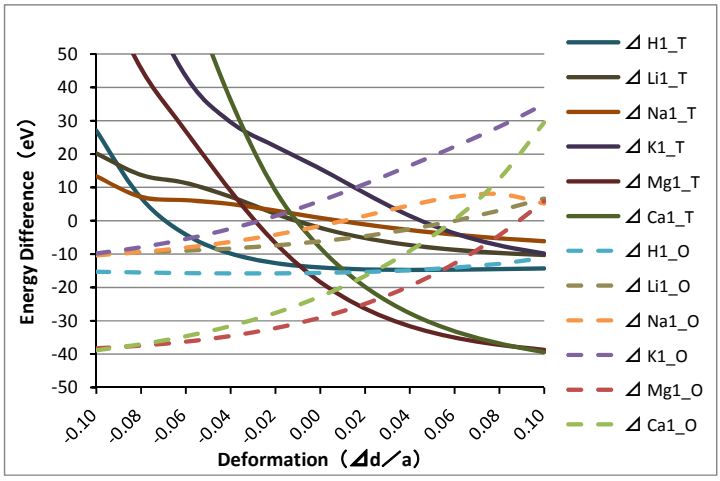

Figure 6 Energy differences between the total energy with the impurity atom and those without it in the opposite-phase contraction or expansion of the tetrahedron and the octahedron.

When the tetrahedron and the octahedron next to each other contract or expand in the in-phase mode (Fig. 5) that is the extreme long wave length vibration, the energy differences of the tetrahedron with each impurity atom do not go under those of the octahedron in the deformation range of atomic vibration at room temperature ($|\Delta d/a| < \sim 0.02$). It seems to be impossible for the impurity atom to move from the O site to the T site by the atomic vibration. In contrast, when the tetrahedron and octahedron next to each other contract and expand in the anti-phase mode (Fig. 6) that is the extreme short wave length vibration, the energy differences of the tetrahedron with each impurity atom go under those of the octahedron in the deformation range of the atomic vibration. It seems to be possible for the impurity atom to move from the O site to the T site by the atomic vibration.

Since the energy difference with the impurity Na or K atom of the T site or the O

site is positive in the deformation range of atomic vibration at room temperature (|⊿d/a| < ～ 0.02), it could not stay on the T site or the O site until the total energy would lowered by some way like electrolytic voltage. However, since the energy difference with the other impurity H, Li, Mg or Ca atom of the T site or the O site is negative in most of the deformation range of the atomic vibration, it could stay on the T site or the O site. At that time, since the energy difference of the expanding tetrahedron goes under the energy difference of the contracting octahedron in the deformation range of the atomic vibration, the impurity atom could move from the O site to the T site.

Especially since the energy difference of the contracting tetrahedron with the impurity Li atom becomes positive slowly at the deformation ⊿d/a < -0.01, it could hop out from the T site and even from the O site pushed by weak force. And since the energy difference with the Ca atom becomes positive rapidly at nearly the same deformation region, it could hop out from the T site and even from the O site pushed by strong force. But since those with the H and Mg atom become positive only at the deformation ⊿d/a < -0.07 and ⊿d/a < -0.03 respectively, the H and Mg atom would be difficult to hop out from the T site by the deformation of mere atomic vibration at room temperature.

(4) Binding Energy of Four H Atoms around the T site with Impurity Atom

We also calculated the binding energy with an impurity H, Li, Na, K, Mg or Ca atom of the T site when the four H atoms are located at the original O sites, which are the energy differences between the two kind of total energy estimated similarly with Fig. 3 of (1). Fig. 7 shows this binding energy by broken lines. And it shows also the same binding energy of the four H atoms around the T site by solid lines as Fig. 3.

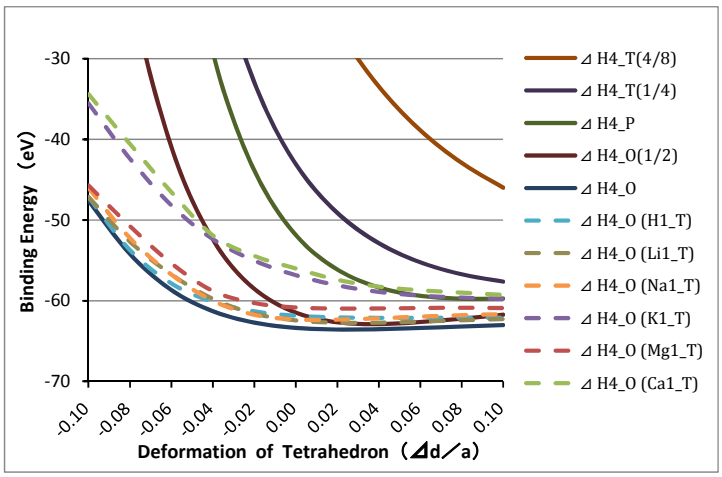

Figure 7 Binding energy of the four H atoms on the original O sites with an impurity atom.

The difference between the binding energy with the impurity K or Ca atom of the T site (light violet or light green broken line) and the binding energy without it (dark blue solid line) when the four H atoms are located at the original O sites is even about 8 eV at the deformation ⊿d/a = 0.00, which is close to the binding energy without it when the four H atoms are located at P points (dark green solid line). However, the difference between the binding energy with the other impurity H、Li、Na or Mg atom and the binding energy without it is only about 1 eV at the deformation ⊿d/a = 0.00.

(5) Hopping out of Impurity Li/Ca Atom to Cause Nuclear Fusion/Transmutation

When the tetrahedral symmetrical arrangement of Pd atoms is broken slightly by non-breathing mode atomic vibrations or other cause, the impurity atom of the T site would receive unsymmetrical forces from surroundings and hop out from the T site. At that time, it might be occurred that tetrahedral symmetrical four H atoms around the T site would be drawn toward it and condense based on TSC Theory if the Coulomb repulsive forces were shielded appropriately by some way.

According to the discussions mentioned above (1)～(4), results of which could apply to the case of D atoms, although the impurity Li atom would have small momentum and energy when it hops out from the T site, four light H atoms drawn toward the T site would get rather rapid movement recoiled by the Li atom to cause mostly nuclear transmutation through collision against the other atoms in/of Pd metal because of the imperfect short time condensation, and four heavy D atoms would get slow movement recoiled by the Li atom to cause mostly nuclear fusion through no collision against the other atoms in/of Pd metal because of the perfect long time condensation. On the other hand, since the impurity atom Ca has large momentum and energy when it hops out from the T site, four light H atoms would get too rapid movement recoiled by the Ca atom to cause any nuclear reaction, and four heavy D atoms would get rapid movement to cause mostly nuclear transmutation. This is, however, the only hypothetical scenario and the detail mechanism is not known to us.

4. Summaries

We carried out the simulation of H states in Pd metal using the first principles electronic state simulation program on a personal computer. And we investigated the energy differences between the total energy with the impurity H, Li, Na, K, Mg or Ca atom of the T site and the total energy without it. It seemed to be improved in the deformation range of atomic vibration that the impurity Li or Ca atom would draw four H atoms toward the T site to cause condensations and nuclear fusion and/or nuclear transmutation. We will carry out the same simulation with Ni metal.

In the case where H atom itself acted as an impurity, it could not hop out from the T site until the lattice contraction deformation of Pd bulk metal became considerably large. This would give us the expectation that an impurity H atom could hop out from the T site in the deformation range of atomic vibration at room temperature which might be large enough in nano-particle metals.

Until now, we have used the simulation program available even to a personal computer to investigate H states near the T site or the O site in the symmetrically deformed octahedron or tetrahedron at 0 K in fragment calculation like a snap shot of the situation because of computational complexity and calculation time. Then hereafter, we will have to improve the precision of simulation considering how this octahedral or tetrahedral symmetrical deformation will take place in the bulk metal and even in the nano-particle metal based on the lattice vibration and impulse propagation theory at proper temperatures.

References

1) H. Miura, Computer Simulation of States of Hydrogen in Metals of Face Centered Cubic Lattice, Proc. of 10th Meeting of Japan CF Research Society, p. 77 (2010)

2) X. Gonze, B. Amadon, P.-M. Anglade, J.-M. Beuken, F. Bottin, P. Boulanger, F. Bruneval,' D. Caliste, R. Caracas, M. Cote, T. Deutsch, L. Genovese, Ph. Ghosez, M. Giantomassi, S. Goedecker, D.R. Hamann, P. Hermet, F. Jollet, G. Jomard, S. Leroux, M. Mancini, S. Mazevet, M.J.T. Oliveira, G. Onida, Y. Pouillon, T. Rangel, G.-M. Rignanese, D. Sangalli, R. Shaltaf, M. Torrent, M.J. Verstraete, G. Zerah, J.W. Zwanziger, Computer Phys. Commun. 180, 2582-2615 (2009).
"ABINIT : First-principles approach of materials and nanosystem properties."

3) X. Gonze, G.-M. Rignanese, M. Verstraete, J.-M. Beuken, Y. Pouillon, R. Caracas, F. Jollet, M. Torrent, G. Zerah, M. Mikami, Ph. Ghosez, M. Veithen, J.-Y. Raty, V. Olevano, F. Bruneval, L. Reining, R. Godby, G. Onida, D.R. Hamann, and D.C. Allan. Zeit. Kristallogr. 220, 558-562 (2005).
"A brief introduction to the ABINIT software package."

4) K. Momma and F. Izumi, "VESTA: a three-dimensional visualization system for electronic and structural analysis," J. Appl. Crystallogr., 41:653-658, 2008.

5) A. Takahashi, Deuteron cluster fusion and related nuclear reaction in metal-deuterium/hydrogen systems, Recent Res. Devel. Phys. 6, 1-28 (2005).

6) A. Takahashi, Chronicle of Condensed Cluster Fusion Models, Proc. of 8th Meeting of Japan CF Research Society, p. 51 (2007).

Proposal to extend the nuclear physics to include the magnetic monopole as an additional ingredient

Tetsuo Sawada
Institute of Quantum Science, Nihon University,Tokyo, Japan, 1018308

It is proposed to extend the nuclear physics to include the magnetic monopole as an additional component to the (p, n) system. The additional interaction of the super-strong magnetic Coulomb field produced by the magnetic monopole *e and the magnetic dipole moments of the nucleons give rise to various new processes which do not appear in the ordinary nuclear physics, whose basic interaction is the short range nuclear potential. Because the *e-p system has the extra angular momentum, which is perpendicular to the orbital angular momentum, we have to generalize the spherical harmonics to the monopole harmonics. As the first step to construct the magnetic monopole-nucleus system, the equation for the *e-N system is solved and it is found that the "hedgehog" state is the ground state of such a system. As the next simpler problem, the binding energy of the *e-d system is calculated and it is found that the binding energy is large enough to close the channels d+d → t+p and d+d→ ^{3}He+n enegetically, which are the main channels in nuclear physics in vacuum. Other new phenomena, which are characteristic to *e-A system, are investigated.

1. Introduction

In 1960's nuclear physics was extended to include the hyperons such as Λ as the additional ingredient. At that time, the main motivation was to check the SU_3 symmetry of the hadron system. However today it grows up to become an important branch of nuclear physics: physics of hyper-nuclei. Although the addition of the new ingredient opens up new branch, mismatch of the characteristic scale of length often leads to the system which is not very interesting or which we know already. For example, the addition of the electron to the proton and the neutron leads to simply the atomic or the molecular system. Our proposal is to add the magnetic monopole (*e) to the proton-neutron system. The interaction potential of the magnetic dipole moment of the nucleon in the magnetic Coulomb field is

$$V_{*e-N} = \kappa_{tot} \frac{*e\, eD}{2m_p} \frac{(\vec{\sigma}\cdot\hat{r})}{r^2} F(r) \quad with$$
$$F(r) = 1 - (1 + ar + a^2 r^2/2)\exp[-ar], \tag{1}$$

where F(r) is the form factor of the nucleon and $a = 6.04\mu_\pi$. From the charge quantization condition, *ee is 1/2. On the other hand, the magnetic charge number D is 1 and 2 for Dirac and Schwinger magnetic monopole respectively. In general when the added ingredient is more "peculiar", we can expect to encounter what is surprising.

In the next section, a brief review of the magnetic monopole is given. In order to symmetrize the Maxwell equations with respect to the electricity and the magnetism, the terms of the magnetic charge density *ρ and its current density ***i** are added to the equations. After such a symmetrization, we can consider a system where the magnetic charge *Q and the electric charge Q coexist. When we compute the total angular momentum L_{extra} stored in space in the form of the electromagnetic field, it becomes (*QQ/c)(**r**/r) where **r** is the position vector connecting two charged particles (from *Q

to Q). If we combine it with the quantum condition that a component of an angular momentum can assume only the integer multiple of (ħ/2), we obtain the charge quantization condition of Dirac: *QQ/ ħc=n/2 with integer n. This condition not only implies the discreteness of the electric charge Q in Nature, but also fixes the value of the magnetic counterpart of the "fine structure constant": $*e^2/\hbar c = 137/4$, which should be compared with the ordinary fine structure constant $e^2/\hbar c = 1/137$, where *e and e are the smallest values of *Q and Q respectively. Therefore since *ee/ħc =1/2, the potential between the magnetic monopole *e and the proton is $V_{*e\text{-}p}(r)$= -14.5 MeV. at r=1.41 fm., which is the Compton wave length of the charged pion. This value is the same order of magnitude as the nuclear potential $V_N(r)$ at the same separation. Therefore our extension of the nuclear physics goes rather smoothly as in the case of the hyper-nuclei. One of the important features of such an extension is that the nuclear fusion reaction such as d+d → ^{4}He or t+p → ^{4}He can proceed even at the zero incident energy. In vacuum such reactions cannot occur because of the Coulomb repulsion, in fact the penetration factors are $T=5.33\times10^{-106}$ and $T=6.78\times10^{-92}$ respectively for (d+d) and (t+p) reactions. On the other hand, if there is a magnetic monopole *e, it can attract the fuel nuclei whenever they have the magnetic dipole moment μ. What is important is that the attractive potential $V_{*e\text{-}p}(r)$ is not the short range type but its asymptotic form is $1/r^2$, and which can compete with the repulsive Coulomb potential at large separation effectively. On the other hand, since the spin of the produced ^{4}He is zero, it is not attracted by the magnetic monopole. In this way the magnetic monopole plays the roll of the catalyst of the nuclear fusion reaction at zero incident energy.

Furthermore there is an additional roll of the magnetic monopole *e to facilitates nuclear fusion reaction. It is known that the Dirac equation of the electron in the external magnetic Coulomb field has a solution whose orbital size is the same order of magnitude as the electron Compton wave length $\hbar/m_ec$. Therefore in the electron-rich circumstance, it can shield the trapped first nucleus and make it easier for the second nucleus to penetrate to the location of *e. When the two nuclei are trapped by the same magnetic monopole whose orbital radii are several fm., the system becomes unstable and they fuse to become the more stable alpha particle. Since α does not have the magnetic moment, it must leave the magnetic monopole, and there remains a fresh magnetic monopole *e, and which must attract the surrounding fuel nuclei again. In this fashion, the chain reaction of the nuclear cold fusion proceeds.

As the first step of the construction of the *e-A system, we shall consider the *e-p and *e-n system. In section 3, the monopole harmonics $Y_{q,\ell,m}(\theta,\phi)$ will be introduced as the generalization of the ordinary spherical harmonics $Y_{\ell,m}(\theta,\phi)$. In section 4 the combination of the monopole harmonics and the spin will be considered and the "hedgehog state" will be introduced, and which appears in the ground state of the *e-p system. As the simplest case to construct the *e-A system, the eigenstates of the nucleon in the magnetic Coulomb field are calculated. In section 5, the Dirac equation of the electron in the magnetic Coulomb field is solved. The *e-d system, which is simple next to the *e-N system, is considered in section 6. It will be found that the binding energy of *e-d exceeds the critical value 2.03MeV.. So if the d+d reaction starts from the doubly bound state (d-*e-d), it is energetically impossible to transit to t+p or to ^{3}He+n, which are the main channel of the d-d reaction in vacuum. The only channel of the final state stays open is ^{4}He. Section 7 is devoted to remarks and comments.

2. Charge quantization condition of Dirac

The Maxwell equations are the fundamental equations of the electromagnetism, however they have a strange feature that the electricity and the magnetism are not treated on the same footing, namely they do not have the duality symmetry. For example, although the electric flux density **D** has the source ρ: div **D** =ρ, the magnetic flux density **B** does not have its source term *ρ: div **B** = 0, in the Maxwell equations. This natural law is the result of the induction from experiments to separate the north and south poles by cutting a magnet. Since the amount of energy poured in the separation experiments in 19 century were limited, it is questionable to use these experiments to establish the fundamental law, instead we may rely on the higher symmetry of the fundamental equations. After Dirac let us modify the Maxwell equations by adding the terms of the magnetic charge density *ρ and its current density ***i**. They become

$$div \quad \vec{D} = 4\pi \rho$$

$$div \quad \vec{B} = 4\pi * \rho$$

and

$$rot \quad \vec{H} - \frac{1}{c}\frac{\partial \vec{D}}{\partial t} = \frac{4\pi}{c}\vec{i} \qquad (2)$$

$$rot \quad \vec{E} + \frac{1}{c}\frac{\partial \vec{B}}{\partial t} = -\frac{4\pi}{c} * \vec{i} \ .$$

These equations are invariant under the duality transformation:

$$\vec{E} \rightarrow \vec{E}' = \vec{H}; \qquad \vec{D} \rightarrow \vec{D}' = \vec{B}$$

$$\vec{H} \rightarrow \vec{H}' = -\vec{E}; \qquad \vec{B} \rightarrow \vec{B}' = -\vec{D}$$

and (3)

$$\rho \rightarrow \rho' = *\rho; \qquad \vec{i} \rightarrow \vec{i}' = *\vec{i}$$

$$*\rho \rightarrow *\rho' = -\rho; \qquad *\vec{i} \rightarrow *\vec{i}' = -\vec{i} \ .$$

When the magnetic charge and its current do not exist, the equations reduce to the ordinary Maxwell equations, however the equations can describe something new. We can consider a system where a particle with the electric charge Q and another particle with the magnetic charge *Q coexist. What is important is that such a system has the angular momentum even if these particles are not moving. To see this we must remember the momentum density **P** of the electromagnetic field: **P**=**S**/c^2 =(**E**×**H**)/4πc, where **S** is the Poynting vector. If *Q is fixed at the origin **r'**=0, and the particle Q is at **r'**=**r**, then the total angular momentum of the electromagnetic fields are the integration of **r'**×**P:**

$$\vec{L}_{em} = \frac{*QQ}{4\pi c}\int d^3 r' \, \vec{r}' \times \left(\frac{\vec{r}'}{r'^3} \times \frac{(\vec{r}' - \vec{r})}{|\vec{r}' - \vec{r}|^3} \right) = -\frac{*QQ}{c}\frac{\vec{r}}{r}. \qquad (4)$$

The appearance of this extra angular momentum is remarkable and this is also obtained by examining the conservation law of the angular momentum of the system.

Let us consider a system where a particle of mass m with the electric charge Q moving in the magnetic Coulomb field produced by the magnetic charge *Q which is fixed at the origin. The equation of motion is

$$m\ddot{\vec{r}} = \frac{Q}{c}\dot{\vec{r}} \times \frac{{}^{*}Q\ \vec{r}}{r^3}\ , \tag{5}$$

and if we make the vector product $\mathbf{r}\times$ of the equation of motion, we get the conservation law of the angular momentum:

$$\frac{d}{dt}(\vec{r} \times m\dot{\vec{r}}) = \frac{{}^{*}Q\ Q}{c}\frac{\vec{r} \times (\dot{\vec{r}} \times \vec{r})}{r^3} = \frac{{}^{*}Q\ Q}{c}\frac{d}{dt}\left(\frac{\vec{r}}{r}\right)\ . \tag{6}$$

Therefore what is conserved in time is the sum of the orbital angular momentum $\mathbf{L}_{orb}$ and the extra angular momentum $\mathbf{L}_{em}$. These angular momentums are perpendicular to each other. In the quantum theory, a component of the angular momentum can assume only the integer multiple of (ħ/2), if we choose (**r**/r) as the quantization axis we obtain the charge quantization condition of Dirac [1] :

$$\frac{{}^{*}Q\ Q}{\hbar c} = \frac{n}{2} \quad with \quad n = 0, \pm 1, \pm 2 \cdots . \tag{7}$$

However Schwinger claimed that, since the extra angular momentum has the classical correspondence, its component can assume only the integer multiple of ħ rather than that of ħ/2. In order to cover both cases, we write the charge quantization condition, by using the magnetic charge number D, as

$$\frac{{}^{*}Q\ Q}{\hbar c} = \frac{D}{2}n \quad with \quad n = 0, \pm 1, \pm 2 \cdots \tag{8}$$

where D=1 and D=2 for Dirac and Schwinger magnetic monopole respectively. If we write the smallest values of the charges *Q and Q as *e and e respectively, from Eq. (8) we can derive the discreteness of the electric charge Q in Nature:

$$Q = \frac{D\hbar c}{2\,{}^{*}e}n \quad with \quad n = 0, \pm 1, \pm 2 \cdots \ , \tag{9}$$

which is known experimentally for long time. Furthermore Eq. (9) indicates the equality of the electric charges of the electron e_e and the proton e_p up to sign, because the pitches of the levels of the electric charges are common. Experimentally the equality is known with very high accuracy: $|e_p-|e_e||/e_p<10^{-21}$.

Another important implication of the charge quantization condition Eq. (8) is that the magnetic Coulomb field of the magnetic monopole is super-strong. By the substitution *Q → *e, Q → e and n → 1 in Eq. (8), we obtain the magnetic counterpart of the "fine structure constant":

$$\frac{{}^{*}e^2}{\hbar c} = \frac{D^2}{4} / \frac{e^2}{\hbar c} = \frac{137.036}{4}D^2 \tag{10}$$

3. Change from spherical harmonics to monopole harmonics

It is well-known that in the quantum mechanics when we describe the motion in the central force potential V(r), the wave function has the form $\Psi = R(r)\,Y_{\ell,m}(\theta,\phi)$, where $Y_{\ell,m}$ is the spherical harmonics and which is the eigen-function of $\vec{L}^{(orb)\,2}$ and $L_z^{(orb)}$ with the eigen-value $\ell(\ell+1)$ and m respectively. Let us start by considering the motion of a point charged particle with mass M and the electric charge Ze in the Coulomb magnetic field B=*Q **r**/r^3 produced by magnetic monopole *Q fixed at the

origin. The standard procedure to include the effect of the magnetic field is to make the gauge substitution **p** → (**p** - (Q/c)**A)** , where **A** is the vector potential whose rotation is magnetic field **B**. In particular, magnetic Coulomb field satisfies

$$div\ \vec{B} = 4\pi\ {}^*Q\ \delta^3(\vec{r}) \tag{11}$$

and if we substitute **B** = rot **A** into Eq.(11) we obtain a contradictory equation, because (div rot) is identically zero if **A** is regular. The standard choice of the vector potential is to use two functions $\mathbf{A}^{(n)}$ and $\mathbf{A}^{(s)}$ defined in the north and south hemisphere respectively, which are connected by the gauge transformation: **A'**=**A**+ grad(χ), where χ is an arbitrary scalar function. The following functions written in the spherical coordinate system do the job [2]

$$\vec{A}^{(n)} = {}^*Q\frac{(1-\cos\theta)}{r\sin\theta}\vec{e}_\phi \qquad (north)$$

and (12) and (13)

$$\vec{A}^{(s)} = -{}^*Q\frac{(1+\cos\theta)}{r\sin\theta}\vec{e}_\phi \qquad (south)$$

since if we remember the formula in the spherical coordinate system

$$\vec{\nabla}\times\vec{A}=\vec{e}_r\frac{1}{r\sin\theta}\left[\frac{\partial}{\partial\theta}(A_\phi\sin\theta)-\frac{\partial A_\theta}{\partial\phi}\right]+\vec{e}_\theta\frac{1}{r}\left[\frac{1}{\sin\theta}\frac{\partial A_r}{\partial\phi}-\frac{\partial}{\partial r}(rA_\phi)\right]+\vec{e}_\phi\frac{1}{r}\left[\frac{\partial}{\partial r}(rA_\theta)-\frac{\partial A_r}{\partial\theta}\right]$$

the rotation of **A** becomes the magnetic Coulomb field namely (*Q / r^2) $\mathbf{e}_r$. Furthermore since the gradient in the spherical coordinate system is

$$\vec{\nabla} = \vec{e}_r\frac{\partial}{\partial r}+\vec{e}_\theta\frac{1}{r}\frac{\partial}{\partial\theta}+\vec{e}_\phi\frac{1}{r\sin\theta}\frac{\partial}{\partial\phi}\ , \tag{14}$$

difference of the two vector potentials of Eq.(12) and (13) is

$$\vec{A}^{(s)}-\vec{A}^{(n)} = -2\,{}^*Q\,Q\frac{1}{r\sin\theta}\vec{e}_\phi = \vec{\nabla}(-2\,{}^*Q\,Q\phi)\ , \tag{15}$$

therefore they are connected by the gauge transformation with the gauge function $\chi = -2\ {}^*Q\,Q\phi$ and describe the same magnetic field. Although the vector potentials Eq.(12),(13) have the string singularity (Dirac string) on the half z-axis, each vector potential is regular in its respective domain of definition.

The Hamiltonian of the system of a particle of mass M and charge Ze in the magnetic Coulomb field produced by a magnetic monopole *Q=*e D is

$$H_0 = -\frac{\hbar^2}{2M}(\vec{\nabla}-i\frac{Ze}{\hbar c}\vec{A})^2 \tag{16}$$

in which **A** is given in Eq.(12) and (13). Let us find the solution of $H_0\Psi = E\Psi$ in the separable form $\Psi=R(r)Y(\theta,\varphi)$. In the spherical coordinate system, if we use the angular momentum **L**, which is defined by:

$$\vec{L} = \vec{r}\times(\vec{p}-\frac{Ze}{c}\vec{A})-\hbar q\vec{e}_r \quad where \quad q = D\,{}^*eZe = \frac{DZ}{2} \tag{17}$$

the Hamiltonian becomes

$$H_0 = -\frac{1}{2M}\left[\frac{\partial^2}{\partial r^2}+\frac{2}{r}\frac{\partial}{\partial r}-\frac{1}{\hbar^2 r^2}(\vec{L}^2-\hbar^2q^2)\right]. \tag{18}$$

In Eq.(17), q is the magnitude of the extra angular momentum and which is perpendicular to the orbital part of the angular momentum. The explicit form of $\mathbf{L}^2$ and L_z are:

$$\vec{L}^2 = -\hbar^2\left[\frac{1}{\sin\theta}\frac{\partial}{\partial\theta}(\sin\theta\frac{\partial}{\partial\theta}) + \frac{1}{\sin^2\theta}\frac{\partial^2}{\partial\phi^2} \mp 2iq\frac{1}{1\pm\cos\theta}\frac{\partial}{\partial\phi} - 2q^2\frac{1}{1\pm\cos\theta}\right]$$

and (19)

$$L_z = -i\hbar\frac{\partial}{\partial\phi} \mp q\hbar,$$

where ± sign corresponds to the north and south hemisphere of the domains. The eigen-function of L_z must have the form $Y=\Theta(z)\exp[\, i\,(m \pm q)\varphi]$, where $z=\cos\theta$. The equation for $\Theta(z)$ is

$$\left[(1-z^2)\frac{d^2}{dz^2} - 2z\frac{d}{dz} - \frac{1}{1-z^2}(m+qz)^2 + \ell(\ell+1) - q^2\right]\Theta(z) = 0, \tag{20}$$

whose solution can be written by using the Jacobi polynomials. However it is more convenient to write the result by using Wigner's d-function of the rotation matrix, because most of the text book of the nuclear physics contains the tables of the d-function. The monopole harmonics Y becomes:

$$Y^{(n)}_{q,\ell,m}(\theta,\phi) = \sqrt{\frac{2\ell+1}{4\pi}}\, e^{+iq\phi} d^{(\ell)}_{-q,m}(\theta)\, e^{+im\phi} \quad in \quad 0 \le \theta < \frac{\pi}{2} + \varepsilon$$

and

$$Y^{(s)}_{q,\ell,m}(\theta,\phi) = \sqrt{\frac{2\ell+1}{4\pi}}\, e^{-iq\phi} d^{(\ell)}_{-q,m}(\theta)\, e^{+im\phi} \quad in \quad \frac{\pi}{2} - \varepsilon < \theta \le \pi, \tag{21}$$

with

$$\ell = |q|, |q|+1, |q|+2, \cdots \quad and \quad m = -\ell, -\ell+1, \cdots, +\ell,$$

which is the generalization of the spherical harmonics $Y_{\ell,m}$.

From Eq. (18), the equation of the radial function R(r) is the Bessel type:

$$\left[-\frac{1}{2Mr^2}\frac{d}{dr}(r^2\frac{d}{dr}) + \frac{\ell(\ell+1)-q^2}{2Mr^2}\right]R(r) = E\,R(r) \tag{22}$$

and the solution which does not blow up at the origin **r** = 0 is

$$R(r) = \frac{1}{\sqrt{kr}}J_\mu(kr)$$

where (23)

$$k = \sqrt{2ME} \quad and \quad \mu = \sqrt{\ell(\ell+1) - q^2 + 1/4} = \sqrt{(\ell+1/2)^2 - q^2} > 0.$$

For E < 0, there is no meaningful solution, and therefore no bound state. So this wave function describes the motion of the spin zero charged particle such as the charged pion, and also in some approximation we can use it for the alpha particle.

4. Nucleon in the magnetic Coulomb field

As the first step to construct the nuclear system in the external magnetic Coulomb field, let us start by considering the system of the nucleon in the magnetic Coulomb field produced by the magnetic monopole *eD fixed at the origin. The first thing to do is to make the spin-angular functions from the 2-component spinor and the monopole harmonics, because $\mathbf{J} = \mathbf{L} + \boldsymbol{\sigma}/2$. Since the spin of the nucleon is 1/2, for given ℓ there exist two states of j: $j = \ell + 1/2$ and $j = \ell - 1/2$. However since j is what is conserved, it is more adequate to reverse the variables in classifying the states, namely for given j there are two states of ℓ: $\ell = j - 1/2$ and $\ell = j + 1/2$ except for the smallest j state ($j = |q| - 1/2$). After Yang, it is convenient to call the former doublet states type-A and the latter singlet state type-B. As usual the combination of two angular momentums is done by using the Clebsch-Gordan coefficients. For given j, there are two types of states :

$$\begin{aligned}\Phi^{(1)}_{j,m} &= \sqrt{\frac{j+m}{2j}}Y_{q,\,j-1/2,\,m-1/2}\begin{pmatrix}1\\0\end{pmatrix} + \sqrt{\frac{j-m}{2j}}Y_{q,\,j-1/2,\,m+1/2}\begin{pmatrix}0\\1\end{pmatrix} \\ &= \begin{bmatrix}\sqrt{\dfrac{j+m}{2j}}Y_{q,\,j-1/2,\,m-1/2}\\ \sqrt{\dfrac{j-m}{2j}}Y_{q,\,j-1/2,\,m+1/2}\end{bmatrix}\end{aligned} \tag{24}$$

and

$$\begin{aligned}\Phi^{(2)}_{j,m} &= -\sqrt{\frac{j-m+1}{2j+2}}Y_{q,\,j+1/2,\,m-1/2}\begin{pmatrix}1\\0\end{pmatrix} + \sqrt{\frac{j+m+1}{2j+2}}Y_{q,\,j+1/2,\,m+1/2}\begin{pmatrix}0\\1\end{pmatrix} \\ &= \begin{bmatrix}-\sqrt{\dfrac{j-m+1}{2j+2}}Y_{q,\,j+1/2,\,m-1/2}\\ \sqrt{\dfrac{j+m+1}{2j+2}}Y_{q,\,j+1/2,\,m+1/2}\end{bmatrix}\end{aligned} \tag{25}$$

for $j \geqq |q| + 1/2$ (type-A). On the other hand for $j = |q| - 1/2$ (type-B), $\mathbf{\Phi}^{(1)}_{j,m}$ of Eq.(24) vanishes, and there remains only one state $\mathbf{\Phi}^{(2)}_{j,m}$ of Eq.(25). It is convenient to introduce a new notation to the type-B state:

$$\eta_m = \begin{bmatrix}-\sqrt{\dfrac{|q|-m+1/2}{2|q|+1}}Y_{q,|q|,\,m-1/2}\\ \sqrt{\dfrac{|q|+m+1/2}{2|q|+1}}Y_{q,|q|,\,m+1/2}\end{bmatrix}. \tag{26}$$

The importance of the type-B state comes from the fact that the ground state is always type-B state, and that it is the eigen-state of the (pseudo-)scalar operator $(\vec{\sigma}\cdot\hat{r})$ with the eigen-value q/|q|, and it is sometimes called "hedgehog state" since the spin direction is outward and spherical.

The Hamiltonian of the proton in the magnetic Coulomb field is:

$$H = \frac{1}{2m_p}(-i\vec{\nabla} - e\vec{A})^2 - \frac{1}{r^2}\frac{b(r)}{2m_p}(\vec{\sigma}\cdot\hat{r}), \tag{27}$$

where the form factor function is

$$b(r) = \bar{b}F(r) = \bar{b}\left\{1 - e^{-ar}(1 + ar + a^2r^2/2)\right\} \tag{28}$$

with

$$\bar{b} = \kappa_{tot}|q| \models 2.7928|q|, \quad q = D/2 \ \textit{and} \ \ a = 6.04\mu_\pi . \tag{29}$$

The parameter a relates to the proton radius, which is 0.811 fm., by $< r^2 >= 12/a^2$.

For the type-B amplitude

$$\Psi = \frac{g(r)}{r}\eta_m , \tag{30}$$

the equation of the radial function g(r) becomes

$$\left[\frac{d^2}{dr^2} - \kappa^2 - \frac{(|q| - b(r))}{r^2}\right] g(r) = 0 \quad with \quad \kappa^2 = -2m_p E . \tag{31}$$

For ar >> 1, b(r) becomes a constant $\bar{b}$ and the equation reduces to the Bessel equation, the solution, which damps for large ar, is

$$g(r) = \sqrt{\kappa r}\ K_{i\mu}(\kappa r) \quad with \quad i\mu = \sqrt{|q|(1-\kappa_{tot}) + 1/4} \ .$$

Since the behavior of g(r) at the origin $C_1 r^\alpha$ is determined by the index relation $\alpha = 1/2 + \sqrt{|q| + 1/4}$, we integrate Eq.(31) to the matching point $ar = ar_m >> 1$. The binding energies of the ground states turn out -E = 0.1882MeV. and 2.4065MeV. for D=1 and D=2 magnetic monopoles respectively, whereas the radii of the orbits of the ground states are $\bar{r} = 11.0\ fm.$ *and* $3.67\ fm.$ respectively. -E of the first few excited states are given also in the Tables below for D=1 and 2. In the same Tables, the values of the parameters μ and C_1 which appear in the infinitely many binding energy levels

$$-E = C_1 \exp[-\frac{2\pi}{\mu}(n-1)] \quad with \quad n = 1, 2, 3\cdots, \tag{32}$$

where n is the principle quantum number, are also given. The level structure of Eq.(32) is the characteristic feature of $1/r^2$ potential. [3]

Although we considered the system of the proton and the magnetic monopole *eD, we can also apply the same technique to other small nuclei of spin 1/2 such as triton (t) and ^{3}He as long as the deformations of the nuclei in the magnetic Coulomb field are negligible, by simply changing the parameters such as the mass m, charge Z, magnetic moment κ_{tot} and a, which relates to the radius of the nucleus $\bar{r}$ by $a^2 = 12/\bar{r}^2$. In the Table 1 and Table 2, the binding energy and the orbital radius $\sqrt{< r^2 >}$ of ttiton and ^{3}He are given in addition those of the neuteron and the proton. Among them n and t have the type-A bound states of the form $\psi = [f(r)\Phi^{(1)}_{j,m} + g(r)\Phi^{(2)}_{j,m}]/r$, whose radial functions f (r) and g(r) satisfy:

$$[\frac{d^2}{dr^2} + 2ME - \frac{R}{r^2}]\begin{pmatrix} f \\ g \end{pmatrix} = 0$$

where

$$R = \begin{pmatrix} (j+\frac{1}{2})(j+\frac{1}{2}) - q^2 + b(r)\frac{2q}{2j+1} & -b(r)\frac{\sqrt{(2j+1)^2 - 4q^2}}{2j+1} \\ -b(r)\frac{\sqrt{(2j+1)^2 - 4q^2}}{2j+1} & (j+\frac{1}{2})(j+\frac{3}{2}) - q^2 - b(r)\frac{2q}{2j+1} \end{pmatrix}. \tag{33}$$

Table 1. The first few binding energies -E and the orbital radii $< r^2 >^{1/2}$ of the n, p, t and ^{3}He in the Coulomb field produced by Dirac's magnetic monopole (D=1). n is the principal quantum number.

D = 1	q	j (type)	n	- E	$< r^2 >^{1/2}$
n	0	1/2 (A)	1 2 ⋮ ∞	37.37 eV. 1.375×10^{-6} eV. (C_1=37.37 eV.)	647.7 fm. 8.57×10^{6} fm. (μ=0.3670)
p	1/2	0 (B)	1 2 3 ⋮ ∞	0.1882 MeV. 70.046 eV. 0.03069 eV. (C_1=0.1884 MeV.)	11.00 fm. 547.6 fm. 27257. fm. (μ=0.8040)
t	1/2	0 (B)	1 2 3 ⋮ ∞	1.516 MeV. 58.085 keV. 2.226 keV. (C_1=1.516 MeV.)	3.820 fm. 19.36 fm. 98.89 fm. (μ=1.9263)
t	1/2	1 (A)	1 2 3 ⋮ ∞	2.178 keV. 24.366 eV. 0.02725 eV. (C_1=2.1783 eV.)	79.19 fm. 748.7 fm. 7079. fm. (μ=1.3984)
^{3}He	1	1/2 (B)	1 2 3 ⋮ ∞	0.2484 MeV. 2.7413 keV. 30.047 eV. (C_1=0.2502 MeV.)	7.371 fm. 70.36 fm. 672.15 fm. (μ=1.3921)

Table 2. The first few binding energies -E and the orbital radii $< r^2 >^{1/2}$ of the n, p, t and ^{3}He in the magnetic Coulomb field produced by Schwinger's magnetic monopole (D=2). n is the principal quantum number of the infinitely many energy levels which converge to -E=0.

D = 2	q	j (type)	n	- E	$< r^2 >^{1/2}$
n	0	1/2 (A)	1 2 3 ⋮ ∞	0.8003 MeV. 1.115 keV. 1.542 eV. (C_1=0.8040 MeV.)	5.728 fm. 158.97 fm. 4139.3 fm. (μ=0.9545)
p	1	1/2 (B)	1	2.4065 MeV.	3.666 fm.

			2 3 ⋮ ∞	15.457 keV. 98.231 eV. (C_1=2.4322 MeV.)	47.70 fm. 598.42 fm. (μ=1.2421)
t	1	1/2 (B)	1 2 3 ⋮ ∞	4.366 MeV. 0.5479 MeV. 57.766 keV. (C_1=5.4085 MeV.)	2.779 fm. 8.464 fm. 26.31 fm. (μ=2.7697)
t	1	3/2 (A)	1 2 3 ⋮ ∞	1.203 MeV. 73.162 keV. 4.2423 keV. (C_1=1.2696 MeV.)	4.651 fm. 19.20 fm. 79.88 fm. (μ=2.2042)
t	1	5/2 (A)	1 2 ⋮ ∞	0.5342 eV. 8.465×10^{-8} eV. (C_1=0.53418 eV.)	3169.1 fm. 7.961×10^{6} fm. (μ=0.4013)
^{3}He	2	3/2 (B)	1 2 3 ⋮ ∞	1.063 MeV. 51.115 keV. 2.3239 keV. (C_1=1.1259 MeV.)	4.596 fm. 21.50 fm. 100.9 fm. (μ=2.0312)

5. Dirac equation of the electron in the magnetic Coulomb field

In the previous section, we studied the system of the spin 1/2 particle in the external magnetic Coulomb field. Such a system has the interaction potential of the form C/r^2, which is too singular at r=0 to solve the Schrödinger equation. For the case of the nucleon this difficulty was avoided by introducing the form factor F(r) as in Eqs.(27) and (28). However what happens, as in the case of the electron, if it reduces to a point particle F=1 or a tends to infinity. As a increases, the binding energy -E also increases and becomes the order of magnitude of the electron mass, so the non-relativistic Schrödinger equation is not adequate and we have to solve the relativistic Dirac equation in the external magnetic Coulomb field.

In the natural unit of $\hbar = c = 1$, the Dirac Hamiltonian is [4]

$$H = \vec{\alpha}\cdot(-i\vec{\nabla} - e\vec{A}) - \beta M + \kappa_a \frac{e}{2M}\beta\begin{pmatrix} \vec{\sigma}\cdot\vec{B} & 0 \\ 0 & \vec{\sigma}\cdot\vec{B} \end{pmatrix}$$

where (34)

$$\vec{\alpha} = \begin{pmatrix} 0 & \vec{\sigma} \\ \vec{\sigma} & 0 \end{pmatrix}, \quad \beta = \begin{pmatrix} I_2 & 0 \\ 0 & -I_2 \end{pmatrix} \quad \textit{and} \quad \vec{B} = *eD\frac{\hat{r}}{r^2}.$$

κ_a is the anomalous magnetic moment of the electron in the unit of the Bohr magneton e/2M, namely $\kappa_a=\kappa_{tot}-1$, and its numerically $\kappa_a \approx e^2/2\pi = 0.00116$, and $\mathbf{I}_2$ is the 2×2 unit matrix. We are going to find the type-B solution of the form:

$$\Psi^{(B)} = \begin{bmatrix} f(r)\eta_m \\ g(r)\eta_m \end{bmatrix}, \tag{35}$$

where η_m is introduced in Eq.(26), which is the eigen-state of $(\vec{\sigma}\cdot\hat{r})$ with the eigen-value q/|q|. It is convenient to write the Hamiltonian in the matrix form:

$$H = \begin{bmatrix} M & \vec{\sigma}\cdot(-i\vec{\nabla} - Ze\vec{A}) \\ \vec{\sigma}\cdot(-i\vec{\nabla} - Ze\vec{A}) & -M \end{bmatrix} - \frac{\kappa_a q}{2Mr^2}\begin{bmatrix} \vec{\sigma}\cdot\hat{r} & 0 \\ 0 & -\vec{\sigma}\cdot\hat{r} \end{bmatrix} \tag{36}$$

and if we use a relation, where f(r) is an arbitrary radial function

$$\vec{\sigma}\cdot(-i\vec{\nabla} - Ze\vec{A})\, f(r)\eta_m = -iq|q|^{-1}(\partial_r + r^{-1})\, f(r)\eta_m \tag{37}$$

we obtain the eigen-value equations for radial functions f(r) and g(r):

$$[M - E - \kappa_a |q|(2Mr^2)^{-1}]f(r) - iq|q|^{-1}(\partial_r + r^{-1})g(r) = 0$$

and (38)

$$-iq|q|^{-1}(\partial_r + r^{-1})f(r) - [M + E - \kappa_a |q|(2Mr^2)^{-1}]g(r) = 0.$$

If we introduce new functions F(r) and G(r) by

$$f(r) = \frac{\kappa_a q}{|\kappa_a q|}\frac{F(r)}{r} \quad \textit{and} \quad g(r) = -i\frac{G(r)}{r}, \tag{39}$$

the equations become simpler:

$$\frac{dG(r)}{dr} = [-\frac{(E-M)\kappa_a}{|\kappa_a|} - \frac{|\kappa_a q|}{2Mr^2}]\, F(r)$$

and (40)

$$\frac{dF(r)}{dr} = [\frac{(E+M)\kappa_a}{|\kappa_a|} - \frac{|\kappa_a q|}{2Mr^2}]\, G(r).$$

If we change the variable to ρ defined by $r = |\kappa_a q|\rho(2M)^{-1}$, the equations become more transparent:

$$\frac{dG}{d\rho} = (A - B - \frac{1}{\rho^2})F \quad \textit{and} \quad \frac{dF}{d\rho} = (A + B - \frac{1}{\rho^2})G,$$

where (41)

$$A = \frac{\kappa_a |q|}{2} \quad \textit{and} \quad B = \frac{\kappa_a |q|}{2M}E.$$

We must find functions which damp for $\rho \to \infty$ and zero at $\rho = 0$ namely F(0)=0 and G(0)=0 by changing the energy variable B. The result is

$$B = 0\,, \quad F = -G = \exp[-A\rho - \frac{1}{\rho}]\,. \tag{42}$$

Or in terms of r, Eq.(42) becomes

$$E = 0\,, \quad F = -G = \exp[-\frac{\kappa_a}{|\kappa_a|} M\, r - \frac{|\kappa_a q|}{2Mr}]\,, \tag{43}$$

and this solution satisfies the requirement at r infinity as long as $\kappa_a > 0$, and the actual electron has such a property: $\kappa_a \approx \frac{e^2}{2\pi} > 0$. In the relativistic theory, E=M is the starting point of the continuous spectrum of the positive energy levels, therefore E=0 is the middle point of the positive and negative energy spectra. In the electron rich circumstance, this orbit is occupied by an electron whose charge density is $F^2 + G^2 \approx \exp[-2Mr]$. Since M is the electron mass, the orbital radius of the electron trapped by the magnetic monopole *e is $\hbar/(2Mc) = 193.1\, fm.$.

It is well-known that the penetration factor T of the nuclear fusion reaction at zero incident energy is too small (T= $10^{-91} \sim 10^{-105}$) in vacuum, so in practice it does not occur in nature. On the other hand when the fusion reaction of the hydrogen isotopes (p, d or t) proceeds under the influence of the magnetic monopole *eD, the penetration factor changes drastically because the repulsive Coulomb is shielded by the electron cloud mentioned above and because of the attractive potential between magnetic monopole and the magnetic dipole moment of the nucleus when its spin orients properly. The formula to evaluate the penetration factor T at zero incident energy E=0 in the WKB approximation is

$$T = e^{-2\tau} \quad with \qquad \tau = \frac{1}{\hbar}\int_a^b \sqrt{2\mu_{red} V(x)}\, dx\,, \tag{44}$$

where μ_{red} is the reduced mass and [a,b] is the domain of the penetration. The first step of the nuclear fusion reaction goes rather freely since it is the process where the first nucleus is trapped by the magnetic monopole and to form the bound state *e-A_1. In the second step, the second nucleus A_2 approaches to the bound system (*e-A_1), and the potential felt by the second nucleus is:

$$V_2(x) = +\frac{e^2}{x}\exp[-2M_e x] - \kappa_{tot}\frac{e\,{}^*eD}{2M_p}\frac{1}{x^2} \tag{45}$$

when the orientation of the magnetic dipole moment of A_2 is the direction opposite to the location of the magnetic monopole. After the penetration two nuclei are trapped by the same magnetic monopole whose orbital radii are several fm.. If the doubly bound states are (d-*e-d) or (p-*e-t), they must transit to a more stable nucleus ^{4}He and *e.

When we evaluate the penetration factor T, it depends on the order of the trapping. So let us introduce the notation such as (p-*e)-t, which means that the proton is trapped first by *e and the triton is penetrating to the bound system (p-*e). If we use the potential $V_2(x)$ of Eq.(45) for V in the penetration formula Eq.(44), the penetration factors T are obtained for D=1 (Dirac) and D=2 (Schwiger) magnetic monopoles, respectively:

$$\begin{array}{lccc} & (t-*e)-p & (p-*e)-t & (d-*e)-d \\ D=1 & T=2.93\times10^{-7} & T=5.39\times10^{-4} & T=6.22\times10^{-9} \\ D=2 & T=1.22\times10^{-4} & T=8.04\times10^{-3} & T=1.43\times10^{-7} \end{array} \quad (46)$$

This list should be compared with the penetration factor T in the vacuum:

$$\begin{array}{cc} t+p & d+d \\ T=6.78\times10^{-92} & T=5.33\times10^{-106} \end{array} \quad (47)$$

To understand the roll of the magnetic monopole, it is interesting to compare $V_2(x)$ of Eq.(45) with the repulsive Coulomb $V_C(x)=e^2/x$. V_2 has two roots a and b, numerically for the proton a=22.85fm. and b=614.9fm., when D=1, the middle region [a,b] is repulsive. The peak of the repulsive region occurs at x_p=41.2fm., and the peak value is only $V(x_p)$= 10.72keV., and this value should be compared with that of the purely Coulomb case, where the peak value is around 1 MeV.. This lowering of the repulsive peak and the narrowing of the penetration region [a, b] is the reason why the nuclear fusion reaction at zero incident energy becomes possible.

6. Hamiltonian of the nucleus in the magnetic Coulomb field

When we extend the nuclear physics to include the magnetic monopole *e, for definiteness we shall set the mass of the magnetic monopole infinity, although Schwinger's estimation is 8GeV., it must be a good approximation when we consider a small nuclear system (A < 5). Our restriction of nucleon number to A < 5 is that we can apply the well-established technique of the few-body system to calculate the matrices of the nuclear reaction from the first principle on one hand, and A is still large enough to include the interesting nuclear fusion reactions such as (p+t → ^{4}He) and (d+d → ^{4}He) on the other hand. Merits of this small system is that we can carry out the calculation with the well-established rules of the quantum mechanics, when the Hamiltonian of the system is given. Our Hamiltonian is

$$H=\sum_{j=1}^{A}[\frac{1}{2m_j}(-i\vec{\nabla}_j-Z_j e\vec{A}_j)^2-\frac{1}{r^2{}_j}\frac{\kappa_{tot}^{(j)}q}{2m_p}(\vec{\sigma}\cdot\hat{r}_j)F(r_j)\,]+\sum_{i>j}V_{i,j}^{(N)},$$

where (48)

$$F(r)=1-e^{-ar}(1+ar+a^2r^2/2) \quad with \quad a=6.04\mu_\pi\ ,$$

in which $q=DZ_j/2$ and Z_j is 0 for neutron and +1 for proton. $V^{(N)}_{i,j}$ is the nuclear potential written symbolically. As a simplest application, we shall consider the system of the deuteron and the magnetic monopole *eD. Since in vacuum the deuteron is a loosely bound particle (B =2,23MeV.) whose radius is 4.32fm., we cannot treat it as a one particle of spin 1 with $\kappa_{tot}=0.8574$ by simply changing the spin matrix $\boldsymbol{\sigma}$ of spin 1/2 to $\boldsymbol{\Sigma}$ of spin 1 in Eq.(27). Therefore we must solve the Schrödinger equation with hamiltonian of A=2 of Eq.(48) honestly.

To estimate the binding energy of the ground state of the *e-d system, we have recourse to the variational calculation by minimizing $<\psi|H|\psi>/<\psi|\psi>$, where ψ is the trial function, in which we applied the Gaussian expansion method (GEM). In GEM, the trial functions are the sum of the Gauss functions of various Jacobi

coordinates, in which the range parameters a_j of $C_j\exp[-a_jx^2]$ form the geometric series. In general, for the 3-body system there are 3 pairs of Jacobi coordinates. However when the mass of a particle, let us call it the particle 0 and fix it at the origin, is infinity, the Jacobi coordinates reduce to two pairs. If the position vectors of the proton and the neutron are respectively $\mathbf{r}_1$ and $\mathbf{r}_2$ measured from the particle 0, Jacobi coordinates are $(\vec{r}_1, \vec{r}_2)$ and $(\vec{R}, \vec{r}) \equiv \left((m_1\vec{r}_1 + m_2\vec{r}_2)/(m_1 + m_2), \vec{r}_2 - \vec{r}_1\right)$, namely the position of the center of the mass point and the relative coordinate. The result of the search of the binding energy of the ground state is 4.76MeV. for $\kappa_{tot}^{(n)} = 0$ whereas 4.45MeV. for the actual value of the neutron magnetic moment namely $\kappa_{tot}^{(n)} = -1.913$. Since the zero of the binding energy is chosen as the state where p, n and *e are separated infinitely, if we remember the binding energy of p and n (namely d) is 2.22MeV., the binding energy of d-*e system is $-E_{*e\text{-}d}$ =2.54 and 2.23MeV. respectively for $\kappa_{tot}^{(n)} = 0$ and for $\kappa_{tot}^{(n)} = -1.913$. It is remarkable that if d+d reaction starts after the two deuterons are trapped by the same magnetic monopole *e, they cannot energetically transit to t+p state as long as the binding energy $-E_{*e\text{-}d}$ exceeds the critical value 2.03MeV., because the binding energy of the triton is B=8.50MeV.. Likewise since the binding energy of ^{3}He is B=7.95MeV., the critical value of the binding energy of d-*e is $-E_{*e\text{-}d}$ =1.75MeV.. Since in general, the variational calculation gives the lower bound of the binding energy $-E_{*e\text{-}d}$,which is 2.23MeV. in our case, the true value could be slightly larger. Even so the fact that the the binding energy $-E_{*e\text{-}d}$ exceeds the critical value does not change, therefore channels t+p and ^{3}He+n stay closed. The only channel, which stays open, is ^{4}He. However since spin of ^{4}He is zero it is not attracted by *e, but the alpha particle must be emitted with the kinetic energy (22.3MeV.-2(-$E_{*e\text{-}d}$)). The magnetic monopole, which is left alone, proceeds to next job to attract the surrounding fuel nuclei.

7. Remarks and comments

The purpose of this article is two-fold that we provide the necessary tools to describe the nucleon-magnetic monopole system, and point out the existence of various processes which look "peculiar" from the point of view of the nuclear physics where only the protons and the neutrons are the building blocks. In the previous sections, we observed new phenomena which come to exist only when the nuclear reaction proceeds under the influence of the super-strong magnetic Coulomb field produced by the magnetic monopole, briefly. However it is important to point out that the set of these new processes are sufficient to materialize the nuclear fusion reaction at zero incident energy (cold fusion), which cannot occur in the nuclear physics.[5]

There are three main mysteries of the nuclear fusion at zero incident energy, when we see it from the nuclear physics in vacuum. It is well-known experimentally that the final states of the low energy (d + d) reactions in vacuum are (t + p) and (^{3}He + n) with 50% each in the branching ratio. We can understand this fact simply by the energy-momentum conservation and the isotopic invariance. Whereas in the nuclear fusion with zero incident energy, the reaction changes to d + d $\rightarrow$ ^{4}He. We can divide the change of the channels into two mysteries: (1) how the channel d + d $\rightarrow$ ^{4}He opens, and (2) why the main channels (t+p) and (^{3}He+n) are closed. Moreover the third mystery

is (3) why the deuterons of zero incident energy can come close and fuse notwithstanding Coulomb repulsion. Let us consider how these mysteries are resolved when the reaction proceeds under the influence of the super-strong magnetic Coulomb field produced by the magnetic monopole *e.

In general, the reaction of (two-body → one-body) type in vacuum is forbidden , when the reaction is exothermic (Q > 0), since this reaction cannot satisfy energy and momentum conservations simultaneously. To see this, let us consider the reaction in the center of mass system, from the momentum conservation the momentum of the final state particle is $\mathbf{p}_f = 0$, whereas the energy conservation reqires $|\vec{p}_f| = \sqrt{2M_4 Q}$, where M_4 is the mass of the final state particle, therefore the two conservation laws are not compatible in vacuum. On the other hand, if there is an external potential V(r), the momentum conservation is recovered by making the momentum transfer $\mathbf{q} = -\mathbf{p}_f$ to the potential V(r). The probability of the momentum transfer is the square of the scattering amplitude a(q), which relates to V(r) by:

$$a(q) = -(2m/4\pi\hbar)\int d^3r' \exp[i\vec{q}\cdot\vec{r}']V(r') . \qquad (49)$$

In particular for (d + d → ^{4}He), numerical value of the momentum transfer is $|\mathbf{q}|$=422.MeV./c, which corresponds to the wave length λ=3.0fm.. Since Eq.(49) is essentially the Fourier transformation, there is the "uncertainty relation" $q\cdot\Delta r \approx \hbar$ between q, where a(q) has appreciable value, and spread Δr of the potential, in which the potential makes appreciable variation. Therefore the large momentum transfer q means sharply localized potential of the size λ/2π , which is around 0.5fm.. It is remarkable that the potential $V_{*e\text{-}p}$ of Eq.(1), which is the interaction energy of the magnetic dipole moment of the proton in the super-strong magnetic Coulomb field, satisfies the requirement to cause such a large momentum transfer. So the mystery (1) is resolved if the reaction (d + d → ^{4}He) proceeds under the influence of the magnetic monopole.

In section 6, it was explained in some detail how to resolve the mystery(2), by evaluating the binding energy of the *e-d system and by comparing it with the critical values of the thresholds of the continuous spectra of the (t+p) and (^{3}He+n) channels, in which they are 2.03MeV. and 1.75MeV. respectively. In the end part of section 5, how the penetration factors of the second nucleus change, is explained. So the mystery(3) is resolved.

Finally, it is interesting to consider how the kinetic energy of the emitted α-particle is transfered to the lattice. Since the stopping range of ^{4}He is around 100μm, the part of the lattice of this size must be heated up and becomes the hot spot. However the trapping potential of the magnetic monopole by the lattice is proportional to $1/\sqrt{k_B T}$, the magnetic monopole must hop to the neighbouring cooler points when its temperature T goes up. In fact we observe the discrete hot spots spreading on the surface of the cathode if we observe it by using the infra-red camera.

Since the nuclear fusion of the zero incident energy relies on the floating magnetic monopole, which is the rare particle, we cannot start the reaction on demand, but it starts rather sporadic manner. Once the reaction starts it continues for relatively long period until it leaves the trapped cathode. Since the magnetic monopole is the catalyst of the nuclear fusion of zero incident energy, the most important thing is to learn how to control the magnetic monopole.

References

1. P.A.M.Dirac, Proc.R.Soc. London **A133**, 60 (1931);
   J.Schwinger, Science **165**, 757 (1969);
   A,O.Barut, Phys.Rev. **D3**, 1747 (1971);
   T.Sawada, Phys.Lett. **43B**, 517 (1973)
2. T.T.Wu and C.N.Yang, Nucl.Phys. **B107**, 365 (1976)
3. T.Sawada, Foundations of Physics, **23**, 291 (1993)
4. Y.Kazama and C.N.Yang, Phys.Rev. **D15**, 2300 (1977)

Cold Fusion Phenomenon in Open, Nonequilibrium, Multi-component Systems – Self-organization of Optimum Structure

Hideo Kozima

421-1202 Yatsu, Aoi, Shizuoka, 421-1202 Japan

Abstract

The cold fusion phenomenon (CFP) is known to occur only in specific systems (CF materials) satisfying several necessary conditions. One of the most important characteristics, which is sometimes put aside not taken into consideration explicitly, is that the system is open, nonequilibrium, multi-component one where complexity reveals various characteristics including the self-organization to realize an optimum structure favorable to some effects. There have been discovered three empirical laws in the CFP; (1) the stability effect on nuclear transmutation products, (2) the $1/f$ dependence of the frequency of occurrence on the intensity of excess energy production, and (3) bifurcation of the intensity of events (neutron emission and excess energy production) in time. Referring to the suggestion given by the three laws that the cold fusion phenomenon belongs to the complexity induced by nonlinear interactions between agents in CF materials (systems composed of regular arrays of transition metals interlaced with those of hydrogen isotopes), such characteristics of the CFP confirmed by experiments as the threshold value of the ratio of D/Pd or H/Ni about 0.8, favor for higher temperature of the system, occurrence of positive feedback, are explained by self-organization of the superlattice composed of a sublattice of the host element (transition-metal or carbon) and another of the hydrogen isotope (p or d) where the super-nuclear interaction of lattice nuclei mediated by interstitial hydrogen isotopes works to realize the neutron bands.

1. Introduction

The science of complexity has developed in the last half of the 20th century to give a rather more complete perspective of the whole nature including human beings than that depicted by the physical science of simple systems developed since the birth of modern science in the 16th century.

Now, our understanding of nature is not confined to the traditional area of natural science described by linear differential equations but extend to the events determined by nonlinear dynamics without quantitative reproducibility.

As we know from the beginning of the research in the cold fusion phenomenon (CFP), there is no quantitative reproducibility and this fact is used sometimes to denounce the value of the investigation in the CFP. This situation is unreasonable if we

recollect the fact that the qualitative reproducibility or probabilistic law is popular in nuclear physics. One of these examples is the α-decay of $^{226}_{88}$Ra nucleus; We can not predict when a specific nucleus $^{226}_{88}$Ra under investigation will decay to $^{222}_{86}$Rn by emission of $^{4}_{2}$He but we know the constant of the decay describing a statistical law for the temporal variation of the number of $^{226}_{88}$Ra nuclei in a system.

It is interesting to notice the existence of several empirical laws or regularities for physical quantities observed in the CFP [Kozima 2006, 2009, 2010, 2012a]. These laws suggest statistical nature of the events in this field. The laws or regularities can be divided into three; (1) the stability effect on nuclear transmutation products, (2) the $1/f$ dependence of the frequency on the intensity of the excess energy production, and (3) the bifurcation of the intensity of events (neutron emission and excess energy production) in time. Recognizing the existence of these laws in this field, we might be able to take a correct point of view for the science of the cold fusion phenomenon (CFP).

In the investigation of events observed in the CFP, we tend to be fascinated by wonderful facts exceeding our common sense in physics and chemistry and to forget fundamental laws in physics underlying the observed events. One of such laws governing the world of the CFP is thermodynamics. Distribution of interstitial atoms (hydrogen isotopes) in an *fcc* (or hcp) lattice of a host metal (e.g. Pd and Ni or Ti) is determined by a condition that the Helmholtz free energy F should be minimum in the equilibrium condition of a closed system. The Helmholtz free energy $F(V, T)$ is expressed by energy E, entropy S and temperature T of the system as

- $F(V, T) = E - TS.$ (1.1)

In a closed equilibrium system at a constant volume and temperature, the state with minimum free energy F is the most stable one and realized at last. When temperature T is zero, the most stable state is that the energy E minimum. However, a higher entropy state with a higher energy is favorable if temperature T is finite.

Therefore, the distribution of deuterons in an *fcc* Pd lattice in a PdD system (cf. Fig. 1.1) is not confined only to octahedral sites but also to tetrahedral sites at finite temperature and the regular distribution of deuteron is not realized even when the Pd lattice is perfect. This fact should be remembered to investigate multi-particle reactions for nuclear transmutations in the CFP.

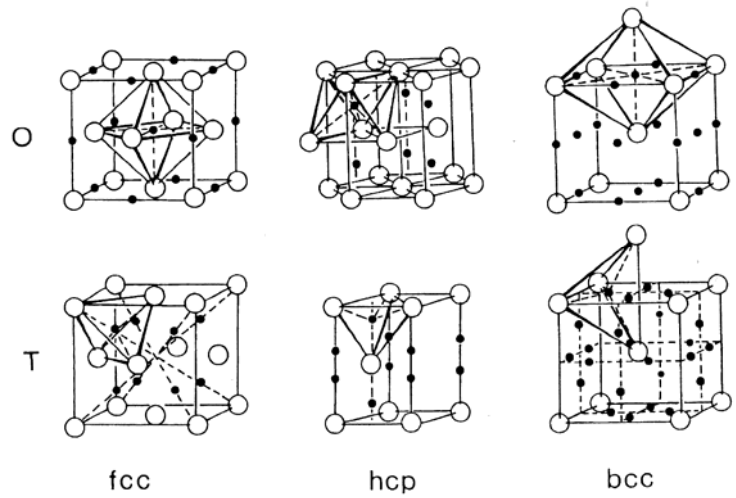

Fig. 1.1 Interstitial sites [octahedral (O) and tetrahedral (T) sites] in *fcc*, *hcp*, and *bcc* lattices [Fukai 2005]

Another fundamental law closely related to events in the CFP is the density dependence of effects in general. It is easy to illustrate several examples of the dependence of an effect y on the density x of an agent causing the effect with a constant c as follows.

1. Single-particle event: $y = cx$ (single-particle events such as the decay of a radioactive nucleus, e.g. α-decay of $^{226}_{88}$Ra)

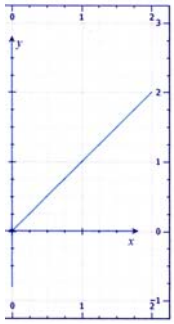

Fig. 1.2 $y = cx$. In the single particle events such as the decay of a radioactive nucleus, the effect y of the event (e.g. emission of alpha particle) is proportional to the density x of the element (e.g. $^{226}_{88}$Ra) causing the effect with a constant c

The effect y (e.g. emission of alphas) is proportional to the density x of the element (e.g. radium nuclei) in the system.

2. Two-body reaction: $y = cx^2$ (e.g. the reaction of two independent particles as (a) the chemical reaction of H and Cl in an aqueous solution of HCl and (b) *d*-*d* fusion

reactions in PdD_x lattice)

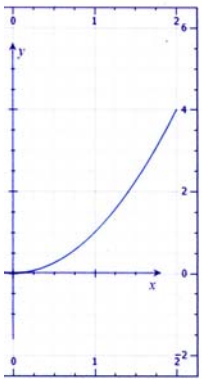

Fig. 1.3 $y = cx^2$. In the cases where the event is caused by two independent elements, the effect y is proportional to the square of the density x of the element with a constant c irrespective of the mechanism causing the event

The effect (e.g. the production of the molecule of HCl in an aqueous solution of HCl or proton and triton pair by a *d-d* fusion reaction) increases as the square (or product) of density (or densities) as shown in Fig. 1.3 without the critical density for the effect. Existence of the critical density in the CFP has been observed in the many experiments and is considered a characteristic of the CFP as illustrated in Fig. 1.7.

3. Four-body reaction: $y = cx^4$ (four-body reaction of independent and equivalent particles in optimum geometrical distribution). Irrespective of the fusion mechanism among four particles (e.g. deuterons) distributed on symmetrical sites, the fusion probability is proportional to x^4 where x is the occupation probability of a particle at the site.

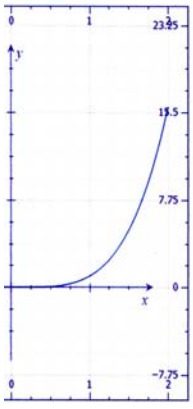

Fig. 1.4 $y = cx^4$. In the cases where the event is caused by four independent elements, the effect y is proportional to the fourth power of the density x of the element with a constant c irrespective of the mechanism causing the event

In this case, the effect remains very small until the density of the agent participating to the reaction reaches at about 0.7 and increases gradually until $x = 1$ and then abruptly. This tendency is rather pronounced in the following cases of six-body and eight-body reactions illustrated only by figures.

4. For six and eight elements (particles) distributed symmetrically, the fusion probabilities are proportional to x^6 and x^8, and are depicted in Figs. 1.5 and 1.6, respectively.

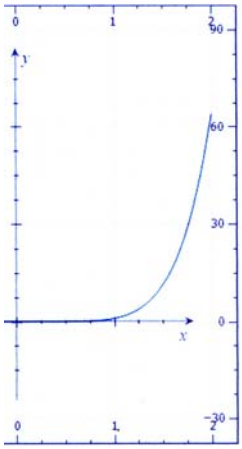

Fig. 1.5 $y = cx^6$. In the cases where the event is caused by six independent elements, the effect y is proportional to the sixth power of the density x of the element with a constant c irrespective of the mechanism causing the event

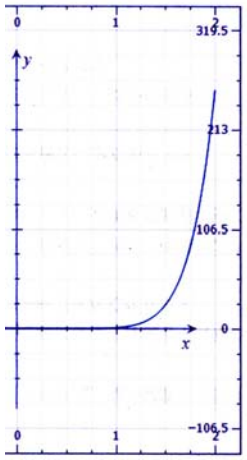

Fig. 1.6 $y = cx^8$. In the cases where the event is caused by eighth independent elements, the effect y is proportional to the eighth power of the density x of the element with a constant c irrespective of the mechanism causing the event

In the cold fusion phenomenon (CFP), we have observed many examples of effect-density relations in this almost a quarter of a century since 1989. The experimental data obtained in this field do not meet with these dependences without criticality shown above in Figs. 1.2 – 1.6 but show the critical behavior that the effect occurs only when the density of H or D in the CF materials exceeds a critical value. This is an obvious indication that the CFP is a cooperative phenomenon but not individual particle one.

An example of typical experimental data of critical behavior showing existence of cooperative phenomenon is the data obtained by an extensive experiment by McKubre et al. [McKubre 1993] shown in Fig. 1.7 where the abscissa is extended to left until

D/Pd = 0.77 to show the criticality more clearly. The compound PdD_x has several phases and α' phase stable at room temperature exists from about $x = 0.6$ to x = 1 as seen in Fig. 1.8.

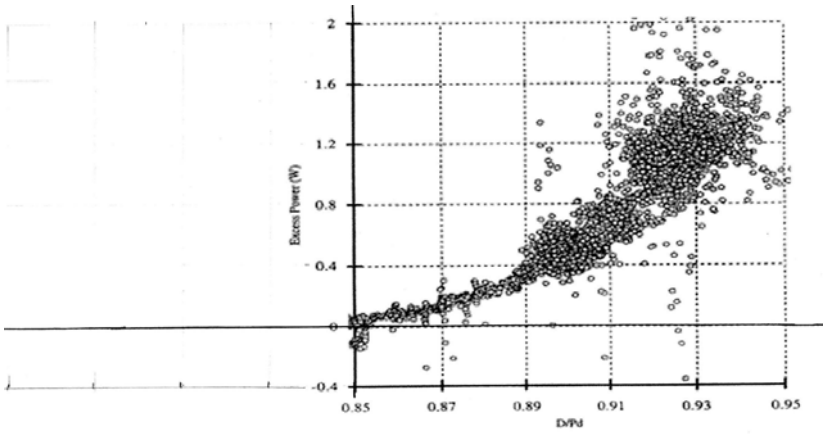

Fig.1.7 Experimental data of excess power vs. D/Pd ratio obtained by McKubre et al. [McKubre 1993]. The abscissa of this figure is extended to left until D/Pd = 0.77 from 0.85 of the original one to show clearly the critical nature of the excess energy generation

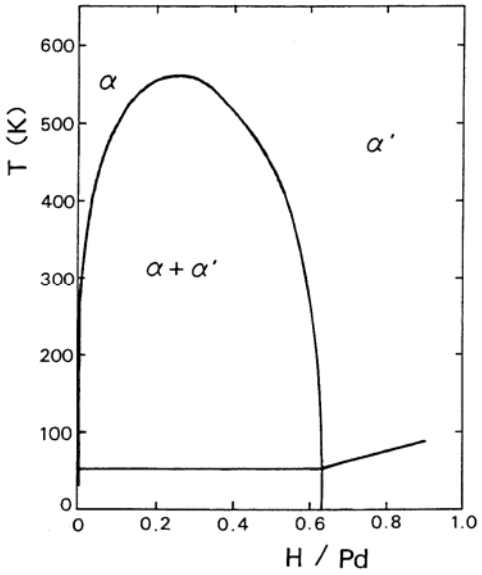

Fig. 1.8 Phase diagram of the Pd-H system which is very similar to that of the Pd-D system [Fukai 2005]

Comparison of Fig. 1.7 with Fig. 1.3 for $y = cx^2$ shows clearly that the reaction resulting in this excess energy generation is not the simple *d-d* fusion reactions often assumed easily in investigations in this field.

Brief survey of the experimental data obtained in the CFP in relation to fundamental laws of physics given above shows us necessity of cooperative consideration for the physics of nuclear reactions in transition metal hydride and deuteride.

We have used phenomenological approach to the CFP for almost more than 20 years using the TNCF model [Kozima 1994] and have given several semi-quantitative explanations for events in this field [Kozima 1998, 2006]. The fundamental premises of the model have been assumed based on the experimental data. The premises on the other hand have been investigated quantum mechanically using such novel knowledge of nuclear physics as exotic nuclei and also of transition metal hydrides as non-local wavefunction of hydrogen isotopes obtained in the last half of 20th century.

One of the fundamental premises of the TNCF model, existence of the trapped neutrons in the metal hydrides, is explained by the neutron band formed as a result of the super-nuclear interaction between lattice nuclei mediated by interstitial protons or deuterons [Kozima 2004, 2006]. As was shown in the trials for neutron band formation, the super-nuclear interaction between neutrons in different lattice nuclei mediated by interstitial protons or deuterons gives an essential effect in the CFP. The super-nuclear interaction, the key concept of the calculation is realized when the superlattice is formed where the sublattice of host metals is interlaced by a sublattice of proton (deuteron) on interstitials. This optimum structure may be realized by self-organization mechanism in the open, non-equilibrium system locally in the CF material but not as a whole. The localization of nuclear reactions observed in the CFP will be related to the localized formation of the optimum superlattice by the self-organization.

We will show indirectly the possible formation of the superlattice by self-organization mechanism in the CFP using known facts related to the complexity.

2. Three Empirical Laws in the CFP deduced from Experimental Data and Their Explanation by Nonlinear Dynamics

In the vast amount of information about events of the CFP obtained in these more than 20 years since 1989, we can recognize several regularities or laws between observables in the CFP. The three laws we have figured out are specified as follows [Kozima 2006, 2008a, 2009, 2010, 2012a]; (1) The stability effect on nuclear transmutation products, (2) the 1/*f* dependence of the frequency of observation on the intensity of the excess energy production, and (3) the bifurcation of the intensity of events (neutron emission and excess energy production) in time. We give a brief explanation for them in this section.

2.1 Stability Law on Nuclear Transmutation Products

If we survey numbers of a specific element produced by the nuclear transmutation in the CFP, we notice that the frequency obtaining the element corresponds to the amount of the element in the universe (e.g. [Suess 1956]). Plotting (i) the number of experiments $N_{ob}(Z)$ where observed an elements ${}_{Z}X$ according to its proton number Z together with (ii) the relative amount $H(Z)$ of the element in the universe in logarithmic scale, we obtain a diagram shown in Fig. 2.1 [Kozima 2006, 2012a]. The coincidence of the numbers (i) and (ii) gives the stability effect on nuclear transmutation products. We may call this regularity the "stability law" for nuclear transmutation in the CFP.

(a)

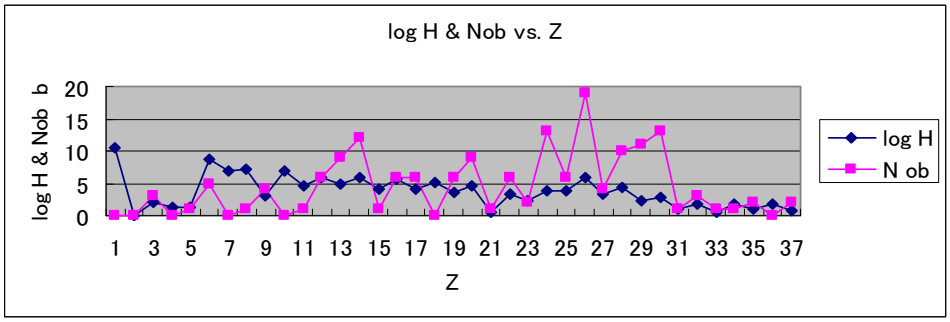

(b)

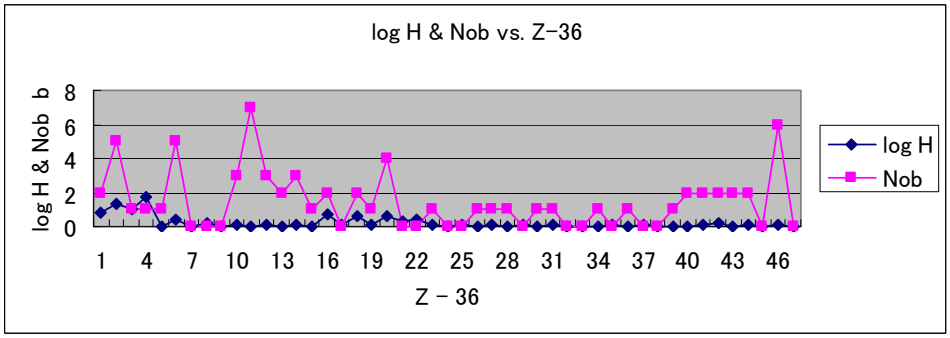

Fig. 2.1. Correspondence between the frequency $N_{ob}(Z)$ observing elements in the CFP and the relative abundances $\log_{10}H(Z)$ of elements in the universe [Suess 1956]: (a) Z = 3 – 38 and (b) Z = 39 – 83 [Kozima 2006]

Another example of this law has been observed by several researchers including Hora et al. [Hora 1998] as shown in Fig. 2.2.

The maxima of $N(Z)$ in many experimental data sets including the data shown in Fig. 2.2 [Hora 1998] rather agree with the magic numbers with exception of the magic number 20 where a clear minimum of $N(Z)$ was observed in all cases. This coincidence of the maxima of $N(Z)$ and the magic numbers is another example of the stability effect

on the nuclear transmutation in the CFP. The exceptional case of $Z = 20$ needs another factor for explanation.

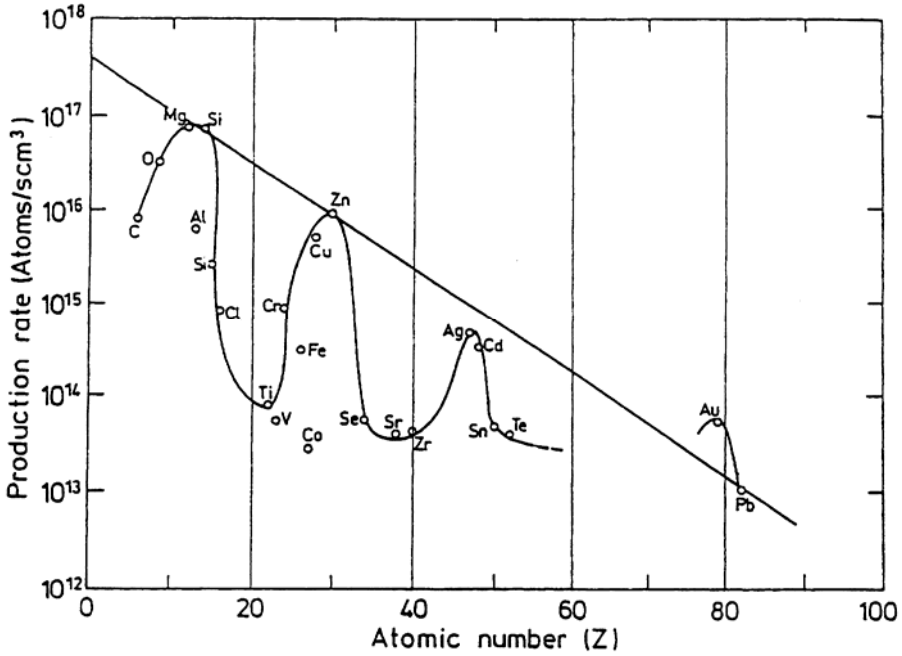

Fig. 2.2 Measured production rate $N(Z)$ of the atom with a proton number Z for the nuclear transmutation vs. the atomic number Z in PdH_x where exponential decay of the maxima on Z follows a relation of an equation $N(Z) = N'\exp(-Z/7.86)$ with $N' = 3.56 \times 10^{17}$ atoms/cm^{3}s [Hora 1998 (Fig. 1)]. The maxima of $N(Z)$ agree with the magic numbers except $Z = 20$.

This law (Stability Law) shows that the stability of a nucleus reveals its nature in the cf-material composed of high density neutrons in the neutron valence band [Kozima 2006 (Sec. 2.4.2)] and spring out as a nucleus just as in the case of nuclear transformation in stars

2.2 Inverse Power Dependence of the Frequency of Observations on the Intensity of Excess Energy Production

In several experimental data sets, we are able to count numbers N_Q of experiments where observed a specific amount Q of excess energy per a definite number of host atoms in CF materials. When we plot them as a function of Q, we obtain N_Q vs. Q plots [Kozima 2006 (Sec. 2.12), 2008a, 2008b, 2012a]. The first plot was obtained for the data by McKubre et al. [McKubre 1993] as shown in Fig. 2.3. This plot clearly shows that there is an inverse power relation of frequency vs. intensity with an exponent of 1.0

famous in the field of complexity [Milotti]. This regularity may be called the "inverse power law" for the frequency on the intensity of the excess energy production.

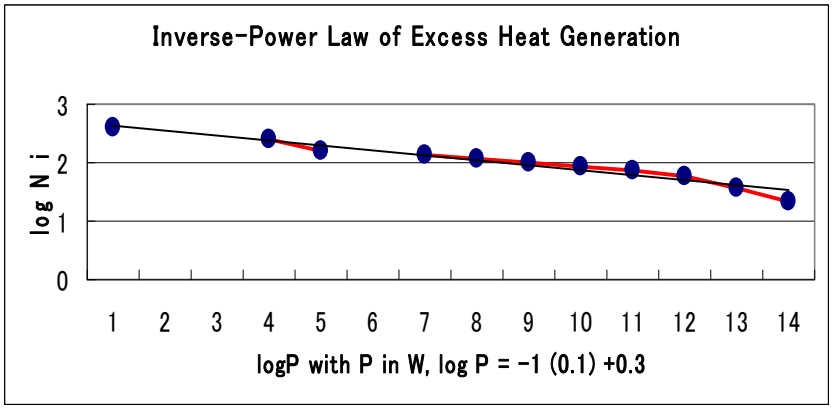

Fig. 2.3. Inverse power law revealed by excess power generation measured by McKubre et al. [McKubre 1993]

Another example of this law is obtained for the data obtained by Kozima et al. [Kozima 2008c] as depicted in Fig. 2.4. In this case, the exponent of the dependence is 2.

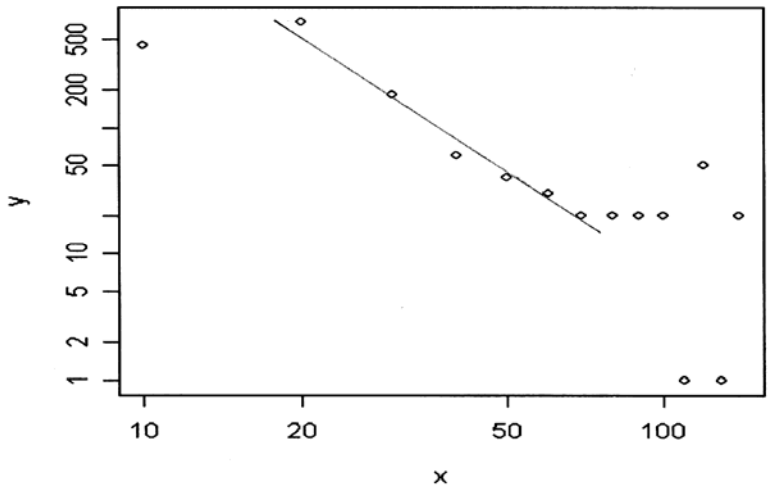

Fig. 2.4. Distribution of the frequency N_p (= y) producing excess power P_{ex} (= x). To depict log-log curve, values of N_p and P_{ex} were arbitrarily multiplied by 10^n (x = 100 in this figure corresponds to P_{ex} = 1 W) [Kozima 2008c]

On the other hand, H. Lietz [Lietz 2008] tried to check the inverse power law using the data accumulated by E. Storms in his book [Storms 2007]. The resulting plot by H.

Lietz is given in Fig. 2.5 which shows the exponent of 1.0.

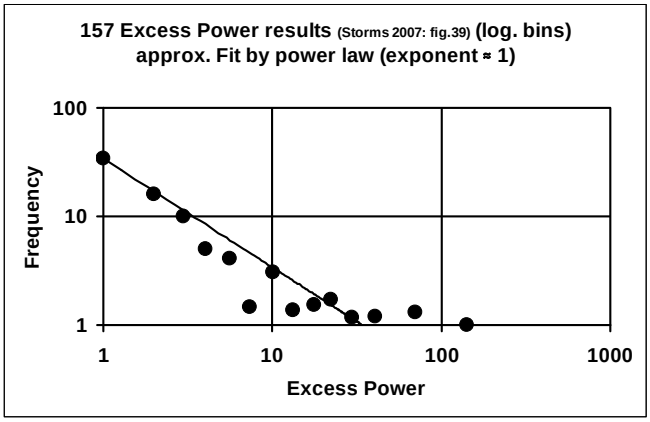

Fig. 2.5. Distribution of 157 excess energy results by Lietz [Lietz 2008] using the data collected by Storms [Storms 2007]. Values have been stored in bins of size 10. The line shows a power-law fit to the binned data with an exponent of 1.0 (r^2 = 90%) (Fig. 3 of [Lietz 2008])

Therefore, we may conclude that the excess energy generation in the CFP satisfies the inverse power law and is governed by a statistical law popular in complexity.

2.3 Bifurcation of the Intensity of Events (Neutron Emission and Excess Energy Production) in Time

The third law in the CFP is a little subtle compared with the former two [Kozima 2012a]. Even if the number of examples is scarce, we have several fortunate data sets of temporal evolution of effects in the CFP. The first one is that of neutron emission from TiD_x obtained by De Ninno et al. in 1989 [De Ninno 1989]. The data are shown in Figs. 2.6 and 2.7.

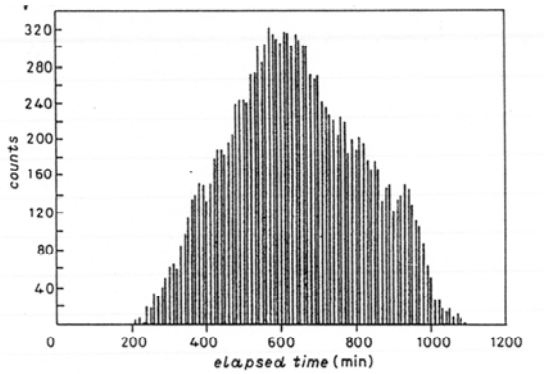

Fig. 2.6. Diagram showing the time evolution of the neutron emission from TiD_x sample during the run *A* (April 15-16, 1989). The values indicated are integral counts over periods of ten minutes [De Ninno 1989]

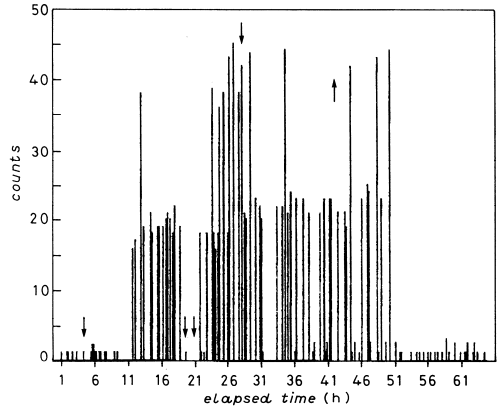

Fig. 2.7 Diagram showing the time evolution of the neutron emission counts (ordinate) during the run B (7-10 April, 1989) by De Ninno et al. The values indicated are integral counts over periods of 10 minutes [De Ninno 1989]

Another data set is the excess energy generation observed by McKubre et al. as shown in Fig. 2.8 [McKubre 1993].

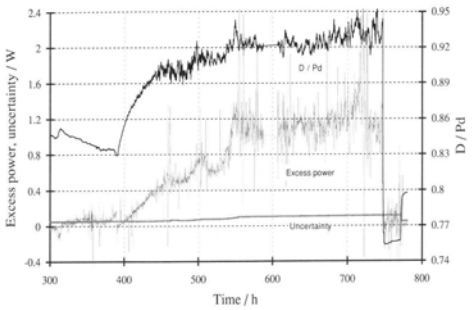

Fig. 2.8 Variations of Excess Power, Uncertainty and Loading ratio [McKubre 1993].

Furthermore, we can cite another example of the temporal evolution of excess energy generation measured by Kozima et al. in Fig. 2.9 [Kozima 2008c].

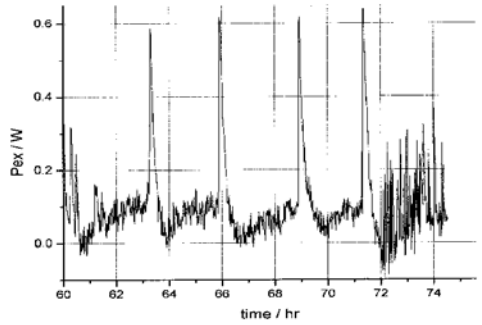

Fig. 2.9 Excess power pulses during a 14 hour period of an experiment (070108) of Kozima et al. which lasted 12 days as a whole [Kozima 2008c]

By the nature of events in complexity, we can give only qualitative explanation of experimental result [Kozima 2008a, 2008b] in analogy to the mathematical results of numerical calculations using the logistic difference equation [Gleick 1987]. The analogical explanations of the laws observed in the CFP will be given in the next section using the nature of an equation of nonlinear dynamics and Feigenbaum's theorem [Feigenbaum 1978].

3. Cold Fusion Material as Open, Nonequilibrium, Multi-component System

We have had enough experience to deduce a few general conclusions on the behavior of cold fusion materials where occurs the cold fusion phenomenon (CFP), i.e. phenomenon including nuclear reactions and accompanying events occurring in solids with high densities of hydrogen isotopes (H and/or D) in ambient radiation belonging to Solid-State Nuclear Physics (SSNP) or Condensed Material Nuclear Science (CMNS).

Several of their characteristics may be listed up as (1) co-existence of host transition metals (or noble metals or carbon) and hydrogen isotopes (protium and/or deuterium), (2) higher ratio of hydrogen to host concentrations, (3) nonequilibrium situation, (4) existence of thermal neutrons, (5) higher temperature of the sample, (6) positive feedback to enhance effects [Kozima 2012b].

The similarity of some behaviors of events in the CFP to those of the nonlinear dynamics shown in the preceding section gives us temptation to investigate the cold fusion materials from a viewpoint related to nonlinear dynamics resulting in complexity.

Some characteristics of complexity we have met in natural phenomena are listed up as follows in relation to the CFP. (i) Self-organization in open, nonequilibrium systems (cf. Sec. 3.3), (ii) bifurcation of possible states (cf. Sec. 3.2), (iii) chaotic behavior of events lacking quantitative reproducibility (cf. Sec. 3.2). The well-known examples of the first are the convection (Bénard) cells in fluid dynamics and Zhabotinsky reaction in chemical reaction. An example of the bifurcation is given by a simple logistic difference equation (l.d.e.) as shown in Fig. 3.4 below. A typical example of the third characteristic is the so-called "butterfly effect" showing uncontrollable effects of a minor change of a part of a system on the tremendous change on the long-range behavior of the system.

We investigate the characteristics of CF systems from the viewpoint of complexity.

3.1 High D/Pd and H/Ni Ratios and High Temperature of Samples

It is fairly well known that it is necessary to have a higher D/Pd (or H/Ni) ratio than

a critical (or threshold) value around 0.8. One of the best known examples was given very early in this field by McKubre et al. (cf. Fig. 1.7) [McKubre 1993]. On the other hand, as we know from many experimental data, it is desirable to have higher temperature of samples to realize pronounced effects in the CFP (e.g. [McKubre 1993]). One of the recent data is given by Celani et al. [Celani 2010].

Furthermore, it is noticed that there is a preferable combination of host metals and hydrogen isotopes; Pd and D, Ni and H, Ti and D are best combinations of elements for the CFP [Kozima 2000].

In the experimental data obtained in metal-hydrogen systems, we have vast number of experimental results concerning properties of hydrogen isotopes in transition metals. We can cite here data on the diffusion of D and H in Ni and Pd as shown in Figs. 3.1 and 3.2, respectively [Birnbaum 1972].

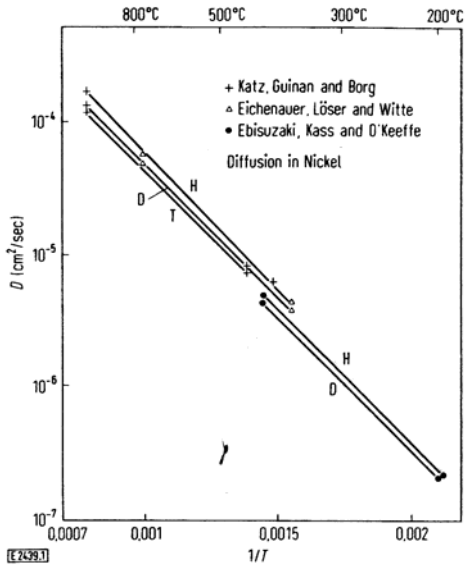

Fig. 3.1 Diffusion coefficients of hydrogen, deuterium and tritium in nickel [Birnbaum 1972]

It is seen in Fig. 3.1 that protium diffuses faster than deuterium in Ni as usually expected by the lighter mass of the former in the whole temperature range from 200 to about 1000 ºC. On the other hand, as we see in Fig. 3.2, the situation in the case of Pd is very different from that in Ni and other ordinary metals. In this case, deuterium is more diffusive than protium in the room temperature range from –73 up to about 200 ºC but is normal in higher temperature range than 200 ºC.

This peculiar behavior of deuterium in Pd is closely related to the CFP in palladium hydrides and deuterides from our point of view. Usually, the CFP is observed in the latter and the former is sometimes used as the blank for the latter. In the higher

temperatures than 200 ºC, however, we can expect the CFP in the former as well as latter which will be checked easily. This point has been partially confirmed by Hioki et al. by experiments using Pd nano-particles in zeolite and FSM (Folded Sheet meso-porous Material) [Hioki 2013]. They observed excess energy production in both hydride and deuteride specimens a little higher value in the latter at room temperature. This fact clearly discards the *d-d* fusion reactions as the principal cause of excess energy generation in the CFP which are not effective in transition-metal hydrides.

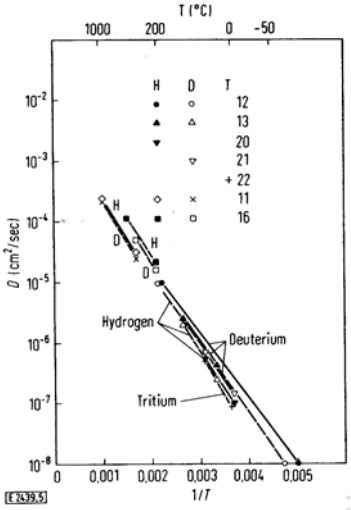

Fig. 3.2 Diffusion of isotopes of hydrogen in palladium [Birnbaum 1972]

Therefore, we have to rely on another mechanism effective for explanation of various events both in deuterium and protium systems such as proposed by us [Kozima 1998, 2006]. The proposed mechanism becomes effective when there is a regular superlattice composed of interlaced sublattices of the host metal (e.g. Pd or Ni) and the hydrogen isotope (D or H). The self-organization of Pd-D or Ni-H lattice in an open, nonequilibrium condition of gas-contact or electrolytic systems serves to realize the superlattice favorable for the mechanism proposed in our papers for the CFP [Kozima 2006 (Sec. 3.7)]. The investigation of the condition to make the self-organization process effective to obtain more complete superlattice structure of interlaced sublattices of host and hydrogen isotope is inevitably qualitative due to the nature of complexity as we know well.

3.2 Positive Feedback for Nuclear Reactions

The change of surface morphology and rare experiences of explosion in CF experiments discussed in other papers [Kozima 2007, 2010, 2011, Smedley 1993] may be an evidence of positive feedback of a parameter (or parameters) for the CFP.

It is possible to contemplate a mechanism of positive feedback of nuclear reactions, if we can identify the parameter n_n in the TNCF model with the variable x_n of the logistic difference equation (l.d.e.);

$$x_{n+1} = b\, x_n(1 - x_n) \quad (n = 0, 1, 2, \text{---}) \tag{3.1}$$

used to describe the bifurcation diagram by J. Gleick [Gleick 1987] (cf. Fig. 3.4).

The scenario goes as follows. By any chance, we have a situation in a CF material in which cf-material is formed in a localized region at surface layers. An alien nucleus in one of the regions interacts with a neutron or a neutron-proton cluster ${}^{A}_{Z}\delta$ and liberates a definite energy [Kozima 2011]. The liberated energy heats up the temperature of the region increasing the value of n_n. The elevated value of n_n increases the reaction probability and the temperature is elevated further. However, this feedback process does not continue without limit. If the temperature becomes too high, the favorable superlattice of the interlaced sublattices of host and hydrogen isotope is destroyed by thermal motion of the nuclei. This destroys the super-nuclear interaction between adjacent lattice nuclei and decreases n_n. This variation of the parameter n_n should be similar to the variation of the recursion function $f(p)$ depicted in Fig. 3.3 (cf. Eq. (3.3)).

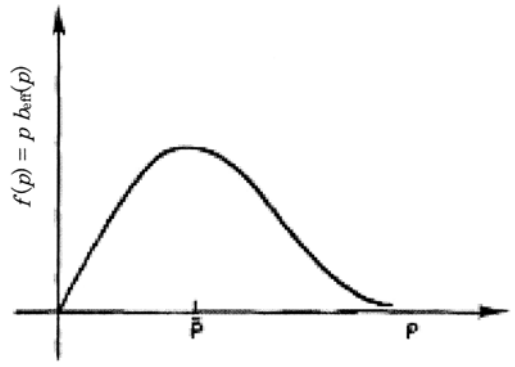

Fig. 3.3 Dependence of the recursion function f in the recursion relations $f(p) = p \cdot b_{\text{eff}}(p)$ on the variable p [Gleick 1987]

The relation

$$f(p) = p \cdot b_{\text{eff}}(p) \tag{3.2}$$

depicted in Fig. 3.3 reduces to the l.d.e. (3.1) $x_{n+1} = b\, x_n(1 - x_n)$, if we take

$$b_{\text{eff}}(p) = b(1 - p). \tag{3.3}$$

Then, the Feigenbaum's theorem says that the bifurcation diagram depicted in Fig. 3.4 describes possible behavior of the CFP assimilated by Eq. (3.1). The parameter b in the l.d.e. (3.1) may be determined by atomic and nuclear states of the surface region of CF materials. The appearance of different features in the CFP as shown in Figs. 2.6 – 2.9 corresponds to different values of the parameter b depending on each situation. It

will be the next step of our future work to clarify nature of the parameter *b* in the CFP and to control the phenomenon as freely as possible.

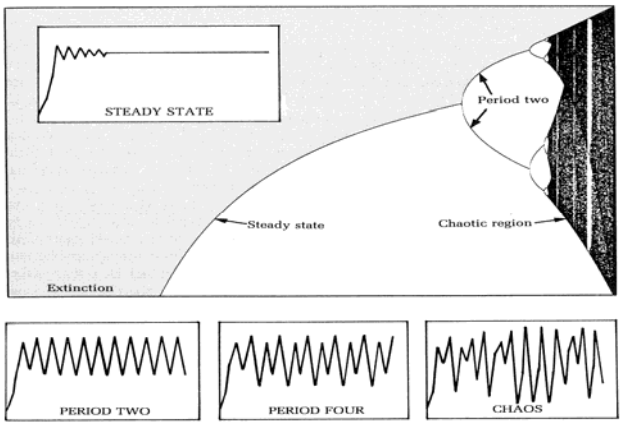

Fig. 3.4 Bifurcation diagrams to show period-doubling and chaos [Gleick 1987]. The main figure depicts x_∞ vs. parameter b, x_∞ on the ordinate (x_∞ is x_n at $n = \infty$) and b of the logistic difference equation, $x_{n+1} = b\, x_n (1 - x_n)$ $(0 < x_0 < 1)$, on the abscissa. The inserted figures, a) Steady state, b) Period two, c) period four, and d) chaos, depict variations of x_n with increase of suffix n (temporal variation if n increases with time) for four values of b; a) $1 < b < 3$, b) $3 < b < 3.4$, c) $b \simeq 3.7$, d) $4 < b$ The region a), b) and d) correspond to "Steady state", "Period two" and "Chaotic region" in the main figure, respectively [Kozima 2012a]

3.3 Self-organization of Optimum Structure (Superlattice) of CF Materials

In the equilibrium state at $T \neq 0$, a state with the entropy $S > 0$ is favorable even if the energy E of the state is higher than the state with $S = 0$ because the equilibrium condition demands that the Helmholtz free energy $F(V, T)$ minimum at constant temperature and volume (Eq. (1.1) recited as Eq. (3.5)) :

$$dF = -p\, dV - S dT = 0, \tag{3.4}$$

$$F(V, T) = E - TS. \tag{3.5}$$

In an open, nonequilibrium condition, it is possible to realize a state with $S = 0$, or a state with perfectly regular array of atoms by self-organization at finite temperature. There are several examples of self-organization in physics, chemistry, biology, and others as illustrated below.

In the open and non-equilibrium dynamical system where energy and component materials are fed from outside, there appears patterns energetically unstable compared to the homogeneous structure without any structure. We can give several examples observed in nature as illustrated in Figs. 3.5 – 3.7.

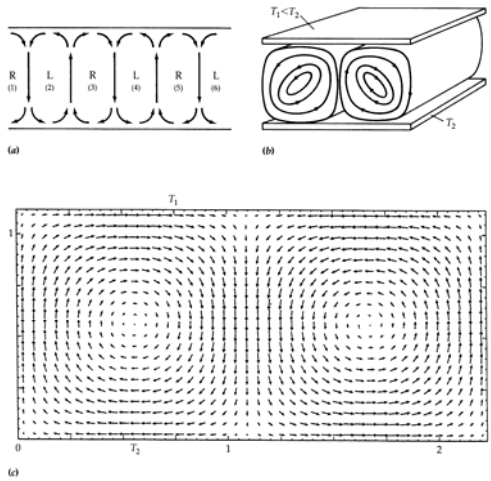

Fig. 3.5 Two views of convection (Benard) cells (a) and (b) and complexity and long-range order out of molecular chaos in a system under nonequilibrium constraint (c) [Nicolis 1989]

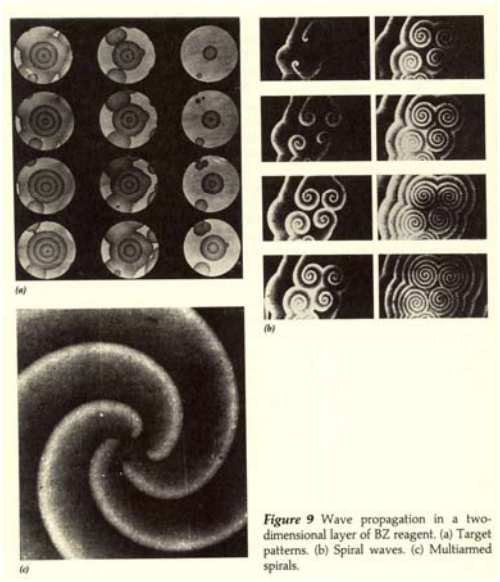

Fig. 3.6 Belousov-Zhabotinski (BZ) reaction [Nicolis 1989]

Fig. 3.7 Cell populations of Dictyostelium discoideum on an agar surface [Nicolis 1989]

In the case of the CFP, the optimum superlattice of the host lattice nuclei (e.g. Pd) and hydrogen isotopes (e.g. D) is apt to be formed in localized regions at surface layers with a width of about several microns where the number ratio $\eta = N_d/N_{\mathrm{Pd}}$ of the hydrogen isotope d and the host metal Pd is expected higher than other parts of the sample. Experimental data show that the formation of superlattice is possible when η becomes larger than ~ 0.8. The superlattice may be localized in small region with a diameter of about several micrometers as experimental facts show.

We can give a schematic structure of the superlattice in Fig. 3.8. In reality, the

wavefunctions of hydrogen isotopes (*d* or *p*) centered at interstitials overlap with nuclear wavefunctions of lattice nuclei Pd (Ni) centered at lattice points. Then, the contact nuclear interaction between them makes possible the super-nuclear interaction between neutrons in the lattice nuclei on lattice points as explained below in Fig. 3.9 [Kozima 2006 (Sec. 3.7)].

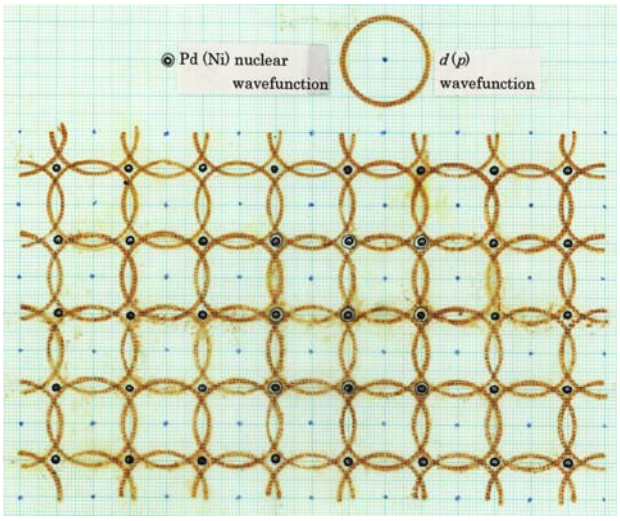

Fig. 3.8 Schematic diagram showing the optimum superlattice of host nuclei (Pd or Ni) at lattice points and hydrogen isotopes (*d* or *p*) at interstitials formed by self-organization in the open, non-equilibrium condition. Nuclear wavefunctions with extension of only a few femtometers of lattice nuclei are exaggerated largely to be seen on the figure. The extension of deuteron (proton) wavefunctions centered at interstitials is represented by a single circle in contact with nuclear wavefunctions at nearest lattice points

When the superlattice is formed at localized regions in the surface layer, it is possible to appear the neutron valence band by the super-nuclear interaction between neutrons in different lattice nuclei mediated by interstitial hydrogen isotopes as illustrated in Fig. 3.9 [Kozima 2006].

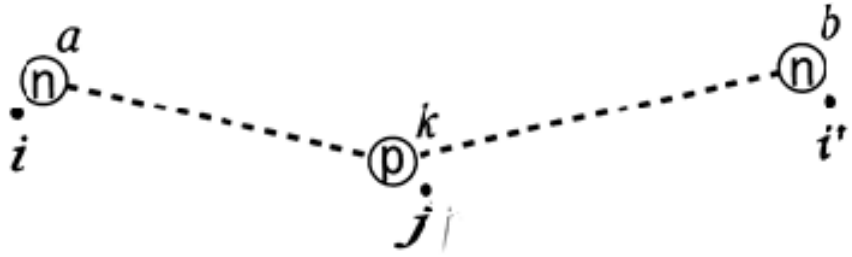

Fig. 3.9 Super-nuclear interaction of two neutrons in different lattice nuclei at site ***i*** an ***i'*** mediated by interstitial protons at sites ***j***'s [Kozima 2006]

The number of states in a neutron valence band formed in a localized cube with side lengths of 10 μm (10^{-5} cm) is about 10^9 because it is the number of neutrons from the lattice nuclei with a lattice constant of 1 A (= 10^{-8} cm) and it should be the number of states in the band (for instance [Seitz 1940 (Sec. 60)]). So, the neutron state density N_n in the localized superlattice is $\sim 10^9 \times 1/(10^{-5})^3 = 10^{24}$ cm^{-3} when the band is fully occupied by neutrons. The TNCF model comparison with experimental data sets has given the neutron number density n_n of about $10^7 \sim 10^{10}$ cm^{-3} for the CFP [Kozima 2006 (Table 2.2)] which seems not inadequate in view of the number of states in the neutron valence band formed at the localized superlattice.

This ratio $n_n/N_n = 10^{-17} \sim 10^{-12}$ is consistent with the assumption of the TNCF model that the trapped neutron behaves as thermal neutrons in the nuclear reactions with other nuclei (cf. electrons in a conduction band of intrinsic semiconductors).

The choice of the side length of 10 μm (10^{-3} cm) for the localized superlattice is based on the experimental facts that nuclear products observed in the CFP are localized in areas of width about a few micrometers in surface layer of a few micrometer depth. Recent experimental data obtained by Hioki et al. suggest Pd nanoparticles with diameters of a few nanometers occluding H or D atoms have shown excess energy generation [Hioki 2013]. This data may suggest existence of the superlattice of Pd-D and Pd-H in surface regions with rather small diameters of about a few nanometers.

When the optimum superlattice is formed at least locally by the self-organization mechanism as observed in the complexity, the super-nuclear interaction illustrated in Fig. 3.9 generates the neutron balance band and realizes the trapped neutrons in the band as assumed in the TNCF model for the CFP.

4. Conclusion

The non-equilibrium condition, one of the necessary conditions for the CFP in the transition-metal hydrides and deuterides, has been investigated from our point of view that the CFP is a phenomenon realized as a complexity consistently with other knowledge of physics of the CFP related to the situation where occurs various nuclear events in the CF materials.

The three empirical laws [Kozima 2012a] explained in this paper suggest that the cold fusion phenomenon (CFP) is characterized by complexity [Gleick 1987]. One of the characteristics of complexity is qualitative reproducibility which is also recognized as a characteristic of the CFP.

The characteristics of complexity include self-organization, bifurcation and chaos.

We have shown examples of experimental events observed in the CFP for the latter two characteristics in our papers [e.g. Kozima 2012a] and also in Sec. 2 of this paper. The first one, however, is not observed directly in the CFP by experiment. Formation of favorable structure for the CFP in the open and nonequilibrium systems (CF materials) may be closely related to the self-organization of a superlattice (double regular arrays) composed of sublattices of host nuclei and hydrogen isotopes, e.g. PdD or NiH, from our point of view. If this is the true scenario for the CFP, it is understandable that the occurrence of the events in this field is subtle and is only qualitatively reproducible as our experience in this field tells us.

It might be possible to show possible realization of super-nuclear interaction [Kozima 2004, 2006] between neighboring lattice nuclei by computer simulation. A simplified schedule can be realized by assuming an *fcc* sublattice of a host nuclei ${}^{A}_{Z}X$ interlaced by another sublattice composed of protons (or deuterons) at octahedral interstitials of the former sublattice. The nucleus ${}^{A}_{Z}X$ has a neutron in the evaporation level with a wavefunction ψ_n extended out beyond ordinary nuclear radius R_0. The proton (or deuteron) centered at an interstitial point is assumed in a level with a wavefunction φ_p (or φ_d) extending out to overlap with the neutron wavefunction ψ_n. The super-nuclear interaction between adjacent lattice nuclei mediated by interstitial proton (or deuteron) is a key factor for the explanation of the CFP common in protium and deuterium systems. It is desirable to check this possibility by simulation to develop the physics of the CFP and will be one of our future projects.

Acknowledgement

The author would like to express his thanks to F. Celani for making possible to use their data [Celani 2010] in this paper.

References

[Birnbaum 1972] H.K. Birnbaum and C.A. Wert, “Diffusion of Hydrogen in Metals” *Berichte der Bunsen-Gesellschaft*, **76-8**, 806 – 817 (1972).

[Celani 2010] F. Celani, P. Marini, V. di Stefano, M. Nakamura, O. M. Calamai, A. Spallone, A. Nuvoli, E. Purchi, V. Andreassi, B. Ortenzi, E. Righi, G. Trenta, A. Mancini, A. Takahashi, and A. Kitamura, “First measurement on nano-coated Ni wire, at very high temperature, under, He, Ar, H_2, D_2 atmosphere and their mixtures,” Paper presented at 9th International Workshop on Anomalies in Hydrogen/Deuterium Loaded Metals, Pontignano 17-19 Sept, 2010.

[De Ninno 1989] A. De Ninno, A. Frattolillo, G. Lollobattista, G. Martinio, M. Martone,

M. Mori, S. Podda and F. Scaramuzzi, "Evidence of Emission of Neutrons from a Titanium-Deuterium System," *Europhys. Lett*. **9**, 221 – 226 (1989).

[Gleick 1987] J. Gleick, *Chaos*, Penguin books, 1987. ISBN 0-14-00.9250-1.

[Feigenbaum 1978] 2.10 M.J. Feigenbaum, "Quantitative Universality for a Class of Nonlinear Transformations," *J. Statistical Physics,* **19**, 25 – 52 (1978).

[Fukai 2005] Y. Fukai, *The Metal-Hydrogen System*, Springer, Berlin 2005. ISBN10 3-540-00494-7

[Hioki 2012] T. Hioki, N. Sugimoto, T. Nishi, A. Itoh and T. Motohiro, "Influence of Pd Particle Size on Isotope Effect for Heat Generation upon Pressurization with Hydrogen Isotope Gases," *Proc. JCF13* (to be published in 2013).
http://jcfrs.org/file/jcf13-proceedings.pdf
And also *Abstract of JCF13*, **13-17** (2012).

[Hora 1998] H. Hora G.H. Miley, J.C. Kelly and Y. Narne, "Nuclear Shell Magic Numbers agree with Measured Transmutation by Low-Energy Reactions," *Proc. ICCF7*, pp. 147 – 151 (1998).

[Kozima 1994] H. Kozima, "Trapped Neutron Catalyzed Fusion of Deuterons and Protons in Inhomogeneous Solids," *Trans. Fusion Technol.* **26-4T**, pp. 508 – 515 (1994). ISSN: 0748-1896.

[Kozima 1998] H. Kozima, *Discovery of the Cold Fusion Phenomenon*, Ohtake Shuppan, Tokyo, Japan, 1998. ISBN 4-87186-044-2.

[Kozima 2000] H. Kozima, "Electroanalytical Chemistry in Cold Fusion Phenomenon," in *Recent Research Developments in Electroanalytical Chemistry,* Edited by S.G. Pandalay, Vol. 2, pp. 35 – 46 (2000). ISBN; 81-86846-94-8.
And also *Reports of CFRL* (*Cold Fusion Research Laboratory*), **12-2**, 1 – 11 (2007).
http://www.geocities.jp/hjrfq930/Papers/paperr/paperr.html

[Kozima 2004] H. Kozima, "Quantum Physics of Cold Fusion Phenomenon," *Developments in Quantum Physics Researches – 2004,* pp. 167 – 196, ed. V. Krasnoholovets, Nova Science Publishers, Inc., New York, 2004. ISBN 1-59454-003-9

[Kozima 2006] H. Kozima, *The Science of the Cold Fusion Phenomenon*, Elsevier Science, 2006. ISBN-10: 0-08-045110-1.

[Kozima 2007] H. Kozima, "Six Sketches on Complexity and Wavefunctions in the Cold Fusion Phenomenon," *Reports of CFRL* (*Cold Fusion Research Laboratory*), **5-1**, 1 (2007). http://www.geocities.jp/hjrfq930/Papers/paperr/paperr.html

[Kozima 2008a] H. Kozima, "The Cold Fusion Phenomenon as a Complexity (2) – Parameters Characterizing the System where occurs the CFP –," *Proc. JCF8* (Nov. 29 – 30, 2007, Kyoto, Japan), pp. 79 – 84 (2008). http://jcfrs.org/file/jcf8-proceedings.pdf

[Kozima 2008b] H. Kozima, "The Cold Fusion Phenomenon as a Complexity (3) – Characteristics of the Complexity in the CFP –," *Proc. JCF8* (Nov. 29 – 30, 2007, Kyoto, Japan), pp. 85 – 91 (2008). http://jcfrs.org/file/jcf8-proceedings.pdf

[Kozima 2008c] H. Kozima, W.W. Zhang and J. Dash, "Precision Measurement of Excess Energy in Electrolytic System Pd/D/H_2SO_4 and Inverse-Power Distribution of Energy Pulses vs. Excess Energy," *Proc*. *ICCF13*, pp. 348 – 358 (2008).
ISBN 978-5-93271-428-7.

[Kozima 2009] H. Kozima, "On the Methodology of the Cold Fusion Research" *Reports of Cold Fusion Research Laboratory* (*CFRL*) **9-5**, pp. 1 – 39 (November, 2009).
http://www.geocities.jp/hjrfq930/Papers/paperr/paperr.html

[Kozima 2010] H. Kozima, "Complexity in the Cold Fusion Phenomenon,**"** *Proc. ICCF14* (August 10 – 15, 2008, Washington D.C., USA), Eds. J. Nagel and M.E. Melich, pp. 613 – 617 (2010). ISBN 978-0-578-06694-3.

[Kozima 2011] H. Kozima, "Localization of Nuclear Reactions in the Cold Fusion Phenomenon," *Proc. JCF11* pp. 59 – 69 (2011).
http://jcfrs.org/file/jcf11-proceedings.pdf

[Kozima 2012a] H. Kozima, "Three Laws in the Cold Fusion Phenomenon and Their Physical Meaning," *Proc. JCF12*, pp. 1 – 14 (2012).
http://jcfrs.org/file/jcf12-proceedings.pdf
And also *Reports of CFRL* (*Cold Fusion Research Laboratory*), **11-6**, 1 – 14 (2011).
http://www.geocities.jp/hjrfq930/Papers/paperr/paperr.html

[Kozima 2012b] H. Kozima, "Cold Fusion Phenomenon in Open, Non-equilibrium, Multi-component Systems," *Reports of CFRL* (*Cold Fusion Research Laboratory*), **12-1**, 1 – 14 (2012). http://www.geocities.jp/hjrfq930/Papers/paperr/paperr.html

[Lietz 2008] H. Lietz, "Status of the Field of Condensed Material Nuclear Science", Working Paper, Mittweida University, August 2008.

[McKubre 1993] M.C.H. McKubre, S. Crouch-Baker, Riley, S.I. Smedley and F.L. Tanzella, "Excess Power Observed in Electrochemical Studies of the D/Pd System," *Proc. ICCF3* (Oct. 21 – 25, 1992, Nagoya, Japan) pp. 5 - 19, Universal Academy Press, Inc., Tokyo, 1993. ISSN 0915-8502.

[Milotti] E. Milotti, "*1/f* Noise: a Pedagogical Review"
http://arxiv.org/ftp/physics/papers/0204/0204033.pdf

[Nicolis 1989] G. Nicolis and I. Prigogine, *Exploring Complexity,* W.H. Freeman and Co., N.Y. 1989. ISBN0-7167-1859-6.

[Seitz 1940] F. Seitz, *The Modern Theory of Solids*, McGraw Hill, New York, 1940.

[Smedley 1993] S.I Smedley, S. Crouch-Baker, M.C.H. McKubre and F.L. Tanzella,

"The January 2, 1992, Explosion in a Deuterium/Palladium Electrolytic System at SRI International," *Proc. ICCF3* (Oct. 21 – 25, 1992, Nagoya, Japan) pp. 139 - 151, Universal Academy Press, Inc., Tokyo, 1993. ISSN 0915-8502.

[Storms 2007] E. Storms, *The Science of Low Energy Nuclear Reaction*, World Scientific, Singapore, 2007, ISBN-10; 981-270-620-8.

[Suess 1956] H.E. Suess and H.C. Urey, "Abundances of the Elements," *Rev. Mod. Phys*. **28**, pp. 53 – 74 (1956).

Macroscopic view of electrified and magnetized interface under long-term evolution of deuterium in 0.1M LiOD -Evaluation of electrode potential and magnetic flux density of electrode/electrolyte interface-

Hiroo NUMATA
Tokyo Institute of Technology, 2-12-1, O-okayama, Meguro Tokyo 152-8552 Japan

Abstract: In the cold fusion experiment, there observed vortex patterns on a thick Pd electrode surface during long-term electrolysis in 0.1M LiOD. To understand the peculiar phenomenon, we had proposed N-cycle model, which is composed of four sequential processes including the CF reaction. Supposing that the hypothetical particles mass evolved due to the CF reaction energy, we performed PC numerical simulation to obtain vortices pattern in the simulation space. In the simulation, the electric and magnetic field of the electrode/electrolyte interface play an important role. To evaluate such influences on the CF reaction, we have examined the structures of the electrode/electrolyte interface with and without deuterium bubble formation. More data compilation with respect to the magnetic property and that of the sub-surface layer is required to perform more accurate simulation incorporating the structure of the layer and the influence of the magnetic field.

Key words: Cold fusion, Nuclear reaction cycle model, vortex, electric field, magnetic field, electrode/electrolyte interface

1 Introduction

During long-term electrolysis for well annealed thick Pd rod (9.0 mmϕ) in 0.1M LiOD, vortex pattern was observed on the electrode surface[1-2]. The morphology of postelectrolysis Pd revealed the two long faults without any cracks on the surface. Since the formation of this peculiar pattern of vortices can be highly plausible to the result of the Cold Fusion (CF) reaction, the precise mechanism of the vortices formation must be elucidated in relation with the solid-state phenomenon accompanied with long-term evolution of deuterium in the Pd cathode in 0.1M LiOD. An in-situ measurement of the solid-state properties of dilation, resistance and electrode potential revealed that the thick Pd rod electrode was composed of the core structure enveloped by the sub-surface layer. The latter exhibits the characteristics of non-equilibrium deuterium absorption/desorption reaction. Then, the conceptual model to explain the CF experiments comprehensively was proposed. N-reaction cycle model [3-4] is composed of four sequential processes: in-taking and compression — triggering (the CF reaction) — scavenger. There the last process: scavenger shows the traces of vortex on the electrode surface as a consequence of the process continuation. In that model, the important role of sub-surface layer was involved. In the last papers[5-6], the vortex pattern was successfully obtained in 2D space analyzing the dynamics of the hypothetical particles

mass by a numerical simulation method: Lattice gas cellular automata (LGCA) numerical simulation. Next we performed the numerical simulation using discretization method for 3D dynamics of the hypothetical particles mass (HPM) in the sub-surface layer[7]. However, there has been unsolved yet in obtaining the real vortex patterns using PC numerical simulation. Further development of this research motivates us; it is necessary to analyze such motion of HPM influenced by a magnetic field induced by a current flow and electric field also.

Table 1 Experimental conditions of Exp.1.

Run No.	Current, $mAcm^{-2}$	Pretreatment
1 st	0.05-40 40-500	Cast, 800°C anneal (10^{-6} Torr)
2nd	40	Polishing, Acid treatment, Evacuation, D_2 gas charge
3rd	40	Evacuation, Polishing, Acid treatment
4th	40	Evacuation, Polishing, Acid treatment

In this study, firstly, the experimental results of the morphology: vortex or vortex thread is briefly described, and secondary we discuss the structure of the electrified interface under an influence of a magnetic field induced by a current flow.

2 Experimental

2.1 Experimental results of vortex for N-reaction cycle model

As shown in Table 1 the electrolysis for deuterium absorption was conducted as follows; the electrode was removed from the cell and carefully re-installed four times during which the diameter of the electrode was measured at three positions (top, middle and bottom). During 1st run, the dilation at the bottom end shows 7 % while those of 2nd - 4th runs the values at these positions approached asymptotically to 7.8 - 8.3 %. Figure 1 shows a significant morphology of a thick rod Pd electrode observed on the surface after long-term electrolysis in 0.1M LiOD [1-2, 8]. It is not the substance adhered on the surface, but is a material on which the pattern was deeply impressed in a shape of a ditch. This is the morphology which formation mechanism will be elucidated in the present study. Alternatively, we have investigated the microscopic structural change of Pd at absorption/desorption of deuterium by electrolysis as a fundamental study of deuterium absorption behavior. Although a precise description is not shown in this paper, structural change of discrimination of the sub-surface and the bulk was developed by the deformation during prolonged deuterium absorption[9-10]. The above results with respect to the structural change of Pd must be useful in the elucidation of intake of

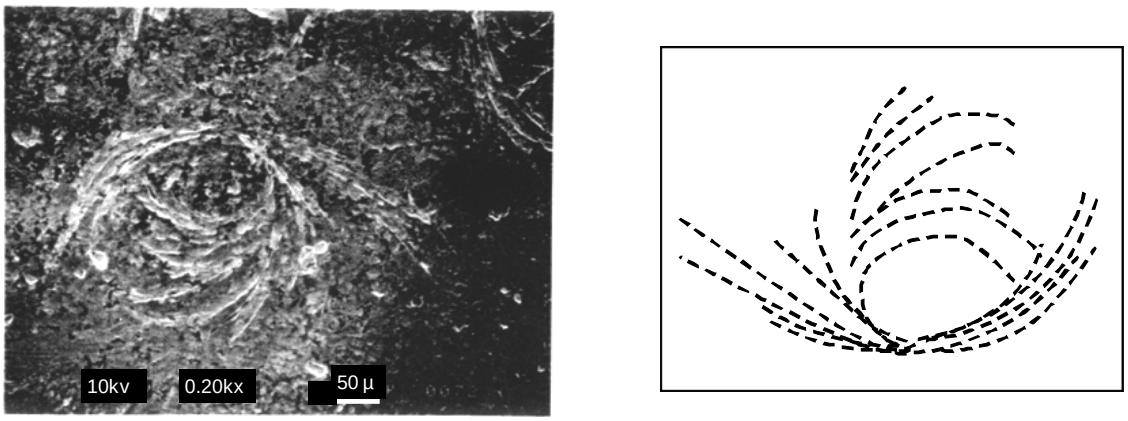

Figure 1 Vortex appeared on Pd electrode surface after long-term electrolysis in 0.1M LiOD (a), Duplicate of SEM picture (b).

reactant followed by compression of N-cycle model (see Ref 9).

3 Results and discussion

3.1 Electrochemical characteristics and structure of electrode/electrolyte interface during deuterium evolution in 0.1M LiOD

As tentative macroscopic structural model is required to determine precise characteristics of the electrified and magnetized interface consisted of working media, solid, liquid and gas, we will presume distributed tunnels inside the electrode and gaseous bubbles on the electrode surface. Here, the electrochemical characteristics involve the variance of the electrode potential differences across the interface vs. the distance from the electrode surface to the bulk electrolyte. Moreover, the electrode potential distribution obtained shows well-defined supplied current dependency, nevertheless those data are related with the given interface structure, electrolyte, metal and reaction.

It is a key point of the CF research to keep high loading of deuterium in Pd during long-term deuterium evolution in 0.1M LiOD. It means that the supply of a negative current has been continued to keep the electrode be subjected to violent deuterium evolution, during which the Pd electrode is actually covered by deuterium bubbles. As another important point, it is insisted that deuterium evolution: one chemical reaction, has no relation with such peculiar morphology but may be concerned with the structure of the electrolyte phase. With these in view, we elucidate the electrochemical characteristics and structure of the electrode/electrolyte interface and that covered by

deuterium bubbles. The structure of the sub-surface layer will be discussed more in next issue.

The total reaction in which deuterium is evolved from alkaline heavy water is

$$2D_2O + 2e^- \rightarrow D_2 + 2OD^- . \quad (1)$$

The product of deuterium gas: D_2 is first absorbed in a Pd electrode, and then this leaves from a solution as bubbles, namely, deuterium evolution reaction. Here, we define stationary "deuterium electrode/electrolyte interface" without bubble formation and "deuterium bubble electrode/electrolyte interface" accompanied with bubble formation (Appendix A) [11].

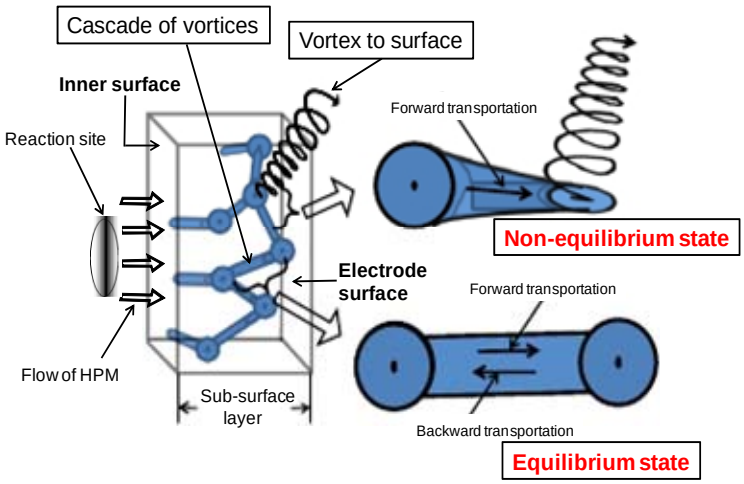

Figure 2 Motion of HPM, transportation phenomenon and evolved cascade vortices in the sub-surface layer

After long-term evolution of deuterium, the structure of the Pd electrode has consisted of the sub-surface layer with voids and/or tunnels and the inner bulk region (the boundary between these two regions is indicated as inner surface in Fig.2 [9-10]). The sub-surface layer might be caused by accumulation of mechanical stresses due to the electrode dilation/contradiction during deuterium evolution. Figure 2 shows the schematic structure of the sub-surface layer, which shows a hexahedron faced by two parallel rectangular plates: inner and electrode surfaces. In Fig.2, there the vortices appeared on the electrode surface (see Fig.1) as a result of the CF reaction; hence the hypothetical particles mass can be transported through the sub-surface layer from the reaction sites (indicated as Flow of HPM in the figure). So far, the precise mechanism of the vortices formation has been the subject of our study employing PC numerical simulation. However, they have been questions posed; what causes such a peculiar morphology; how it moves as for the space with a given electric and magnetic field.

In general, for a moving particle with velocity **v** and charge q its motion is described by a kinetic equation, where Lorentz force **F** exerts

$$\mathbf{F} = q\mathbf{v} \times \mathbf{B}. \quad (2)$$

While magnetic field **B** coexists with electric field **E**, it is further generalized as

$$\mathbf{F} = q(\mathbf{E} + \mathbf{v} \times \mathbf{B}). \quad (3)$$

Thus, since the moving particles mass through the interface experiences the influence of the field, it is important to clarify the microstructure or morphology of the electrode/electrolyte interface accompanied with such an electric and magnetic field. Although postelectrolysis Pd is used to reveal heavily deformed features, such as blisters, voids, Li deposition, etc.; the microstructural change is here limited to voids and tunnel formation in the sub-surface layer.

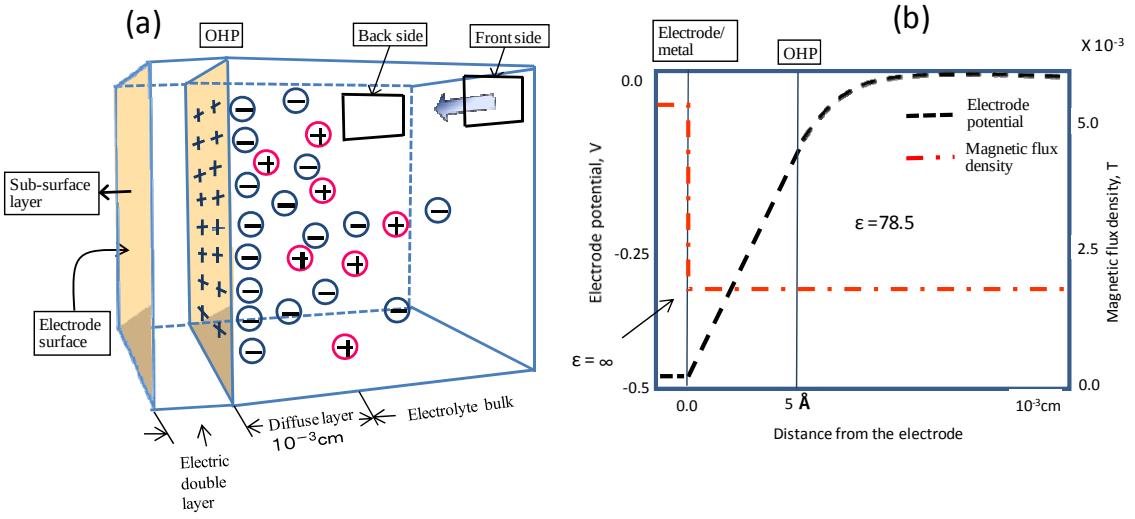

Figure 3 Structure of deuterium electrode/electrolyte interface. The arrow indicates vector of magnetic flux density (a), and electrode potential and magnetic flux density distributions of deuterium electrode/electrolyte interface (b).

3.2 Electrode potential and magnetic flux density distributions of deuterium electrode/electrolyte and deuterium bubble electrode/electrolyte interfaces

Prior to describing the interface microstructure, note that unavoidable situation of bubble evolution on the electrode surface might be different from that of the electrode thoroughly absorbed by deuterium. This study involves the results of the electrode/electrolyte interface without bubble and that with bubbles adhered on the electrode surface. Figure 3 (a) shows schematic of well-known electrified metal/electrolyte interface as the deuterium electrode/electrolyte interface, where the following phases are situated in parallel: charged metal (indicated as electrode surface in the figure), electric double layer and electrolyte. It is noted that an electrified interface is given as a capacitor and resistor connected in parallel as an equivalent circuit. In addition, the position of the sub-surface layer locates more left hand side to

the electrode surface. While Fig. 4 (a) shows how deuterium bubbles disturb the stationary electrode reaction resulting in different magnetic and electric fields.

Figure 3 (b) shows the electrode potential distribution of the deuterium electrode/electrolyte interface vs. the distance from the electrode surface to the bulk of the electrolyte, where the potential is calculated by eq. [4] as shown below. Here, the longitudinal axis is the electrode potential referred to that of the bulk of the electrolyte. In Fig. 3(b) the magnetic flux density distribution is also plotted referred to on the right hand axis, where for convenience, the arbitrary magnetic flux density is plotted together with the electrode potential distribution (Appendix B).

As for a planer electrode, the electrode potential distribution with respect to diffuse layer is given by the Poisson's equation

$$\rho(r)/\varepsilon_0 = -\nabla \cdot [\varepsilon(r)\nabla\phi(r)], \qquad (4)$$

$$\rho\,(\mathrm{r}) = \rho\,(\mathrm{r})_{\text{electrolyte}} + \rho\,(\mathrm{r})_{\text{electrode}},$$

where the charge density (taken as plus or minus for cations or anions): $\rho(r)$ is the sum of those at electrode and electrolyte, ε_0 and $\varepsilon(r)$ are the permittivity of free space and the dielectric constant of material, respectively, $\phi(r)$ is the potential difference referred to that of the bulk solution, and r is the distance from the electrode surface towards the bulk of the electrolyte. In eq. [4] $\mathbf{E} = -\nabla\phi(r)$ is applied, and hence the potential distribution of an individual layer can be calculated based on, e.g. GCS model and the potentials of the boundaries of each layer are estimated from given experimental conditions. Here, the charge of the electrolyte distributes on the Outer Helmholtz Plane (OHP) and that of the diffuse layer spreads into the electrolyte bulk obeying Gouy-Chapman theory (Appendix C).

As shown in Fig.3 (b), almost potential drop develops within the electric double layer, so for ions' movement the influence of acceleration or deceleration due to this electric field is taken into account. On the other hand, the magnetic flux density was calculated [12-13)] using the 3D FEM program (ANSYS). For the analysis of magnetic flux density near the electrode surface and at the electrolyte bulk, the amplitudes of those vectors were averaged where the cell geometry was made for the boundary conditions.

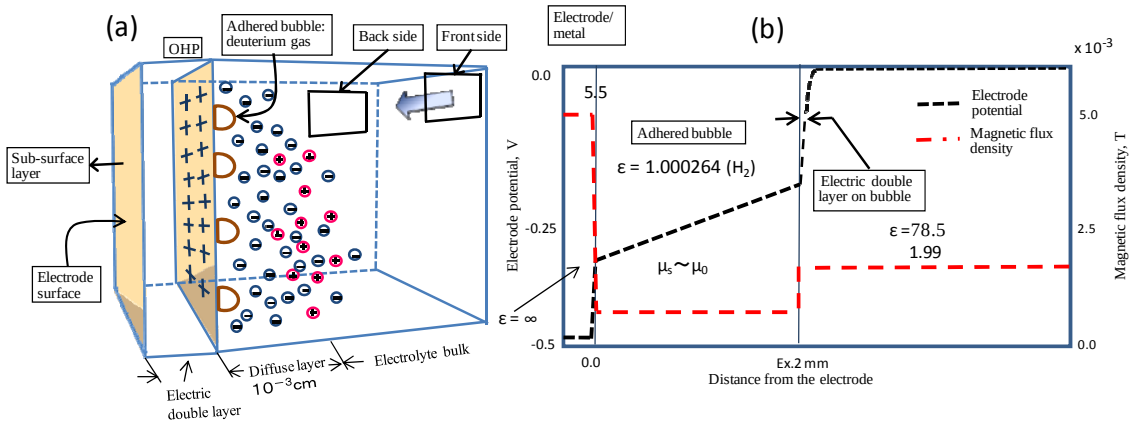

Figure 4 Structure of deuterium bubble electrode/electrolyte interface. For clarification the size of bubbles has been here chosen arbitrarily. The arrow indicates vector of magnetic flux density (a), and electrode potential and magnetic flux density distribution s of deuterium bubble electrode/electrolyte interface (b).

Figure 4 (b) shows schematic of the electrode potential and magnetic flux density distributions, where there may be no significant difference in the values of the magnetic flux density. Considering that these properties correspond to just on the bubble, the rest of the electrode surface behaves similar to the electrode free from bubble adhesion. As far as the electrode surface is not covered completely by bubbles, no distinct difference is seen between these two cases.

On focusing deuterium bubble, there exist significant potential differences within bubble itself and somewhat on the bubble/electrolyte interface. In the latter, the charge of the electrolyte is induced by the electrified solid particles where the potential difference is measured as Zeta potential. In the case of the bubble/electrolyte interface, it amounts to several 10^{-1} V for the ordinary electrolyte solution. Opposite side at the interface is occupied by deuterium gas resulting in the charged state; the polarization of molecule may be accomplished by deviation of electron clouds from one to another atom. Because of not strong dielectric characteristics, accompanied with the values of Zeta potential, electric discharge might not occur in a bubble. This conclusion is consistent with the experimental observation.

4 Summary

The structure of the electrode/electrolyte interface during deuterium bubble evolution in 0.1M LiOD was discussed by referring knowledge regarding the structure of the electrified electrode/electrolyte interface and bubbles adhered thereon. The electrode potential distribution is consistent with the experimental results, however, determining the magnetic flux density distribution awaits further compilation of knowledge and numerical calculation results.

The hydrogen (deuterium) evolution reaction has been widely studied but the

magnetic property of the electrode/electrolyte interface during the reaction occurrence will be new topics in interdisciplinary fields.

Appendix A (Electrochemical kinetic equation of deuterium evolution reaction)

When a current (negative current) i is supplied from a connecting wire to an electrode/electrolyte interface, a unique η (overpotential) is settled obeying the Butler-Volmer equation,

$$i = i_0 e^{[-\beta F\eta / RT]} \qquad (at\ \eta \geq 0.1\,V)\,. \qquad (5)$$

where i_0 is the exchange current density, β is the symmetry factor, which decides how much of the electrical energy $F\eta$ at the interface is available for the rate of the electrode reaction. As shown in eq. [5], the Butler-Volmer eq. describes the relation between the velocity of electronic current i and the potential difference η at an electrified interface. Since the potential difference across the electrode/the connecting wire can be zero, a potential drop arises between an electrode and in bulk of an electrolyte.

Appendix B (Plot of magnetic flux density)

The magnetic flux density of the electrode/electrolyte interface was calculated by multiplying the magnetic field using the magnetic permeability of materials. First, the magnetic field distribution calculated using commercial software was plotted on the cylindrical coordinate system. On the calculation a stationary cathodic current was supplied to the apex of the cylindrical electrode, subsequently the whole current distributed homogeneously towards every electrode surface area. Hence, the current passed at the apex amounts the whole value and they gradually decrease with a decrease in the height of the electrode (the height above the base plane of the cylinder was used in this case).

In this paper, the calculation was conducted incorporating the above specified conditions, however the result was expected to show some deviation from that obtained for a thick cylindrical electrode with infinitely large length. Apart from above inconvenient situation, it gives an apparent variation with respect to r. Raw data from commercial software were, then averaged over the corresponding space (defined by specifying the variable r) at every position along the height of the cylindrical electrode. For overall evaluation, the magnetic flux density at the apex was chosen as data in Figs. 3(b) and 4(b); hence we can estimate only maximum value of the magnetic flux density distribution. Since this electrolysis apparatus was modeled as the cylindrical electrode supplied by a stationary negative current, the vector of the magnetic flux density was

directed from the front side to back one, as shown in Figs. 3(b) and 4(b).

Appendix C (Eq. [4])

For the electrolysis apparatus employed here, the cylindrical coordinate system can be assigned, and consequently eq. [4] regarding a planer electrode can be derived provided that the following considerations are made:

On the cell design and setting up the apparatus, the cylindrical electrolysis apparatus was employed; a Pd cylinder electrode was set in the center of a cylindrically-shaped mesh counter electrode, and hence the distances between the Pd surface and the counter electrode remained strictly same throughout the experimental periods. Taking into account the electrolysis apparatus (see the dimensions and arrangement of the cell[13]), and considering the whole structure of the electrolysis cell analogous to a coaxial cable, the supplied currents to the cylindrical electrode flow towards the counter electrode surface with axial symmetry. That is, the direction of every current vector distributes equally 2π with same given current density in magnitude, thus the dependency of these current vectors on azimuth angle was negligible. Furthermore, the equations with the potential distribution on the cylindrical coordinate system can be reduced to a one dimensional equation with the only variable r. This is valid only when the areas concerned with this study are microscopic (that is, in the vicinity of given r) and the distance from the electrode center possesses a comparably large value, because the mathematical simplification including the boundary conditions can be available.

In addition, the following assumptions have been made:

- electrolysis at a negative stationary current is performed under a steady-state condition; so a potential drop arises at an electrode/electrolyte interface obeying the Butler-Volmer eq. (**Appendix A**),
- only deuterium evolution reaction occurs,
- an electrode exhibits a uniform current density distribution.

References

1) H. Numata et al.: Proc. Conf. Science of Cold Fusion, Vol.33, pp.71, T.BRESSANI et al. eds., SIF, Bologna, Italy (1991).

2) R. Takagi et al.: Fusion Technol., **19** (1991) 2135.

3) H. Numata et al.: Proc. Mini. Symp. Cold Fusion, Tokyo Metropolitan Univ., pp.129 (1990).

4) H. Numata: Proc. Conf. 3rd New Hydrogen Energy Basic Research, (1996)55.

5) H. Numata and M. Ban: Proc.JCF9, pp.74 (2009).

6) H. Numata and M. Ban: Proc.JCF10, pp.68 (2010).

7) H. Numata and M. Ban: Proc.JCF11, pp.70 (2011).
8) H. Numata and I. Ohno: Fusion Technol., **38**, 206(2000).
9) H. Numata and I. Ohno: **ICCF6**, Toya Japan, vol.**1**, pp.213 (1997).
10) H. Numata and M. Ban: Proc.JCF7, pp.6 (2006).
11) J. O'M. Bockris and A. K. K. Reddy, "Modern Electrochemistry Volume 2," Plenum Press, N.Y. (1970).
12) H. Numata and M. Ban: **ICCF12**, Yokohama, pp.411-420(2005).
13) H. Numata and M. Ban: Proc.JCF6, pp.32 (2005).

Acknowledgements

The authors thank S. Numata for the preparation of conference fee.

Measurement of Low Energy Nuclear Reaction in Deuterium Discharge Experiment

S. Narita, H. Yamada, A. Tamura, R. Omi

Department of Electrical Engineering and Computer Science
Iwate University, Morioka, Iwate, 020-8551, Japan

ABSTRACT

The rate of a low energy DD reaction in a metal needs to be studied to clarify the mechanism of cold fusion phenomenon. In this study, we carried out long-term discharge experiment with a Pd cathode in deuterium atmosphere, and tried to find particles that result from a DD reaction using a CR-39 track detector. In the analysis, we considered triple-tracks that were supposed to be due to the carbon breakup reaction by a high energy neutron generated by a series of reactions of DD followed by a DT. We found a total of 11 triple-tracks that were registered on the CR-39 after 150 hours of discharge experiment.

Keywords: DD reaction, DC glow discharge, CR-39, triple-tracks.

1 Introduction

Investigation of the rate of a low energy DD reaction in a metal is necessary for clarifying the mechanism of cold fusion phenomenon. Several researchers have reported the existence of non-negligible screening effects in low energy DD reactions, which were observed in deuterium bombardment of solid state targets. Kasagi *et al.* used an accelerator beam with the energy of E_d = 2.5 keV to measure the DD reaction rate in several metal and metal-oxide targets [1]. When Pd was used as a target, the screening potential was found to be 310 eV, which was much larger than that measured for gaseous targets. Although the accelerator experiment is a useful method for studying the DD reaction systematically, the range of deuteron energies is limited above E_d > 2.0 keV owing to the drastic decrease in the beam current with decreasing E_d. Alternatively, a deuterium discharge experiment is a suitable method that allows measuring the DD reaction at energies below 2.0 keV. Lipson *et al.* used a Ti cathode to measure the screening energy in a deuterium glow discharge, and found it to be 610±150 eV for

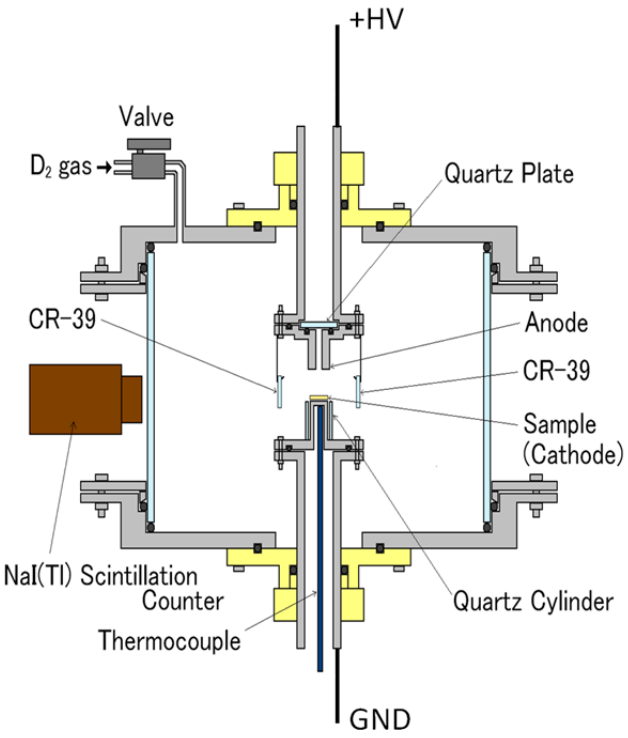

Figure 1. The discharge cell.

deuteron energies in the range of $0.5 < E_d < 2.45$ keV [2]. However, it is interesting to investigate the low-energy DD reaction under different conditions.

In this study, we carried out a long-term discharge experiment with a Pd cathode in deuterium atmosphere, and we measured the DD reaction that was induced on the cathode. Based on the results of this experiment, we discuss the probability of the reaction.

2 Experiment

A Pd foil of dimensions 10 mm × 10 mm × 0.1 mm and purity of 99.95% was washed in the acetone for 20 min and then was transferred into an evacuated cell (~10^{-3} Pa) and annealed for 10 h at 900 °C to create uniform crystallographic structure. After the sample was taken out from the cell, it was washed with aqua regia to remove metallic impurities, and ultrasonic cleansing was performed for 20 min using ultra pure water.

In the discharge experiment, the sample was placed on the cathode of the discharge cell shown in Fig. 1. The anode and the cathode were made of stainless steel

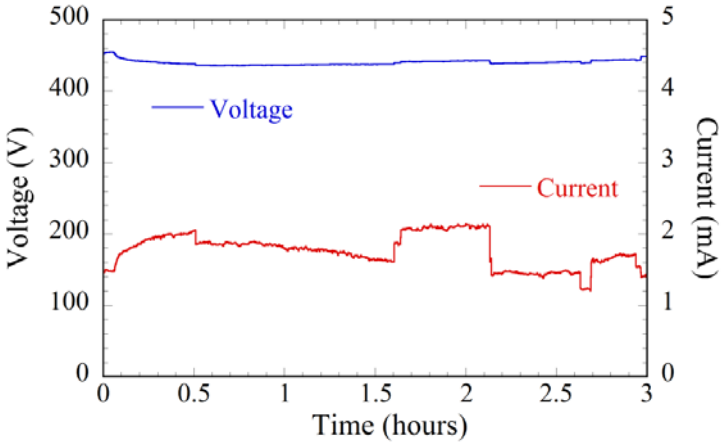

Figure 2. Temporal variation of voltage and current.

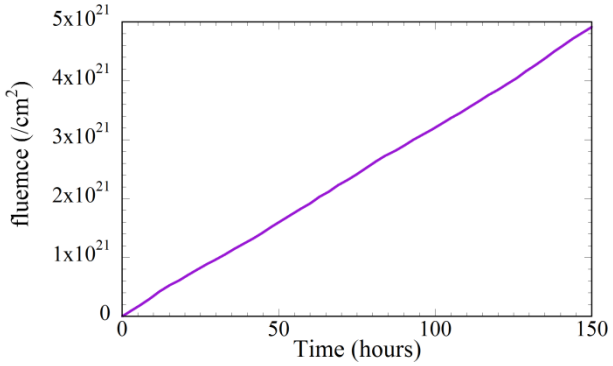

Figure 3. Integrated fluence of D ions.

(SUS304). The side surface was covered with quartz cylinder. After evacuating the cell to a pressure of 10^{-3} Torr, deuterium gas was supplied until the internal pressure rose to ~1 Torr. At this stage a DC voltage was applied, and the sample was exposed to the discharge. In each experimental run, the discharge continued for 3 h. Thus far, we have performed 50 experimental runs, totaling 150 h of discharge. The bias between the anode and the cathode, the current on the cathode, and the cathode temperature were monitored during the experiment. Figure 2 shows typical time dependence of the monitored voltage and current. Since the sample placed on the cathode easily moved in the discharge and the inside pressure of the cell increased gradually due to air leakage, the discharge was not stable. Therefore, we needed to adjust the applied voltage continuously during the experiment to keep the discharge going. This resulted in step-like changes in current, as shown in Fig. 2.

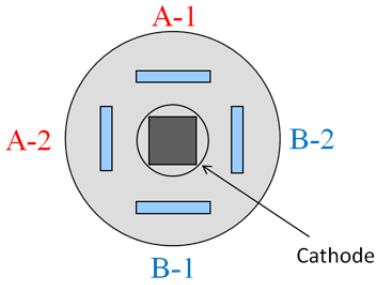

Figure 4. Arrangement of CR-39 (Top view of the discharge cell).

The integrated fluence of D ions can be calculated if we assume that the currents that were monitored were generated by the impinging D ions. Figure 3 shows the integrated fluence as a function of elapsed time. In a total of 150 h of discharge, the total fluence was 4.9×10^{21} /cm^2.

The CR-39 track detector (BARYOTRAK; Nagase Landauer Ltd.) was used to detect the radiation. As shown in Fig. 4, four pieces of CR-39 were placed around the cathode sample to detect the radiation. The detection area of each piece was 1×1 cm^2. Two of these pieces, A-1 and A-2, were replaced after every run, and the other two pieces, B-1 and B-2 were used in all 50 runs. The detector is made of diethyleneglycol-bis-allylcarbonate and has a thickness of 0.9 mm. When a charged particle or a neutron crosses the detector, the material is damaged along the trajectory. Because the velocity of etching in the chemical reagent for the damaged zone is larger than that for other areas, a track pit appears after etching. In the present study, the etching was done using 5 N NaOH solutions at 70 °C for 8 h. After etching, the surface of the CR-39 was surveyed using a digital microscope to observe the pit tracks.

In principle, CR-39 can detect the charged particles and neutrons generated by the following DD reaction:

$$D + D \rightarrow T\ (1.01\ MeV) + p\ (3.02\ MeV) \qquad (1)$$

$$\rightarrow n\ (2.45\ MeV) + {}^3He\ (0.82\ MeV) \qquad (2)$$

However, it is very difficult to distinguish the tracks due to the objective particles from background events. This is because in the current experimental conditions, the reaction is rarely induced, even if we consider a recoil track.

The following secondary reaction is expected to occur on the cathode:

$$D + T \rightarrow \alpha\ (6.7\text{-}1.4\ MeV) + n\ (11.9\text{-}17.2\ MeV) \qquad (3)$$

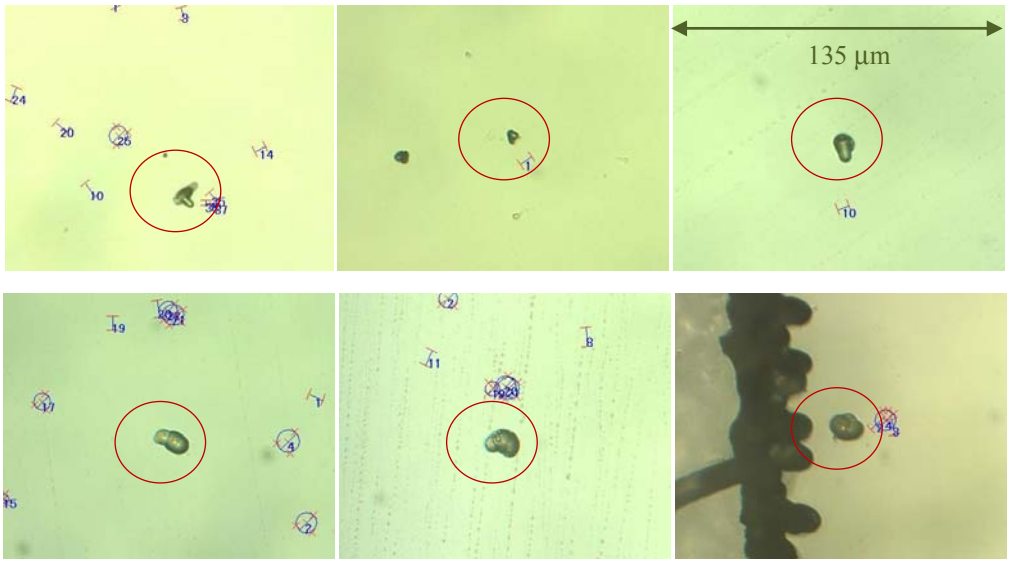

Figure 5. Triple-tracks observed in a set of CR-39 A-1 and A-2 (indicated in a red circle). Numbers shown in each figure are just markers in the microscope view.

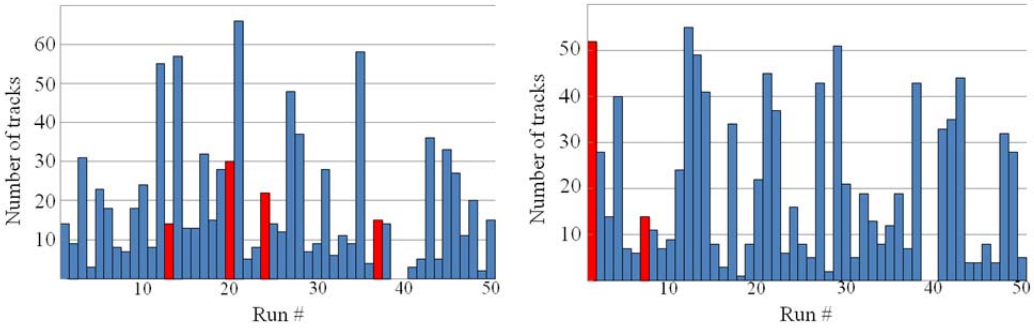

Figure 6. Number of tracks observed in CR-39 A-1 (left) and A-2 (right).

Then, a high energy neutron (E > 9.6 MeV) generated in this reaction causes the carbon breakup reaction ^{12}C(n,n')3α in the CR-39, and the fragmented α particles can be registered as a triple-track (three clustered tracks) in the CR-39 [3-5]. In condensed matter nuclear science studies, this method is often used to identify a neutron emission reaction [6,7]. Therefore, we searched for such triple-tracks on the CR-39 to specify the occurrence of a DD reaction, and tried to estimate the reaction rate.

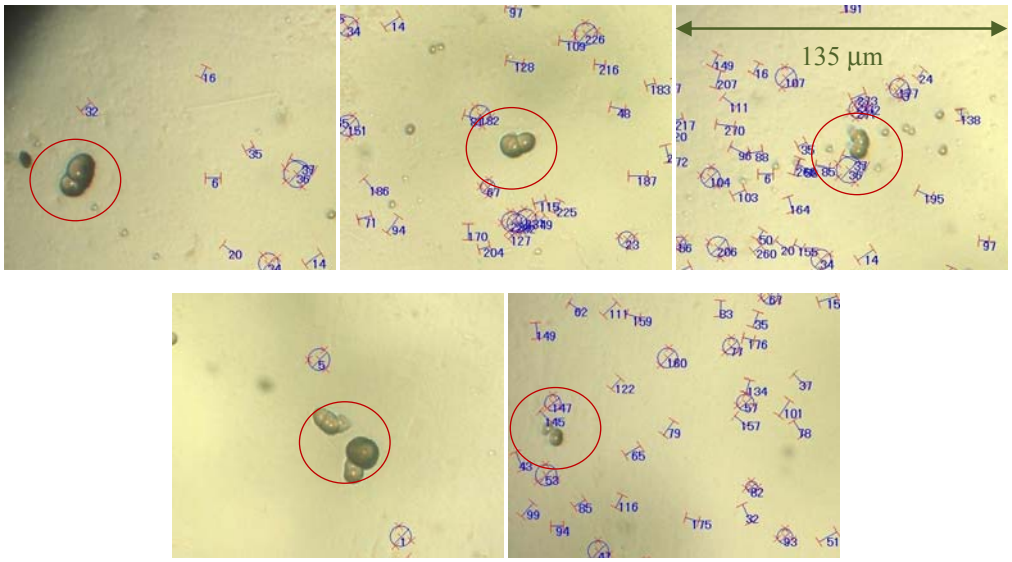

Figure 7. Triple-tracks observed in a set of CR-39 B-1 and B-2 (indicated in a red circle). The numbers shown in each figure are just markers in the microscope view.

3 Results and Discussion

In the 150 h of discharge, we found 6 triple-tracks on a set of CR-39 A-1 and A-2, which were replaced after every run. The images of the triple tracts are shown in Fig. 5. The size of a cluster was 10–20 µm. Figure 6 shows the number of tracks observed on the CR-39 A-1 and A-2 for each run. Note that no data was found in Runs #39 and #40 because we failed to process the CR-39 for these runs. The red-colored runs in the histogram indicate the runs in which a triple-track was observed. For runs in which the triple-tracks were observed, we did not see any peculiarities in the number of tracks. We analyzed 96 pieces of CR-39 (*i.e.* 2 pieces × 48 runs) and found 1920 tracks in total. The averaged density of tracks on a CR-39 was 20 /cm^2. Most of these tracks were considered to be the background ones. In general, the background tracks could be formed mainly as a result of the environmental radiation, the latent defects in the constituent molecules of CR-39 [8], or the accidental surface damage during the experiment. Such background tracks should appear consistently in every run. However, we found a large variation in the number of tracks observed. We could not clarify the reason for this variability.

We also analyzed a set of CR-39 B-1 and B-2, which were fixed in the cell for 50 runs, and found 5 triple-tracks shown in Fig. 7. The number of triple-tracks is

consistent with what was observed on A-1 and A-2. Thus, we observed 11 triple-tracks in total.

Now we estimate the reaction probability. We assume that: 1) the current monitored is generated by the impinging ions, 2) the entire cathode area was uniformly exposed to the discharge, and 3) an α particle always generated a track in CR-39. As mentioned above, after 150 h of discharge, we found 11 triple-tracks, and if we consider the detector's coverage, we can estimate these triple-tracks to be caused by ~1100 events. The total fluence for the 150 h of discharge was ~5 × 10^{21} /cm^2, and the branching ratio of the reaction in Reaction (1) is 0.5. Therefore, the DD reaction probability *P* can be expressed as:

$$P \sim 4\times10^{-19}\frac{1}{\varepsilon_1\varepsilon_2}$$

where ε_1 and ε_2 are the reaction probabilities of D+T → α+n and ^{12}C(n,n')3α, respectively. In a rough estimation, it is supposed that the reaction rate of Reaction (2) is on the order of ~10^{-5} and the cross section of the carbon breakup reaction ^{12}C(n,n')3α is 0.2–0.3 barn [9]. Note that the DD reaction cross section with gas targets was calculated to be much smaller than 10^{-8} barn at this energy range [10].

Now, we should consider the possibility that fake tracks were counted as candidates. In order to identify which of the candidate triple-tracks are the true tracks, statistics needs to be improved by iterating the experiment to accumulate a sufficient number of objective events. In addition, we may obtain kinematical information of a particle if we reconstruct its three-dimensional trajectory in the CR-39. Since the energy of neutron generated in the process of DD followed by the DT reaction is in the range of 11.9–17.2 MeV, such topological analysis can help us examine whether the triple-track observed is caused by the neutron. Furthermore, it is still necessary to understand systematic uncertainties such as the energy spread of ions exposed to the discharge, the properties of the impinging ions (that is D^+ or D_2^+), and the relation between the fluence and the monitored currents.

4 Summary

We investigated a low energy DD reaction by DC glow discharge in deuterium atmosphere using a Pd cathode. We found 11 triple-tracks registered on CR-39, which were considered to be due to the carbon breakup reaction by a high energy neutron generated by a series of reactions (DD followed by DT). In order to be able to precisely determine the DD reaction rate, we should continue the experiment and accumulate a

sufficient number of triple-track events to allow the analysis of systematic uncertainties. It is also necessary to improve the track-characterizing technique of the CR-39 to be able to identify the true events.

References

1. J. Kasagi et al., J. Phys. Soc. Jpn. 71 (2002) 2881.
2. A. G. Lipson et al., Proc. of ICCF10 (2006) 635.
3. B. Antolkovic et al., Nucl. Phys. A 237 (1975) 235.
4. A. M. Abdel-Moneim and A. Abdel-Naby, Rad. Meas. 37 (2003) 15.
5. L. Sajo-Bohus et al., Rad. Meas. 40 (2005) 442.
6. P. A. Mosier-Boss et al., Eur. Phys. J. Appl. Phys. 46 (2011) 30901.
7. P. A. Mosier-Boss et al., J. Condensed Matter Nucl. Sci. 6 (2012) 13.
8. R. Mishra et al., Rad. Meas., 40 (2005) 325.
9. K. Kondo et al., J. Nucl. Sci. Eng. 90 (2008) 103.
10. H. S. Bosch and G. M. Hale, Nucl. Fusion 32 (1992) 611.

Verification of excess heat from PdD_x irradiated by infrared laser

Shigeki Ohshima and Tomoyoshi Motohiro
Toyota Central R&D Labs., Inc.
Nagakute, Aichi, 480-1192, Japan

Abstract

Numerical analysis of the phonon shows that there is the triple deuterium counter oscillation mode in $PdD_{0.75}$ where D atoms are located at the tetrahedral-site. The result of the numerical simulation also shows that its frequency range is 19 ~ 24 THz. If this phonon mode can be excited, the triple D reaction may be occurred. The frequency of the CO_2 laser is around 28.5 THz, which is suitable for exciting such phonon mode, taking possible deviation of the simulated frequency from the experimentally obtained frequency into consideration. To test this hypothesis, we made an experimental apparatus using a CO_2 laser and measured the temperature elevation in PdD_x. The excess heat was measured and verified by the theoretical heat flow analysis.

1. Introduction

The reaction rate of the nuclear fusion which produces ^4He such as the D-T reaction is generally high. To produce ^4He using only deuterium, we assume that the triple deuterium reaction described as $D + D + D \rightarrow {}^4He + D$ plays a key role because of the law of conservation of momentum. In this case, one of three D atoms acts just as a catalyst. However, the probability of the simultaneous collision of three D atoms in the plasma gas is extremely low because of the random motion of plasma particles. On the other hand, D atoms dissolved in Palladium are arranged at the specific site and they vibrate around these lattice points coherently. If a specific mode of the phonon can be excited in PdD_x , the triple D reaction may possibly occur. Of course, its reaction rate is very low because vibration energy is very small, but its collision rate is very high because of the harmonic oscillation of D atoms.

In this paper, we will introduce results of the numerical analysis of the phonon in PdD_x first, and then discuss the excess heat measured experimentally from PdD_x irradiated by an infrared laser. Similar experiment has been done by Hagelstein et al [1]. But the target band of phonon is different from that in our study and they don't mention about the triple deuterium reaction.

2. Numerical Analysis of Phonon in PdD_x

D atoms dissolved in palladium are arranged at the specific site of the face-centered

cubic (fcc) cell. In general, it is said that D atoms in palladium are located at the octahedral site (o-site) [2]-[3]. However, the numerical simulation using CASTEP [4] shows that the tetrahedral site (t-site) of fcc also traps D atoms. Figure 1 shows the location of D atoms in a unit cell of palladium in both cases of the o-site and the t-site when four D atoms are stored in it. Dark blue spheres are Pd atoms and white spheres are D atoms. The lattice parameter and the dissolution energy obtained by the numerical simulation are shown in Table 1. Parameters for the simulation are also shown in the table. The functional used in the simulation is GGA-PBE [5] and the ultra-soft pseudo-potential are used for core electrons. From these results, it seems that the dissolution energy in the case of the t-site is a little larger than that in the case of the o-site. However, when the LDA-PBE [6] functional is used, it is known that the dissolution energy of the o-site becomes large. This shows the precision limit of the simulation using CASTEP. At least, it can be said that D atoms can be located not only at the o-site but also at the t-site. Figure 2 shows the location of the D atom in the case of both the o-site and the t-site using primitive cell expression. From these two figures, it can be seen that there is no physical obstacle between two sites. This allows the migration of the D atom between two sites relatively easily. The transition diagram of the SCF energy from the o-site to the t-site obtained by using CASTEP is also shown at the lower side in the Fig. 2. The activation energy is 0.262 eV. In this model, because of a restriction of CASTEP, the lattice is rigid and can't expand while D atom goes through. It is reasonable to think that the practical value of the activation energy is lower than 0.262 eV. This means that the D atom trapped at the o-site has a good chance to move to the t-site in a usual high temperature condition around several hundred K.

In the numerical analysis mentioned above, Pd_4D_4 (or PdD) is used for convenience. However, it is very difficult to realize PdD state in a normal condition. Figure 3 shows the p-x-T diagram of PdH_x [7]. 'p' means "pressure", 'x' means the loading rate, and 'T' means "temperature". From this diagram, it is found that the loading rate is at most ~0.75 at room temperature and 0.2~0.5 MPa (white area). Figure 4 shows the phonon density of states (DOS) diagram of $PdD_{0.75}$ (o-site) calculated by CASTEP. The lattice group of $PdD_{0.75}$ (o-site) is $Pm\bar{3}m$. The major domain of the phonon DOS is located around 3 ~ 5 THz. On the other hand, the lattice group of $PdD_{0.75}$ (t-site) is $P\bar{4}3m$ and the phonon DOS diagram is very different (Fig. 5). There are two major domains of the phonon DOS. One has almost the same range to that of $PdD_{0.75}$ (o-site), but the other domain is located around 19 ~ 24 THz. Additional vibration analysis shows that only D atoms can oscillate in this range. Furthermore, a counter-oscillation mode by

three D atoms is also included in it. Its location is estimated in the neighborhood indicated by the yellow arrow in Fig. 5. This means that the harmonic oscillation by three D atoms may be excited effectively from the external source and the triple D reaction described as D + D + D $\rightarrow$ ^{4}He + D may occur. Figure 6 shows the electron DOS diagram of $PdD_{0.75}$ (t-site). A dashed vertical yellow line indicates the Fermi level. It is found that $PdD_{0.75}$ (t-site) is an electric conductor judging from this diagram. From these results, one excitation scenario for the triple D reaction can be made. Figure 7 shows the flow chart of this process. First, the CO_2 laser (28.5 THz) is irradiated to palladium in which D atoms are dissolved (PdD_x). The laser photon is absorbed by electrons in the conduction band. The energy transfer occurs from electrons to D atoms. Only D atoms start their oscillation and the mode transfer will occur. Finally, there may be the triple D reaction excited by the CO_2 laser.

3. Experimental apparatus

Figure 8 shows a schematic diagram of the experimental apparatus to verify that the excess heat is generated from PdD_x, or not. There is a sample Pd powder (100 mesh size, 99.9% purity and 0.1g weight) with an SUS304 hexagonal Petri-dish in an SUS304 pressure vessel. A K-type thermocouple is attached on the bottom of the Petri-dish to measure the temperature of the sample. The CO_2 laser beam comes from the top of the pressure vessel through a ZnSe window and irradiates the sample. This experimental apparatus also has a gas exchange system. Both H_2 and D_2 gas are available to compare the heat generation rate.

4. Experimental results

Figure 9 shows the time evolution of the temperature of the sample palladium powder when the laser beam irradiates it. The orange line shows the temperature of the sample in which D atoms are not dissolved, and its rate of heating is slow. On the other hand, the light blue line shows that of PdD_x, and the temperature rises very rapidly. The reason of this difference can be thought as follows. The energy of the laser is absorbed by electrons in both cases. However, in the former case, the absorbed energy can’t be transferred effectively to Pd atoms because of the difference of their energy level. Then the greater part of the absorbed energy is reradiated by the electron. On the other hand, in the latter case, the laser energy absorbed by the electron is quickly transferred to the D atoms and the phonon is generated effectively, and then the temperature rises very rapidly. This experimental result supports the scenario mentioned in the previous section. Table 2 shows the averaged elevated temperature of

each case when the laser power (180 mW and 220 mW) and a kind of the gas (H_2 and D_2) are selected as parameters. When the laser power is selected as a parameter, it is found that the elevated temperature of PdD_x is larger than that of PdH_x in both cases. Then, it seems apparently that the excess heat occurs in PdD_x. However, the sample is exposed to H_2 or D_2 gases during the experiment. The heat conductivity of the H_2 gas (λ_{H2}) is different from that of the D_2 gas (λ_{D2}), and λ_{H2} is larger than λ_{D2} generally. For example, values of λ_{H2} and λ_{D2} are 0.1684 $Wm^{-1}K^{-1}$ and 0.1306 $Wm^{-1}K^{-1}$, respectively at 273 K and 0.1 MPa. Therefore in this stage, it is too early to conclude that the excess heat is generated in PdD_x irradiated by the CO_2 laser.

5. Theoretical analysis of heat transfer

The theoretical analysis of the heat transfer is needed to verify if there is the excess heat from PdD_x irradiated by the CO_2 laser or not. Figure-10 shows a cylindrical model for the heat-flow analysis. In the figure, P_0 is the laser power. Q is the heat flow from the sample to the inner wall of the vessel. P_n is the excess heat from the sample if it is generated. T_S and T_0 are the temperature of the sample and the wall of the vessel, respectively. S is the surface area of the sample. From equation of continuity and Fourier's law, the temperature elevation (ΔT) at the thermal equilibrium state is led theoretically by the following numerical formula in the cylindrical coordinate system.

$$\Delta T \equiv T_S - T_0 = \frac{r_{cyl}(\kappa P_0 + P_n)}{S\lambda},$$

$$r_{cyl} \equiv r_S log \frac{r_0}{r_S},$$

where, κ is the laser absorption rate of the sample, r_S is the distance from the surface of the sample to the wall of the vessel, r_0 is the radius of the vessel and λ is the heat conductivity of the atmosphere (H_2 or D_2) in the vessel. Using the above formula, the temperature elevation for each H_2 and D_2 are expressed as follows.

$$\Delta T_H = \frac{r_{cyl}}{S} \cdot \frac{\kappa_H P_0}{(\lambda_H + \lambda_m)}.$$

$$\Delta T_D = \frac{r_{cyl}}{S} \cdot \frac{(\kappa_D P_0 + P_n)}{(\lambda_D + \lambda_m)},$$

where, λ_m is an additional heat conductivity value which originates in the heat conduction of the holder of the Petri-dish mainly. However, there are still unknown values. It is difficult to estimate values of r_S in r_{cyl}, S and λ_m. Then, a peculiar performance index α is defined to eliminate these unknown values.

$$\alpha \equiv \frac{\Delta T_D}{\Delta T_H} = \frac{(\lambda_H + \lambda_m)}{(\lambda_D + \lambda_m)} \cdot \frac{\kappa_D P_0 + P_n}{\kappa_H P_0}.$$

If it is assumed that the heat conductivity, such as λ_H, λ_D and λ_m, and the absorption rate such as κ_D and κ_H, are almost constant in the temperature range of the experiment, α is described as a function of P_0.

$$\alpha = C_\lambda \frac{\kappa_D + p_n(P_0)}{\kappa_H}.$$

$$C_\lambda \equiv \frac{\lambda_H + \lambda_m}{\lambda_D + \lambda_m} \approx const.\ , \qquad p_n(P_0) \equiv \frac{P_n(P_0)}{P_0}$$

The differential coefficient of α by P_0 indicates important information for the generation of the excess heat. If $P_n(P_0)$ is defined by the following formula to estimate its rate of monotonic increase,

$$P_n(P_0) \equiv k{P_0}^\gamma, \quad k = const.,$$

the differential coefficient of α by P_0 becomes,

$$\mu \equiv \frac{d\alpha}{dP_0} = \frac{C_\lambda}{\kappa_H} k(\gamma - 1){P_0}^{\gamma - 2}.$$

If $\gamma > 1$, which means the accelerated monotonic increase of $P_n(P_0)$, μ becomes larger than 0. On the other hand, if $\gamma = 1$, or $P_n(P_0) = 0$, μ becomes 0.

6. Estimation of excess heat

Experimental results were investigated using the performance index α defined in the previous section. Table 3 shows performance indices α obtained from experimental results (ΔT_D and ΔT_H) and μ values. In the experiment, the Ag powder was also used to get reference data for comparison. It is well known that H_2 or D_2 gas cannot be dissolved in Ag, therefore the excess heat never occurs. The table shows three sets of data. First row shows values of α and μ in the case of Ag and two lower rows are in the case of Pd. Two sets of data in the case of Pd were measured on different days. In the case of Ag, there is no excess heat generation basically, then μ is almost equal to zero. The value of -0.05 is caused by the measurement error. On the other hand, the values of μ in the case of Pd are clearly different from zero and are enough larger than the error value. This shows that there is the excess heat from PdD_x irradiated by the CO_2 laser, and the excess heat increases with P_0 at an accelerated rate.

7. Discussion

The excess heat generation from PdD_x irradiated by the CO_2 laser was verified qualitatively by the theoretical analysis and the experiment. However, there are several

assumptions in the theoretical analysis of the heat flow. Therefore, it is difficult to dare to say that it is the excess heat by the “nuclear reaction”. The best way to say that the nuclear fusion occurs is to show the products by the nuclear fusion. However, we don’t have means to detect them at present. Our hypothesis mentioned first is that there occurs the triple Deuterium reaction in PdD_x by irradiating it by the CO_2 laser. Further investigation to detect He atoms, especially ^4He atoms is necessary in the future.

References

[1] P. L. Hagelstein, D. Letts and D. Cravens, “Terahertz difference frequency response of PdD in two-laser experiments”, J. Condensed Matter Nucl. Sci. 3, pp.59-76(2010).

[2] H. Okuyama, W. Siga, N. Takagi, M. Nishijima and T. Aruga, “Path and mechanism of hydrogen absorption at Pd(100)”, Surf. Sci. 401, pp.344-354(1998).

[3] D. K. Ross, V. E. Antonov, E. L. Bokhenkov, E. G. Ponyatovsky and J. Tomkinson, “Strong anisotropy in the inelastic neutron scattering from PdH at high energy transfer”, Phys. Rev. B, 58(5), pp.2591-2595(1998).

[4] A full-featured materials modeling code based on a first-principles quantum mechanical description of electrons and nuclei. cf. http://www.castep.org/ (accessed March 3,2013).

[5] GGE stands for Generalized Gradient Approximation which was introduced in the following literature by the authors PBE taking their initial characters; J. P. Perdew, K. Burke, and M. Ernzerhof,” PBE**:** Generalized Gradient Approximation Made Simple”, Phys. Rev. Lett. 77, 3865 (1996)

[6] LDA stands for Local Density Approximation which was introduced in the following literature for the first time; W. Kohn and L.J. Sham, “Self-Consistent Equations Including Exchange and Correlation Effects”, Phys. Rev. 140, A1133 (1965) .

[7] The p-x-T diagram of PdH_x appears in P.81 in E. Wicke, H. Brodowsky and H. Zuchner, “Hydrogen in palladium and palladium alloys” in “Hydrogen in Metals II”, Eds: G. Alefeld and J. Volkl, in the series of “Topics in Applied Physics” 29, pp.73-155 (Springer-Verlag, Berlin, 1978).

Figures and Tables

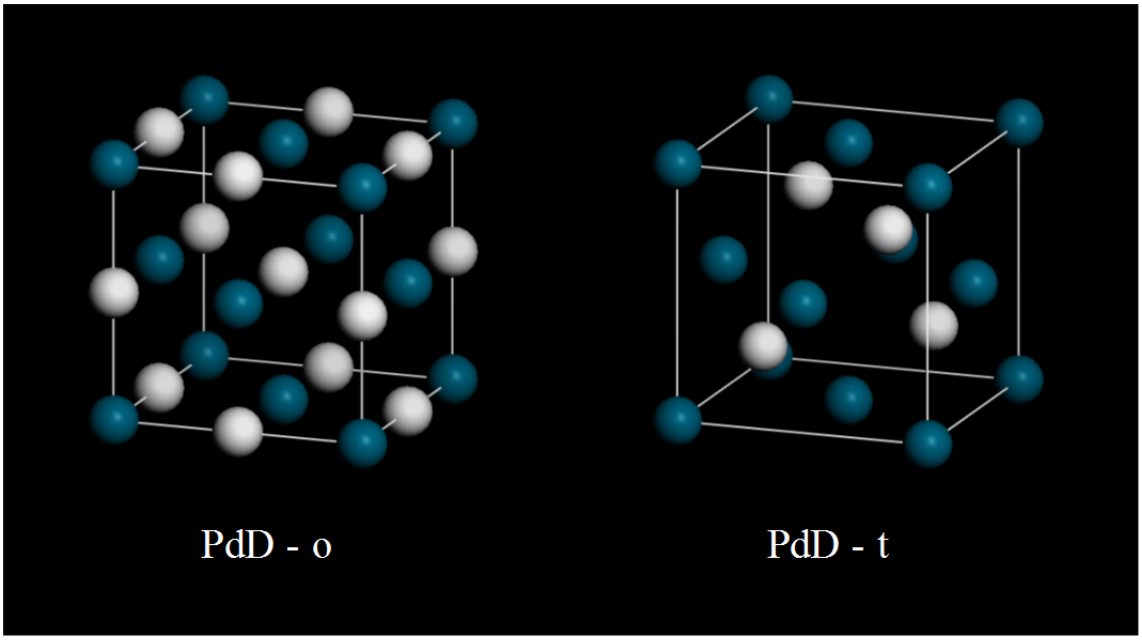

Fig. 1 Location of D atoms in a unit cell of palladium (the left figure shows “o-site” and the right figure shows “t-site”)

Table-1 Lattice parameter and dissolution energy

Software : CASTEP		
Functional : GGA-PBE		
Location of D atom	o-site	t-site
Dissolved Energy	1.02 eV/cell	1.09 eV/cell
Lattice Size	4.11 Å	4.22 Å

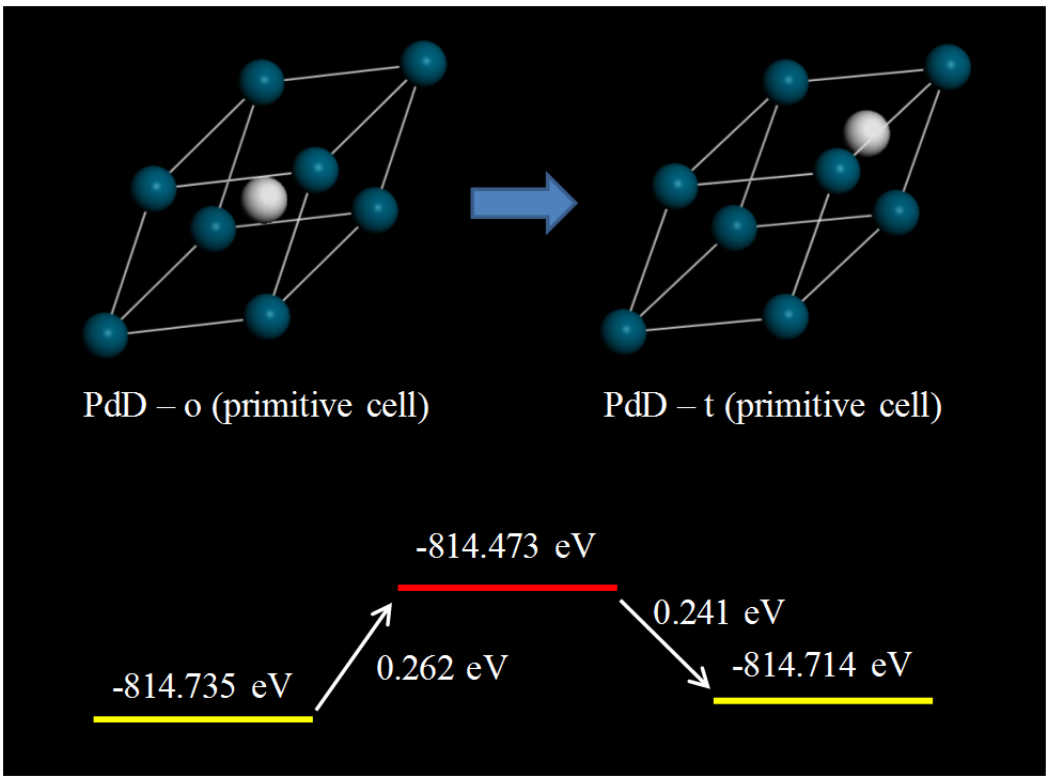

Fig. 2 Transition diagram of the SCF energy of PdD per primitive cell from the o-site to the t-site

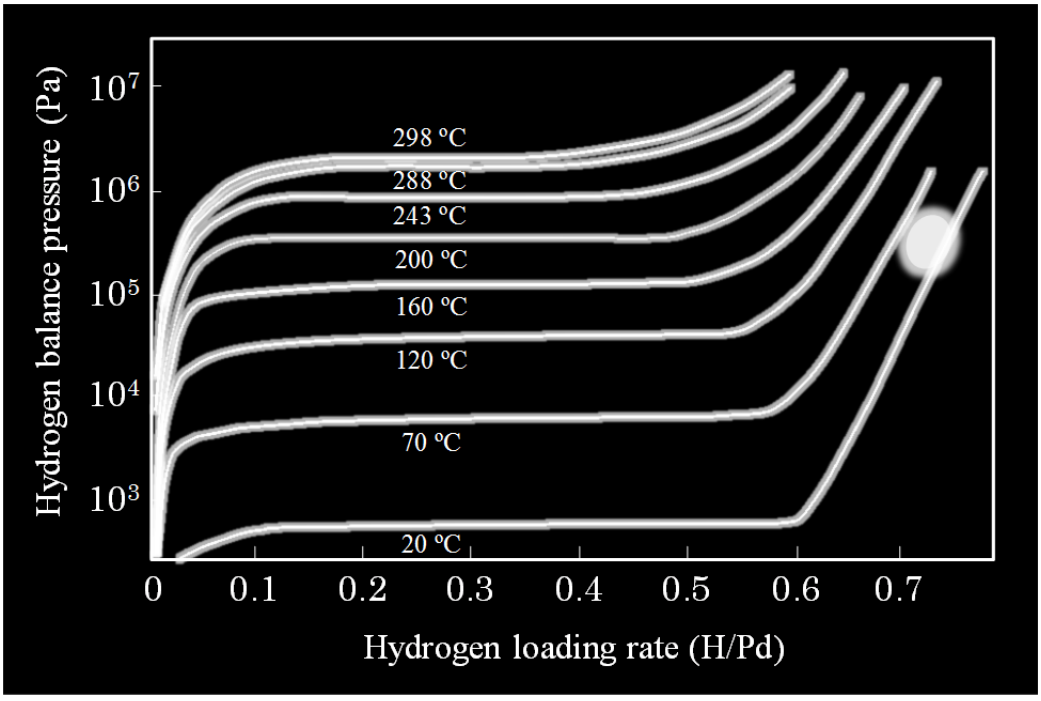

Fig. 3 p-x-T diagram of PdH_x

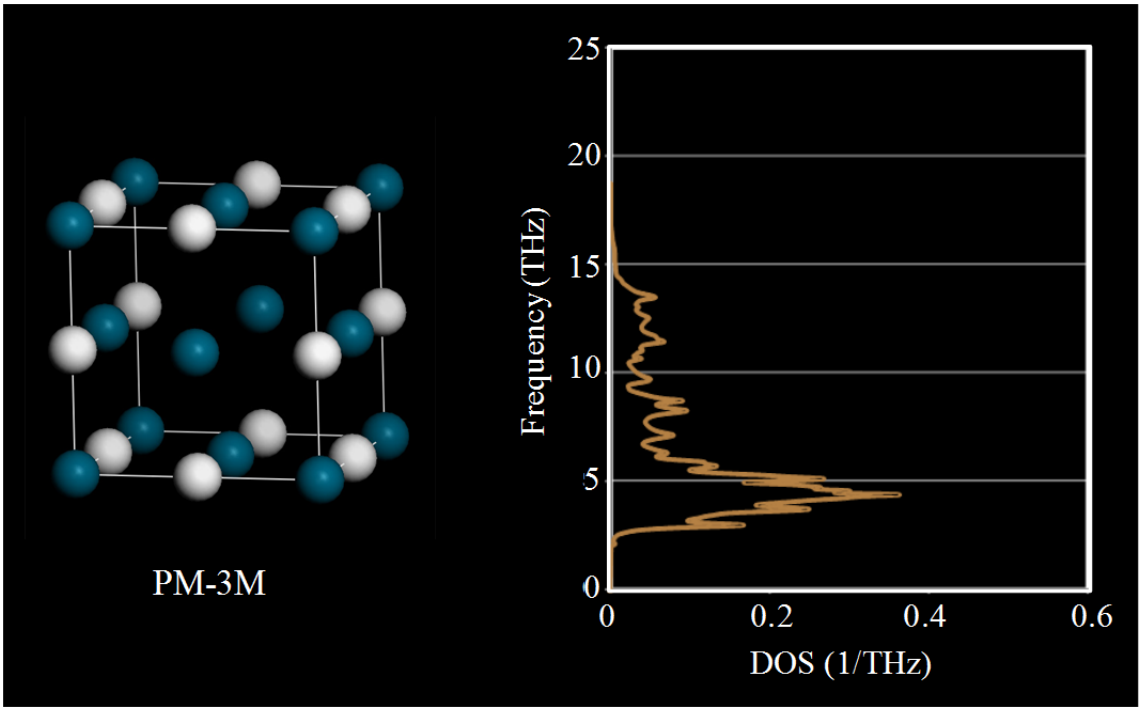

Fig. 4 Phonon DOS diagram of $PdD_{0.75}$ (o-site)

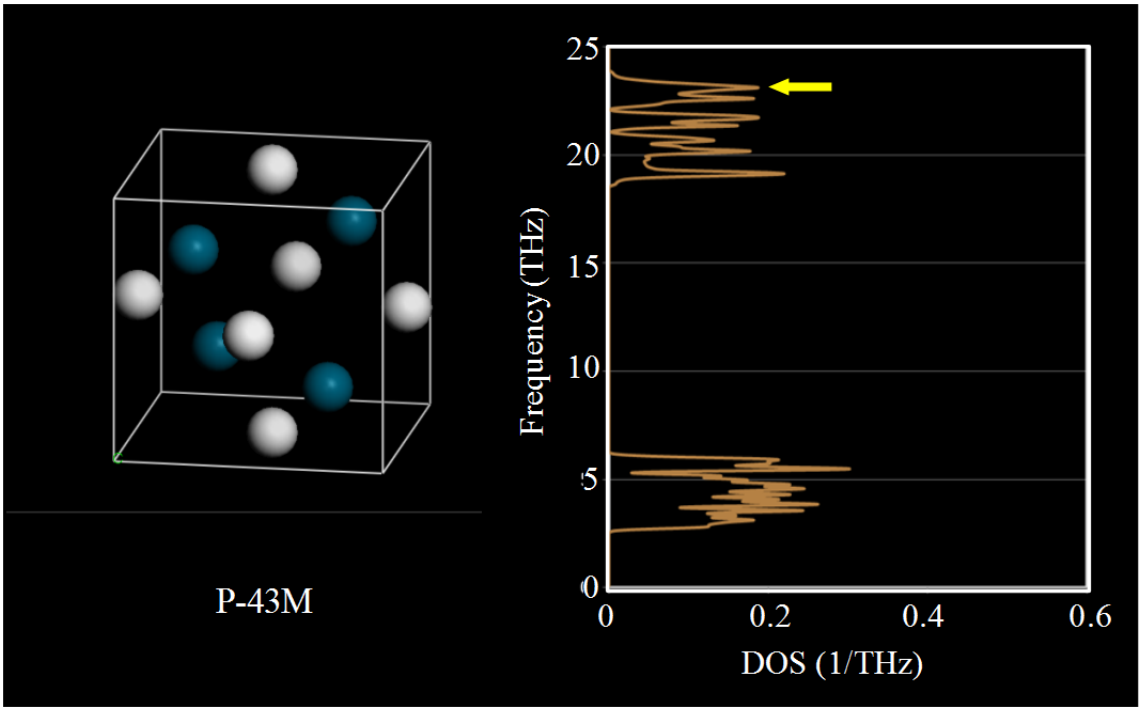

Fig. 5 Phonon DOS diagram of $PdD_{0.75}$ (t-site)

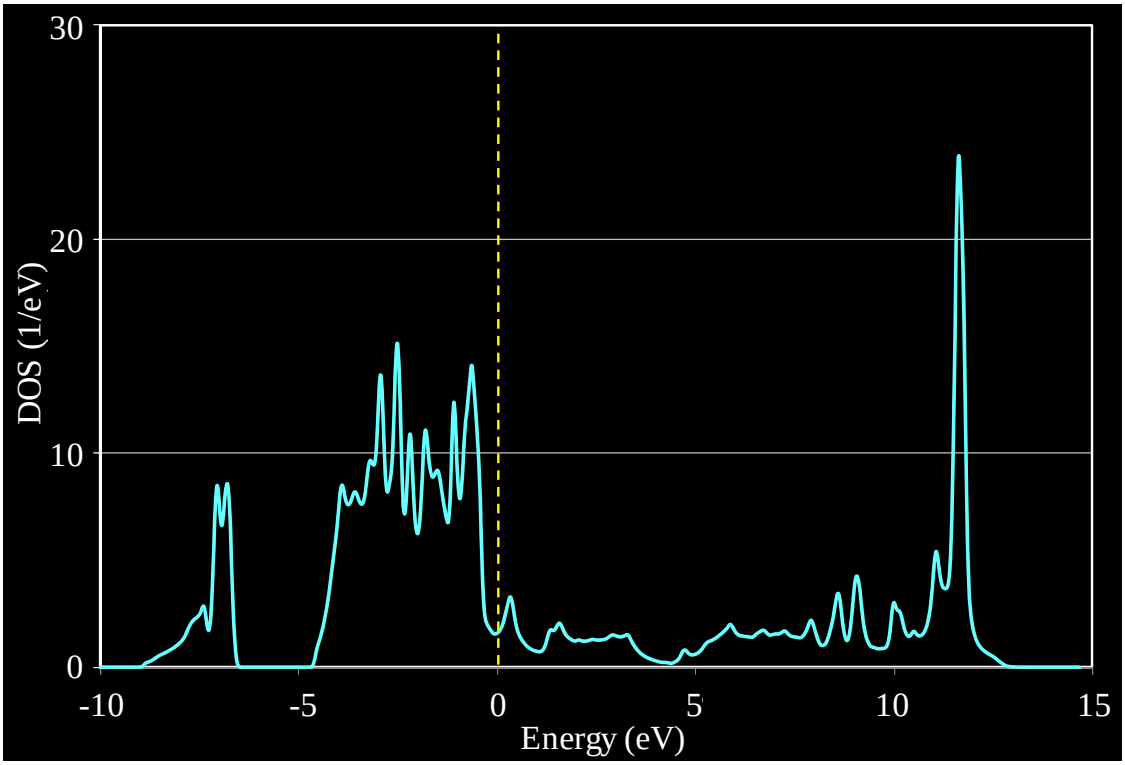

Fig. 6 Electron DOS diagram of $PdD_{0.75}$ (t-site)

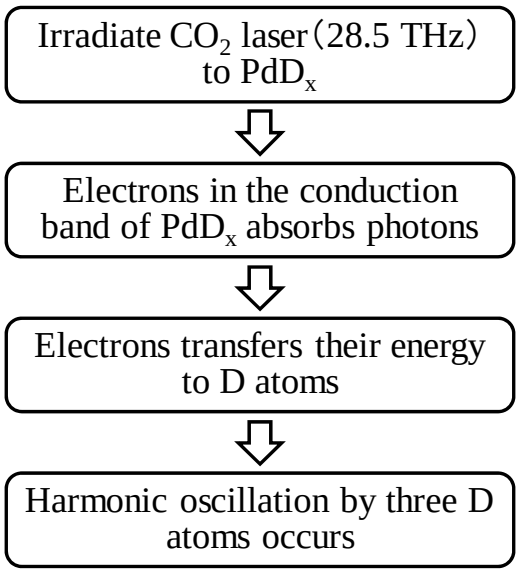

Fig. 7 Flow chart to excite triple D reaction

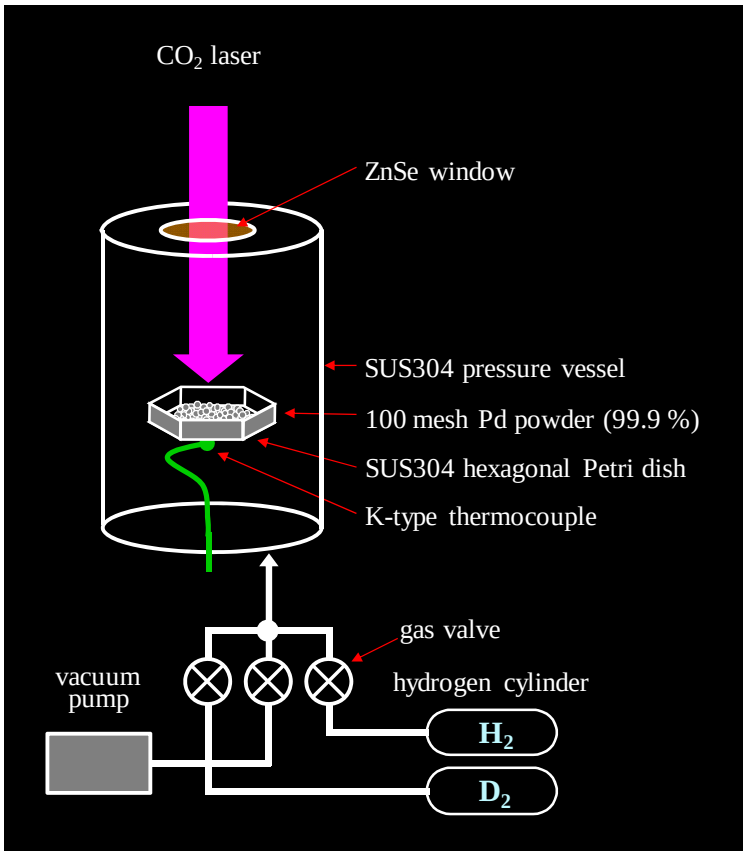

Fig. 8 Schematic diagram of the experimental apparatus to measure excess heat

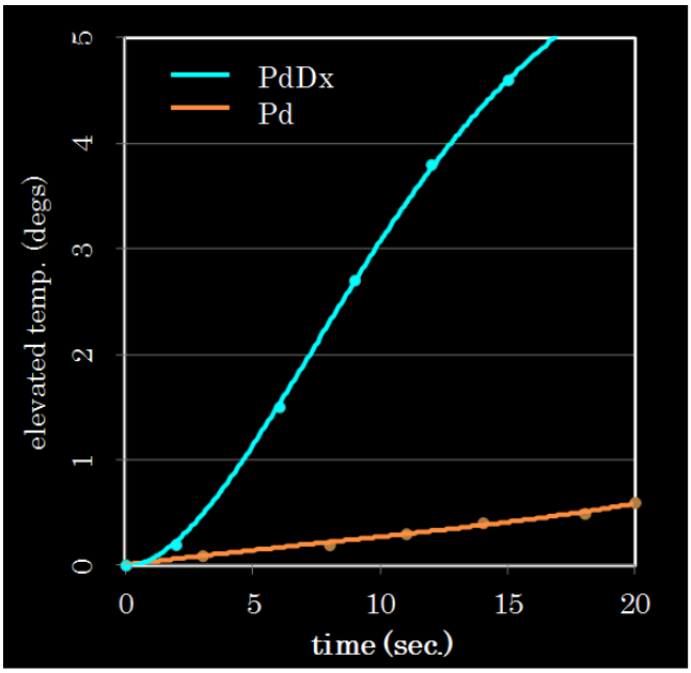

Fig. 9 Time evolution of temperature of palladium powder irradiated by CO_2 laser

Table 2 Matrix table of averaged elevated temperature (ΔT_D and ΔT_H) for each case

		Laser Power	
		180 mW	220 mW
Gas	H_2	7.866 °C	8.598 °C
	D_2	9.174 °C	10.370 °C

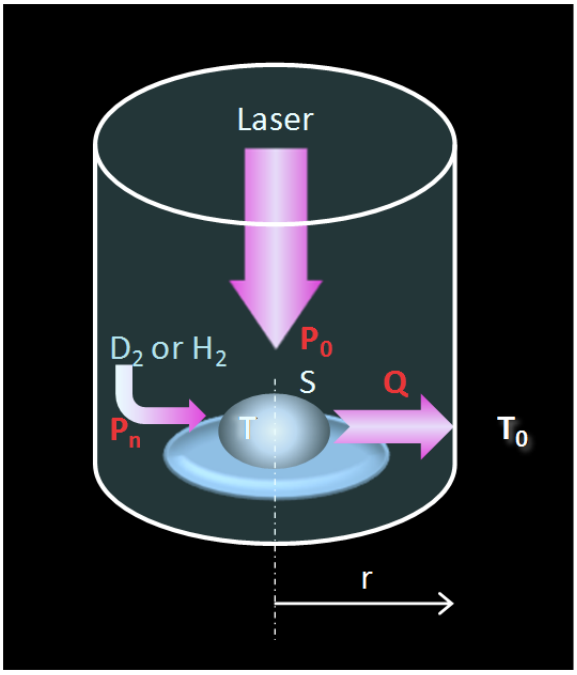

Fig. 10 Cylindrical model for heat-flow analysis

Table 3 Performance indices α obtained from experimental results and μ values

	P_0 = 180 mW	P_0 = 220 mW	μ
Ag	1.236	1.234	-0.05
Pd - No.1	1.165	1.202	0.91
Pd – No.2	1.168	1.202	0.86

Characterization of deuterium loading/unloading behavior for various types of multi-layered metal sample

G.Hosokawa†, M.Kawashima, N.Oikawa, H.Yamada, S.Narita

Department of Electrical Engineering and Computer Science, Iwate University
Morioka, Iwate, 020-8551, Japan
†t2312030@iwate-u.ac.jp

ABSTRACT

We performed deuterium loading/unloading experiment with various types of multi-layered metal sample to characterize deuterium dynamics in each sample, which is supposed to be concerned with a trigger condition of a low energy nuclear reaction in condensed matter. We found the sample with CaO membrane had higher D/Pd, and it seemed to be likely to hold D atoms. The sample with Pd membrane promotes the deuterium desorption effectively.

Keywords: multi-layered metal sample, deuterium, loading ratio, desorption

1. Introduction

Charged particle emission and anomalous heat evolution have been observed in a deuterium desorbing process with a multi-layered Au/Pd/MnO sample by Yamaguchi *et al.* [1]. Besides, a selective transmutation was observed in deuterium permeation with multi-layered Pd/CaO complex sample by Iwamura *et al.* [2]. These phenomena were supposed to be attributed to a low energy nuclear reaction in condensed matter. In addition, anomalous heat evolution was found in deuterium loading/unloading experiment with Pd-Ni binary nano-particles by Kobe-Technova group [3]. Considering these experimental results, we performed deuterium loading/unloading experiments using various types of multi-layered metal samples such as *Au*/Pd/*CaO*, *Pd*/*CaO*/Pd/*Au,* Pd/*CaO*, Pd/*Ni*, Pd/*Ag*.

In this paper, we report the characteristics of the deuterium loading/unloading behavior, which is supposed to be closely connected with the trigger condition for inducing a nuclear phenomenon, for various types of multi-layered sample.

2. Characteristics of the metal for hydrogen/deuterium diffusion

In general, metals are classified into exothermic and endothermic absorbers of hydrogen. Table 1 shows heat of hydrogen dissolution for several types of metals. Pd and Ti, which have a negative value of hydrogen solution, are exothermic absorber for hydrogen dissolution and Au, Ni, Ag, and Al are endothermic one.

Hydrogen/deuterium diffusion rate is the other important factor to define hydrogen/deuterium dynamics in metal. A hydrogen/deuterium diffusion rate is expressed as follows;

$$D=D_0 exp(-E_a/kT) \quad (1)$$

where E_a is the Activation energy of a specified metal, k is the Boltzmann constant,T is temperature and D_0 is the diffusion coefficient of hydrogen [6].

Figure 1 shows diffusion rates as a function of temperature for several metals. Pd is found to have the highest diffusion rate, and Ni has the lowest rate. In a multi-layered sample, local hydrogen/deuterium density in the interface of the composite metals is supposed to be concerned with the difference of the diffusion rate between them. We may expect higher hydrogen/deuterium density at the boundary of Pd-Ni binary metal since a difference of their diffusion rate is larger.

Table 1. Hydrogen heat of solution of the metal

	value of the heat of solution [kJ/molH]
Pd	-10
Au	36
CaO	—
Ni	16
Ag	68
Al	67
Ti	-53

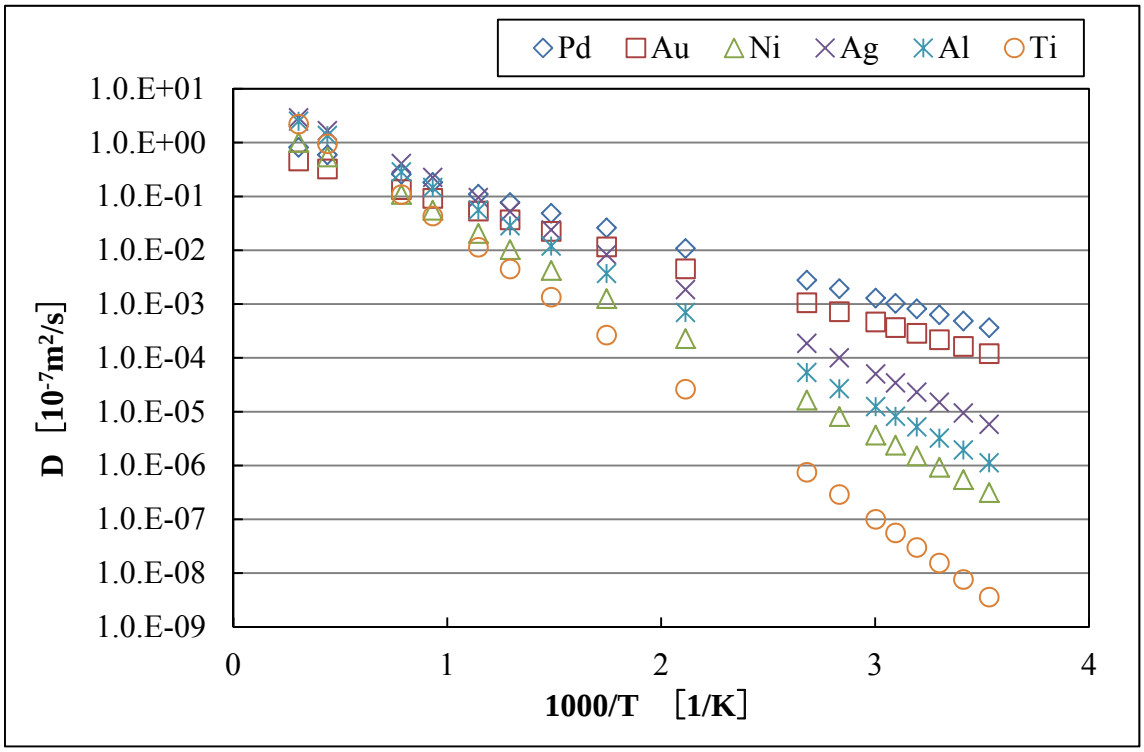

Fig 1. Rate of diffusion of deuterium in the metal

3. Experiment

In this study, we investigated deuterium loading/unloading behavior for multi-layered metal samples as follows: *Au*/Pd/*CaO*, *Pd*/*CaO*/Pd/*Au*, Pd/*CaO*, Pd/CaO complex (MHI-type sample), Pd/*Ni* and Pd/*Ag*. The sample was prepared by the following procedure. The Pd foil (10 mm x 10 mm / 4 mm x 25 mm, t = 0.1/0.3/0.5 mm,) was washed by acetone followed by being annealed at 900 ℃ for 10 hours. After annealing, the surface contaminants were removed by aqua regia again. Then, each type of layer was deposited onto the sample surface by Ar ion beam sputtering, as shown in Fig. 2. The thickness of each layer is also shown in Fig.2.

Then, the deuterium loaded sample was exposed to 5 atm D_2 gas for 20 hours. The weight of the sample was measured before and after loading, and the loading ratio (D/Pd) was calculated from the weight difference. Note that the loading ratio of complex sample was calculated assuming to be composed of Pd only. After loading, the sample was set into the chamber which has a cylindrical shape with a volume of 880 cm^3 equipped with a turbo-molecular evacuating pump. The sample was left in the chamber evacuated to less than 10^{-3} Pa for 24 hours in the unloading test. In some

experiments the sample was heated by applying DC current to prompt unloading of deuterium. In order to investigate nuclear phenomena, we measured sample temperature with a thermo-couple and charged particle emission by CR-39 track detector.

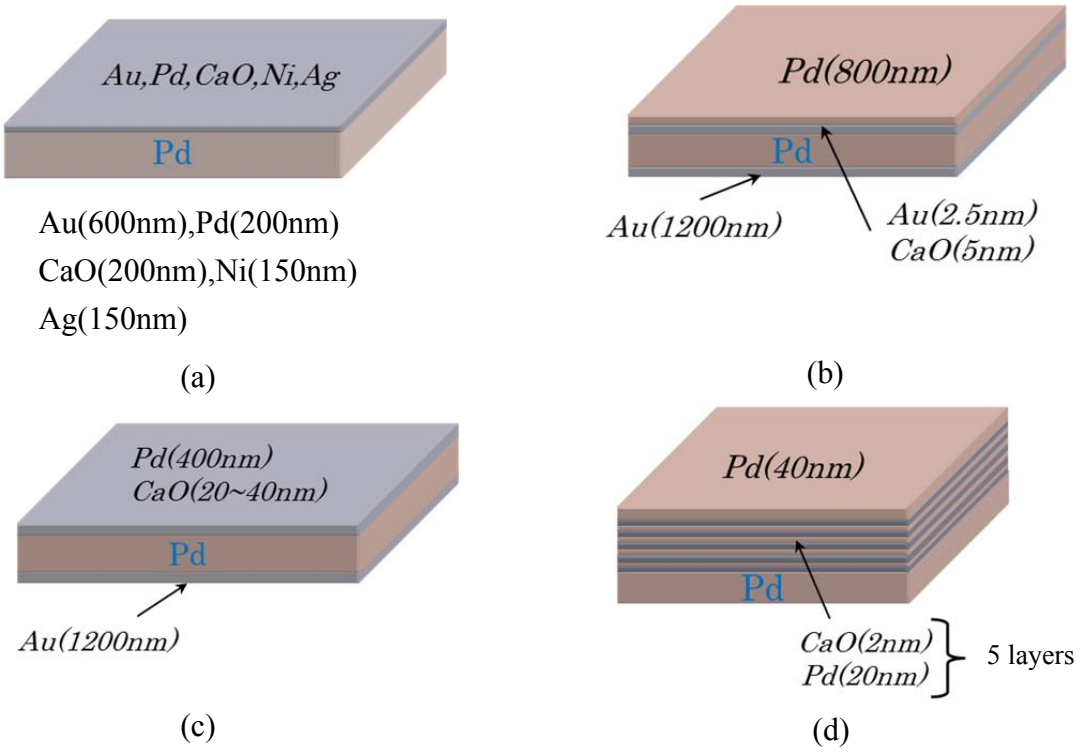

Fig. 2. Sample structure

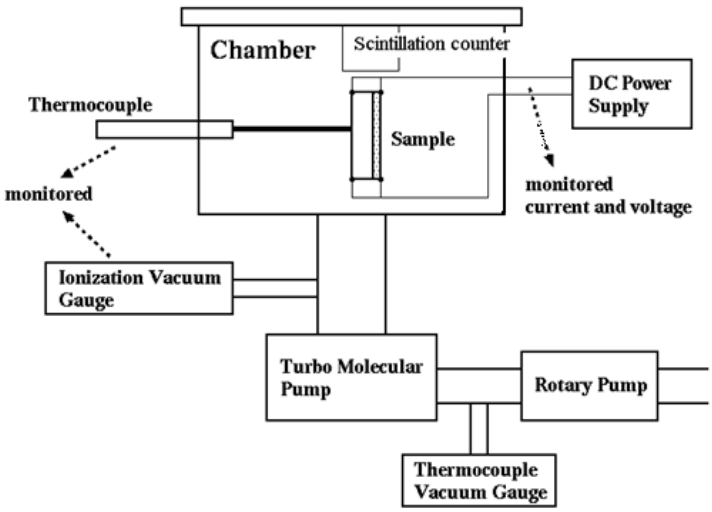

Fig 3. Experimental apparatus

4. Results and Discussion

Table 2 shows D/Pd before and after unloading test for each multi-layered sample.

Table 2. Average value of D/Pd ratio

sample	Number of run	D/Pd After loading	D/Pd after unloading	
			Current application	No current application
Au/**Pd**	11	0.64	0.07	0.59
CaO/**Pd**	10	0.69	0.05	0.57
CaO/**Pd**/*Au*	9	0.71	0.03	0.56
Pd/**Pd**	4	0.13	–	0.11
Pd/**Pd**/*Au*	4	0.23	–	0.01
Pd/Au/**Pd**/*Au*	3	0.19	–	0.01
Pd/CaO/**Pd**/*Au*	20	0.36	–	0.14
CaO/**Pd**(MHI-type)	28	0.68	0.07	0.59
Ni/**Pd**	36	0.67	0.01	–
Ag/**Pd**	24	0.64	0.10	0.59

Figure 4 shows D/Pd just after loading for various multi-layered samples. The mean D/Pd ratios of the samples except for ones containing Pd membrane were typically 0.6-0.7. The D/Pd for the sample with CaO membrane layer is found to be relatively higher. One can suppose a coupling of D and O atoms. Considering the following processes, D atoms may be present in the sample as D_2O and $Ca(OD)_2$.

$$CaO \rightarrow Ca + O \quad (2)$$

$$2D + O \rightarrow D_2O \quad (3)$$

$$CaO + D_2O \rightarrow Ca(OD)_2 \quad (4)$$

However, taking into account the thickness of the CaO and the number of O atoms, contribution of the D atoms in the compounds is very small for D/Pd. It is estimated to be 10^{-5}. Therefore, there might be other properties of CaO to achieve higher D/Pd.

We also found that the D/Pd for the sample with Pd membrane was varied. Even just after loading experiment, quite low D/Pd can be observed. The D/Pd for the sample with Pd membrane was lower. It was supposed that loaded gas was desorbed before weighing the sample due to high activity in diffusion in the Pd membrane and recombination on the surface of the Pd membrane. Deformation of the sample was

observed at the same time. All sample containing Pd membrane bent by a thin film on the inside (Fig. 5). This may indicate that deuterium has been released from a certain direction. These properties are considered to be due to differences in the surface structure of the thin film and bulk.

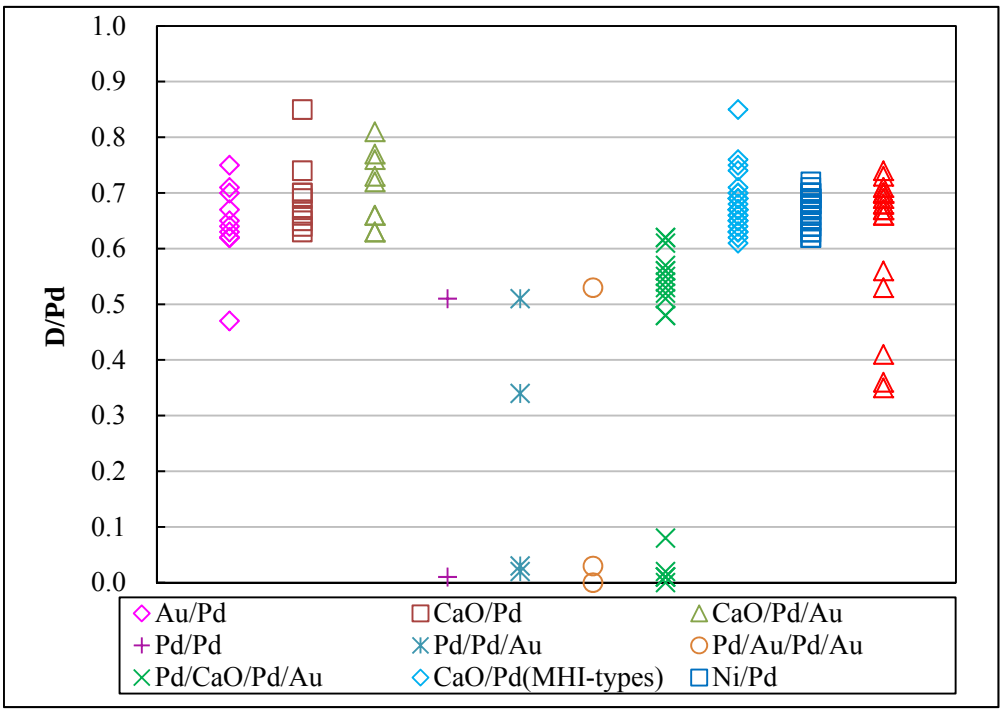

Fig 4. D/Pd ratio for each multi-layered sample

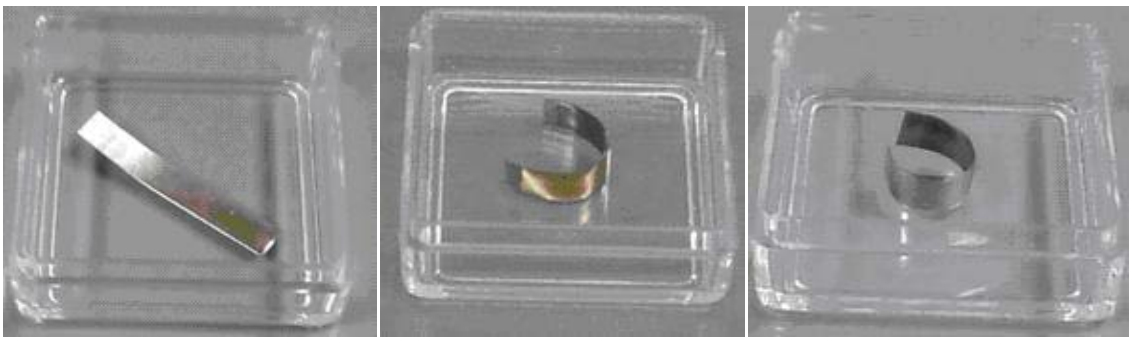

(a) (b) (c)

(a) Pd thin film samples before loading, (b) *Pd*/**Pd** samples after loading, (c)*Pd*/**Pd**/*Au* samples after loading

Fig 5. Deformation of the sample

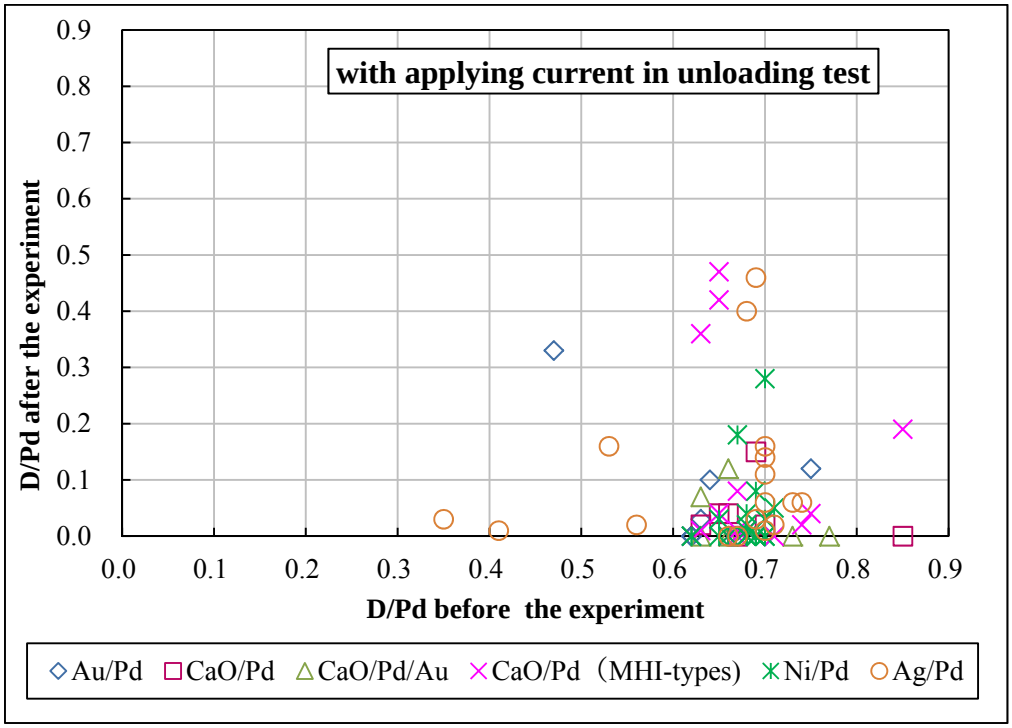

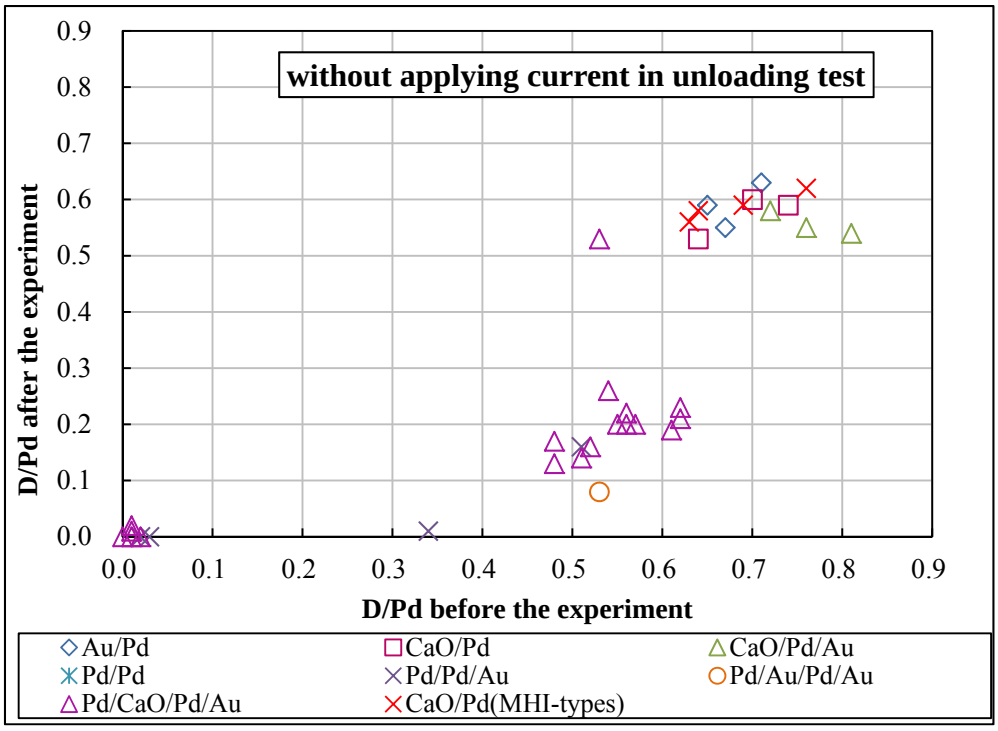

Fig 6. D/Pd before and after unloading test with applying current (top) and without applying current (bottom)

Figure 6 shows the change of D/Pd ratio before and after desorption experiment. Most of samples show that deuterium was not remained in case of applying DC current in the unloading test. However, we found that it remained for a few samples. This may indicate that just a small difference in the surface condition may affect the deuterium loading/unloading behavior. In the unloading test without applying the current, the sample with CaO and/or Au membrane shows high D/Pd even after the experiment. It is supposed that such samples are capable to keep D atoms inside.

Although we expected locally high D/Pd for Pd/*Ni* samples, as mentioned above, we could not confirm such tendency from the results.

5. Summary

We have examined the deuterium loading/unloading behavior for various types of multi-layered metal sample. We found the sample with CaO membrane had higher D/Pd, and it seemed to be capable to hold D atoms. The sample with Pd membrane promotes the deuterium desorption effectively. At the same time, significant deformation of the sample is observed in unloading process. Understanding the unique properties of each multi-layered metal sample in deuterium dynamics is necessary to clarify the mechanism inducing nuclear reaction in the material.

References

[1] E. Yamaguchi *et al*.,Jp. J. Appl. Phys. 29 (1990) L666
[2] Y. Iwamura *et al*., Jp. J. Appl. Phys. 41(2002) 4642
[3] H. Sakoh *et al*., Proc of JCF11 (2011) 16.
[4] S. Narita *et al.*, Proc. of JCF9 (2009) 11.
[5] M.Kawashima *et al*., Proc of JCF11 (2011) 29
[6] Y. Fukai *et al.*, “Suiso-to-kinzoku” (2002) (in Japanese)

Increase of Transmutation Products in Deuterium Permeation Induced Transmutation

Y. Iwamura, S. Tsuruga, T. Itoh

Advanced Technology Research Center, Mitsubishi Heavy Industries, ltd., Yokohama, 220-0012, Japan

Abstract

Low energy nuclear transmutations have been observed in the nano-sized Pd complexes, which are composed of Pd and CaO thin film and Pd substrate, induced by D2 gas permeation. In order to increase the transmutation products, we tired two types of experimental approaches. One is the electrochemical deuterium permeation method to increase the surface deuterium density near the surface of the nano-structured Pd multilayer film. The other is the laser irradiation method for making electron rich state near the surface. The electrochemical deuterium permeation method gave us increased transmutation products, although the effect of the laser irradiation method was not clear. Many kinds of transmuted products were obtained and gamma-ray emissions were observed by the electrochemical deuterium permeation method.

INTRODUCTION

Transmutation reactions in nano-structured material have been observed in nano-structured Pd multilayer thin film which is composed of Pd and CaO thin film and Pd substrate, induced by D_2 gas permeation[1]-[5]. Experimental data that indicates the presence of transmutation have been accumulated and experimental conditions for inducing low energy transmutation reactions are gradually becoming clear, although systematic experimental study is still insufficient. Replication experiments have been performed by some researchers and similar results have been obtained [6]-[8]. Potential applications would be expected as an innovative nuclear transmutation method of radioactive waste and a new energy source.

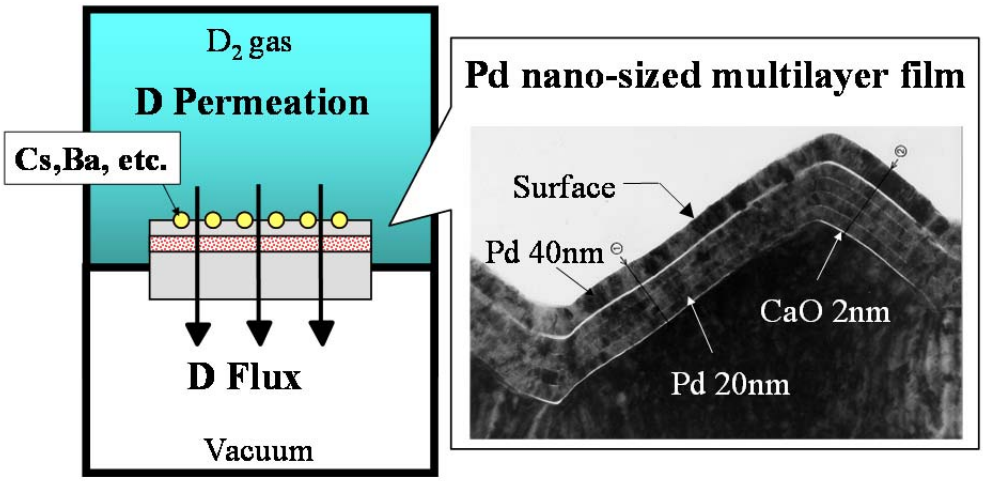

Fig.1 Experimental Method for Permeation Induced Nuclear Transmutation.

Figure 1 shows schematic of our experimental method. Our approach can be characterized by the permeation of D_2 gas through the nano-structured Pd complex and the addition of an element that is specifically targeted to be transmuted. Permeation of deuterium is attained by exposing one side of the Pd multilayer thin film to D_2 gas while maintaining the other side under vacuum conditions. The surface of the plate was covered by layers of CaO and Pd, which were obtained by five times alternately sputtering 2-nm-thick CaO and 20-nm-thick Pd layers. Then a 40nm-thick Pd layer was sputtered on the surface of the CaO and Pd layers. These processes were performed by the Ar ion beam sputtering method. After fabricating a Pd complex, Cs was deposited on the surface of the thin Pd layer. After fabricating a Pd complex, Cs, Ba, or other element is deposited on the surface of the top thin Pd layer. The added elements can be transmuted.

Reactions observed so far in our group are shown in TABLE 1. Based on these experimental results, alkali elements seem to be transmutable by our method. In other words, chemically active elements that can easily emit electrons might be transmutable. And the obtained experimental results so far suggest that a certain rule seems to exist. We can notice that 2d, 4d or 6d look like reacting with deposited elements. Multi-body reactions like 2d, 4d and 6d require sufficient number of d. Therefore we can see that sufficient deuterium density would be important to induce transmutation reactions.

TABLE1 [1]-[5]
TYPICAL REACTIONS OBSERVED SO FAR

Elements		Assumed Reactions
Cs	4d	$^{133}_{55}Cs \xrightarrow{4d(2\alpha)} {}^{141}_{59}\mathrm{Pr}$
Ba	6d	$^{138}_{56}Ba \xrightarrow{6d(3\alpha)} {}^{150}_{62}Sm$, $^{137}_{56}Ba \xrightarrow{6d(3\alpha)} {}^{149}_{62}Sm$
W	4d or 2d	$^{182}_{74}W \xrightarrow{4d(2\alpha)} {}^{190}_{78}Pt$, $^{186}_{74}W \xrightarrow{2d(\alpha)} {}^{190}_{76}Os$

Table 2 shows correlation between intermediate material in Pd multilayer film and transmutation results. If we replaced CaO with MgO, we did not obtain any positive transmutation products; we could not observe any transmutation reactions. It means that MgO cannot work instead of CaO. Three cases out of the three experiments using MgO show no Pr by ICP-MS measurements, although D_2 gas Flow rates were enough (2-3sccm) in all cases. However, if we replaced CaO with Y_2O_3, we could observe transmutation reactions from Cs to Pr. Y_2O_3 works like CaO. Work functions for MgO, Y_2O_3 and CaO are shown in the Table 2. Although it is difficult to make conclusive results, the existence of low work function of intermediate material might have some effects to induce transmutation.

TABLE2
CORRELATION BETWEEN INTERMEDIATE MATERIAL IN PD MULTILAYER FILM AND TRANSMUTATION RESULTS

Intermediate Material	Work Function (eV)	Results for analysis after permeation
CaO	1.2	Pr detected >100cases
Y_2O_3	2.2	Pr detected >10cases
MgO	3.3	No Pr (3cases)

The permeation induced transmutation technology would be expected as an innovative nuclear transmutation method for radioactive waste and a new energy source. However, it is necessary to increase the amount of transmutation products for commercialization.

The author is now assuming that the following two conditions are important to increase up transmutation products based on the experimental results.

i) Local deuterium density is sufficiently high.
ii) Electron rich state is important.

According to these assumptions, we tried to increase the amount of transmutation products by the increase of deuteron density and the excitation of surface Plasmon on the Pd multilayer.

INCREASE OF DEUTERON DENSITY USING AN ELECTROCHEMICAL METHOD

Figure 2 shows the transmutation products dependence on D_2 gas pressure in the case of Cs transmutation into Pr. Conversion rate means how much portion of initial Cs was transmuted into Pr. Amount of Pr is expressed as the mass of Pr divided by the permeated surface area. Typical permeated surface area is about 1.0cm^2.

It is possible to see that the amount of Pr and conversion rate increase as the D_2 gas pressure increase. It is reasonable that multi-body reactions observed in the permeation induced transmutation require sufficient number of deuterium. Therefore we need high D_2 gas pressure since it gives much deuterium near the surface.

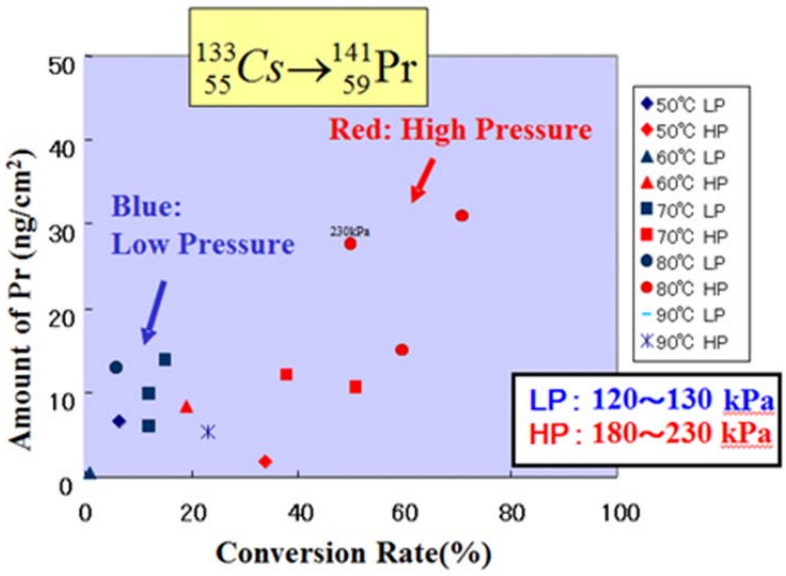

Fig.2 Pr Dependence on D_2 gas pressure.

An electrochemical method is applied to increase deuterium surface density as shown in Fig.3. A photo of our apparatus is shown also in the Fig.3. If we apply this method, we can provide very high deuterium density by controlling applied voltage between the Pd/CaO multilayer thin film and the anode made of Platinum. Simple

pressurization is, off course, one of the solutions which give high deuterium density, however, it needs relatively large-scale apparatus. Therefore we choose this electrochemical method for giving high deuterium density to the Pd surface, taking into the consideration of future commercialization.

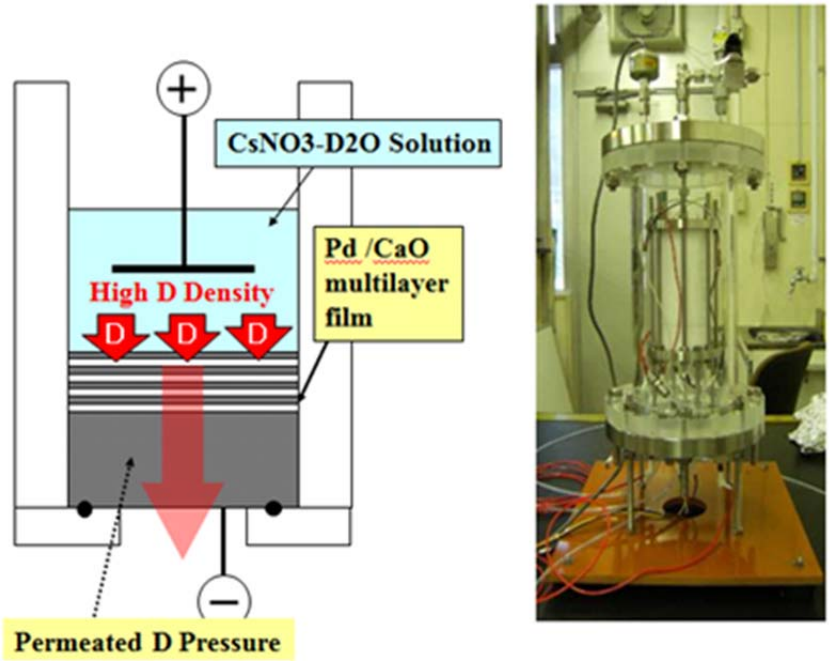

Fig.3 Electrochemical Deuterium Permeation Apparatus aiming the Increase of Deuterium Density.

An example of experimental results is shown in Figure 4 and 5. A 0.1M $CsNO_3$-D_2O solution was used for this experiment. Purity for both NO_3 and D_2O is more than 99.9%. Mass distributions by SIMS (Secondary Ion Mass Spectrometry) are plotted in the Fig.4 and mass distributions by ICP-MS (Inductively Coupled Plasma Mass Spectrometry) for the same sample: E006 are shown in Fig.5.

We can postulate that nuclear transmutation reactions occur at the permeated part of the Pd multilayer sample (center), however, no reactions occur at the part where no D permeated (corner). In advance, Cs ion implantation (20kV, 10^{16} ions/cm^2) were applied to Pd multilayer.

SIMS counts are plotted in a logarithmic scale in Fig. 4(a). SIMS analysis was performed by O^{2+} ions and the analyzed area was circle in 60□m diameter. Mass 133 corresponds to Cs and SIMS counts for mass 133 of E006-corner are larger than those of E006-center as shown in Fig. 4(a). It means that ^{133}Cs decreased at the center of E006. On the contrary, SIMS counts around mass 140 of E006-center are larger than

those of E006-corner. It means that elements or molecular compounds that have mass number around 140 increased at the deuterium permeated point where SIMS analysis was performed. As a reference, SIMS mass distributions for no Cs implantation sample are plotted for both center and corner. The increase of SIMS counts around mass 140 cannot be seen as for the no implantation sample.

The magnified mass spectra from mass 130 to mass 150 is shown in Fig 4(b) where SIMS counts are plotted in a linear scale. It can be seen that SIMS counts around mass 140 are greatly increased only for the E006-center.

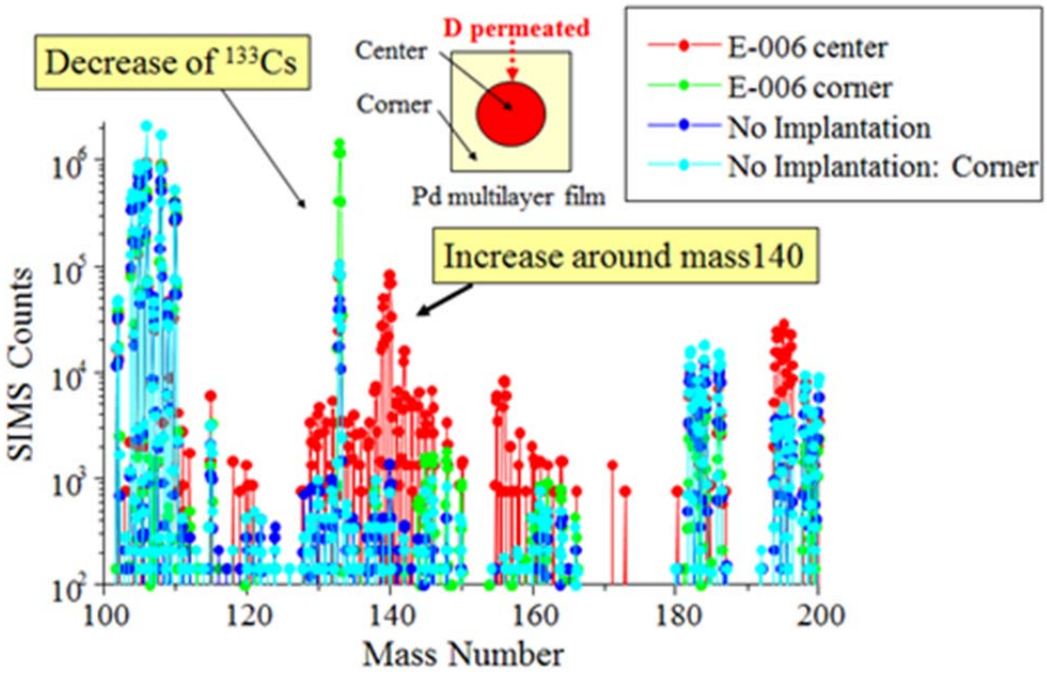

(a) Wide SIMS Spectra in a logarithmic scale

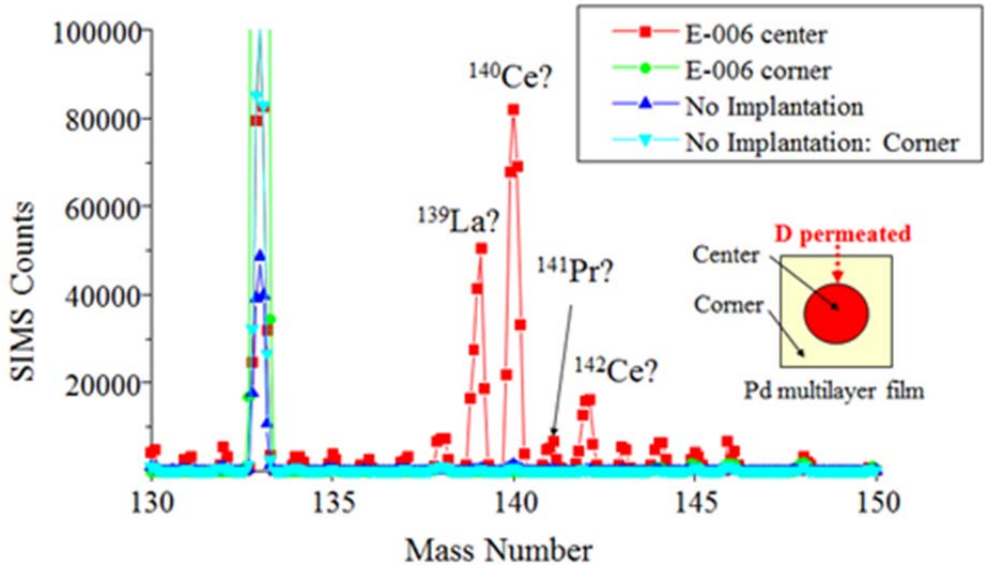

(b) Magnified SIMS Spectra from mass 130 to mass 150 in a linear scale.

Fig.4 Comparison of SIMS Mass Spectra between E006 and No Cs Implantation sample.

We performed ICP-MS analysis to confirm the obtained results by SIMS analysis. Basically, the mass information obtained by SIMS is at the analyzed small point. In contrast, the information obtained by ICP-MS is from the sample surface because mass distribution was analyzed for the HNO_3 solution that contains the surface of Pd multilayer thin film. In the ICP-MS analysis, we cut a permeated Pd multilayer sample into 1/4 size and put it into 68% high purity HNO_3 solution and analyzed the HNO_3 solution that contained the surface part of it.

Figure 5 (a) shows ICP-MS results for E006 and the no Cs implantation and D permeated sample. ICP-MS counts around mass 140 of E006 are larger than those of no Cs implantation sample. It means that elements or molecular compounds that have mass number around 140 increased on the dissolved surface by HNO_3. The magnified mass spectra from mass 130 to mass 150 are shown in Fig 5(b) where ICP-MS counts are plotted in a linear scale. It would be possible to say that Fig.4 and Fig.5 are similar around mass 140, although the difference of signals between E006 and no Cs implantation is smaller for Fig.5. It is reasonable because SIMS data is taken from the point where transmutation reactions were supposed to occur, however, ICP-MS results contained corner part where no D was permeated and therefore no transmutation reactions were supposed to occur.

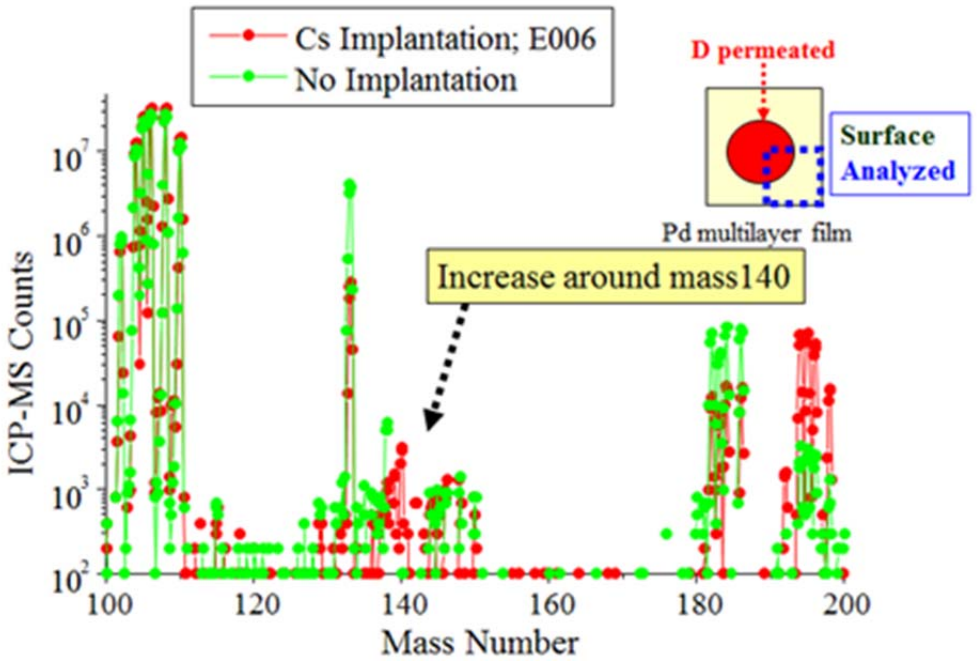

(a) Wide ICP-MS Spectra in a logarithmic scale

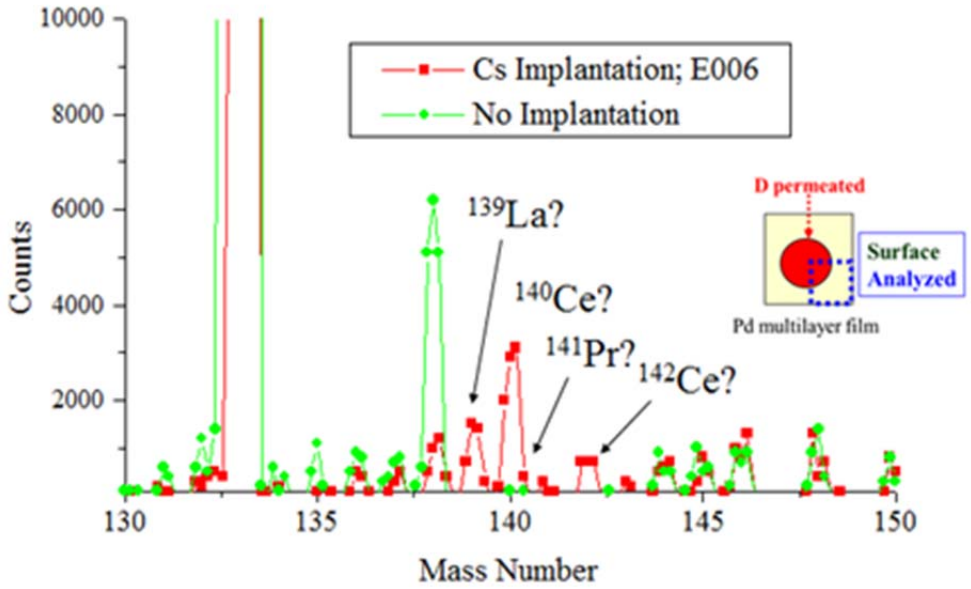

(b) Magnified SIMS Spectra from mass 130 to mass 150 in a linear scale

Fig.5 Comparison of ICP-MS Mass Spectra between E006 and No Cs Implantation sample.

Next we examined the formations of compound species for mass 139 and 140 that large increases were observed. Possible compounds for mass 139 and 140 are shown in TABLE 3. If we carefully examine and take natural abundances for each element into consideration, mass 139 and 140 cannot be explained by these compounds. Therefore mass 139 and 140 would be ^{139}La and ^{140}Ce, respectively. Off course, it is preferable to make cross check by the other analysis methods that have other measurement principle, for example, XRF or XPS. It is the next step work to confirm these results by the other methods.

TABLE 3
POSSIBLE COMPOUNDS FOR MASS 139 AND 140

Possible compounds for mass 140		
^{138}Ba(71.7%)D	^{133}Cs (100%)^{7}Li (92.4%)	^{110}Pd ^{30}Si(3.1%)
^{106}Pd ^{34}Si(4.3%)	^{109}Ag(48.1%) ^{31}P(100%)	^{104}Pd ^{36}Ar(0.33%)
^{102}Pd ^{38}Ar(0.06%)	^{110}Pd ^{28}Si(92.3%)D	^{108}Pd ^{30}Si(3.1%)D
^{105}Pd ^{33}Si(0.8%)D	^{102}Pd ^{36}Si(0.02%)D	^{102}Pd ^{36}Ar(0.3%)D
Possible compounds for mass 139		
^{137}Ba(11.2%)D	^{133}Cs (100%)^{6}Li (7.6%)	^{110}Pd ^{29}Si(4.7%)
^{106}Pd ^{33}Si(0.8%)	^{104}Pd ^{35}Cl(75.8%)	^{102}Pd ^{37}Cl(24.2%)
^{110}Pd ^{27}Al(100%)D	^{106}Pd ^{31}P(100%)D	^{105}Pd ^{32}S (94.9%)D
^{104}Pd ^{33}Si(0.8%)D	^{105}Pd ^{32}Si(94.9%)D	^{102}Pd ^{35}Cl(75.8%)D

According to our experimental results using D_2 gas permeation, we usually observed transmutation of Cs into Pr, in other words, mass 133 decreased and mass 141 increased. In this new apparatus, however, mass 139, 140, 141 and 142 increased while mass 133 decreased. The differences between D_2 gas permeation and electrochemical D permeation can be attributed to the effective deuterium density and/or source of deuterium.

Let us consider about contamination due to the $CsNO_3$-D_2O solution. If we analyzed the $CsNO_3$-D_2O solution, we could not see any mass numbers of 139, 140, 141, 142 (La, Ce, Pr). Furthermore, we make comparison between E006 and the D permeated sample. The D permeated sample was contacted with $CsNO_3$-D_2O solution and almost the same current was applied. The other experimental conditions except Cs

implantation were all the same. However, the only permeated part of E006 has different mass distribution as shown in Fig.4 and 5. So it is very difficult to assume that obtained mass difference between D_2 gas permeation and electrochemical D permeation are derived from the contamination of $CsNO_3$-D_2O solution. Therefore we might consider the effective deuterium density make effects on the transmutation reaction pass. Anyway, we should make more experiments using the other measurement methods and improve the reliability of our experiments.

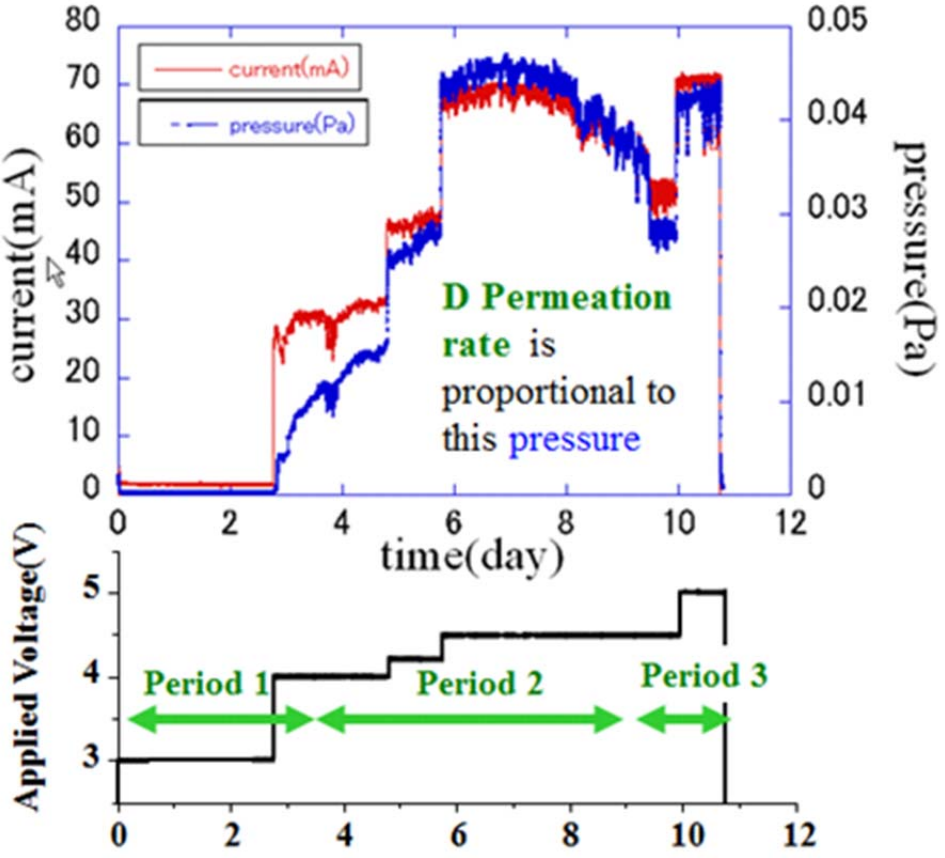

Fig.6 Time variation of Applied Voltage, Current and Pressure during an experiment E16.

Let us move onto the next point. We describe an example of gamma-ray detection during an electrochemical D permeation experiment. In the Fig.6, applied voltage and corresponding current between Pd multilayer thin film and Pt anode, pressure at the exit side of Pd multilayer cathode are plotted as a function of time. Deuterium permeation rate is proportional to the pressure described here. At the beginning of the experiment, applied voltage was 3V and the current was low. If we increased the voltage up to 4 V, the current increased and permeated D increased correspondingly, as shown in Fig.6.

If we increased the voltage up to 4.5V, current amounted to 70mA and deuterium permeation increased, however, the current and D permeation decreased gradually even though we did not change the applied voltage.

In this experiment, $Pd/Y_2O_3/Pd$ multilayer thin film with Cs implantation and 0.5M CsNO3-D2O solution were used.

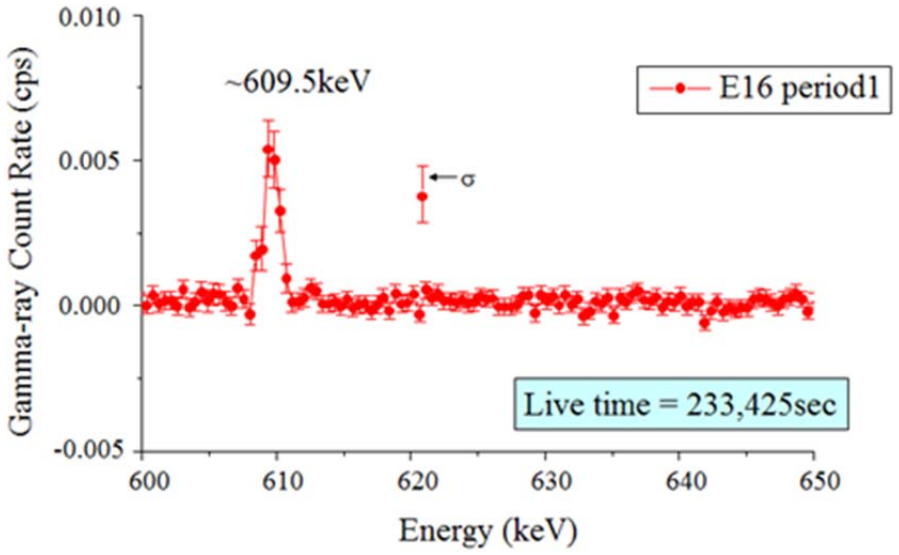

(a) Gamma-ray Energy Spectrum emitted during Period 1

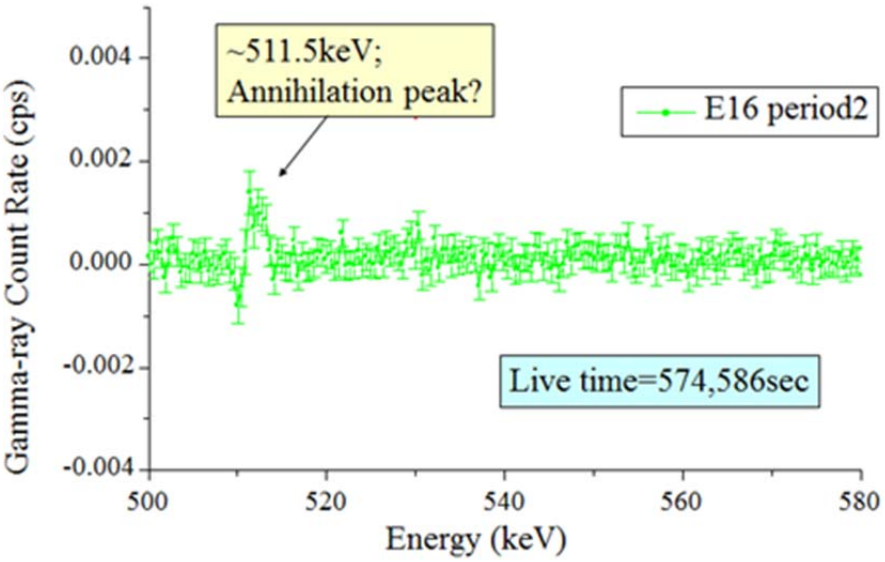

(b) Gamma-ray Energy Spectrum emitted during Period 2

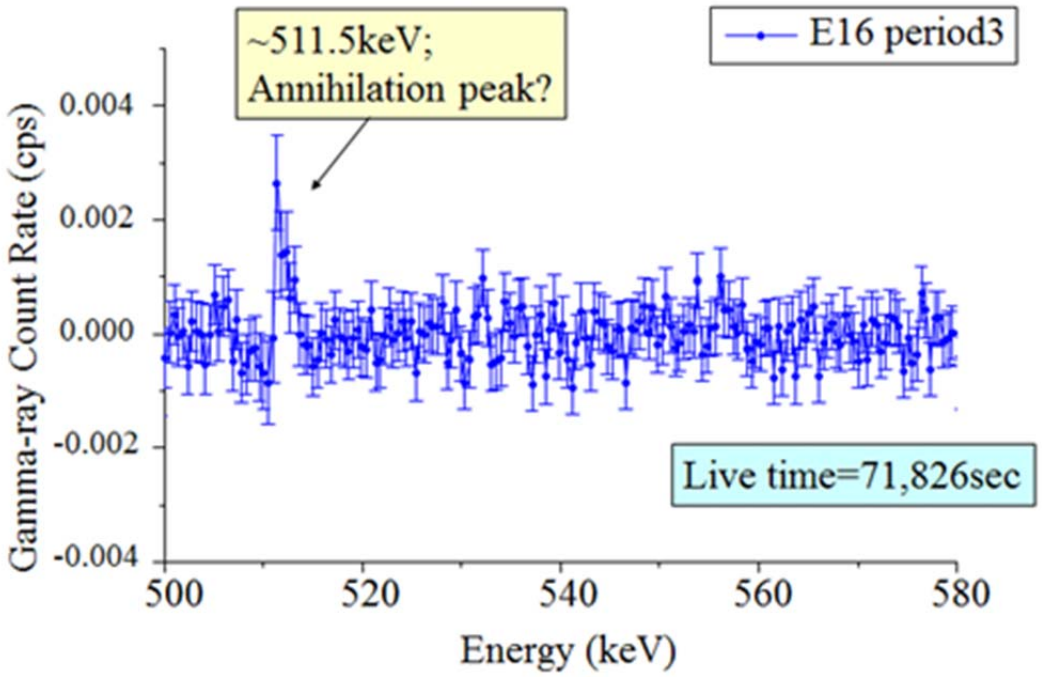

(c) Gamma-ray Energy Spectrum emitted during Period 3

Fig.7 Gamma-ray Emissions during an electrochemically D permeation experiment E16.

Gamma-ray measurements using a Germanium detector were performed during electrochemical D permeation experiments. In this experiment (E16), gamma-ray energy spectra were obtained for 3 periods shown in Fig.6. We deducted background energy spectra from obtained gamma-ray spectra during period 1, 2 and 3.

Emitted gamma-ray spectra are plotted in Fig.7 (a), (b) and (c), which correspond to period 1, 2 and 3, respectively. Standard deviations are also plotted for each point in all spectra. During period 1, very low current and low permeation rate, a clear gamma-ray peak around 609keV exceeding statistic error was detected. During period 2 and 3, relatively high current and large amount of D permeation, the 609keV gamma-ray vanished and a peak around 511keV was detected. There was no 511keV peak during period 1.

Gamma-rays were not always detected. Energy spectra, in most cases, were exactly the same as background spectra, which were taken several times using the same set-up without D permeation. In the case of experiment E16, as well as a few experiments, gamma-rays exceeding statistical errors were detected. Ge detector and experimental

apparatus were fixed during the experiments, off course.

We could not observe clear gamma-ray emissions for D_2 gas permeation experiments for long time. What does it mean that we can observe weak gamma-ray emissions recently from the electrochemical D permeation? The electrochemical D permeation method gives us more transmuted products than D_2 gas permeation method. Detection of gamma-ray might be correlated to the increase of the transmuted products. The 511keV gamma-ray is closed to annihilation energy and we might have some unstable nuclear species that emit positron. Further study is necessary to identify the source of the gamma-ray emitter. We are now planning to suppress the background gamma-rays in order to obtain better statistic results.

EFFECT OF LASER IRRADIATION

As I described in the TABLE 2, work function of the intermediate layer seems to be important. Then we assumed that electron rich state was important. In order to make electron rich state near surface of the Pd multilayer thin film, we tried to use laser stimulation method that was reported by Letts [9] to enhance excess heat generation.

If we irradiate the surface of the Pd multilayer, surface Plasmon is excited. So we would have a lot of high electron density region by the Plasmon excitation. As the Plasmon has pico-second order wave and typical nuclear reaction occurs within the order of femto-second, high electron density region would be kept high during nuclear transmutation reaction proceed. Therefore it might be possible to enhance the rate of nuclear transmutation reaction by laser irradiation.

Figure 8 shows a schematic of the experimental set-up for Plasmon excitation by laser irradiation. A fiber UV-laser that has 355nm wave length was applied. The multilayer Pd complexes are Pd/CaO/Pd and D_2 gas permeation experiments with laser irradiation were performed 3 times.

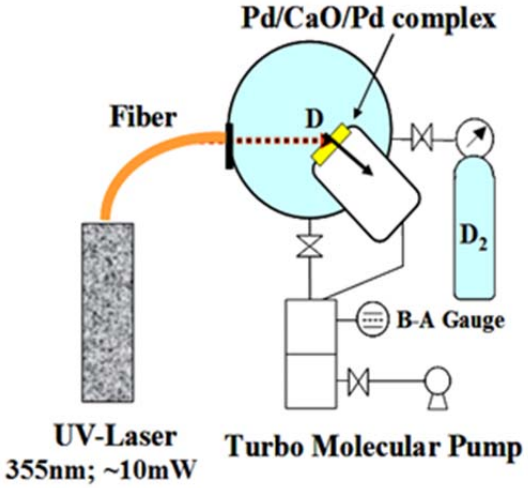

Fig.8 Schematic of the Experimental Set-up for Plasmon Excitation by Laser Irradiation.

An example of experimental results is shown in Fig.9. SIMS spectra for the permeated with laser irradiation and no permeation samples are plotted. As you can see, ^{133}Cs decreased and ^{141}Pr emerged in a very similar way to the original D_2 gas permeation experiments. According to this result, we cannot find enhancement by laser irradiation.

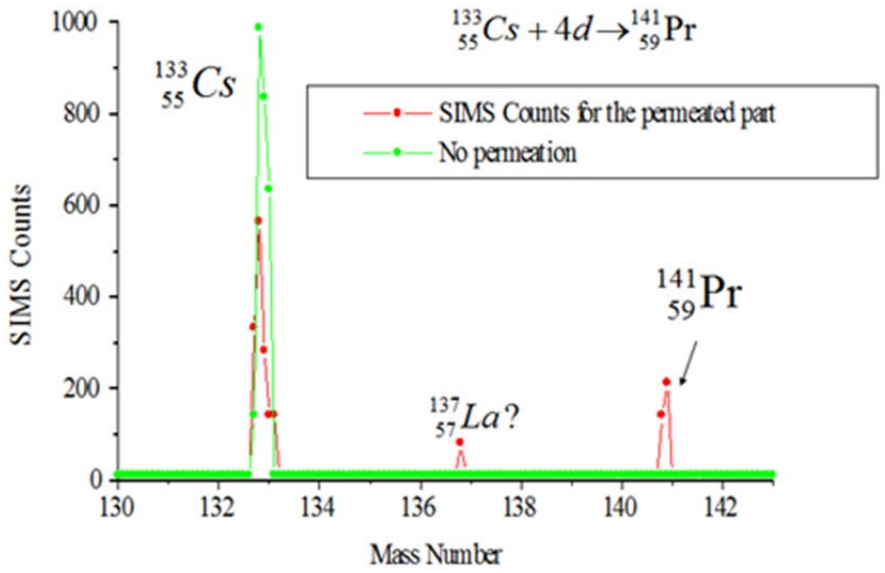

Fig.9 SIMS Spectra for the Permeated with Laser Irradiation and No Permeation Samples.

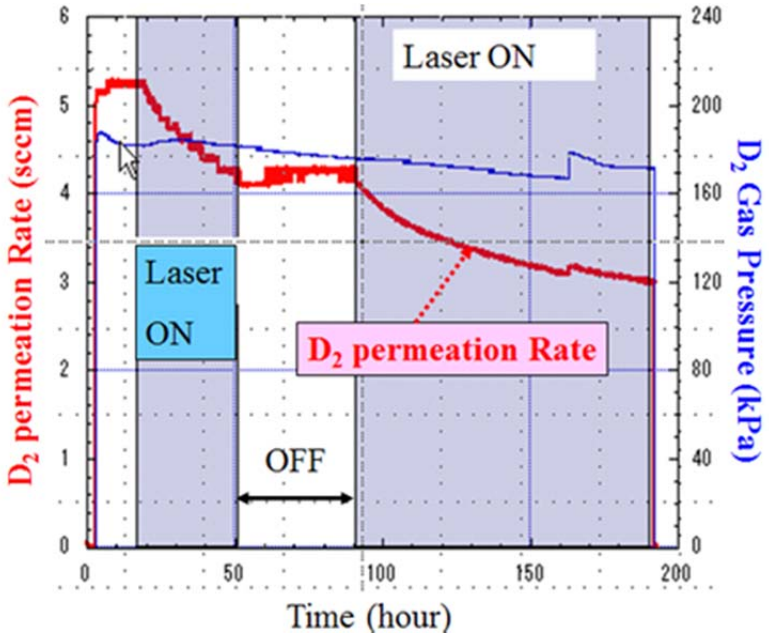

Fig.10 Effect of Laser Irradiation on D_2 Gas Permeation Rate

The effect of laser irradiation on D_2 gas permeation rate is shown in Fig.10. The laser irradiated periods are painted with blue color. D_2 gas permeation rate decreased when the laser was irradiated for all the cases as shown in the Fig.10. The mechanism for this phenomenon is not clear but deuterium absorption process might be influenced by laser irradiation. D_2 gas permeation rate is one of the important factors to induce permeation transmutation reactions [4]; laser irradiation method is not so desirable in the view of the permeation rate.

CONCLUDING REMARKS

We tired two types of experimental approaches in order to increase transmuted products in the deuterium permeation induced transmutation reactions. One is the electrochemical deuterium permeation method to increase the surface deuterium density near the surface of the nano-structured Pd multilayer film. The other is the laser irradiation method for making electron rich state near the surface. The electrochemical deuterium permeation method gave us increased transmutation products, although the effect of the laser irradiation method was not clear. Many kinds of transmuted products were obtained and gamma-ray emissions were observed by the electrochemical deuterium permeation method. It is necessary to perform more experiments from different viewpoints using the other measurement methods and improve the reliability

of our experiments.

ACKNOWLEDGMENT

The authors would like acknowledge Prof. K. Fukutani, Prof. D. Sekiba, Dr. C. Nishimura, Prof. A.Takahashi, Prof. J. Kasagi, Dr. Hioki, Dr. F. Clelani, Prof. M. Melich, Dr. K. Grabowski, Prof. H. Yamada and Prof. S. Narita for their supports and valuable discussions.

REFERENCES

[1] Y. Iwamura, M.Sakano and T.Itoh, "Elemental Analysis of Pd Complexes: Effects of D2 Gas Permeation", *Japanese Journal of Applied Physics*, Vol.41, (2002) pp. 4642-4650.

[2] Y. Iwamura, T. Itoh, N.Yamazaki, J. Kasagi, Y. Terada, T. Ishikawa, D. Sekiba, H. Yonemura and K. Fukutani, "Observation of Low Energy Nuclear Transmutation Reactions Induced by Deuterium Permeation through Multilayer Pd and CaO thin Film", *J. Condensed Matter Nucl. Sci.* vol.4 (2011) pp.132–144.

[3] Y. Iwamura, T. Itoh, M. Sakano, S. Kuribayashi, Y. Terada and T. Ishikawa, "Observation of Surface Distribution of Products by X-ray Fluorescence Spectrometry during D2 gas permeation through Pd Complexes", Condensed Matter Nuclear Science, ed. by A. Takahashi et.al, World Scientific, New Jersey, (2006) pp.178-187.

[4] Y. Iwamura, T. Itoh, M. Sakano , S. Sakai and S. Kuribayashi, "Low Energy Nuclear Transmutation in Condensed Matter induced by D2 Gas Permeation through Pd Complexes: Correlation between Deuterium Flux and Nuclear Products", Condensed Matter Nuclear Science, ed. by P. H. Hagelstein and S. Chubb, World Scientific, New Jersey, (2006) pp.435-446.

[5] Y. Iwamura, T. Itoh, N. Yamazaki, N. Watari, H. Yonemura, K. Fukutani, D. Sekiba, "Recent Advances in Deuterium Permeation Transmutation Experiments", *Proc. of ICCF16*, to be published.

[6] N. Takahashi, S. Kosaka, T. Hioki and T. Motohiro, "Detection of Pr in Cs ion-implanted Pd/CaO multilayer complexes with and without D_2 gas permeation," *Proc. of ICCF17*, to be published..

[7] T. Higashiyama, M Sakano, H. Miyamaru and A. Takahashi, "Replication of MHI Transmutation Experiment by D_2 Gas Permeation Through Pd Complex", Proceedings of 10th International Conference on Condensed Matter Nuclear Science,

edited by P. H. Hagelstein et al., Condensed Matter Nuclear Science, World Scientific, New Jersey (2006) pp.447-454.

[8] H. Yamada et.al., Producing Transmutation Elements on Plain Pd-foil by Permeation of Highly Pressurized Deuterium Gas, Proceedings of 12th International Conference on Condensed Matter Nuclear Science, ed. by A. Takahashi et al., Condensed Matter Nuclear Science, World Scientific, New Jersey (2006)pp.196-205.

[9] Letts, D. and D. Cravens. "Laser Stimulation of Deuterated Palladium: Past And Present", *Proc. of ICCF10*, 2003. Cambridge, World Scientific, Inc (2006) pp.159-170.

Heat release characteristics of Ni-based samples absorbing hydrogen isotopes at higher temperature

H. Sakoh[1]*,Y. Miyoshi[1], A. Taniike[1], Y. Furuyama[1], A. Kitamura[1,2], A.Takahashi[2,3], R. Seto[2], Y. Fujita[2], T. Murota[4] and T. Tahara[4]

[1]Graduate School of Maritime Sciences, Kobe University, Higashinada-ku, Kobe 6580022, Japan
[2]Technova Inc, Chiyoda-ku, Tokyo 1000011, Japan
[3]Osaka University, Suita 5650871, Japan
[4]Santoku Corp., Higashinada-ku, Kobe 6580013, Japan
*118W509W@stu.kobe-u.ac.jp

Abstract: We observed anomalous excess heat release from the Ni-based nano-compound samples at temperatures higher than 500K. The η value defined as the output energy per one hydrogen isotope atom absorbed/adsorbed showed anomalously large values exceeding 100 eV/atom-H for the Cu-Ni/ZrO_2 samples, and the integral output energy reached 800 eV/atom-Ni. Since such a large excess energy cannot be caused only by chemical reactions, it is strongly inferred that some kind of nuclear process participates in the phenomena.

Keywords: Ni, Cu-additive, nano-compound, anomalous excess heat, protium-absorption

1. Introduction

Recently, several researchers claimed excess heat from Ni-based binary-metal nano-meter-size samples under application to gas-phase protium absorption experiments instead of expensive Pd-based nano-compounds [1,2]. In our past study, Pd_1Ni_7 nano-particles dispersed in a ZrO_2 supporter (PNZ2B), supplied by B. Ahern, showed excellent characteristics for anomalously large excess heat release and H/Ni loading ratios under hydrogen absorption at room temperature [3]. Although the sample of Ni-nano-particles alone in ZrO_2 supporter did not absorb hydrogen isotopes at room temperature, it was found that the small amount of Pd additive-atoms acted as a strong catalyst for hydrogen absorption of the Ni nano-particles.

From a practical industry application point of view, Pd is too expensive to be used as the component-material of energy source device. In the present study, we examine possibility of substitution of Cu for Pd as the catalyst, and try to find better concentration of Cu as additive atoms for the better catalytic activity.

2. Experimental apparatus and procedure

Physical properties of the samples used in the present study, Ni(0.36)/ZrO_2 (NZ), Cu(0.08)·Ni(0.36)/ZrO_2 (CNZ) and Cu(0.214)·Ni(0.215)/ZrO_2 (CNZII), are tabulated in Table 1. The molar fraction is the fraction of metallic elements only.

Table1. Physical properties of the used NZ, CNZ and CNZII sample.

	NZ 20[g]			CNZ 10[g]			CNZII 20[g]		
	Cu	Ni	ZrO_2	Cu	Ni	ZrO_2	Cu	Ni	ZrO_2
Average grain size(nm)	---	23.3	---	6.8	24.5	---	24.2	18.2	---
Molar fraction(%)	0	35.8	64.2	7.9	36	56.1	21.4	21.5	57.1
Weight content(g)	0	5.4	14.6	0.49	2.07	7.44	2.64	2.44	14.9
Specific surface area(m^2/g)	27.6			45.3			44.2		

We have used a twin absorption system consisting of two equivalent chambers for hydrogen isotope gas absorption / adsorption experiments. Figure 1 shows a schematic of one-part of the twin system. The samples are put in the reaction chambers, and the outer chambers are evacuated for thermal insulation during hydrogen isotope absorption / adsorption. Sheath heaters with resistance of 37.9 Ω and 53.8 Ω wound around the reaction chambers in the A_1 and A_2 systems, respectively, are used for sample baking and also for sample heating in the cases of absorption runs at elevated temperatures.

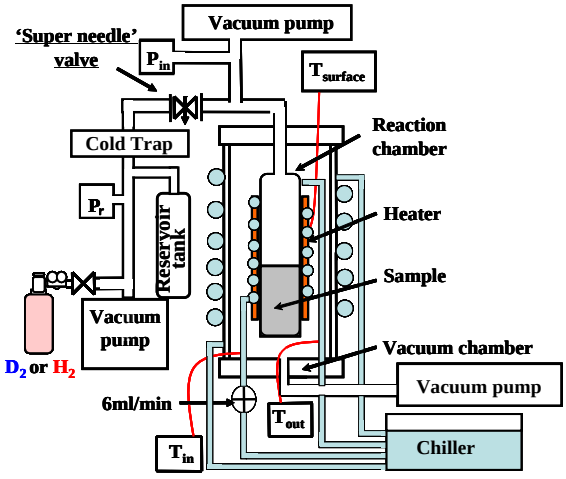

Fig. 1. Functional view of the system A_1. Water cooling of the reaction chamber with a flow rate of 6 ml/min was done only in the #1 run at room temperature, while the pipe was emptied in the #5 runs at elevated temperatures without cooling.

Alumel-chromel thermo-couples are used to measure temperatures. In order to make influence of environmental temperature change as small as possible, only the outer vacuum vessel was cooled with water at constant temperature (regulated within 0.1 °C variation) and the experimental room was air-conditioned to keep temperature change within 0.1 °C.

Figure 2 shows the experimental procedure. The reservoir tank is filled with D_2 (H_2) gas at a pressure of 0.3 MPa, typically, before an absorption run starts. The reaction chamber and the outer chamber are evacuated, and the coolant water is run for the outer chamber. The reaction chamber is then heated to a prescribed temperature. When the chambers attain the constant temperature, the D_2 (or H_2) gas is fed with a flow rate adjusted and regulated through a "Super Needle" valve.

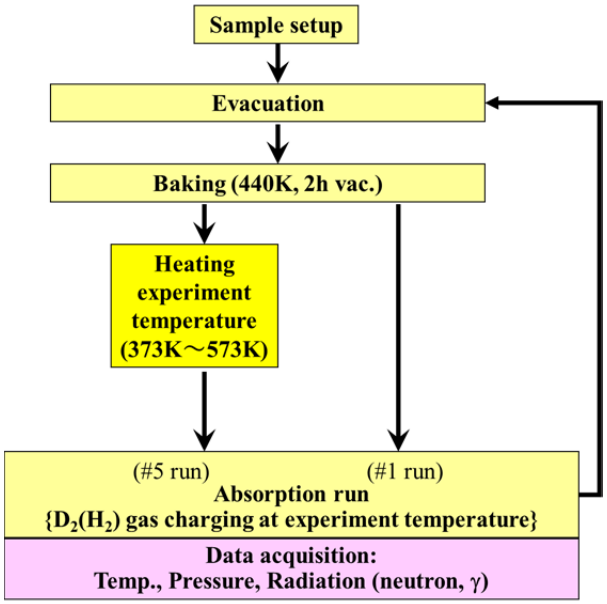

Fig. 2. Flow chart of the experimental procedure.

The run number is designated as "G-PN#M", where G is the gas species (D or H); P the type of the powder (PZ, NZ, CNZ, etc.); N the powder identification number; and M the type of the run, e.g., #1 for a virgin sample at room temperature and #5_*T*K for a used sample run at an elevated temperature of *T* K. When the same sample was subjected to a run with the same condition, a letter "_*n*" is appended. Thus, for example, "H-NZ2#5_523K_2" designates the second protium run at an elevated temperature of 523 K using the sample NZ2. Using the A_1-A_2 twin system, we perform the runs for protium and deuterium simultaneously, which will be expressed as, e.g., "runs D(H)-NZ1(2)#5_523K_2"

3. Results and discussion

3.1. Runs at room temperature

Figure 3 shows typical variation of the heat output powers, $W_D(t)$ and $W_H(t)$, pressures in the twin reaction chambers, $P_D(t)$ and $P_H(t)$, the loading ratios, $L_D(t)$ and $L_H(t)$, in the hydrogen isotope absorption run at 293 K for as-received samples,

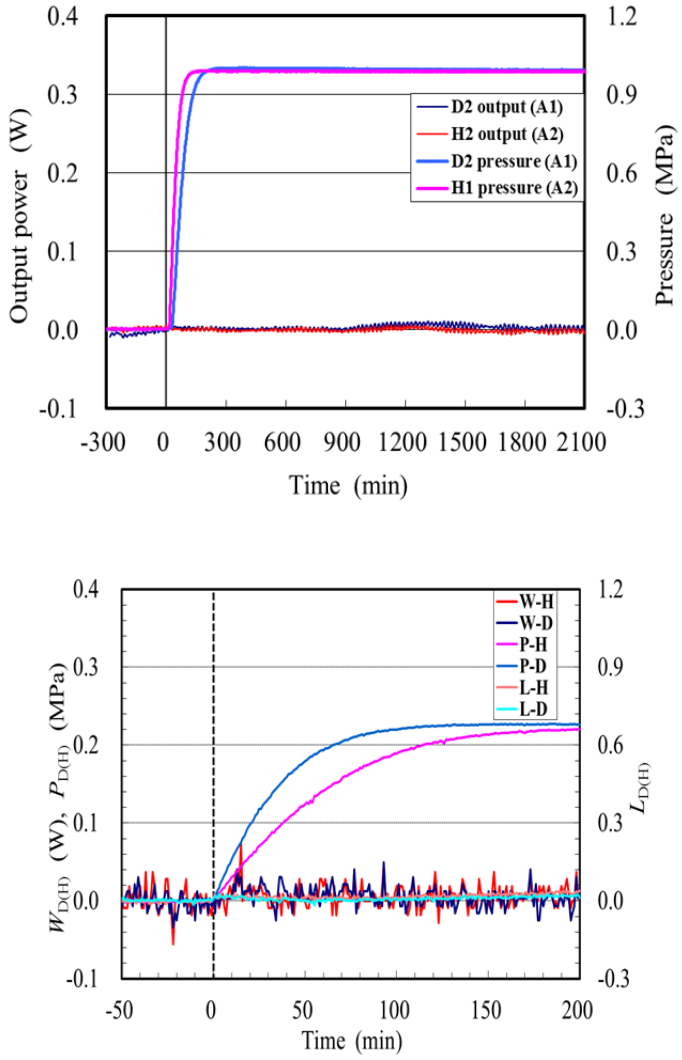

Fig.3. Time dependence of D_2/H_2 absorption parameters for Ni·Zr (upper) and Cu·Ni·Zr (lower) oxide compounds; the run numbers are D(H)-NZ1(2)#1 and D(H)-CNZ1(2)#1, at 293 K (room temperature).

D(H)-NZ1(2)#1 and D(H)-CNZ1(2)#1, respectively. We have observed negligible absorption of hydrogen isotopes accompanied by very small exothermic temperature change, confirming that nickel doesn't absorb hydrogen at room temperature.

Activation of the H(D)-gas absorption reaction is expected at higher temperature. Therefore, the experiments were also conducted at elevated temperatures up to 573 K with use of the heater input power of up to 105 W.

3.2. NZ samples at elevated temperatures

All traces for runs at elevated temperatures shown below are corrected for temperature variation due to introduction of cool gas by subtracting the temperature traces obtained in "blank" runs which should give null output power. As the blank run at each temperature, the reaction chamber was filled with helium gas. Figure 4 shows an example of the variation of the temperatures in the He blank run for the CNZ sample at 573 K. Taking account of difference in heat capacity between He and hydrogen isotopes, the temperature decreases are subtracted from the traces obtained in the CNZ**#5_573K runs.

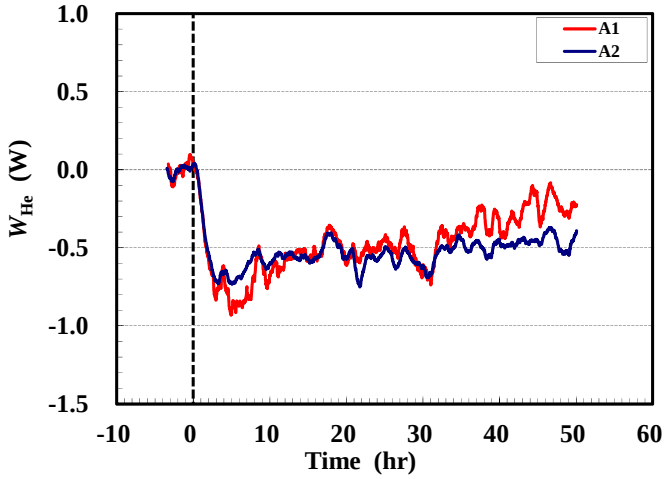

Fig. 4. Temperature variation in the He blank run operated at 573 K.

Figures 5-(a) through (d) show typical variation of the heat output power. In evaluating the runs, we take notice of the fact that the runs for the present Ni-based nano-compound samples have a phase after tentative saturation of the pressure in which appreciable absorption or even desorption takes place. We call the period before the tentative saturation the transition(T)-phase, and that after the saturation the saturation(S)-phase.

At 373K and 473 K, we didn't observe appreciable exothermic temperature change exceeding an error range of ± 0.2 W determined from the temperature variation in blank runs introducing He gas instead of D_2/H_2. It should be noted, however, that appreciable increases in the loading ratios, $L_D(t)$ and $L_H(t)$, occur in the S-phase.

In the protium absorption run at 523K an exothermic tendency with the maximum output power exceeding 1.0 W (0.2 W/g-Ni) was registered. Although it is only a small change compared with the input heater power of 70 W, it continued for about 40 hours. It is rather interesting that the loading ratio was almost same as that in the H-NZ3#5_473K run, H/Ni = 0.21. It is even smaller than that in the deuterium run

D-NZ4#5_523K; D/Ni = 0.26.

In the second protium run at 573 K, the excess power increased gradually to reach about 2 W (0.4 W/g-Ni), and the exothermic tendency continued for 250 hours. However, the sample absorbed deuterium with much less output power, and sometimes even endothermic phenomenon was seen. The loading ratio there was larger than those in any other runs, i.e. H(D)/Ni = 0.68(1.0) or would have been much larger, if the run would have been continued further. The observed specific output energy E_H exceeding 2×10^2 eV/atom-Ni for the S-phase is too high to be explained only by known chemical processes of heat release.

It is worthwhile to note that the samples show significant hydrogen absorption also in the T-phase at 573 K with appreciable output power reaching 0.5 W (0.1 W/g-Ni). The above observations are in contradiction to our knowledge that nickel as a bulk sample does not absorb hydrogen. The experimental evidences indicate that nickel as a nanoparticle sample has absorption or/and adsorption sites which are activated at the elevated temperatures. In other words, the activation energy, or the barrier potential at the surface, is rather high.

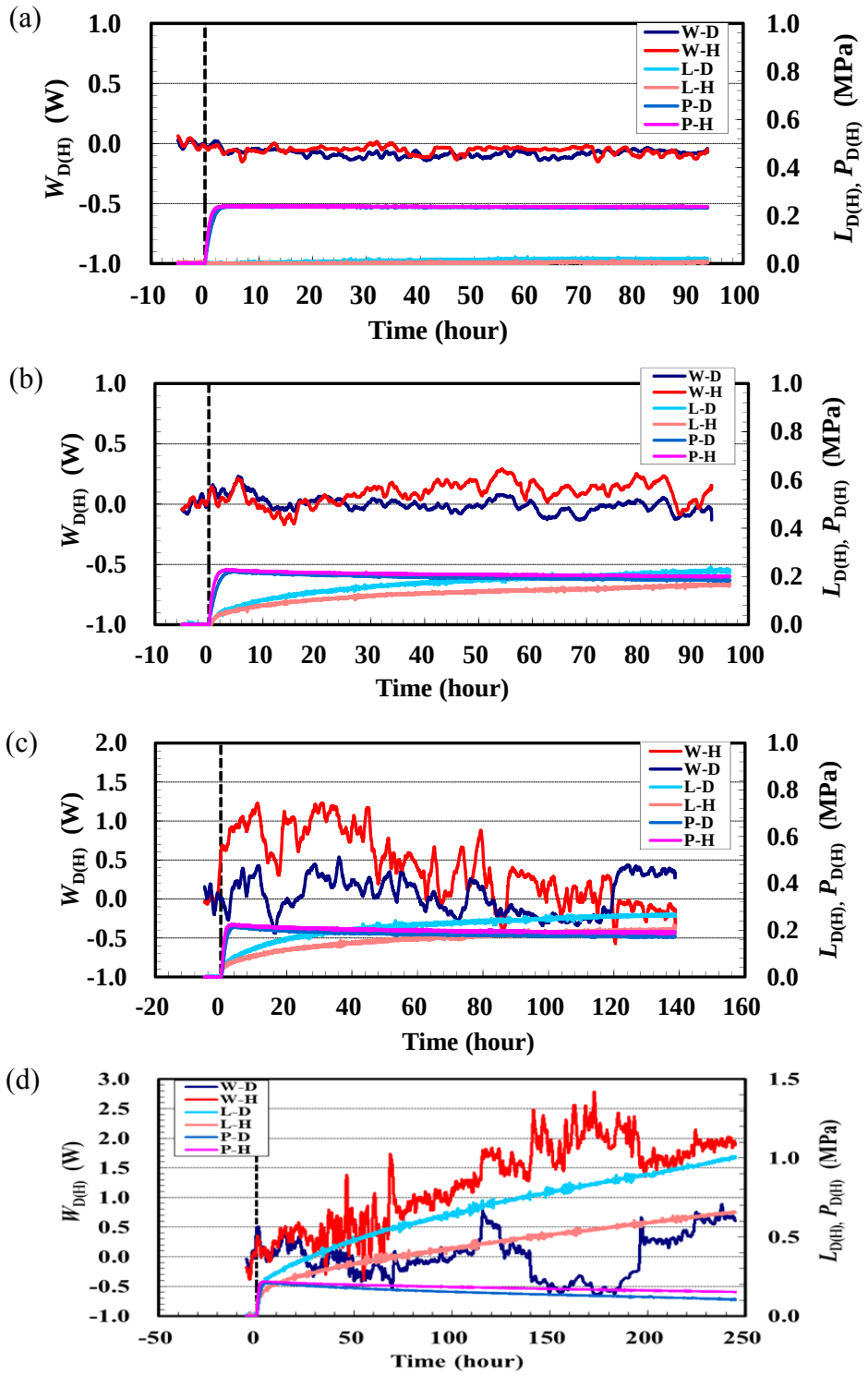

Fig.5. Time-dependent absorption parameters for Ni·Zr oxide compound samples; the run numbers are (a) H(D)-NZ3(4)#5_373K, (b) H(D)-NZ3(4)#5_473K, (c) H(D)-NZ3(4)_523K, (d) H(D)-NZ3(4)#5_573K_2.

3.3. CNZ samples at elevated temperatures

Figures 6-(a) through (d) show the absorption parameters of the Cu(0.08)·Ni(0.36)/ZrO_2 samples in the runs D(H)-CNZ1(2)#5_373K through D(H)-CNZ1(2)#5_573K. Both at 373K and 473K, we didn't observe exothermic temperature change. It is similar to the case of the NZ sample, although at 473K, the loading ratios had very large values reaching about 1.0. At 523K, the loading ratios were one-fifth of those at 473 K. However, the exothermic temperature change appeared clearly in the protium run and continued for about 180 hours. The excess power increased gradually to reach about 2 W (1.0 W/g-Ni). The observed specific output energy E_H approaching 3×10^2 eV/atom-Ni for the S-phase was very large and even increasing in view of the continued positive power.

Also at 573K, although the loading ratios remained almost same as those at 523K, the sample absorption of protium continued for about 100 hours with the maximum output power reaching 2.0 W (1.0 W/g-Ni). The specific output energy E_H exceeding 6×10^2 eV/atom-Ni in the S-phase is too high to be explained only by conventional chemical processes of heat release. This is about twice as large as that of the NZ sample at the same temperature. We infer that the Cu additive-atoms may act as a strong catalyst for hydrogen absorption of the Ni nano-particles.

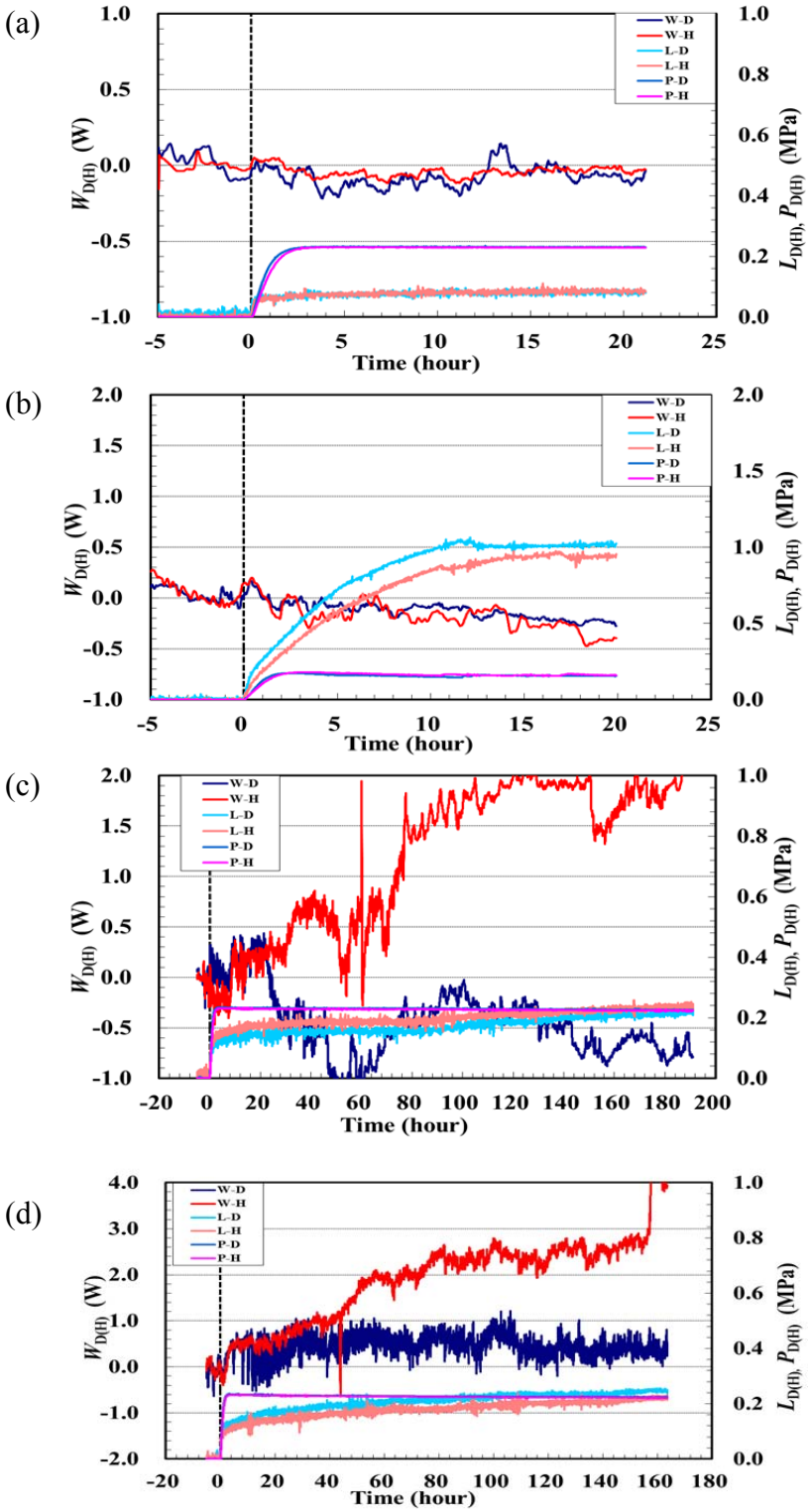

Fig.6. Time-dependent absorption parameters for Cu·Ni·Zr oxide compounds; the run numbers are (a) D(H)-CNZ1(2)#5_373K, (b) D(H)-CNZ1(2)#5_473K, (c) D(H)-CNZ1(2)_523K and (d) D(H)-CNZ1(2)#5_573K.

Quantitative reproducibility of the heat output is not always good. We repeated the CNZ runs to confirm the qualitative repeatability of the phenomena. The reaction chambers A1 and A2 were exchanged for this purpose. Figure 7 shows traces of the absorption parameters in the H(D)-CNZ3(4)_573K run after the exchange. We find that the protium run using A1 chamber yet yields higher power than the deuterium run using the A2 chamber, making us confirm the existence of the exothermic phenomenon in the protium charged sample.

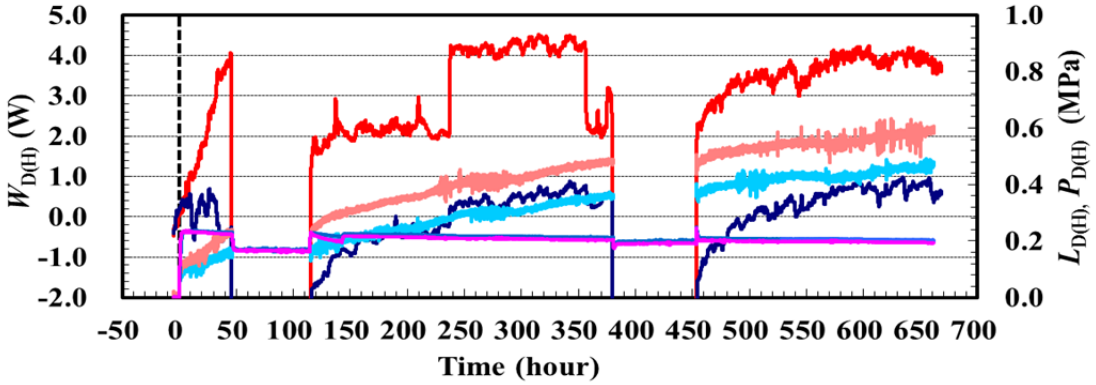

Fig.7. Time-dependent absorption parameters for Cu·Ni·Zr oxide compounds; the run numbers are H-CNZ3#5_573K_2 and D-CNZ4#5_573K_2.

The heater power was intentionally off during the periods from 45 hr to 115 hr and from 373 hr to 454 hr. The data logger failed to retrieve the data of the heater input power in the period from 115 hr to 230 hr. Time-integrated parameters shown below for this run don't include the period from 115 hr to 369 hr.

The loading ratio was H(D)/Ni = 0.60(0.47) at 650 hr, and still increasing. The exothermic temperature change with the maximum output power exceeding 4.0 W continued for long time. The observed integrated value of specific output energy E_H exceeding 8×10^2 eV/atom-Ni in the S-phase is again too high to be explained only by known chemical processes of heat release.

3.4. CNZII samples at elevated temperatures

Now we examine a sample containing almost equal amount of Cu and Ni. Figures 8-(a) through (d) show the absorption parameters in the runs, H(D)-CNZII1(2)#5_373K through H(D)-CNZII1(2)_573K.

Net hydrogen absorption by this sample was observed to begin at lower temperature. At 373K, the loading ratio was H(D)/Ni = 0.42(0.30). These values are larger than those for the NZ and the CNZ samples at the same temperature. However, we didn't observe exothermic tendency at this temperature similarly to the NZ and CNZ samples.

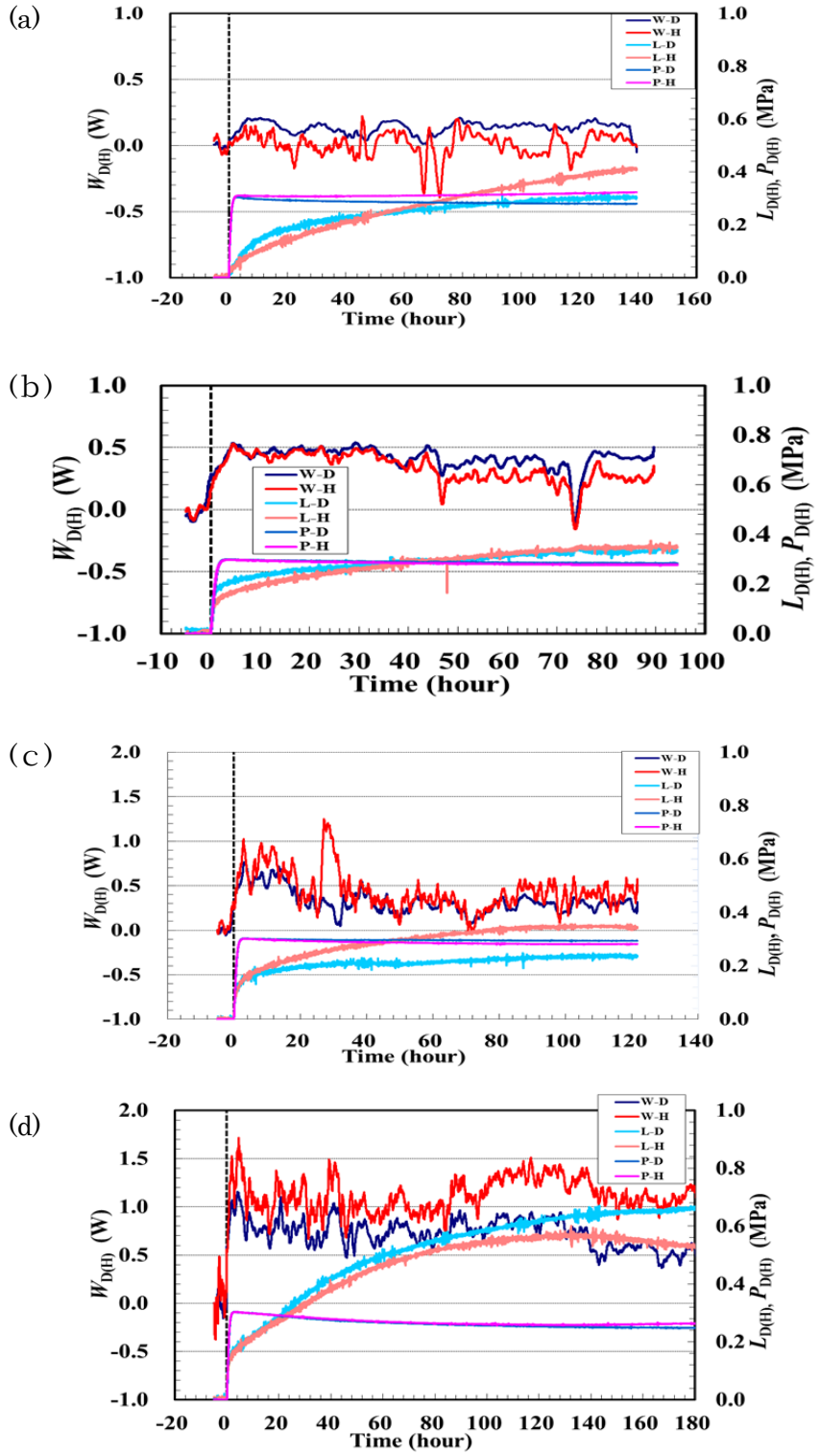

Fig.8. Time-dependent absorption parameters for Cu·Ni·Zr oxide compounds; the run numbers are (a) H(D)-CNZII1(2)#5_373K, (b) H(D)-CNZII1(2)#5_473K, (c) H(D)-CNZII1(2)#5_523K, and (d) H(D)-CNZII1(2)#5_573K_2.

At 473 K, similar amounts of the loading ratio, H(D)/Ni = 0.35(0.33), were observed with appreciable output power of about 0.5 W which is larger than the error range. And at 523 K, the excess power increased to 1 W for the deuterium run, and continued for more than 120 hours, while the loading ratios were almost same as those in the 473 K run. At 573 K, both the loading ratios and the excess power increased further; H(D)/Ni = 0.57(0.67), and $W_{H(D)} \approx 1.5(1.0)$ W for more than 130 hours.

The above-mentioned heat release of the Cu(0.214)·Ni(0.215)/ZrO_2 samples were smaller than those of the Cu(0.08)·Ni(0.35)/ZrO_2 sample at temperatures higher than 500 K. The PNZ2B sample which showed prominent heat release and absorption characteristics has similar composition with a rather small amount of Pd; Pd(0.04)·Ni(0.29)/ZrO_2. Therefore, we infer that the molar ratio of the additive element of binary nano-particle having the catalytic activity should have the optimum portion value of around 1/4 ~ 1/8.

3.5. Pretreatment

In the course of the elevated temperature runs, we have noticed that the temperature and the pressure change in the first 573-K runs showed anomalous behavior. The first 573-K runs for the NZ, CNZ and CNZII samples are shown in Figs. 9-(a) through (c). There are seen negative spikes in the traces of the excess power that are coincident with positive spikes in the pressure traces which are considered to be a result of instantaneous desorption. This kind of behavior of the temperature was never observed in other runs.

It seems possible to assume that there occurs endothermic emission of host atom clusters to produce vacancy clusters in the Ni substrate. Another reason for the negative spikes could be that the samples undergo self-organization or self-reconstruction from isolated particles of Ni(O), ZrO_2 and Cu(O) to a merged structure suitable for hydrogen absorption during the first 573-K runs. Anyway, we regard the first 573-K runs as pretreatment. Necessity of pretreatment, though only thermal treatment without hydrogen, is also claimed by Celani et al. [2] for their Ni·Cu·Mn alloy micro-wires to yield several tens of watt under protium absorption.

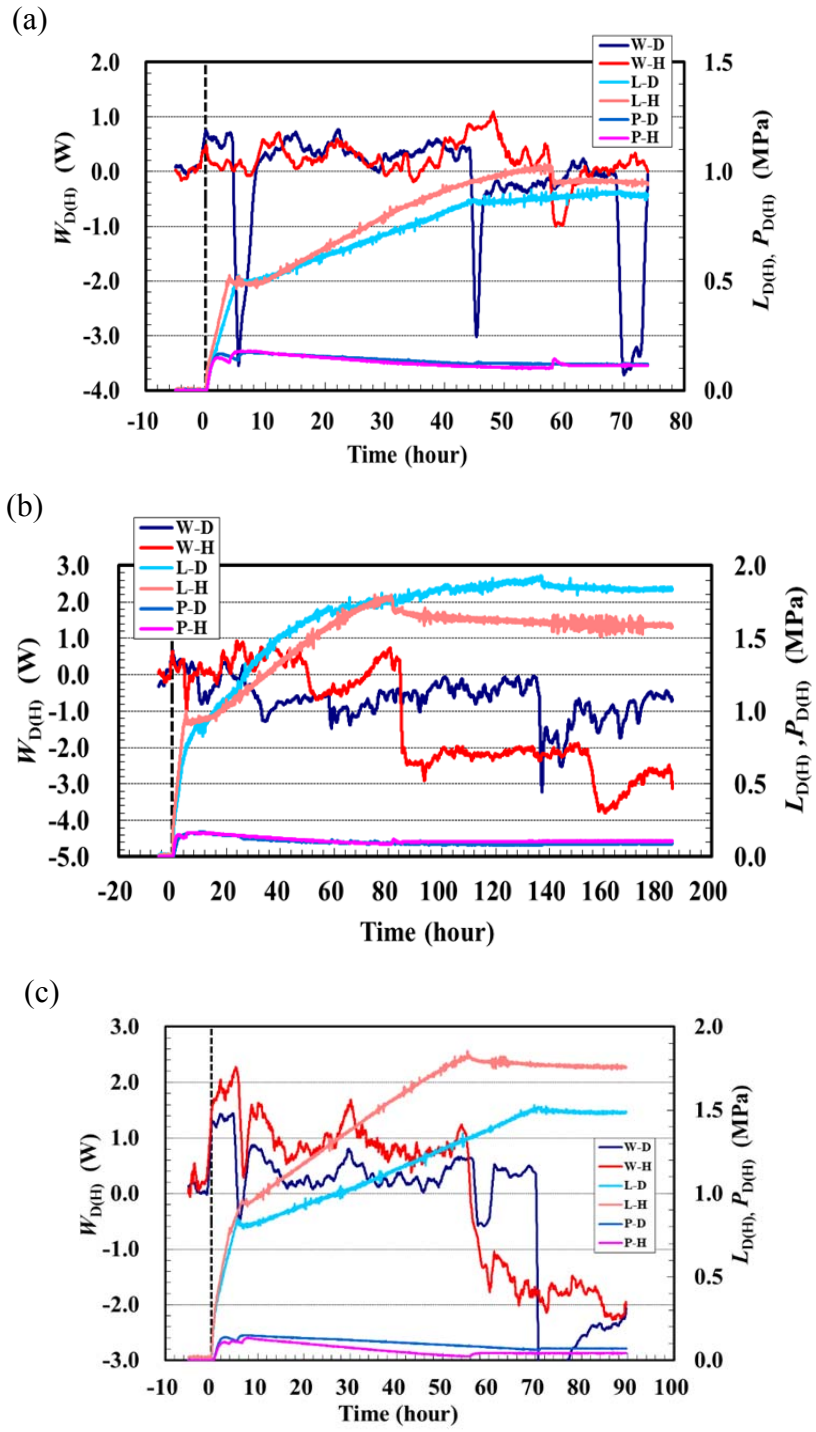

Fig.9. Time-dependent absorption parameters for Ni·Zr oxide compounds; the run numbers are (a) H(D)-NZ3(4)#5_573K (b) H(D)-CNZ3(4)#5_573K (c) H(D)-CNZII1(2)#5_573K.

The desorption process is better analyzed with use of the time-resolved specific sorption energy, or differential heat of hydrogen uptake, $\eta_{D(H)}$, which is defined as the output energy per one hydrogen isotope atom absorbed/adsorbed;

$$\eta(t) \equiv \frac{\int_t^{t+\Delta t} W_{\text{true}}(t)\mathrm{d}t}{L(t+\Delta t)-L(t)} \approx \frac{\int_t^{t+\Delta t} \overline{W(t,\tau)}\mathrm{d}t}{L(t+\Delta t)-L(t)}, \text{ where } \overline{W(t,\tau)} = \frac{\int_t^{t+\tau} W_{\text{mead}}(t)\mathrm{d}t}{\tau}$$

It should be noted that $\eta(t)$ is positive also for the endothermic desorption process.

The time-variation of $\eta_{D(H)}(t)$ values in the H(D)-CNZ3(4)#5_573K_2 runs are shown in figure 10. Very large values of $\eta_{D(H)}(t)$ ranging from 100 eV/H to 600 eV/H and exceeding 100 eV/D are too high to be explained by simple chemical desorption mechanism. We infer that these are the energy necessary for the self-reconstruction or the merging to some nanocomposites of Cu, Ni and ZrO_2 assisted by hydrogen incorporation. We may consider also the possibility of some kind of nuclear events.

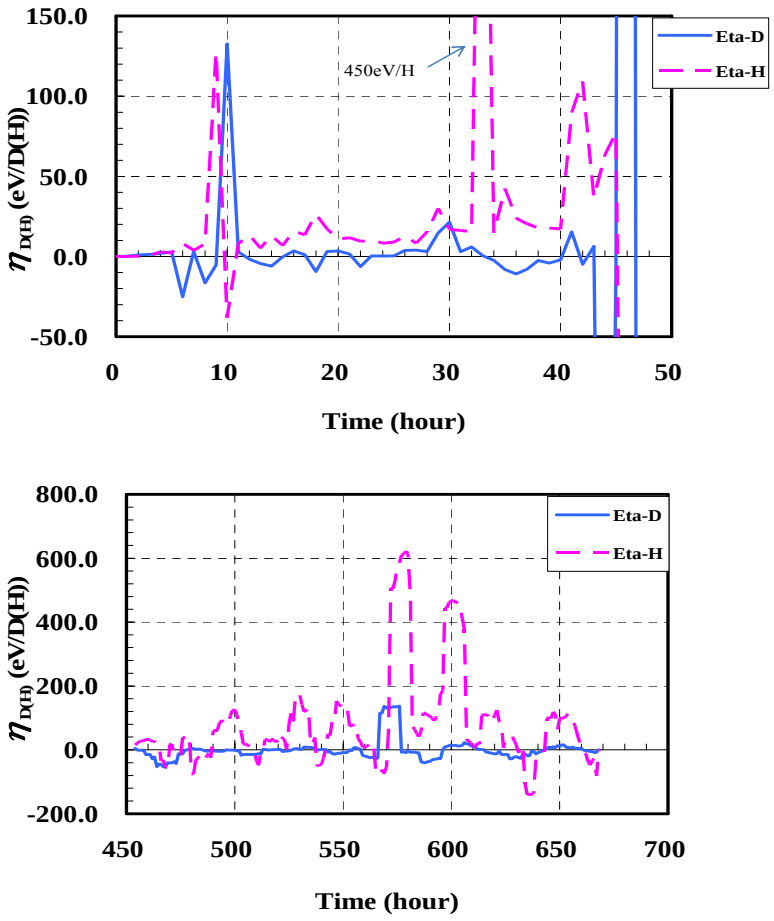

Fig.10. The time-dependent absorption energy, $\eta_{D(H)}$ for the runs H(D)-CNZ3(4)#5_573K_2.

4. Summary

Hydrogen isotope absorption runs showed chemical-like heat release in the T-phase and anomalous excess heat in the S-phase. Figures 11-(a) and (b) are histograms showing the specific output energy in the S-phase of the four runs operated at temperatures 373K through 573K. The following conclusions are derived.

- The Ni-based nano-compound samples showed apparent heat release at temperatures higher than 500 K. As the sample temperature was made higher, the heat release became larger.
- The exothermic tendency was more prominent in the protium runs than in the deuterium runs.
- The integrated heat release of the CNZ and CNZII samples were larger than NZ samples. The optimum value of the Cu/Ni content ratio appears to lie in a range between 1/4 to 1/8 for Cu additive-atoms to work catalytically for the heat release under hydrogen isotope absorption.
- In the 573-K run of the CNZ sample η_H reached 600 eV/H with E_H ~ 800 eV/atom-Ni. These large values can never be explained by known chemical reaction.
- Although some kind of nuclear process seems to be involved in these phenomena, there have been observed no increase in counting rates of neutrons and γ rays over natural background levels up to now.

In the above discussion, we have ignored a possibility that the ZrO_2 matrix could have some contribution to the heat release. In view of the fact that silica-included Pd (PS), or silica-included Pd·Ni (PNS) samples show hydrogen absorption characteristics equivalent to those for ZrO_2-based samples [4], we can assume that the ZrO_2 contribution is not so large at least at room temperature. However, we have no comparison to mention the possibility of ZrO_2 contribution at elevated temperatures. We are now undergoing measurements using NZ samples with various Ni/Zr ratios, the results of which would give a solution to this problem.

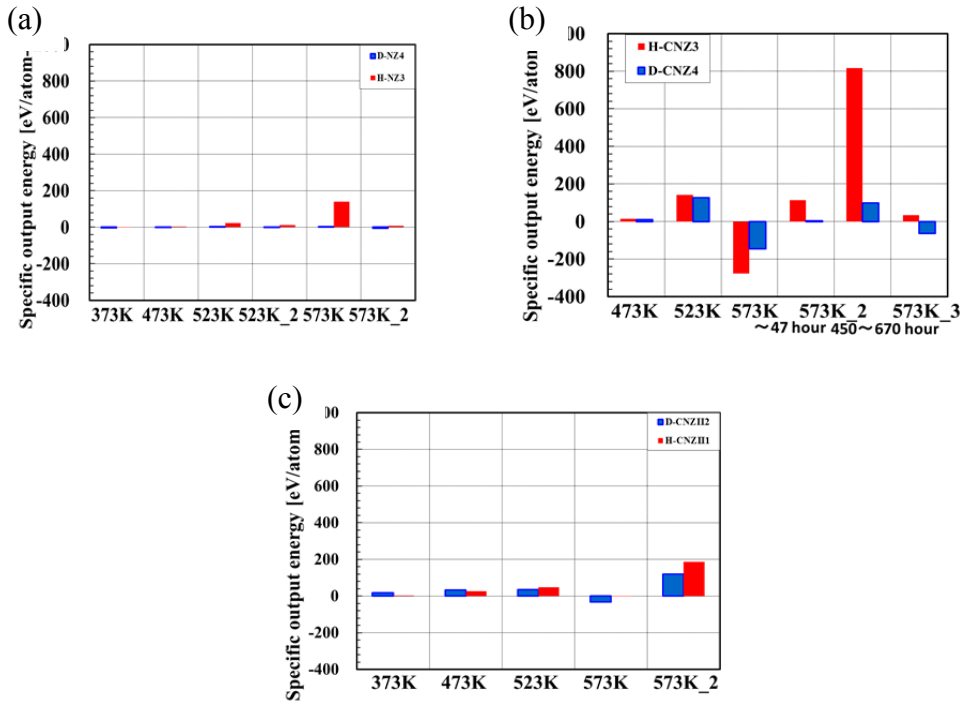

Fig. 11. Specific output energy in the S-phase of the sample (a) H(D)-NZ, (b) H(D)-CNZ and (c) H(D)-CNZII. The graphs include the pretreatment runs which give negative thermal output power as explained earlier.

References

[1] Focardi, S., Gabbani, V., Montalbano, V., Piantelli, F. and Veronesi, "Evidence of Electromagnetic Radiation From Ni-H Systems," Proceedings of the Eleventh International Conference on Condensed Matter Nuclear Science, Marseilles, France, (2004).

[2] F. Celani, *et al*. Cu-Ni-Mn alloy wires, with improved sub-micrometric surfaces, used as LENR device by new transparent, dissipation-type, calorimeter Proceedings of ICCF17, Daejeon, Korea (2012), to be published.

[3] H. Sakoh, Y. Miyoshi, A. Taniike, A. Kitamura, A. Takahashi, R. Seto and Y. Fujita; Proc. JCF11 (2011) 16-22.

[4] A. Kitamura, H. Sakoh, Y. Miyoshi, A. Taniike, Y. Furuyama, A. Takahashi, R. Seto and Y. Fujita; to be published in Proc. JCF13 (the paper JCF13-16 in this meeting).

Hydrogen isotope absorption/adsorption characteristics of mesoporous-silica-included samples

A. Kitamura*[1,2], H. Sakoh[1], Y. Miyoshi[1], A. Taniike[1], Y. Furuyama[1], A. Takahashi[2,3], R. Seto[2] and Y. Fujita[2]

[1]Graduate School of Maritime Sciences, Kobe University, Kobe 6580022, Japan, [2]Technova Inc., Tokyo 1000011, Japan, [3]Osaka University, Suita 5650871, Japan
*kitamuraakira3@gmail.com

The effect of mesoporous-silica-inclusion of Pd nanoparticles (PSII sample) and Pd·Ni nanoparticles (PNS sample) on repeated use for hydrogen absorption characteristics has been examined. The room-temperature runs of as-received PSII samples showed very large loading ratio D(H)/Pd reaching 3.5 and 1st-phase absorption energy E_1 exceeding 2.5 eV/atom-Pd. Based on observation that contribution of the reaction of oxygen pickup from PdO to the loading ratio and the first phase output energy is small, the time-resolved specific sorption energy is evaluated to reveal very large values of about 1 eV/atom-D (or H). It has been confirmed that silica-inclusion of Pd nanoparticles is effective to make the sample reusable to the hydrogen isotope absorption / adsorption.

The PNS samples subjected to room-temperature runs have shown that Pd atoms are acting as a catalyst for hydrogen absorption of Ni nanoparticles, and the energy level of the hydrogen absorption sites, -1.0 eV for H and -1.2 eV for D, is deeper than those in other samples ever tested. Elevated-temperature runs of the PNS sample have revealed existence of another absorption site with rather high barrier energy which causes higher temperature to fill the sites with hydrogen isotopes.

Keywords **-- hydrogen isotope absorption, inclusion, nanoporous-silica, Pd·Ni nanoparticles, .**

I. INTRODUCTION

It is well known that Pd nanoparticles clump together to become agglomerated, when simple nanoparticle samples of Pd are subjected to repeated use for gas-phase hydrogen isotope absorption experiments including baking-out processes. This causes substantial decrease in absorbed amount of hydrogen isotopes and induced heat release in the subsequent use. It has been reported that large heat release with isotopic difference was observed under hydrogen isotope absorption by Pd nanopowders included in the basket structure of mesoporous materials, i.e., zeolite [1], alumina [2] and silica [3, 4] Purpose of inclusion in the basket structure is to prevent agglomeration of nanoparticles of Pd under repeated use.

On the other hand, it has been found that addition of a small amount of Pd to the Ni nanoparticle sample changes the absorption characteristics of Ni drastically to enhance the loading ratio and heat release [5, 6]. The additive Pd atoms are considered to work as a catalyst for hydrogen isotope absorption of Ni nanoparticles.

In the present study we have tested mesoporous-silica-included Pd·Ni nanoparticle (PNS) samples manufactured by Admatechs Co., Ltd., and compared the hydrogen absorption characteristics with those of mesoporous-silica-included Pd nanoparticle (PSII) samples used in references [3, 4] and those of the PNZ2B sample used in references [5, 6, 7]. The PNS sample was fabricated to have a mixture of Pd and Ni with a molar fraction of about 0.01 and 0.06, respectively, in expectation of the similar function of the Pd atoms in the PNZ2B sample.

II. Experimental Apparatus and Procedure

We have used a twin absorption system consisting of two equivalent chambers for hydrogen isotope gas absorption / adsorption experiments. Figure 1 shows a schematic of one-part of the twin system. The samples are put in the reaction chamber, and the outer chamber is evacuated for thermal insulation during hydrogen isotope absorption/adsorption. Sheath heaters with resistance of 37.9 Ω and 53.8 Ω wound around the reaction chambers in the A_1 and A_2 systems, respectively, are used for heating samples in the cases of baking, forced deoxidation, forced oxidation and absorption runs at elevated temperatures. Alumel-chromel thermo-couples are used to measure temperatures.

For the PSII samples, mass flow calorimetry had been employed. The coolant water temperature is maintained constant (within ±0.1 °C) at near-room-temperature with a chiller, and the flow rate is controlled with a digital coolant feeder at a rate of 12 cc/min, which recovers heat with an efficiency of 90.0 ±1.7 %. Calorific power is calculated from temperature difference between the exit and the entrance of water coolant. There is a delay in the response of the temperature difference due to the indicial response with a time constant of 2.2 minutes. The calibrated conversion factor is 0.929 W/K.

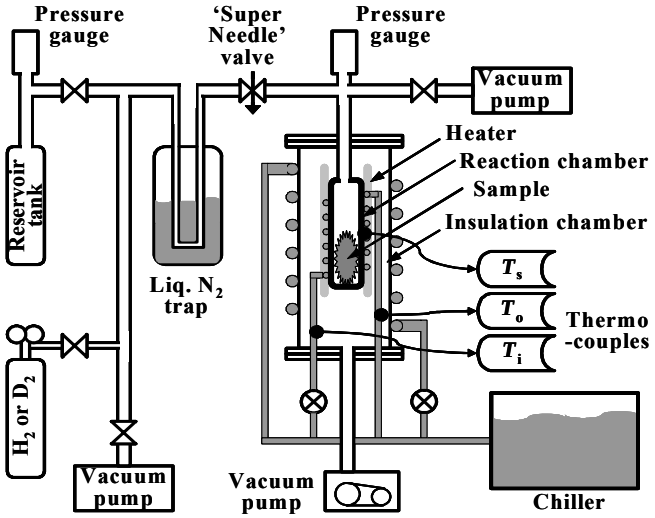

Fig. 1. Schematic of one-part of the twin system.

On the other hand, since we expected that the PNS sample exhibits better performance at elevated temperatures [5], the power measurement in the PNS absorption runs were performed by isothermal calorimetry. In this case, water was taken out of the coolant pipe, and the output power was deduced from the relation between the temperature of the reaction chamber wall and the thermal power input. The thermocouples were rearranged to measure the temperatures of the surface of the reaction chamber at the bottom, the side and the top.

This relation was obtained beforehand in the calibration runs using the power supplied to the heater, and is shown in Table 3 of ref. [8]. The conversion factor to the power depends on temperature, and is 0.16 W/K at room temperature, and about 1.0 W/K at 573 K. Since the major path for the heat loss is absent, the time constant

becomes much larger than in the case of the mass-flow calorimetry. It was measured in the above calibration using a stepwise variation of the heater power to reveal two components in the temperature decay curve with time constant of 16 min and 45 min due to radiation and conduction, respectively. The chamber temperatures were corrected for fluctuation of the heater input power due to instability of AC 100-V power line. The range of this correction was within 0.5 W at the highest.

Figure 2 shows the experimental procedure. The run number expresses the conditions of the sample used in the run, using the letters defined in Table 1. The as-received sample is baked at 440 K for 2 hours in vacuum, and subjected to the D_2 (H_2) absorption run (#1 run). The sample is reused either without any treatment (A or B run) or after the specified treatment; forced deoxidation (#2 run) or forced oxidation (#3 run) or passive oxidation (#4 run). The run at an elevated temperature of *T* K is designated as "#*n*_*T*K" run.

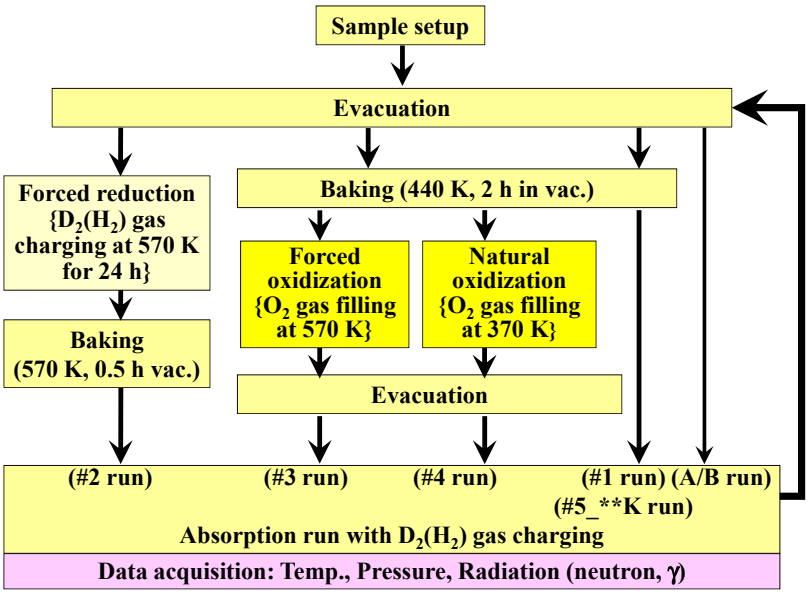

Fig.2. Flowchart of the experimental procedure.

Table 1. Nomenclature for the run number.

#1	Absorption run using a virgin sample
#2	Absorption run after forced deoxidation
#3	Absorption run after forced oxidation
#4	Absorption run after natural oxidation
#*n*A	Absorption run following #*n* without baking
#*n*B	Absorption run following #*n*A without baking
#*n*(N)d	Desorption run by evacuation after an absorption run #*n*(N)
#5_*T*K	Absorption run at an elevated temperature of *T* K

The detailed descriptions of the run procedures are found in other papers; *e.g.*, ref. [4] for the room-temperature runs with mass flow calorimetry, and ref. [8] for the high-temperature runs with isothermal calorimetry.

Figures 3 and 4 show TEM photographs of the PSII sample and the PNS sample, respectively. The PSII sample is composed of mesoporous silica particles with a mean size of 4 μm and nanoparticles of Pd with the size ranging from about 3 nm to 150 nm, with 90 % being 3 - 10 nm. In the PNS sample having a composition with a molar ratio of Pd(0.011)Ni(0.062)Si(0.927), the particle diameter of Pd and Ni ranges from about 3 to 80 nm.

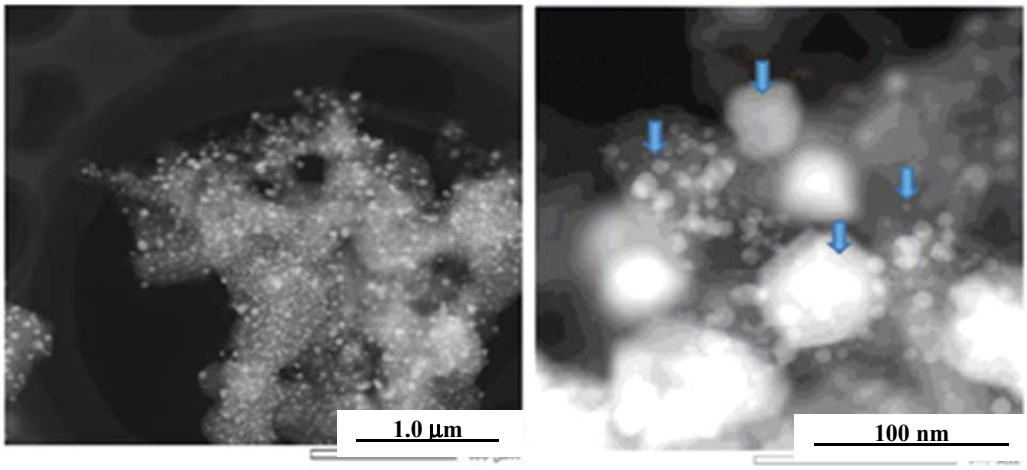

Fig. 3. TEM photographs of the PSII sample.

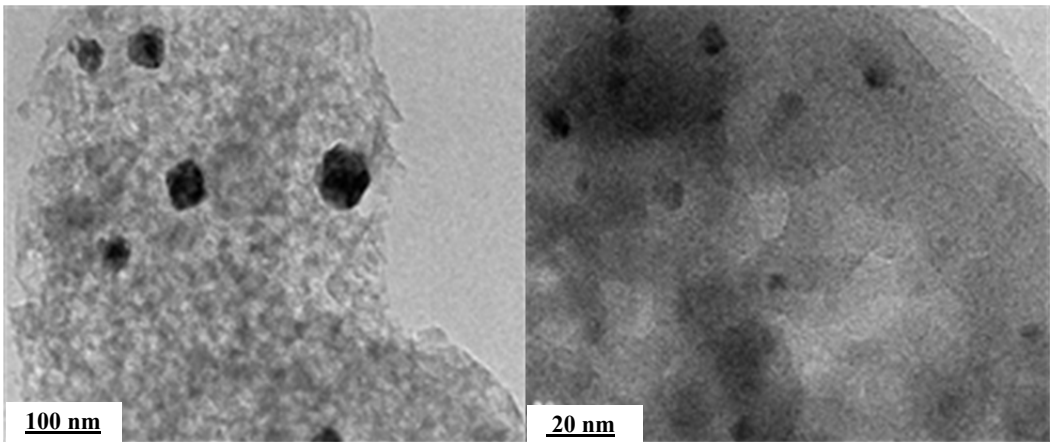

Fig. 4. TEM photographs of the PNS sample.

III. Results and Discussion

A. PSII sample at room temperature

First we review the absorption characteristics of the PSII sample, showing only a few examples of the figures cited from our earlier papers [3, 4]. Figure 5 shows as an typical example of evolution of the heat output, $W_D(t)$ and $W_H(t)$, pressure in the reaction chamber, $P_D(t)$ and $P_H(t)$, and the time-dependent loading ratio, $L_D(t)$ and $L_H(t)$, in the hydrogen isotope absorption run for as-received samples, D-PSII3 and H-PSII4, respectively. The D(H)-PSII3(4)#1 runs have extraordinary large loading ratios $L_{D(H)}(t)$ which reach $L_{D(H)sat}$ (= D(H)/Pd) ≈ 3.6 (3.5) at the end of the exothermic phase. This

phase is thought to be dominated by chemical processes, and is called the first phase in the present work.

The specific heat release, is also very large; $E_1 \approx 2.7$ (2.4) eV/atom-Pd for D (H). The values of the loading ratio are more than 4 times larger than the maximum value of 0.85 ever observed for loading bulk Pd metal, while the values of the specific heat release evaluated as energy per one D (H) atom absorbed give 0.75 (0.69) eV/atom-D(H), which is also about 4 times larger than 0.2 eV/atom-H for bulk-Pd metal, and even a factor of 1.5 (1.4) larger when compared with the surface adsorption energy of 0.5 eV/atom-H for bulk-Pd metal.

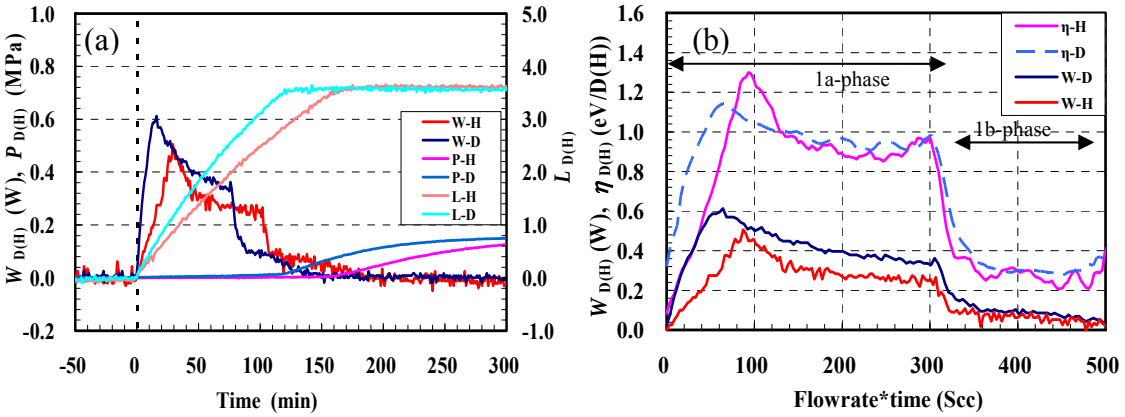

Fig. 5. (a) Evolution of thermal power $W_{D(H)}$, pressure $P_{D(H)}$ in the reaction chamber after introduction of D_2 (or H_2) gas, and the time-dependent loading ratio $L_{D(H)}$; (b) Time-dependent absorption energy, $\eta_{D(H)}$, in comparison with WD(H) in the runs D(H)-PSII1(2)#1.

It has been assumed here that the oxygen pickup reaction contributes almost nothing to the energy E_1 as described in ref. [7]. It is inferred that the oxidation energy Q_O becomes much larger than 0.886eV for the bulk value due to a size effect of a nanoparticle to reduce the oxygen pickup reaction energy substantially. Physical basis of this claim is consistent with our claim that the hydridation energy becomes much larger than those (0.2 eV/atom-D(H) for absorption and 0.5 eV/atom-D(H) for absorption) for the macroscopic particles.

The time-resolved specific sorption energy, or differential heat of hydrogen uptake, $\eta_{D(H)}(t)$, defined as the output energy in a time-interval Δt divided by the number of hydrogen isotope atoms absorbed / adsorbed during the same time-interval Δt [7], is also shown in Fig. 5 as a function of the time-integrated amount of gas flow. Temporal variation of $\eta_{D(H)}(t)$ is very similar to that for the PZ sample [4]. In the #1 run the first phase is clearly divided into two sub-phases, 1a and 1b. In the 1b-phase both η_D and η_H values are nearly equal to about 0.2 eV for the bulk Pd, while they are extraordinarily large in the 1a-phase. However, the #2 run loses the 1a-phase. And in the #3 absorption run of the oxidized sample, the 1a-phase with the large values of $\eta_{D(H)} \approx 1.0$ eV/atom-D(H) is recovered. As for the isotope effect, the value of η_D/η_H sometimes exceeds unity especially in the beginning of the 1a-phase of the #1 runs, and also in the 1a-phase of the #3 run. It seems that η_D/η_H exceeding about 1.1 can hardly be explained solely by chemical isotope effect.

Figure 6 shows the time-resolved relation between the loading ratio $L_{D(H)}(t)$ and the pressure $P_{D(H)}(t)$ for the PSII in comparison with the PNZ2B samples. The latter is a sample of nanoparticles of Pd·Ni compound dispersed in ZrO_2 prepared by B. Ahern with the melt-spinning method [5]. The hydrogen absorption characteristics of the PNZ2B sample was described in ref. [7] in detail. Here we refer only to the $P_{D(H)}(t)$-$L_{D(H)}(t)$ diagram. After hydrogen isotope gas introduction, pressure increases without significant increase in $L_{D(H)}(t)$ up to about 50 kPa, at which the pressure abruptly decreases down to 7 - 8 kPa, making a pressure hump. This pressure hump is considered to be typical of supersaturation followed by condensation of the $D(H)_2O$ vapor into liquid with a vapor pressure of about 4 kPa at room temperature.

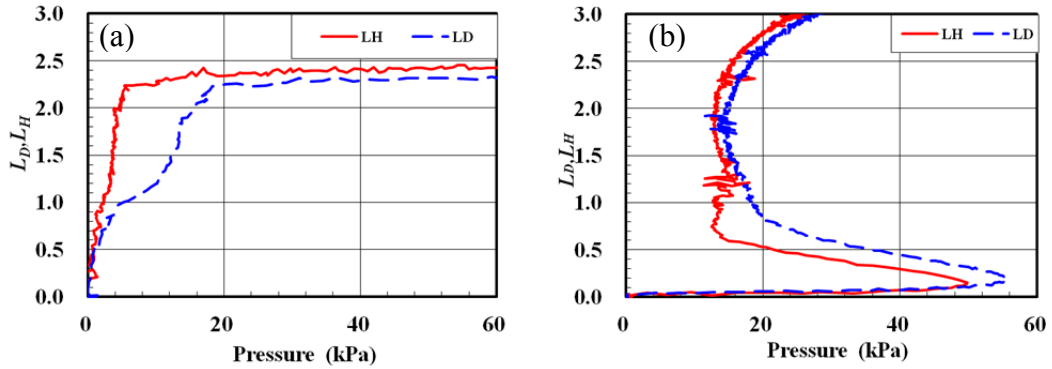

Fig. 6. Comparison of the $L(t)$-$P(t)$ diagram between the D(H)-PSII1(2)#3 runs (a) and the PNZ2B#1 runs (b).

On the other hand, the pressure hump is not observed in the PSII sample runs. After $L_{D(H)}(t)$ increased above 1.0, $P_{D(H)}$ rose above 10 (4) kPa with a large isotope effect, which seems to be never related to oxygen pickup reaction, but is common to bulk absorption [2, 5]. The isotope effect in the pressure could be explained by the difference in velocity leading to a difference in probability of tunneling through the periodic potential barriers between the lattice atoms. It is therefore inferred that $D_2O(H_2O)$ formation is negligible for the present PSII sample.

Figures 7 (a) through (f) show the parameters D(H)/Pd, E_1 and $Q_{D(H)}$ for runs #1 through #4_3 as histograms, which show that the PSII sample can be reused with little deterioration. The PSII sample serves our purpose.

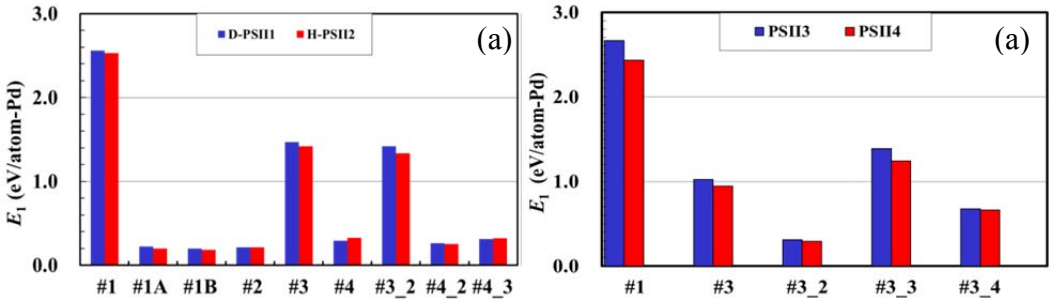

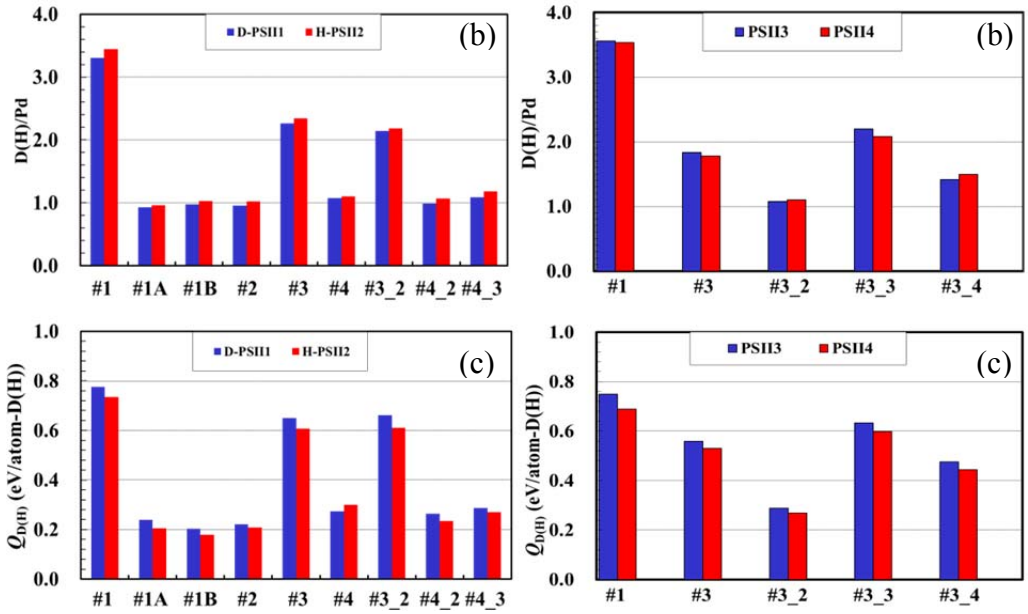

Fig. 7. Loading ratio D(H)/Pd (a), specific heat release E_1 (b), and hydridation energy $Q_{D(H)}$ (c) of the samples D-PSII3 (left) and H-PSII4 (right).

B. *PNS samples at room temperature*

The isothermal calorimetry has been employed in absorption runs for the PNS samples including the room-temperature runs. Figure 8 shows evolution of the absorption parameters in the room-temperature runs using 10-g aliquots of the PNS sample containing 0.78 gram of the Pd_1Ni_6 nanopowders.

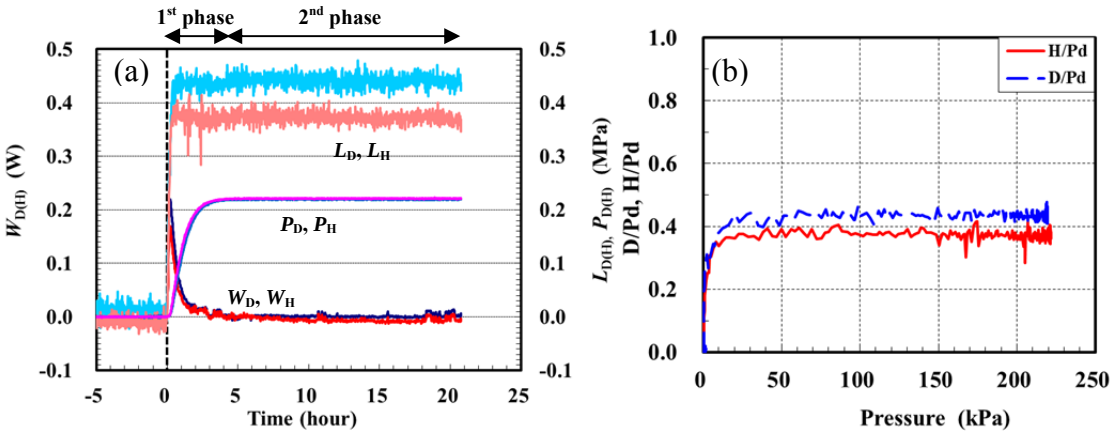

Fig. 8. (a) Time-dependent absorption parameters of the PNS samples in room-temperature runs, D-PNS1#1 and H-PNS2#1. The isothermal calorimetry was employed to obtain the thermal power, $W_{D(H)}$. (b) Time-resolved relationship between the loading ratio $L_{D(H)}(t)$ and the pressure $P_{D(H)}$.

We see clearly sharp 1st-phase peaks of the thermal output power $W_{D(H)}(t)$ with a width of about 35 min, which are coincident with sharp rising-up of the loading ratio $L_{D(H)}(t)$ to the saturation value $L_{D(H)sat}$ (= D(H)/Pd·Ni) = 0.43 (0.39). The powers are

integrated to give the specific output energy $E_{1D(H)}$ = 0.51 (0.39) eV/atom-M, where M stands for the metal host atom with the averaged composition of Pd_1Ni_6. These are reevaluated as the energy per one hydrogen isotope atom absorbed to be $Q_{D(H)}$ = 1.2 (1.0) eV/atom-D(H).

The absorption parameters of the PNS sample are compared with those of the PSII and the PNZ2B samples in Table 2. The values of $L_{D(H)sat}$ and $E_{1D(H)}$ evaluated as per one host metal atom (M) are rather modest in comparison with those for the PSII sample. Here Pd and Ni atoms are assumed to act equivalently in hydrogen absorption. However, if we assume that Ni atoms had no effect on the hydrogen absorption, the values would have been seven times larger, which would be unacceptably large.

Moreover, the $L_{D(H)}(t)$-$P_{D(H)}(t)$ diagrams shown in Fig. 8(b) indicate absence of the 1b-phase, which was observed in most Pd-containing samples, PZ, PP, PB and PSII, with unique exception of the PNZ2B sample [7]. the $L_{D(H)}(t)$-$P_{D(H)}(t)$ diagrams for the PNS samples are very similar to those for the PNZ2B#2 runs. The PNS sample is considered to be qualitatively different from PZ, PP, PB and PSII samples, and similar to the PNZ2B sample in this regard. It is easy to deduce that the major constituent Ni is absorbing hydrogen isotopes. We can conclude therefore that the Pd atoms in the present configuration are acting as catalyzer for hydrogen absorption of Ni nanoparticles.

It is also interesting to note that $Q_{D(H)}$ for the PNS samples are larger than those not only for the PSII sample but also for the PNZ2B sample. The energy level of the hydrogen absorption sites in the present configuration of the PNS sample is deeper than those in the PSII and the PNZ2B samples.

Table 2. Comparison of the absorption parameters at room temperature.

	PSII	PNS	PNZ2B		
	(Pd/SiO_2)	(Pd_1Ni_6/SiO_2)	(Pd_1Ni_7/ZrO_2)		
	Run #1	Run #1	Run #1	Run #2	Run #3
M	Pd	Pd·Ni	Pd·Ni		
L_{Dsat} (= D/M)	3.3	0.43	3.3	2.6	2.8
L_{Hsat} (= H/M)	3.5	0.39	3.3	2.5	3.3
E_{1D} [eV/atom-M]	2.5	0.51	1.4	1.4	1.4
E_{1H} [eV/atom-M]	2.5	0.39	1.3	1.3	1.4
Q_D [eV/atom-D]	0.76	1.2	0.43	0.52	0.48
Q_H [eV/atom-H]	0.72	1.0	0.40	0.51	0.41
1b-phase	yes	none	none	none	none

C. PNS samples at elevated temperatures

Generally, Ni-based samples are known to produce heat at elevated temperatures. We then expected even better absorption characteristics at elevated temperatures also for our PNS sample. Absorption runs at temperatures of 373 K, 473 K, 523 K and 573 K were performed similarly to those for the NZ and the CNZ samples [8, 9]. The absorption parameters are shown in Fig. 9.

In the low temperature runs, the time-dependent loading ratio $L_{D(H)}(t)$ rises up in the beginning of the run, the transition phase (T-phase), to reach saturation in the saturation phase (S-phase). As the temperature goes up higher, absorption in the S-phase

becomes prominent, and the temperatures become noisy, even though the signals from the thermocouples are averaged over periods of one hour. Moreover, the temperatures go down to negative values.

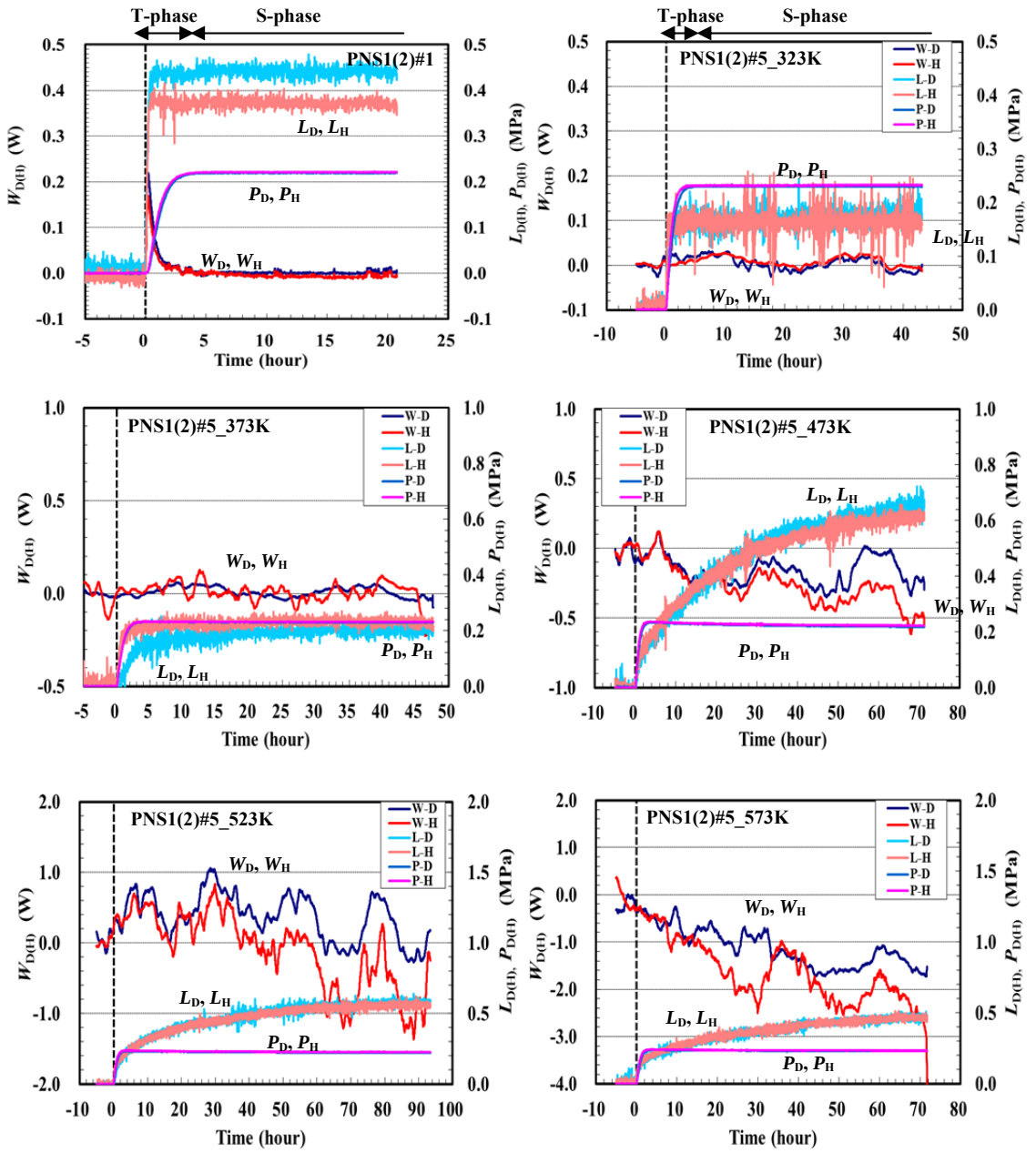

Fig. 9. Time-dependent absorption parameters of the PNS samples in elevated temperature runs at 343 K, 373 K, 473 K, 523 K and 573 K. Those in the room-temperature runs, H(D)-PNS1(2)#1 are also shown for comparison.

The physical reason of the anomalously endothermic tendency, which seems to continue further, is not known at the moment. We stopped the runs, however, before observing strict saturation of both the loading ratio and the temperature to see the magnitude of the anomaly. The loading ratio H(D)/Pd·Ni at the end of the T-phase and at the moment we finished the run are shown in Fig. 10 as a function of temperature

together with time-integrated temperature change, which is regarded as the absorption energy and evaluated per one atom of Pd or Ni. Note the two-orders-of-magnitude difference in the ordinate between the graphs for the T-phase and the S-phase.

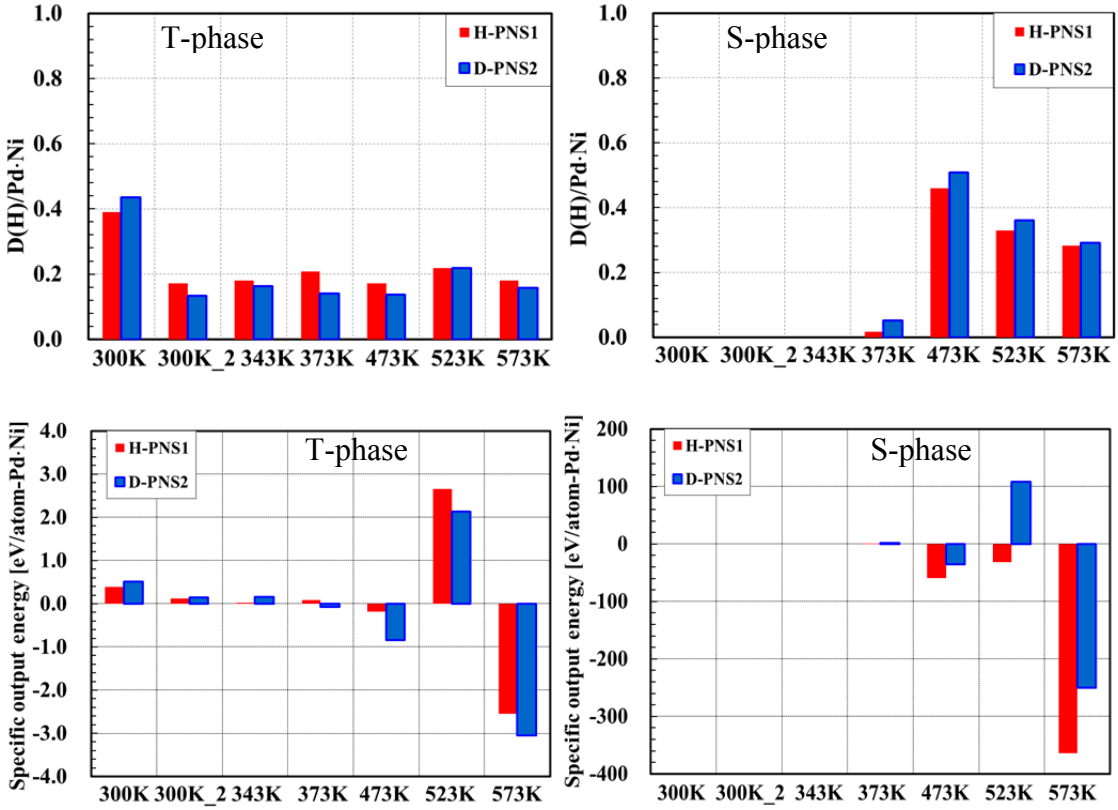

Fig. 10. Temperature dependence of time-integrated absorption parameters of the PNS samples in the elevated temperature runs including the #1 runs at room temperature.

The loading ratio in the T-phase decreases at elevated temperatures, and keeps a constant value of about 0.2, while that in the S-phase grows at elevated temperature with apparent threshold temperature of about 400 K. This infers that the PNS material has another absorption site. The high threshold temperature means that the activation energy for the absorption is rather high, or the absorption site has rather high barrier energy. The energy level of this second site appears to be positive, since we have negative absorption energy in the S-phase except for D-PNS2#5_523K as seen in the figure.

It is, however, premature to conclude the last point of negative absorption energy. The reasons are that the value of the energy depends not only on the temperature but also on the duration of the run, and that the negative value itself exceeding -200 eV/atom-Pd·Ni is far beyond the chemically possible one and is not explainable by any nuclear process. Determination of the energy level of the 2nd site requires extended experiments with higher S/N ratio.

IV. CONCLUSION

--For 1st phase heat evolution in room temperature runs of the PSII samples, we repeat here the conclusion given in ref. [4]:

(1) The as-received PSII samples showed very large loading ratio reaching 3.5 and absorption energy exceeding 2.5 eV/atom-Pd, both being much larger than other Pd nanoparticle samples ever used [7].
(2) Subsequent runs without baking and runs after forced de-oxidation showed almost the same characteristics; D(H)/Pd ≈ 1.0, and E_1 ≈ 0.2 – 0.3 eV/atom-Pd. These are slightly larger than or equal to those of bulk Pd. However, forced oxidation recovered large values of D(H)/Pd exceeding 2.2 and E_1 exceeding 1.3 eV.
(3) Silica-inclusion of nanoparticles of Pd is effective to make the sample reusable to the hydrogen isotope absorption / adsorption without substantial deterioration.
(4) The isotope effect in the heat release in the first phase is rather large.
(5) It has been inferred that contribution of the reaction of oxygen pickup from PdO to the observed loading ratio and the first phase output energy is small. This means that both loading ratio D(H)/Pd and the hydridation energy $Q_{D(H)}$ are rather large compared with bulky Pd samples.

--The PNS samples have also shown interesting absorption characteristics at room temperature:

(6) Pd atoms are acting as a catalyst for hydrogen absorption of Ni nanoparticles.
(7) The energy level of the hydrogen absorption sites, -1.0 eV for H and -1.2 eV for D, in the present configuration is deeper than those in other samples ever tested.

--The PNS samples have been operated also at elevated temperatures to reveal that;

(8) The sample has another absorption site with rather high barrier energy; Absorption into this site requires elevated temperature higher than 400 K.

ACKNOWLEDGEMENTS

The authors appreciate Admatechs Co. Ltd. which provided the silica-included samples.

REFERENCES

[1] D. A. Kidwell, A. E. Rogers, K. Grabowski and D. Knies; Proc. ICCF15, Rome, Italy, 2009.
[2] T. Hioki, N. Sugimoto, T. Nishi, A. Itoh and T. Motohiro; To be published in Proc. ICCF17, Korea, 2012.
[3] H. Sakoh, Y. Miyoshi, A. Taniike, A. Kitamura, A. Takahashi, R. Seto and Y. Fujita; Proc. JCF12 (2012) 10-18.
[4] A. Kitamura, Y. Miyoshi, H. Sakoh, A. Taniike, Y. Furuyama, A. Takahashi, R. Seto, and Y. Fujita, T. Murota and T. Tahara; To be published in Proc. ICCF17, Korea, 2012.
[5] B. Ahern; Private communication.
[6] A. Takahashi, A. Kitamura, Y. Miyoshi, H. Sakoh, A. Taniike, R. Seto, and Y. Fujita; 16th Int. Conf. Condensed Matter Nuclear Science, Chennai, India, 2011; Session of New Energy Technology, 241st ASC National Meeting, Mar. 2011.
[7] Y. Miyoshi, H. Sakoh, A. Taniike, A. Kitamura, A. Takahashi, R. Seto, and Y. Fujita; J. Condensed Matter Nuclear Sci., **10** (2013) 46-62

[8] Y. Miyoshi, H. Sakoh, A. Taniike, A. Kitamura, A. Takahashi, T. Murota and T. Tahara; Proc. JCF12 (2012) 1-9.
[9] H. Sakoh, Y. Miyoshi, A. Taniike, Y. Furuyama, A. Kitamura, A. Takahashi, R. Seto, Y. Fujita, T. Murota and T. Tahara; 17th Int. Conf. Condensed Matter Nucl. Sci., Daejeon, Korea, Aug. 2012.